School of Physics and Astronomy

Electromagnetic Follow-Up of Gravitational Wave Candidates

L. K. Nuttall

Declaration of Authorship

- DECLARATION:
  This work has not been submitted in substance for any other degree or award at this or any other university or place of learning, nor is being submitted concurrently in candidature for any degree or other award.

  Signed: .... (candidate) Date: ....

- STATEMENT 1:
  This thesis is being submitted in partial fulfillment of the requirements for the degree of Doctor of Philosophy (PhD).

  Signed: .... (candidate) Date: ....

- STATEMENT 2:
  This thesis is the result of my own independent work/investigation, except where otherwise stated. Other sources are acknowledged by explicit references. The views expressed are my own.

  Signed: .... (candidate) Date: ....

- STATEMENT 3:
  I hereby give consent for my thesis, if accepted, to be available for photocopying and for inter-library loan, and for the title and summary to be made available to outside organisations.

  Signed: .... (candidate) Date: ....

- STATEMENT 4: PREVIOUSLY APPROVED BAR ON ACCESS
  I hereby give consent for my thesis, if accepted, to be available for photocopying and for inter-library loans **after expiry of a bar on access previously approved by the Academic Standards & Quality Committee.**

  Signed: .... (candidate) Date: ....

Summary of Thesis

Observations of astrophysical systems in different wavelengths can reveal insights in to systems which are not available from a single wavelength. The same can be expected from multi-channel observations of systems which also produce gravitational waves (GWs). The most likely source of strong, detectable GWs, which will also produce an electromagnetic (EM) signature, is the merger of compact objects containing neutron stars (NS) and black holes (BH), namely NS-NS and NS-BH systems. The focus of this thesis is to summarise current and past efforts to detect an EM counterpart of a GW event, with emphasis on compact merger sources.

To begin, the formulation of GWs in general relativity is briefly discussed, as well as the main classes of GW sources. The global networks of GW interferometers in the recent past and near future are described, together with brief explanations of operational principles and the main challenges GW detectors face to make a confident detection.

Current literature is reviewed to give a brief summary of the most promising sources which produce both GW and EM signals. Emphasis is given to gamma-ray bursts (GRBs), their afterglows, and kilonovae. In addition a brief description of GW searches triggered by an external source (such as a GRB) is given. A new form of search is then discussed in which GW events are used to point conventional EM telescopes, with emphasis on rapidly slewing, wide field of view optical telescopes. The main challenge in this form of search is that timing information from a network of GW interferometers yields large error regions for the source sky direction making it difficult to locate an EM transient. Therefore a new statistic is presented in which galaxies (taken from a galaxy catalogue) within this search region are ranked. The probability of identifying the host galaxy of a GW signal from NS-NS and NS-BH systems is investigated and results presented for past and future GW detector configurations.

The ROTSE-III telescope system took part in this first search for EM counterparts of GW triggers. With four identical robotic telescopes located across the world it responded to five GW events. Presented is an automation of the ROTSE image processing pipeline which allows large-scale processing and automated validation and classification of candidates. A background study was conducted to better understand the optical transient background and to determine the statistical significance of candidates. Pipeline performance is tested by inserting simulated transients following kilonova and GRB lightcurves in to images; an efficiency study is described. Finally the results of the images taken in response to the five GW events are presented and discussed.

For Dad, Mum, Amy, and Grandma

Ad Astra Per Aspera
'A rough road leads to the stars'

Acknowledgements

To my parents and sister, Amy - this thesis is dedicated to you. Thank you for your constant support, being proud and always believing in me, no matter what I've done. Having the three of you right behind me has meant the world. Also to my family, the Garlands and the Nuttalls, thank you for always asking about my work and when I'm next coming home. I am truly blessed to have all of you in my life.

To Patrick Sutton, I couldn't have asked for a better supervisor...or done this without you! Thank you for being an endless source of knowledge and for your patience and inspiration. Thanks for making me in to the researcher I am today. I hope we get to work together again soon. Also to my second supervisor Stephen "boss" Fairhurst, who has the answer to every question. Thanks for all the discussions, support and nicking my sweeties.

A special thanks goes to David Burton, my master's supervisor, who gave me my first opportunity to work in this exciting field. Thanks for taking a chance on me and developing a project as we went along. It was enormous fun and obviously got me hooked. I wouldn't be here today if it weren't for you.

To the Cardiff Gravitational Wave or "Gravy Wave" Group. A massive thanks to all my office mates throughout my time at Cardiff - Thomas Adams, Thomas Dent, Ioannis Kameretsos, Sebastian Khan, David McKechan, Patricia Schmidt, Andrew Williamson and particularly to Ian Harry and Duncan Macleod. Thanks to Ian for teaching me to use linux the hard way and Duncan for being my partner in crime throughout all our gravy wave adventures. To both of you, thank you for answering all my daft computing questions and being kind when I'm having a blonde moment. To everyone in the office, thanks for the laughs, the discussions, and the backgammon. As well I'd like to thank the rest of the Gravy Wave Group past and present - James Clark, Mark Hannam, Paul Hopkins, Gareth Jones, Erin Macdonald, Chris Messenger, Frank Ohme, Valeriu Predoi, Michael Puerrer, Craig Robinson, Sathyaprakash, and John Veitch. I've been extremely fortunate to work with all you talented people and hope to again soon. Meet you in the bar at the next meeting!

To all you wonderful people in the Cardiff School of Physics and Astronomy, there are too many to name individually. You have made the last three and a half years some of the best of my life. Thanks for all the fun, tea times and gravy wave bashing. I'll smile every time I think of you all and wish you luck in all that you do. In particular I'd like to thank all the postgrad students. We've become a really tight knit team and will miss you, particularly at cake and pub time. I'll have to continue our traditions wherever my life takes me.

It's true what they say, it's not the place but the people and I will miss you all enormously.

To everyone in the LIGO Scientific Collaboration and Virgo Collaboration. Thank you to those who I've been fortunate to work with, in particular the LOOC UP and GEO teams. You've taught me so much and molded my studies. Also to those lovely people who work on completely different things, but we meet over a drink. See you for more fun at future meetings...bring on the first detection.

To my team of examiners - Sathyaprakash, Eric Chassande-Mottin and Carole Tucker. Thanks for the intense discussion, getting the best from me and most importantly you allowed me to prove to myself that I actually know what I'm talking about. Thank you.

To all my friends scattered across the world, thank you for always being there. Particularly the girls - Sarah, Jen, Phoebe, Meg, and Hayley. Thanks for always being proud of me. To everyone in Bolton and Lancaster, especially Lucy, Judd, Jim, and Kerry, who have heard me chat about gravy waves for many years. Thanks for the support and constant interest. Also to Llanrumney ladies netball team. Thank you for the giggles and odd bit of exercise. Finally a special thanks to my lovely housemates throughout my time at Cardiff - Ciara, Rav, Marie, and Nisha. Much love to all.

And finally to Grandma, to whom this thesis is dedicated, I'll keep going as far as I can...

Contents

List of Tables

List of Figures

Co-authored Papers and Results Disclaimer

Some sections of this thesis include co-authored work which has previously been published, in addition to pieces of work which are currently under internal review before publication.

- Chapter 3 presents a ranking statistic to better localise a gravitational wave (GW) source than using timing information from a network of GW detectors alone. Part of this chapter's findings are found in "Identifying the Host Galaxy of Gravitational Wave Signals" [199]. L.K. Nuttall is lead author of this paper.

- Chapter 4 presents an automated image processing pipeline for analysing images taken by the ROTSE telescopes in response to GW triggers. This chapter also presents the analysis of a set of images taken from the ROTSE archives to show performance. This chapter is taken from "Large-Scale Image Processing with the ROTSE Pipeline for Follow-Up of Gravitational Wave Events" [225]. L.K. Nuttall is the lead author of this paper.

- Chapter 5 presents the analysis and results of images taken by ROTSE in response to GW events between September 2 to October 20 2010. The results are currently under review by the LIGO Scientific Collaboration and Virgo Collaboration and are therefore subject to change. Upon completion of this review the results will be presented in a forthcoming collaboration paper [173].

Chapter 1

Gravitational Waves: Theory, Sources, and Detectors

1.1 Introduction

General relativity describes gravity quite differently to classical Newtonian mechanics. Instead of gravity being some force which acts between two bodies, general relativity describes gravity as a curvature of spacetime determined by the distribution of energy-momentum. General relativity was presented in a series of papers, by Albert Einstein, almost a century ago [1, 2, 3, 4]. In these papers the existence of curvature disturbances on a flat and empty spacetime are predicted, which propagate from the source at the speed of light; gravitational waves (GWs). These waves are produced by the acceleration of matter, in a similar fashion to the production of electromagnetic (EM) waves from the acceleration of charge. Unlike EM waves however, GWs interact extremely weakly with matter. In addition GWs attenuate with distance; the amplitude of the wave decreases inversely proportional with the distance to the source. These two factors make detection of GWs difficult, which is why today they have yet to be directly detected.

Hermann Bondi was one of the first to realise the physical existence of GWs. In his gedanken experiment, he argues that there would be a transfer of energy from a GW to two beads moving along a stick (with friction) by an impinging wave as heat would be produced [5]. This was one of the first arguments for the possibility of GW detection.

Indirect evidence of GWs first came about in 1974 when Joseph Taylor and his then research student Russell Hulse discovered the binary system PSR1913+16. This system consists of a pulsar and an unknown compan-

ion, thought to be a neutron star. GW emission by a binary system should remove energy from the system and cause the orbit to decay (for very compact binaries). After four years of observing this system it was announced that the orbital period of the binary pulsar was decreasing, measured to be $(2.435 \pm 0.010) \times 10^{-12}$ seconds per second [6]. The error is in observational accuracy. Over a period of forty years the scientists observed this system and found that the observed decrease in orbital period agreed remarkably well with that predicted from general relativity, to better than 0.3% [7]. This agreement can be seen in Figure 1.1. For the first time this was indirect evidence of the reality of GWs; Hulse and Taylor were awarded the Nobel prize in 1993 [8].
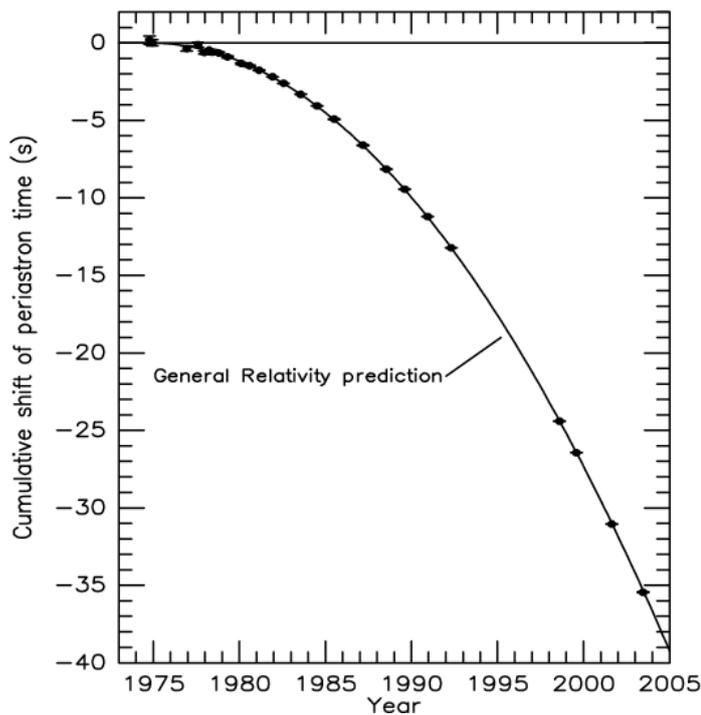
Figure 1.1: The cumulative shift of the periastron time (orbital period) against time for the Hulse-Taylor binary pulsar. The decrease in orbital period is due to the companion arriving earlier at the periastron due to the decrease in separation between them. The points are the observational data and the solid line is the theoretical shift as predicted from general relativity. Taken from [9].

Since then other indirect evidence has come to light, one example being in the form of PSR J0737-3039. This is another highly relativistic binary system which shows a decrease in orbital period due to the emission of GWs. Unlike PSR1913+16 though, both components are seen as pulsars as the orbital plane is almost face on. This therefore enables quite precise and easier tests to be made of general relativity. All observations, such as the change in the periastron and gravitational redshift, have been consistent with the predictions

made by general relativity [10, 11]. In particular it was found that relativistic corrections applied to the Keplerian description of orbital motion agree to within measurement uncertainties by only 0.05% [11].

The quest to directly detect GWs came about due to Joseph Weber who, in the 1960s, developed and built the first resonant bar GW detector [12]. His aim was to monitor a massive aluminium cylinder for minute oscillating vibrations caused by passing GWs. In 1969 Weber claimed that a pair of such detectors were registering coincident signals of astrophysical origin [13]. The scientific community rushed to verify Weber's findings, and as such the era of GW experiments began. Unfortunately no such signals were seen by any other experiments. Today, resonant bar detectors can reach sensitivities four orders of magnitude (in energy) better than Weber's initial detector, but are still only sensitive enough to detect strong sources within our Galaxy or in the immediate galactic neighbourhood (which are rare and no confirmed detections to date) [14]. With the advancement of technology, GW detectors have moved on to an interferometric configuration. Several kilometer scale instruments have been built across the world, such as the Laser Interferometric Gravitational Wave Observatory (LIGO) which operates two detectors in the USA (a more detailed discussion of current and future GW detectors will follow in Section 1.4). These detectors have paved the way for the era of "advanced" GW detectors that are currently being constructed and will begin taking data c. 2015. The Advanced detectors are expected to achieve the first direct detection of GWs.

1.2   The Theory of Gravitational Waves

A brief introduction to GW theory will be presented in this section. This is by no means a comprehensive description, for which the reader is encouraged to consult [14, 15, 16, 17], which this section is drawn heavily from.

1.2.1   Einstein's Equations

The Einstein equations are a quantitative description of general relativity, which describe gravity in terms of spacetime curvature due to the presence of matter and energy. In standard tensor notation they are given as

$$G_{\mu\nu} = R_{\mu\nu} - \frac{1}{2}g_{\mu\nu}R = \frac{8\pi G}{c^4}T_{\mu\nu}. \tag{1.1}$$

$R_{\mu\nu}$ is the Ricci tensor, $g_{\mu\nu}$ is the four dimensional spacetime metric, R is the Ricci scalar and $T_{\mu\nu}$ is the energy-momentum tensor of matter. Due to the symmetry in $R_{\mu\nu}$, $g_{\mu\nu}$, and $T_{\mu\nu}$ the Einstein equations describe ten equalities rather than sixteen.

1.2.2 Linearized Gravity and Gauge Transformations

To consider GWs as simply as possible linearized gravity is used. This is an approximation where non-linear terms of the spacetime metric, $g_{\mu\nu}$, are ignored. This both simplifies the calculations and gives good approximate results rather than the exact solutions. Linearized gravity is valid when an observer is placed sufficiently far away from a source so that the gravitational field is weak. This is known as the weak-field approximation. In this weak field scenario the spacetime metric will differ from its Minkowskian form (which characterises a flat spacetime)

$$\eta_{\mu\nu} = diag\left(-1, 1, 1, 1\right) = \eta^{\mu\nu} \tag{1.2}$$

only by small perturbations, $h_{\mu\nu}$:

$$g_{\mu\nu} = \eta_{\mu\nu} + h_{\mu\nu}. \tag{1.3}$$

It is required that the magnitude of these perturbations are much less than unity ($|h_{\mu\nu}| \ll 1$) to be considered in a weak gravitational field. Working within the linearized gravity regime means that second order or higher terms of $h_{\mu\nu}$ are discarded. Also indices of $h_{\mu\nu}$ can be raised or lowered by multiplication of the flat metric $\eta_{\mu\nu}$, e.g.

$$h^{\alpha\beta} = \eta^{\alpha\mu}\eta^{\beta\nu}h_{\mu\nu}. \tag{1.4}$$

By substituting into the Ricci tensor and the Ricci scalar, the Einstein equations can be shown to depend on the metric perturbation as

$$\begin{aligned} G_{\mu\nu} =\ & R_{\mu\nu} - \tfrac{1}{2}g_{\mu\nu}R \\ =\ & \tfrac{1}{2}\left[\Box h_{\mu\nu} + \partial_\mu\partial_\nu h - \partial_\nu\partial^\alpha h_{\mu\alpha} - \partial_\mu\partial^\alpha h_{\nu\alpha} - \eta_{\mu\nu}\left(\Box h - \partial^\alpha\partial^\beta h_{\alpha\beta}\right)\right] \end{aligned} \tag{1.5}$$

where $\Box$ denotes the d'Alembertian or the flat-space wave operator,

$$\Box = \eta^{\mu\nu}\partial_\mu\partial_\nu = \partial^\mu\partial_\mu. \tag{1.6}$$

Coordinates are arbitrary and if a coordinate system is chosen to exploit the gauge freedoms within the Einstein equations in the weak field, various terms in equation (1.5) can be made to vanish. Consider a coordinate translation which keeps the metric perturbations small, such as

$$x^\mu \rightarrow x'^\mu = x^\mu + \xi^\mu \tag{1.7}$$

where ξ^μ are four arbitrary functions and the derivatives $|\partial_{\mu\nu}\xi^\mu|$ are of the same order as the metric perturbations $|h_{\mu\nu}|$. This therefore preserves the condition $|h_{\mu\nu}| \ll 1$. The form of the metric in this new coordinate system is invariant,

$$g'_{\mu\nu}(x') = \frac{\partial x^\alpha}{\partial x'^\mu}\frac{\partial x^\beta}{\partial x'^\nu}g_{\alpha\beta}(x) = \eta_{\mu\nu} + h'_{\mu\nu} \tag{1.8}$$

with the new perturbation given by

$$h'_{\mu\nu} = h_{\mu\nu} - \partial_\mu\xi_\nu - \partial_\nu\xi_\mu. \tag{1.9}$$

It is also possible to perform Lorentz transformations or rotations of the coordinate system,

$$x'^\mu = \Lambda^\mu{}_\nu x^\nu, \tag{1.10}$$

where the matrix $\Lambda^\mu{}_\nu$ satisfies

$$\Lambda_\mu{}^\alpha \Lambda_\nu{}^\beta \eta_{\alpha\beta} = \eta_{\mu\nu}. \tag{1.11}$$

In this transformation the metric is again invariant and takes the form

$$g'_{\mu\nu}(x') = \eta_{\mu\nu} + \Lambda_\mu{}^\alpha \Lambda_\nu{}^\beta h_{\alpha\beta}(x). \tag{1.12}$$

This rotation will also keep the condition, $|h_{\mu\nu}| \ll 1$. Consequently in linearized theory it is possible to perform translations, rotations or boosts (Poincaré transformations) without varying the Einstein equations.

In linearized theory the trace of the metric perturbation is

$$h = \eta^{\mu\nu}h_{\mu\nu} \tag{1.13}$$

and we can define the trace-reversed perturbation

$$\bar{h}_{\mu\nu} = h_{\mu\nu} - \frac{1}{2}\eta_{\mu\nu}h. \tag{1.14}$$

Therefore the Einstein equations (equation (1.5)) become

$$\Box \bar{h}_{\mu\nu} - \partial_\nu \partial^\alpha \bar{h}_{\mu\alpha} - \partial_\mu \partial^\alpha \bar{h}_{\nu\alpha} + \eta_{\mu\nu} \partial^\alpha \partial^\beta \bar{h}_{\alpha\beta} = -\frac{16\pi G}{c^4} T_{\mu\nu}. \tag{1.15}$$

By fixing the gauge it is possible to work within a gauge coordinate system in which linearized gravity is simplest. Utilising the gauge freedoms already discussed, we can choose a coordinate system in which $h_{\mu\nu}$ satisfies the Lorenz gauge condition,

$$\partial^\mu \bar{h}_{\nu\mu} = 0. \tag{1.16}$$

In this gauge the Einstein field equations reduce to a simplified form

$$\Box \bar{h}_{\mu\nu} = \frac{-16\pi G}{c^4} T_{\mu\nu}. \tag{1.17}$$

Equation (1.17) is written in the presence of matter and energy. In vacuum the Einstein equations become the familiar wave equations

$$\Box \bar{h}_{\mu\nu} = 0 \tag{1.18}$$

as the energy-momentum tensor is equal to zero. These second order partial differential equations will have plane-wave solutions of the form:

$$\bar{h}_{\mu\nu} = A_{\mu\nu} e^{ik_\alpha x^\alpha}. \tag{1.19}$$

$A_{\mu\nu}$ is a constant, symmetric second order tensor and $k^\alpha = (w, k^i)$ is a constant plane wave vector that satisfies

$$k_\alpha k^\alpha = 0 \tag{1.20}$$

$$k^\mu A_{\mu\nu} = 0. \tag{1.21}$$

Equation (1.20) shows that $\omega^2 = |k_i|^2$, and from $|k_i| = \omega/v$ it can be seen that these waves must propagate at speed $v = 1$, whereas equation (1.21) implies the waves are transverse. Therefore general relativity predicts GWs that are transverse plane waves that propagate at the speed of light.

1.2.3 The Transverse Traceless Gauge

The Lorenz gauge proved useful to demonstrate the reality of GWs within Einsteins field equations. There are however further gauge freedoms which can be applied to further simplify the form of $h_{\mu\nu}$. Within the Lorenz gauge, the amplitude of the GW $A_{\mu\nu}$ has six independent components. This does not uniquely fix the gauge, and so it is possible to make a further transformation such that

$$A_{\mu\nu}u^{\mu} = 0 \tag{1.22}$$

$$A^{\mu}{}_{\mu} = 0 \tag{1.23}$$

where u^{μ} is a four-velocity that is constant throughout all of spacetime. The gauge is now fixed, and the following constraints

$$A_{\mu\nu}u^{\mu} = 0 \ , \ \ A^{\mu}{}_{\mu} = 0 \ , \ \ k^{\mu}A_{\mu\nu} = 0. \tag{1.24}$$

make up the transverse-traceless (TT) gauge conditions. In this gauge only the spatial components (in the coordinate system of the observer with four-velocity u^{μ}) are nonzero and the wave perturbation is divergence free and trace free. The trace condition ($A^{\mu}{}_{\mu}=0$) implies

$$\bar{h}^{TT}_{\mu\nu} = h^{TT}_{\mu\nu}. \tag{1.25}$$

If we were to consider a wave propagating in the z-direction then $h_{\mu\nu}$ can be written

$$h_{\mu\nu} = \begin{pmatrix} 0 & 0 & 0 & 0 \\ 0 & h_{+} & h_{\times} & 0 \\ 0 & h^{\times} & -h^{+} & 0 \\ 0 & 0 & 0 & 0 \end{pmatrix}. \tag{1.26}$$

where

$$h_{+} = A_{+}\cos(w(t-z)+\phi_{o}) \tag{1.27}$$

$$h_{\times} = A_{\times}\cos(w(t-z)+\phi_{o}) \tag{1.28}$$

are specific cases of a plane wave solution. General solutions are any two functions of the form $h_{+}(t-z)$ and $h_{\times}(t-z)$. Equation (1.26) shows the metric perturbation has only two degrees of freedom, h_{+} and $h_{\times}$. These two independent components represent the two polarisations of a GW.

1.2.4 How Gravitational Waves Interact with Matter

It has been shown in the previous section that a combination of the Lorenz and TT gauges show GWs to consist of two independent components, namely the + (plus) and ×(cross) polarisations. Within the TT gauge it can be proven however that if a particle were at rest before a GW arrived, it would remain at rest even after the wave arrived [14]. This is only an effect of the TT gauge, therefore it is important to consider a specific gauge or reference frame to understand how a GW interacts with matter. Alternatively consider a coordinate invariant quantity, such as the proper distance between two particles which will be affected by a passing GW. Still working within the TT gauge, if a GW were to propagate in the z-direction, the metric takes the form

$$ds^2 = -dt^2 + (1 + h_+)dx^2 + (1 - h_\times)dy^2 + dz^2 \qquad (1.29)$$

By considering a + polarised GW and two particles at positions $(x_1, 0, 0)$ and $(x_2, 0, 0)$ at some random time t, the metric is

$$ds^2 = (1 + h_+(t - z))(x_1 - x_2)^2 \qquad (1.30)$$

and the proper distance estimated ($h_+ \ll 1$ in the weak field limit) as

$$ds \approx (1 + \frac{1}{2}h_+(t - z))(x_1 - x_2). \qquad (1.31)$$

From this it is evident the change in proper distance is proportional to the GW amplitude. The proper motion between two particles is best illustrated by considering a ring of particles. Figure 1.2 shows how a propagating GW, in the z-direction as already discussed, changes the proper distances between particles in a ring orthogonal to the direction of propagation of the wave. This figure shows the effect of the + (top) and × (bottom) polarisations separately. Note the two polarisations only differ by a 45° rotation.

1.2.5 The Generation of Gravitational Waves

GWs which originate from a rapidly varying source with strong curvature can only be modelled by numerical solutions of the full nonlinear Einstein equations. However to gain a physical understanding for many sources it is sufficient to solve the linearized Einstein equations (equation (1.17)) for a given source $T_{\mu\nu}$. For a distant observer at $\mathbf{x}$, the metric perturbation due to a source
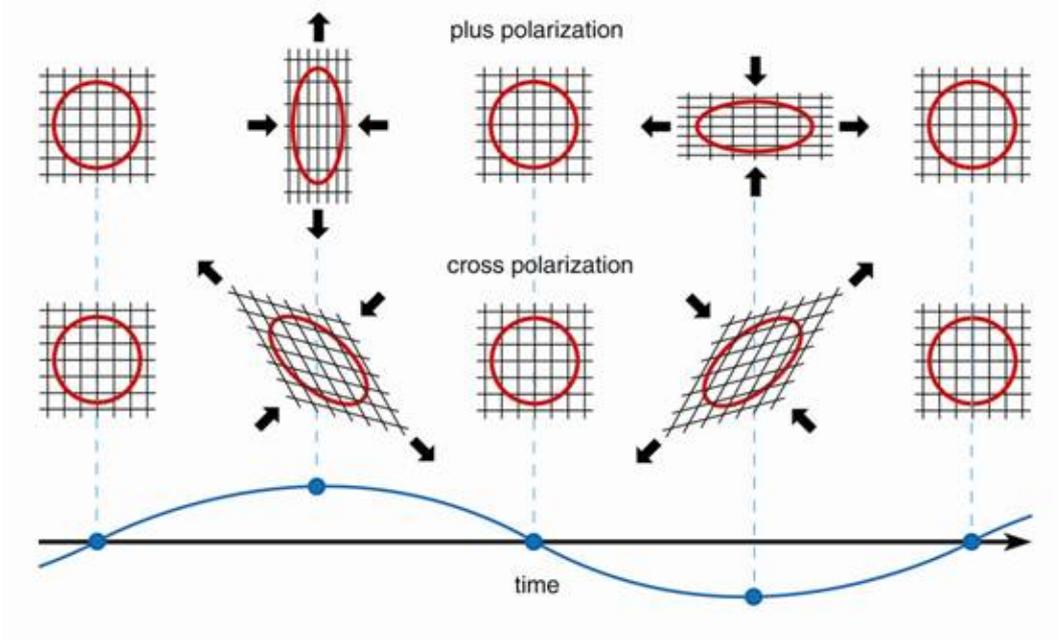
Figure 1.2: The effect on a ring of particles in the $x - y$ plane caused by a propagating GW in the z-direction. The top plot illustrates a $+$ polarised GW and the bottom plot a $\times$ polarised GW. The five deformations show the phase at $0, \frac{\pi}{2}, \pi, \frac{3\pi}{2}, 2\pi$. Taken from [18].

$T_{\mu\nu}$ is given explicitly as

$$\bar{h}_{\mu\nu}(t, \mathbf{x}) = \frac{4G}{c^4} \int \frac{T_{\mu\nu}(t - \frac{|\mathbf{x} - \mathbf{x}'|}{c}, \mathbf{x}')}{|\mathbf{x} - \mathbf{x}'|} d^3x'. \tag{1.32}$$

Choosing the notation $\hat{\mathbf{x}} = \hat{\mathbf{n}}$, where $|\mathbf{x}| = d$ and provided the radius, r, of the source is much smaller than distance from the source (i.e. $r \ll d$), the following approximation can be made:

$$|\mathbf{x} - \mathbf{x}'| = d - \mathbf{x}' \cdot \hat{\mathbf{n}} + \mathcal{O}(\frac{r^2}{d}). \tag{1.33}$$

Keeping the leading term, equation (1.32) can be written as

$$\bar{h}_{\mu\nu}(t, \mathbf{n}) = \frac{4G}{dc^4} \int T_{\mu\nu}(t - d, \mathbf{x}') d^3x'. \tag{1.34}$$

To be simplified further, in the TT gauge, equation (1.34) will take the form

$$h_{\alpha\beta}^{TT}(t, \mathbf{n}) = \frac{4G}{dc^4} |J_{\alpha\beta}(t - d)| \tag{1.35}$$

where

$$J_{\alpha\beta}(t) = \int T_{\alpha\beta}(t, \mathbf{x}')d^3x' \tag{1.36}$$

since the time components can be omitted as defined by the TT gauge conditions (equation (1.24)). To understand the meaning of $J_{\alpha\beta}$, split the energy-momentum tensor $T^{\alpha\beta}$ to separately consider the energy density (T^{00}) and the linear momentum ($T^{0\alpha}/c$). Therefore

$$M(t) = \frac{1}{c^2} \int T^{00}(t, \mathbf{x})d^3x, \tag{1.37}$$

$$M^{\alpha}(t) = \frac{1}{c^2} \int T^{00}(t, \mathbf{x})x^{\alpha}d^3x, \tag{1.38}$$

$$M^{\alpha\beta}(t) = \frac{1}{c^2} \int T^{00}(t, \mathbf{x})x^{\alpha}x^{\beta}d^3x, \tag{1.39}$$

where equation (1.37) is the mass monopole, equation (1.38) the mass dipole and equation (1.39) the mass quadrupole. The equivalent momentum terms are

$$P^{\alpha}(t) = \frac{1}{c} \int T^{0\alpha}(t, \mathbf{x})d^3x, \tag{1.40}$$

$$P^{\alpha,\beta}(t) = \frac{1}{c} \int T^{0\alpha}(t, \mathbf{x})x^{\beta}d^3x, \tag{1.41}$$

$$P^{\alpha,\beta\gamma}(t) = \frac{1}{c} \int T^{0\alpha}(t, \mathbf{x})x^{\beta}x^{\gamma}d^3x. \tag{1.42}$$

There are, of course, higher terms however the highest which shall be considered here is the quadrupole. In linearized theory the mass and momentum monopole are the total mass and momentum of the system respectively. Within this theory the Lorenz gauge condition (equation (1.16)) is valid and considering the divergence theorem ($\partial^{\mu}T_{\mu\nu}=0$) the following identities can be obtained [14]

$$\dot{M} = 0, \tag{1.43}$$

$$\dot{M}^{\alpha} = P^{\alpha}, \tag{1.44}$$

$$\dot{M}^{\alpha\beta} = P^{\alpha,\beta} + P^{\beta,\alpha}, \tag{1.45}$$

$$\dot{P}^{\alpha} = 0, \tag{1.46}$$

$$\dot{P}^{\alpha,\beta} = J^{\alpha\beta}, \tag{1.47}$$

$$\dot{P}^{\alpha,\beta\gamma} = J^{\alpha\beta,\gamma} + J^{\alpha\gamma,\beta}. \tag{1.48}$$

These identities, as well as $J^{\alpha\beta} = J^{\beta\alpha}$, lead to the following identity

$$J^{\alpha\beta} = \frac{1}{2}\ddot{M}^{\alpha\beta}. \tag{1.49}$$

This shows that GWs have no monopole or dipole components, and so the quadrupole moment is the leading order term, as $J^{\alpha\beta}$ is the leading term in the $h^{\alpha\beta}$ expansion. If the higher order terms within the approximation given by equation (1.33) were taken in to account, it can be shown that GWs have higher order components coming from the mass and momentum octopole, as well as other higher order terms [14]. Considering the dominant quadrupole moment only, equation (1.35) takes the form

$$h_{\alpha\beta}^{TT}(t) = \frac{2G}{dc^4}\ddot{M}^{\alpha\beta}(t-d). \tag{1.50}$$

For example, for a GW propagating in the z-direction the $+$ and $\times$ polarisation amplitudes are

$$h_{+} = \frac{1}{d}\frac{G}{c^4}(\ddot{M}_{11} - \ddot{M}_{22}), \tag{1.51}$$

$$h_{\times} = \frac{2}{d}\frac{G}{c^4}\ddot{M}_{12}. \tag{1.52}$$

The total power emitted in GWs by a source is given by the quadrupole approximation as [14]

$$P_{quad} = \frac{G}{5c^5}\langle \dddot{M}_{\alpha\beta}\dddot{M}_{\alpha\beta} - \frac{1}{3}(\dddot{M}_{\gamma\gamma})^2\rangle \tag{1.53}$$

where $\langle...\rangle$ shows the quantity is averaged over time (several wave cycles).

1.3   Gravitational Wave Sources

Any non-axisymmetric mass which accelerates will produce GWs. However the GW community focus their efforts on GWs from some of the most violent

sources which produce the strongest, detectable GWs. One source which unfortunately will never be detected are man-made GWs. If we were to build the largest possible GW emitter on Earth the GWs would be far too small to contemplate detecting. Sathyaprakash et al. [19] estimate for a centrifuge, consisting of two masses of 10^3 kg each, separated by a beam of 10 m, rotating at 10 Hz, GWs with a wavelength similar to the Earth's diameter would be produced. To detect a GW the detector must be at least one wavelength from the source. Therefore this man-made source would produce GWs with amplitude $\sim 10^{-42}$, over 10^{20} smaller than the current GW interferometers are capable of detecting.

In a single GW detector the signal to noise ratio (SNR), ρ, of a GW signal, $h(f)$, is defined as [14]

$$\rho^2 = 4 \int_0^\infty df \frac{|\tilde{h}(f)|^2}{S(f)} \tag{1.54}$$

where $S(f)$ is the noise power spectral density and $\tilde{h}(f)$ is the fourier transform of $h(t)$, given as

$$h(t) = F_+ h_+ + F_\times h_\times. \tag{1.55}$$

Equation (1.55) represents a linear combination of the detector responses (F_+ and $F_\times$) to the two GW polarisations (h_+ and $h_\times$). To be considered interesting a GW signal would need to produce a SNR of at least 8 in a single detector.

We will focus this section on astrophysical sources which emit GWs in the frequency range which ground based GW detectors are sensitive to ($\sim 1 - 10^4$ Hz) and produce GWs with a sufficient amplitude to be detected by current or future GW detectors.

1.3.1 Transient Sources

Transient or "burst" sources are systems which produce strong GWs over a short period of time, typically less than seconds. Such sources can include, for example, supernova explosions, the final stages of compact object merger or gamma-ray bursts (GRB) [20, 21]. For the GW network of LIGO and Virgo between 2009-2010, to detect a GW with strain 10^{-21} between 100-1000 Hz, the minimum GW energy emission detectable for a source at 10 Mpc is $E_{GW} \sim 10^{-2} M_\odot c^2$ to $10 M_\odot c^2$ [22]. Some of the most extreme scenarios (for example see [23] for a description) for GWs emitted by long gamma-ray bursts (LGRBs) have energies $E_{GW} \sim 10^{-2} M_\odot c^2$ to $10^{-1} M_\odot c^2$ in the 50-1000 Hz frequency range. However this scenario is thought to be unlikely (for example

[24]). One of the likely candidates for the central engine of a LGRB is a collapsar, a black hole with an accretion disk (for example [25]). In this model GWs, in the range 100-few 1000 Hz, are expected to be produced during the newborn black hole formation. Another source is a supernova, however it is only thought GWs from this source can be detected within our galaxy, as the GW strain is expected to be $h \sim 10^{-20}$ at 10 kpc [26]. There is however an incomplete understanding of the GW emission mechanisms, in addition to the event rate being low. Therefore within our galaxy we expect one event every 30-100 years [27, 28].

The search for burst signals is performed without assuming detailed knowledge of the GW waveform and is therefore unbiased by any theoretical assumptions. This is known as an unmodelled search which will look for instances of excess power in GW data. As such GWs could be detected from a source which has previously not been considered. For details of recent searches to detect burst sources see [29, 30, 31, 32, 33].

1.3.2 Compact Binary Coalescences

The merger of compact objects such as neutron stars and or black holes are likely to produce strong GWs in the frequency band of the ground-based detectors. These detectors are optimised for detecting mergers of compact objects; the standard performance of a detector is determined by the average distance to which a binary neutron star (BNS) system can be detected. For the LIGO-Virgo network during their "initial" phase (2002-2007) this distance is ~ 15 Mpc and for Advanced LIGO (aLIGO) ~ 200 Mpc [34]. The signal spectrum of GWs goes as

$$h(f) \sim M^{\frac{5}{6}} f^{-\frac{7}{6}} \tag{1.56}$$

where f is the frequency and M is the chirp mass [14]. From equation (1.56) it is evident the distance range is mass dependent. Therefore for binary systems containing heavier objects than a neutron star (such as black holes) the GW detector range increases. It is estimated that the coalescence rate for a BNS system is between 0.01-10 Mpc^{-3} Myr^{-1} [34]. This translates to a detection rate for the initial detectors between $2 \times 10^{-4} - 2 \times 10^{-1}$ per year and $4 \times 10^{-1} - 4 \times 10^{2}$ for the Advanced detectors [34].

As two objects orbit around their common centre of mass, energy and angular momentum will be lost due to the emission of GWs. This will result in the separation between the objects decreasing, causing the GWs to increase

in frequency with time. This resulting GW signal is called a chirp. The process continues for some time ($\sim$Gyr) until the objects eventually merge, radiating, within fractions of a second, GWs up to a few percent of their total mass [14]. Therefore the signal from the inspiral is strongest.

Post-Newtonian expansion and numerical relativity are able to accurately model the waveforms of these systems (for example [20]), meaning that a matched filtering search can be applied to detect GWs from these sources. Prior knowledge of the expected signal can be utilised to eliminate most of the detector noise and search for weaker signals [19]. Details of recent searches which have used this technique can be found in [22, 35, 36, 37].

1.3.3 Periodic Sources

Periodic sources continuously emit an almost monochromatic GW signal, an example being a rapidly spinning, spherically asymmetric neutron star. The limit on the observation of a periodic GW source comes from the total observation time available. The minimum detectable amplitude is proportional to the square root of the observation time. Therefore the greater the observation time, the more sensitive searches become to periodic GW signals.

Spinning neutron stars or pulsars will lose energy over time, partly due to the emission of GWs as well as other mechanisms, however it is uncertain how much energy is released in the form of GWs; we do not know what emission mechanism to expect [38]. As the pulsar loses energy, the spin gradually slows. This is known as spin-down. The best opportunity to detect continuous GWs, using the future GW detectors, is by monitoring the spin-down of the Crab pulsar. Provided all the spin-down energy from the Crab pulsar is emitted in GWs, the GW strain amplitude will be $\sim 1.4 \times 10^{-24}$ [38]. A search for continuous GWs from the Crab was performed using the Initial GW detectors and the results can be found in [38]. Although no GWs were detected, upper limits could be placed on the spin-down energy of the pulsar. It was found that less than 6% of the spin-down energy is radiated in GWs. Details of how the search for periodic GWs is performed as well as recent searches can be found in [39, 40, 41, 42]. The expected strain amplitude from the Crab is below the sensitivity of the Advanced detectors. However the pulsar can be monitored over a period of years which will make the signal within the limit of future detectors.

1.3.4 The Stochastic Background

The Cosmic Microwave Background (CMB) is thermal radiation, a relic of the early Universe some 10^5 years after the Big Bang [14]. Similar to the CMB, there is expected to be a stochastic background of GWs generated from the Big Bang [43]. In addition there could also be a GW background generated from the superposition of a large number of unresolved astrophysical sources [44]. The strength of the stochastic background is quite uncertain. If found the stochastic background could give invaluable information on the moments after the Big Bang (a GW ~ 100 Hz would have been generated $\sim 10^{-22}$ s after the Big Bang [45]) as well as information on the evolution of compact objects, such as neutron stars and black holes, with redshift, and the rate of compact binaries, to name but a few [45]. Details of recent searches and how the search for the stochastic background is performed can be found in [44, 46, 47, 48].

In a search for the GW stochastic background the background is usually described in terms of the GW spectrum:

$$\Omega_{GW}(f) = \frac{f}{\rho_c} \frac{d\rho_{GW}}{df} \qquad (1.57)$$

where $d\rho_{GW}$ is the energy density of gravitational radiation contained in a frequency range f to $f + df$ and ρ_c is the critical density of the universe [47]. Within the LIGO frequency range theoretical models are characterised by a power law spectrum. Therefore a GW spectrum following a power law, α, is assumed [47]

$$\Omega_{GW}(f) = \Omega_\alpha (\frac{f}{100\text{Hz}})^\alpha. \qquad (1.58)$$

From Big Bang Nucleosythesis alone it is expected that $\Omega_{GW} < 10^{-5}$ [19]. Using data taken by LIGO between 2005-2007, a 95% confidence upper limit of $\Omega_0 < 6.9 \times 10^{-6}$ can be placed on the frequency independent GW spectrum ($\alpha = 0$) [47]. The data rules out various evolutionary models of the early universe which are detailed in [47]. The Advanced detector era is expected to be able to probe regions of the stochastic background at $\Omega_{GW} \sim 10^{-9}$ [47].

1.4 Gravitational Wave Detectors

Despite GWs being theorised almost one hundred years ago, it is only in the last fifty years that the search for GWs has been conducted. Initially resonant mass or bar detectors were constructed which typically consist of a cylinder

of aluminium of length $\sim$3 m, a mass of $\sim$1000 kg and a narrow resonant frequency between 500 Hz - 1.5 kHz [19]. In this system a passing GW will transfer some energy to the cylinder which will cause it to vibrate at its resonant frequency. A GW burst with strain $h \sim 10^{-21}$ will cause the mass to oscillate with an amplitude of $\sim 10^{-21}$ m [19]. There are a number of sources of noise which a bar detector must overcome to be capable of detecting a GW of this amplitude (all of which are discussed in Section 1.4.3), the main source being thermal noise. Even modern detectors such as Nautilus and EX-PLORER [49], which are cryogenically cooled, have thermal noise vibrations of amplitude $\sim 10^{-17}$, some four orders of magnitude larger than the GW amplitude. However since a GW burst will only affect the system for 1 ms, the random walk of the thermal noise will give an expected amplitude $\sim 10^{-20}$ m [19]. This is an assumption that the signal is brief ($\sim$ 1 cycle). Once the thermal noise has been overcome, the quantum limit for a bar detector (with a 1 kHz frequency) is approached, which has a limit of $\sim 10^{-21}$ m. These factors indicate that a bar detector would have some difficulty detecting a GW burst signal. As well bar detectors are only sensitive to a narrow band around their resonant frequency. Consequently today laser interferometry is the preferred technique in the quest to detect GWs.

1.4.1 The Global Network of Interferometers

The early 1980s saw the first prototype GW interferometers in Glasgow, Garching and MIT [50], as advancements in laser and mirror technology saw GW detectors turn from bar detectors to interferometers. LIGO was founded in 1992 with construction of the GW observatories in Hanford, Washington (also known as LHO) and Livingston, Louisiana (also known as LLO) beginning in 1996. The Livingston site houses a GW interferometer with 4 km arms (L1) while the Hanford site comprises of two interferometers with 4 km (H1) and 2 km (H2) arms [51]. As well as the three LIGO detectors there is the French-Italian Virgo detector in Cascina, Italy with 3 km arms [52]; the 600 m British-German GEO600 detector in Ruthe, Germany [53] and the TAMA300 detector (300 m arms) in Japan [54].

The LIGO Scientific Collaboration (LSC), comprising of the LIGO and GEO600 detectors, started taking science quality data in 2002 and have since then completed a number of "science runs", starting with S1 through to S5 which completed in 2007. Throughout this "Initial" GW detector period, the sensitivity of the LIGO detectors improved with each run as illustrated in

Figure 1.3. The LIGO detectors achieved design sensitivity during S5 with a strain sensitivity better than $10^{-22}\mathrm{Hz}^{-\frac{1}{2}}$ at a few hundred Hz. During this run the detectors were joined by the Virgo detector forming the most sensitive worldwide network of GW detectors. This joint science run was known as S5/VSR1. A description of the workings of the interferometers during this Initial period is given in Section 1.4.2.
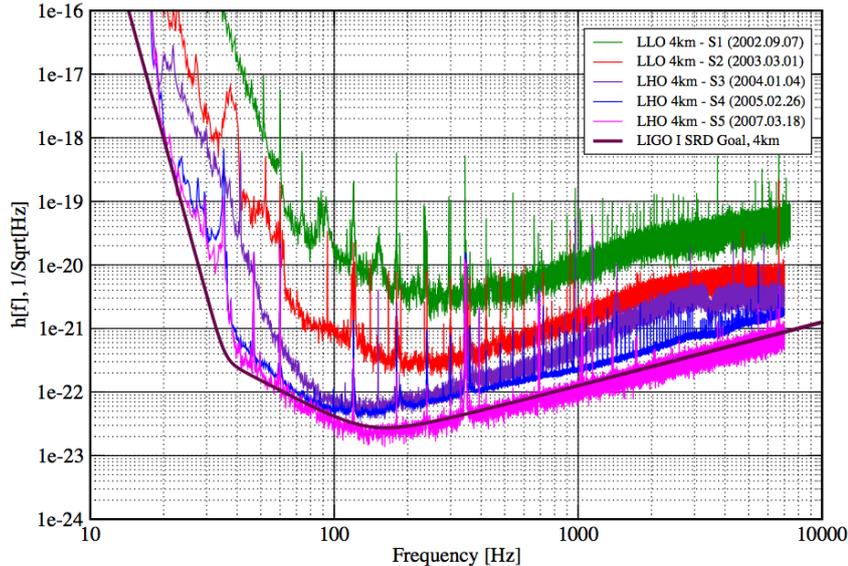
Figure 1.3: The best noise spectral densities as a function of frequency for the LIGO detectors during S1-S5. The design sensitivity is shown by the black curve. The most sensitive frequency range is ∼100-300 Hz. Taken from [55].

After S5 was completed the LIGO detectors (H1 and L1) were taken offline to undergo a number of upgrades to reduce the effect of noise sources (discussed in Section 1.4.3) which hindered the previous science runs. Improvements included the installation of a higher powered laser, the implementation of a DC readout system and output mode cleaner (these systems are discussed in more detail in Section 1.4.2) and improvements to seismic isolation systems [22]. The Virgo detector also went through a similar upgrade phase. During this upgrade period the 2-km detector at Hanford (H2) and the GEO detector were left on line.

Enhanced LIGO and Virgo conducted a science run from July 2009 until October 2010 known as LIGO S6 and Virgo VSR2/3. During this science run the two 4 km LIGO detectors and Virgo detector were all taking data, however the 2-km Hanford detector was left offline. The sensitivity of these three interferometers is shown in Figure 1.4 with the Hanford H1 detector being the most sensitive. At its most sensitive, the H1 detector was able to

detect a BNS system, of mass $1.4 - 1.4 M_\odot$, with a SNR of 8 to $\sim$45 Mpc.
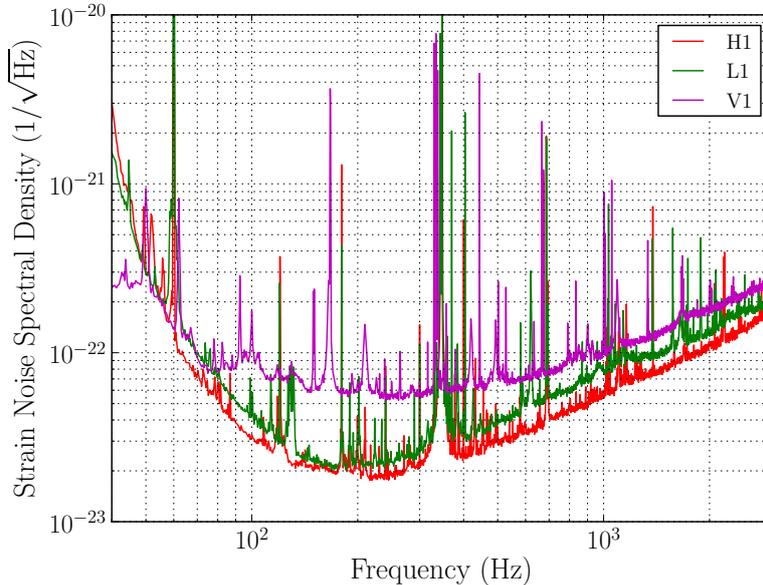
Figure 1.4: The typical strain noise spectral density of the two LIGO (H1 and L1) and Virgo (V1) detectors during S6,VSR2/3. Taken from [22].

Since the completion of S6,VSR2/3 the LIGO and Virgo detectors once again went offline to undergo a more thorough upgrade to the Advanced detectors. aLIGO [56] and Advanced Virgo (AdV) [57] are expected to be approximately ten times more sensitive in amplitude than the original detectors and directly observe GWs for the first time. The three detectors are currently within this upgrade phase and the aLIGO detectors are expected to perform their first science run in 2015, with AdV joining in 2016 [58]. When the Advanced detectors come back online they are expected to have sensitivities comparable to their Enhanced counterparts. It will take several science runs and commissioning phases over the course of a few years for the Advanced detectors to achieve design sensitivity. The expected progression of the Advanced detector sensitivities is illustrated in Figure 1.5.

The original plan for Advanced LIGO was that the 2 km H2 detector be upgraded to an Advanced detector with 4 km arms, meaning that two identical interferometers were to be operated at Hanford. However there is great scientific benefit if GW interferometers are built at different locations across the world, in particular, a network with long baselines greatly improves source localisation. Therefore in 2011 LIGO and the IndIGO consortium in India proposed installing the Advanced H2 detector at a new observatory in India (LIGO-India) [58]. It is expected this installation will go ahead and that a
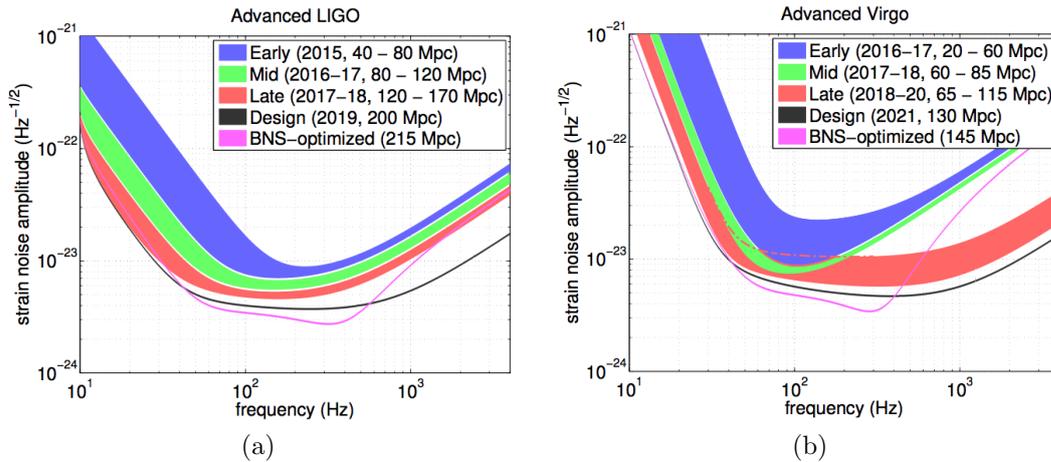
Figure 1.5: One possible evolution of the (a) aLIGO and (b) AdV expected strain sensitivities with frequency. The curves are shown for early, middle, and late commissioning periods, in addition to the final design sensitivity and the BNS-optimised sensitivity. The target date to achieve these sensitivities is shown as well as the average distance a BNS signal could be seen. Taken from [58].

four detector network (H1, L1, V1 and LIGO-India) at full sensitivity will be operating c. 2022 [58].

1.4.2 Operating Principles of Gravitational Wave Interferometers

A Simple Interferometer

It was Michelson and Morley who first used an interferometer to prove the non-existence of the ether in 1887, and it is on a simple Michelson interferometer which modern GW interferometers are based. An interferometer measures any change in the difference between the length of two orthogonal arms. In Section 1.2.4 it was shown that GWs have two polarisations which cause the proper distance between two particles to stretch and squeeze in perpendicular directions. Therefore if a GW were propagating normal to the plane of the interferometer, it would induce changes in the length, of opposite sign, in the two arms.

A GW interferometer in its simplest form is a Michelson-type interferometer, where monochromatic light from a laser is perfectly split in two beams (by a beam splitter) and then sent along two arms that are orthogonal to one another. The light is then reflected from mirrors at either end of the arms

and sent back to the beam splitter where they recombine and the resulting beam is read at the photodetector as illustrated in Figure 1.6. The passing GW will change the relative length of the arms, changing the path length or phase of the light beams, thereby changing the interference pattern read at the photodetector.
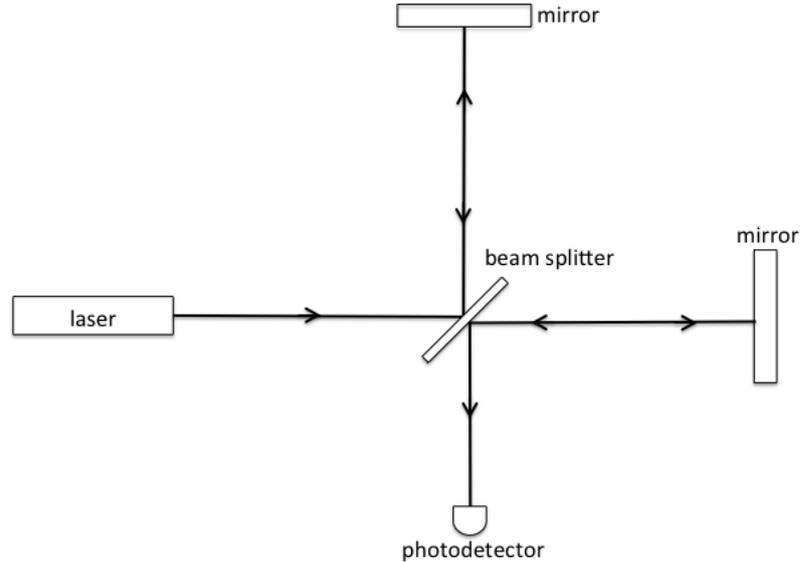
Figure 1.6: A Michelson-type interferometer - a simplified layout of a GW interferometer.

To estimate the amount of power at the photodetector, the electric field incident at the beam splitter may be written as

$$E_0 e^{-i w_L t + i \mathbf{k}_L \cdot \mathbf{x}} \tag{1.59}$$

where the subscript L denotes the laser, w_L is the frequency of the laser ($w_L = |\mathbf{k}_L|$), $\mathbf{k}_L$ is the wavenumber of the laser light and E_0 is the amplitude of the electric field. By considering a photon exiting the laser and arriving at the beam splitter, a part of the electric field will be transmitted by the beam splitter and will travel the x-arm to the mirror at a distance of L_x where it will be reflected back to the beam splitter. The same can be assumed for the other part of the electric field which is reflected by the beam splitter and travelled the y-arm. The two electric fields will recombine at the beam splitter at some time t given by [14]:

$$E_1 = -\frac{1}{2} E_0 e^{-i w_L t + 2 i k_L L_x} \tag{1.60}$$

and

$$E_2 = \frac{1}{2} E_0 e^{-i w_L t + 2 i k_L L_y}. \tag{1.61}$$

It is important to note the phase change due to travelling the length of the arms twice. The total electric field is a superposition of the electric field from the two arms (i.e. $E_{out} = E_1 + E_2$) and can be written as

$$E_{out} = -iE_0 e^{-iw_L t + ik_L(L_x + L_y)} \sin[k_L(L_y - L_x)]. \qquad (1.62)$$

Therefore the power measured at the photodetector is

$$|E_{out}|^2 \propto E_0^2 \sin^2[k_L(L_y - L_x)]. \qquad (1.63)$$

Equation (1.63) clearly shows that a variation in the arm length difference will cause the power received at the photodetector to change. As well, the power change at the photdetector is $\propto hL$. Therefore phase changes of $\sim 10^{-12} \times 2\pi$ are needed to be detected.

Initial and Enhanced Gravitational Wave Interferometers

In the previous section a simple interferometer was described, however there are many additions and modifications to this basic system to make the detection of GWs a reality (i.e. to attain sensitivity for $h \sim 10^{-22}$ or smaller). Figure 1.7 is a schematic of the layout for the LIGO interferometers during the Initial and Enhanced phases of operation (for a more detailed discussion of the detectors during these two epochs see [51] and [59]). There are clearly many additions to this layout compared to the simple interferometer, such as the input and output mode cleaners, power recycling mirror and Fabry-Perot arm cavities.

The Initial configuration is set up in such a way that the difference between the two arms causes the recombined light at the beam splitter to interfere destructively, so that no light exits the beam splitter to the photodiode (the "dark fringe"). The two LIGO arms are in fact built with a macroscopic difference of 355 mm, known as the Schnupp asymmetry [61]. The interferometer is operated near its dark fringe by use of signal sidebands.

A GW incident on the interferometer will produce differential phase modulations in the arms. To detect these GW signal sidebands with the photodiode, a local oscillator (LO) field is added to the input laser beam which produces power variations [61]. The GW detectors use a heterodyne detection scheme [62] whereby two strong radio frequency (RF) sidebands are produced by this LO field, separated by 25 MHz from the main beam or carrier light [61]. These LO sidebands will interfere with the sidebands induced by a GW and produce a power modulation at the RF frequency and its amplitude will be modulated
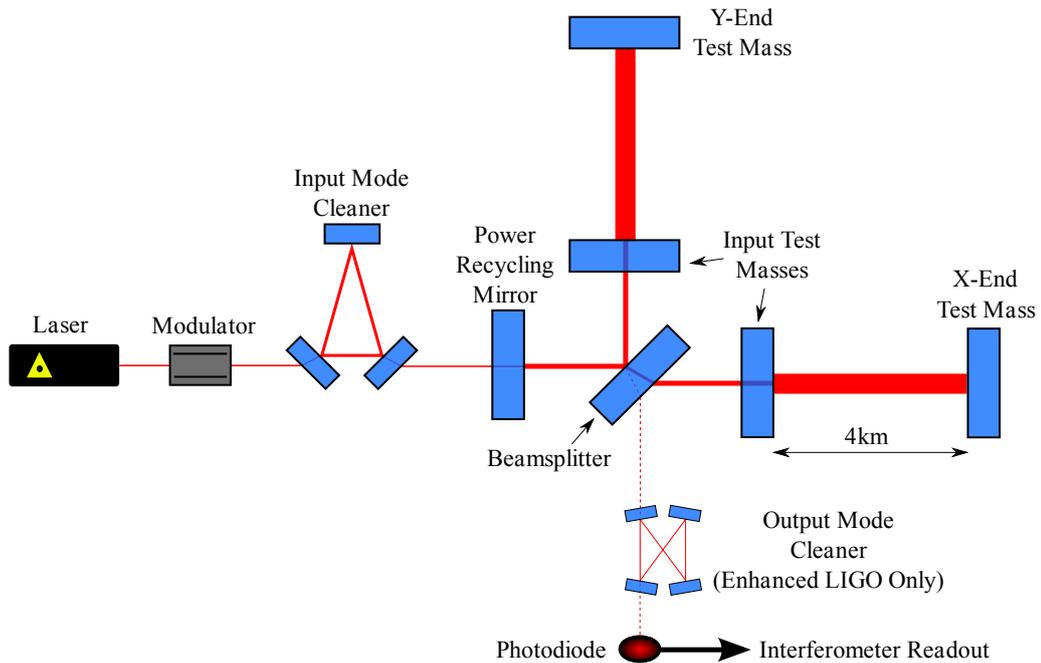
Figure 1.7: A simplified layout of the LIGO detector during Initial and Enhanced LIGO. The output mode cleaner was only added for the Enhanced configuration. Taken from [60].

by the GW amplitude [61]. By electronically demodulating the photodiode signal at the RF frequency the GW signal can be recovered. This is known as RF readout. These sidebands are added to the carrier light at an early stage (before the input mode cleaner) in the interferometeric configuration by an electro-optic modulator as they have many uses beyond just extracting the GW signal. These include sensing the degrees of freedom within the interferometer, such as the length of the power recycling cavity (the mean distance from the power recycling mirror to the two input test masses) and the mean length of the arm cavities (the distance between the input and end test masses) [61].

In the Initial configuration a 10 W laser is used which produces amplitude and frequency stabilised light at 1064 nm [60]. The light then passes through an electro-optic modulator which adds the RF frequency sidebands to the carrier light. The modulated beam is then passed through the input mode cleaner, a triangular configuration 24 m in length [60]. Within this cavity the beam is stabilised in position and frequency by removing higher order beam modes. The beam passes through the power recycling mirror to the

beam splitter, where it is separated in to two and sent up each arm of the interferometer. The optimal length of the interferometer is that which causes the light to spend half the period of the GW within the arms or one quarter the wavelength of a GW signal. Therefore for a GW signal at 150 Hz the optimal length of the arms would nominally be 2000 km [60]. As the LIGO detectors only have arms of 4 km, the Fabry-Perot cavities, formed by the input and end test masses, effectively lengthen the arms by a factor of a hundred by storing light within the arms. The power recycling cavity on the other hand effectively increases the input laser power to the interferometer by a factor of 40, by reflecting light, which is initially reflected back from the input test masses, back in to the interferometer. This is particularly important because the amplitude sensitivity of the detector increases by the square root of the input power at high frequencies (the shot-noise regime, discussed in Section 1.4.3) [60].

To keep the interferometer stable, the orientation and position of each optic is monitored and controlled by actuators. These consist of magnets, that are attached to the back of the optic, and coils (electromagnets), which are affixed to the adjoining support structures [60]. In addition the various length and angular degrees of freedom are monitored via RF modulation/demodulation techniques already described. As well there are many servos used to monitor and stabilise other variables, such as the power of the laser.

In the Enhanced GW detector era, some upgrades were conducted on the interferometer in an attempt to improve the sensitivity. Firstly, the laser power was increased from 10 W to 35 W. In addition the GW readout was switched from RF readout to a "DC readout". In this configuration the power variation measured at the photodiode, due to the interference between the GW induced sidebands and the LO sidebands, reproduces the GW signal [61]. DC readout is a form of homodyne detection [63] where the LO sidebands are produced by introducing a difference in the arm cavity lengths so that carrier light reaches the photodiode. Therefore the interferometer is operated slightly away from the dark fringe ($\sim$10 pm) [60]. Some degrees of freedom within the interferometer are still monitored and measured with RF readout however.

The main hardware difference between Initial and Enhanced LIGO is the addition of a four mirror bow-tie configuration known as the output mode cleaner. The output mode cleaner is installed in the vacuum system before the beam reaches the photodiode. Its objective is to "'clean" the DC readout signal by discarding light from higher order modes and removing RF sidebands

that add noise rather than contribute to the measured signal [60].

Advanced Gravitational Wave Interferometers

The layout of the Advanced GW interferometers is shown in Figure 1.8. Although the layout is very similar to that of the Enhanced detectors, all the hardware is completely new. The same buildings and vacuum will be used however and the Advanced detector will be in a DC readout configuration.
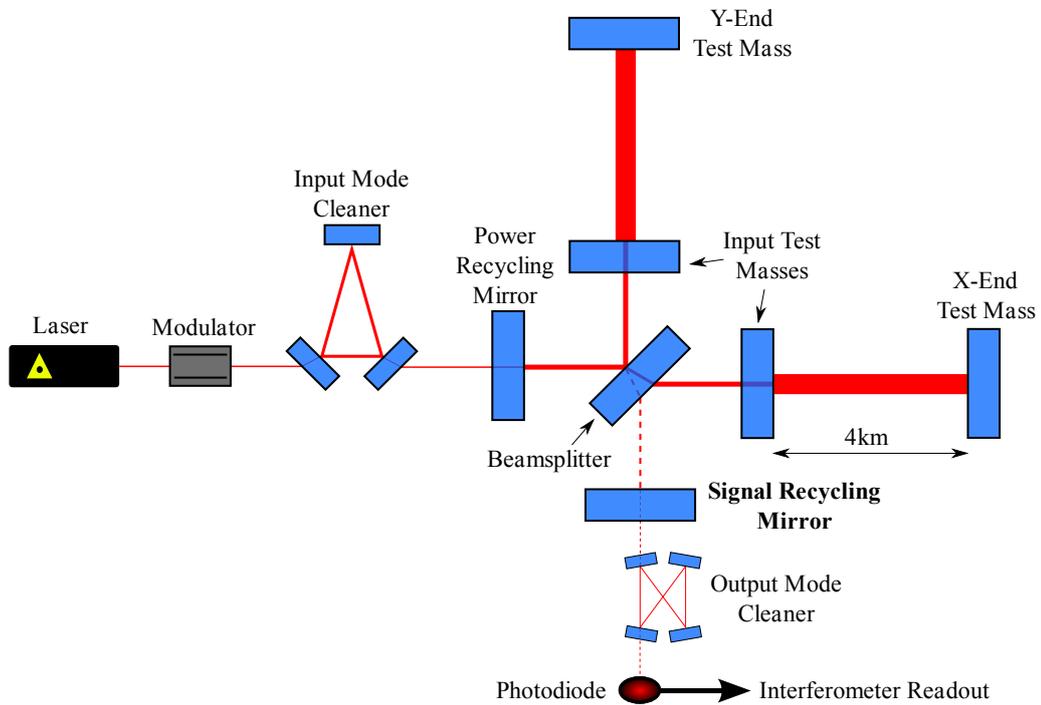
Figure 1.8: A simplified layout of the LIGO detector during Advanced LIGO, taken from [60]. The signal recycling mirror is main hardware addition from Enhanced LIGO (Figure 1.7)

The main addition to the optical layout is a signal recycling mirror. This forms a new optical cavity (between the signal recycling mirror and the input test masses) which allows sidebands induced by a GW to be reflected back in to the interferometer. These sidebands can be stored or extracted depending on the resonance condition of the signal recycling cavity [60]. This cavity allows the sensitivity of the interferometer, at higher frequencies, to be tuned so the detector can be optimised to detect GW signals from specific sources.

1.4.3   Noise Sources

To detect a GW of strain amplitude $\sim 10^{-21}$ with one of the 4-km LIGO detectors, we need to be able to detect a variation in the arm length of order

$$\delta l_{gw} \sim hl \sim 4 \times 10^{-18} \text{m}. \tag{1.64}$$

Unfortunately there are a great many sources of noise which can impede efforts to detect such small length or phase variations, which can be separated in to two classes; stationary and non-stationary noise sources. Stationary noise sources represent those sources of noise which can be predicted and constantly limit the performance of the GW interferometers. The main sources of stationary sources which constantly limit the performance of a detector are shown in Figure 1.9 and are now briefly discussed. For more details of these noise sources see [19, 64].
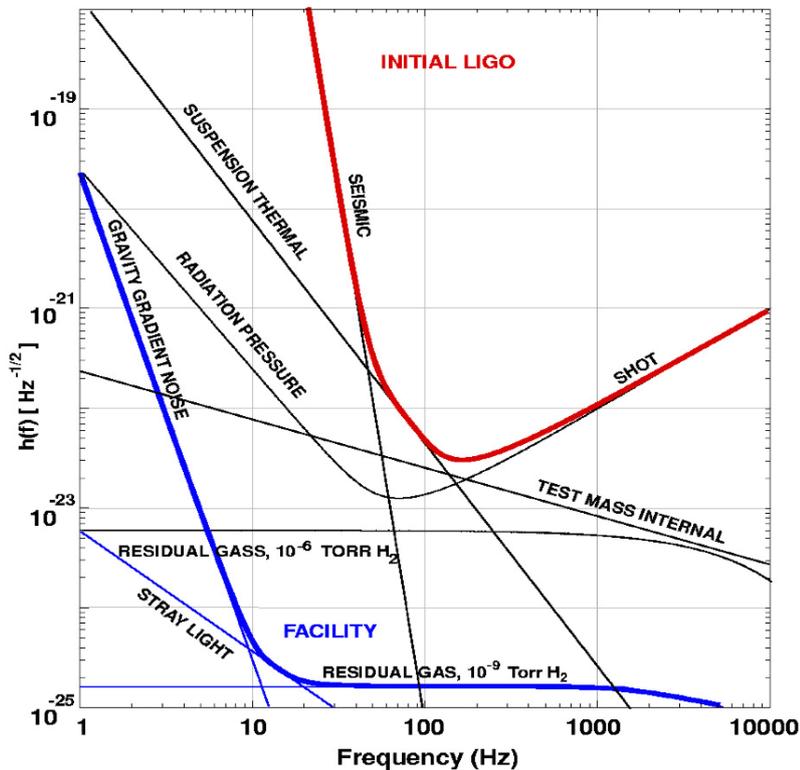
Figure 1.9: The design sensitivity of Initial LIGO (red line) and the main sources of stationary noise which limit this sensitivity. Taken from [65].

Seismic Noise

Ground vibrations produced from seismic activity, man-made objects or even the oceans crashing in to the continent on which the interferometer is located will cause seismic noise. This is the dominant form of noise which limits the sensitivity of current interferometers at the smallest frequencies, particularly below 40 Hz. To combat this form of noise the main optics within the interferometer are suspended from sophisticated isolation systems. These systems are based on multi-stage pendulums, since they are good filters for reducing motion above their natural frequency. These pendulums are located on isolation platforms which are separate from the ground. For Advanced LIGO the seismic noise will still be one of the limiting factors, however more sophisticated technologies, such as Hydraulic External Pre-Isolators (HEPI), will be employed to achieve better sensitivities at the smallest frequencies.

Shot Noise

Photons within the laser beam, because of their quantised nature, will arrive at random times and cause fluctuations in the intensity of the light as measured at the photodetector. This form of noise is the limiting factor at frequencies above a few hundred Hz. More photons will reduce the relative size of the fluctuations (scales as $P^{-\frac{1}{2}}$ where P is the power of the laser). However to achieve a shot noise level below that of the expected phase shift a GW would induce on the interferometer, the highest powered laser currently available is not sufficient. Therefore in addition to a high powered laser, power recycling techniques are employed (power recycling cavity) which increases the amount of power within the interferometer by a factor of $\sim$40 [60]. For the Advanced detector era, as well as a laser which is 18 times more powerful than that used in Initial LIGO, a signal recycling mirror will also be installed and will aid in reducing this form of noise.

Radiation Pressure Noise

Radiation pressure is caused by momentum transferred to the mirrors as photons are reflected by them. To reduce this form of noise (scales with $P^{\frac{1}{2}}$) the laser power must decrease, however this in turn will increase the shot noise. Therefore a balance must be reached which optimises the trade-off between the radiation pressure and shot noise. They are both not at their lowest level, but instead the quadrature sum of the two is minimised. This occurs when

the two noise sources are of equal amplitude at some target frequency.

Thermal Noise

Vibrations of the optics themselves or the suspensions due to their nonzero-temperature limit the sensitivity of an interferometer at a few hundred Hz, its most sensitive region. The resonant frequency of the suspension systems and optics are designed to be far away from the frequencies of interest. For the suspensions this is usually on the order of a few Hz while the natural frequencies of the optics are several kHz. This source of noise is also reduced by ensuring the materials have a high quality factor, which confines most of the noise to a narrow bandwidth around the resonant frequency. This permits interferometers to operate at room temperature. This form of noise could be reduced by cooling the optics, which is proposed in the Japanese KAGRA project [66].

Gravity Gradient Noise

Gravity gradients, caused by the direct gravitational coupling of mass density fluctuations, particularly in seismic motion, to suspended optics are a form of noise which cannot be screened out. Environmental noise comes from man-made and natural sources, such as changes in air pressure. Although this form of noise has not limited the GW interferometers thus far, in the Advanced detector era the sensitivity of the instrument approaches this rigid limit at frequencies ~ 1 Hz and below. The only opportunity to search for GWs below this limit is by placing the detector in space, such is the plan for eLISA/NGO [67].

Non-stationary Noise

Non-stationary noise sources represent those sources which are unpredictable, such as the weather or local disturbances like a truck driving near the detector. The truck would cause the ground to vibrate which would then couple to the mirrors and cause them to move, perhaps causing an effect which may mimic a GW signal. In an attempt to identify these non-stationary sources of noise or "glitches" auxiliary channels are constantly monitored and times in the data with glitches are discarded. The techniques used to identify glitches and remove them from a GW search are described, for example, in [68, 69, 70, 71].

1.4.4 Localising a Source with a Network of Gravitational Wave Interferometers

The performance of a GW interferometer is generally determined by its ability to detect a signal from a BNS system. The greater the detector range, the more sources fall within the search volume which increases the chance of detecting a GW signal. With the GW detectors as they were in the last science run (S6,VSR2/3) the LIGO-Virgo network was capable of detecting a GW signal from a BNS system at a distance of 33 Mpc [34]. This translates to an estimated rate of GW detections within the range $2 \times 10^{-4} - 2 \times 10^{-1}$ signals per year [34]. A second important quantity of measure for a network of GW detectors is its ability to determine the direction to a GW source, for example for follow-up observations.

GW detectors are sensitive to signals from most parts of the sky (except for directions in the plane of the detector) which presents a challenge for determining the source of a signal. One detector alone cannot localise a GW signal, however a network of GW detectors can use the observed time delay between sites to triangulate a position on the sky [72]. If two GW detectors are separated by a baseline $\mathbf{D}$ and a source is located on the unit sphere at a position $\mathbf{R}$, the difference in the signal arrival time between the two detectors is

$$t_1 - t_2 = \mathbf{D} \cdot \mathbf{R}. \tag{1.65}$$

The maximum time delay between detectors is known as the light travel time and between the LIGO detectors is $\sim$10 ms. Therefore the localisation is dependent upon the ability to accurately determine the time the signal was recorded in each detector. Fairhurst [72] gives the timing accuracy of a GW signal to be approximately:

$$\sigma_t \sim \frac{1}{2\pi\sigma_f\rho}, \tag{1.66}$$

where σ_f is the effective bandwidth of the signal and ρ is the SNR. A typical timing accuracy is $\sim 10^{-4}$ s for nominal values of $\sigma_f = 100$ Hz and $\rho = 8$. This sets the scale for source localisation [58].

Triangulation between only two detectors will produce an annulus on the sky of hundreds to thousands of square degrees as shown in Figure 1.10. Additional information regarding properties of the GW signal can limit the locali-

sation to only parts of this annulus. However by adding a third detector to the network two more annuli are created which limit the localisation to only two regions. Using amplitude consistency checks between the detectors it is often possible to discard one of the regions, leaving only one source region which is typically tens to hundreds of square degrees [72]. Adding more detectors at different locations will cause the localisation region to become smaller, particularly if the detectors are separated by large distances across the world. For four sites (aLIGO, AdV and LIGO-India) the localisation region from timing alone is typically expected to be under ten square degrees as shown in Figure 1.11. This network is not expected to be operating at full sensitivity until c. 2022. For comparison, in this same plot, the localisation abilities of the aLIGO-AdV network circa 2016 is shown.
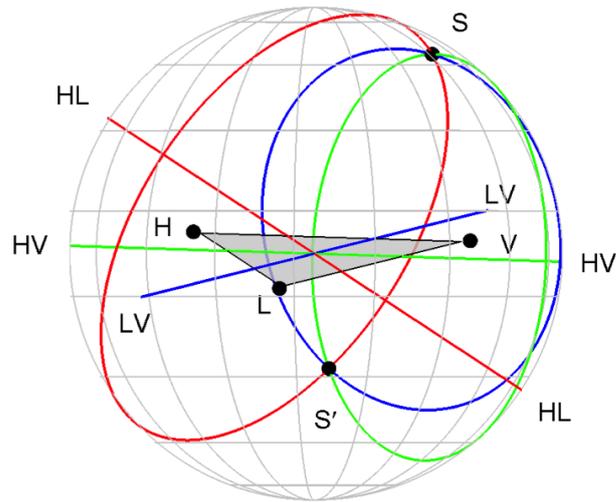
Figure 1.10: Localisation of a source using triangulation for the aLIGO-AdV network. The annuli, formed by the constant time delay between two detectors, intersect in two locations, S (the true source location) and S' (the mirror image with respect to the plane passing through the three detectors). Taken from [58].
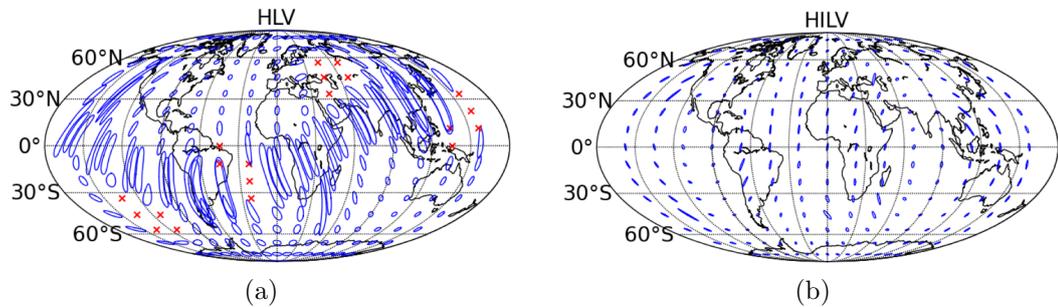
Figure 1.11: The network localisation accuracy for an optimally oriented BNS system at 80 Mpc / 160 Mpc in the early aLIGO-AdV (left) / aLIGO-AdV-LIGO-India era (right). The ellipses show the 90% confidence areas while the red crosses illustrate regions where a GW signal could not be detected confidently. For the left plot these regions are typically tens or hundreds deg^2 whereas the ellipses in the right plot are only a few deg^2 in size. Taken from [58].

Chapter 2

Multi-messenger Astronomy

2.1 Introduction

Multi-wavelength observations of astrophysical systems can yield insights in to the system that are not available from a single wavelength. For example, to understand how galaxies evolve the total star formation rate is needed [73, 74]. The ultraviolet regime will give the rate of unobscured stars, however there are many more which are hidden by dust. The mid/far-infrared wavelengths can penetrate this. It is therefore vital that a combination of wavelengths is used to gain a full understanding. Similarly the detection of gamma-ray-burst (GRB) systems in the x-ray, optical and radio bands have led to the identification of host galaxies as well as their redshifts, in addition to tests of theoretical models [75, 76, 77]. Comparable benefits may be expected from multi-channel follow up of systems that emit gravitational waves (GW).

GW interferometers are inherently noisy; the background noise is non-stationary and contains many transients due to environmental factors. Consequently a confident detection would only be realised if a signal appeared significantly above the background. If there was a signal around the threshold of detectability, where the majority of signals are likely to be, it would be difficult to claim a detection unless there was an associated electromagnetic (EM) transient.

Joint GW-EM observations could also help understand the nature of the source. While GWs trace the bulk motion of mass within a source, EM signals typically come about due to the interaction of matter with the interstellar medium or from out-flows. This will give complementary information concerning a source. This may help identify the nature of some EM phenomena. For example, the nature of short-hard gamma-ray bursts (SGRBs) remains un-

certain. Indirect evidence points towards the progenitor being from an older stellar population than long-soft gamma-ray bursts (LGRBs) [75, 76], namely that of compact binary mergers consisting of neutron stars (NS) and black holes (BH), i.e. NS-NS or NS-BH [78, 79]. However there are a number of other possible sources which could produce a SGRB, such as a giant flare from an extragalactic soft-gamma repeater (SGR) [76, 80]. A joint GW-EM signal could finally confirm or exclude these and other models.

One of the main advantages from the EM signature will be to greatly enhance the precision of the source localisation (typically GW position uncertainties are $\mathcal{O}(10)$ deg^2 or more). This could allow the host galaxy to be identified as well as an associated redshift, which will set an energy scale and allow an independent measurement of H_0 or other cosmological parameters [81, 82, 83]. In addition the physics underlying a core-collapse supernova explosion is far from understood. During a supernova the stellar core collapse releases $\sim 10^{53}$ ergs of gravitational binding energy in less than a second [84] and there exists various mechanisms that have the potential to produce strong GWs [21, 85]. However these mechanisms would only be detectable for a galactic supernova, or perhaps one in the Local Group in the more extreme cases. In addition to GWs, approximately 99% of the binding energy is expected to be released as neutrinos. The three channels together (GW-EM-neutrino) could shed light on the supernova engine, amongst other workings of the supernova, which would not be found from a single channel alone.

2.2 The Most Promising Gravitational Wave and Electromagnetic Sources

To maximise the scientific return of a GW detection the study of a coincident EM counterpart is needed [86, 87, 88, 89, 90]. Ground based GW interferometers are optimised to detect signals from mergers of compact binaries, consisting of neutron stars and black holes. These are the best understood sources in terms of GW range and expected rates [22, 34, 91]. Aasi et al. [58] outline the expected evolution of the detectors between 2015-2022+, also known as the "advanced" detector era. 2015 will see the Advanced LIGO (aLIGO) detectors enter their first science run, with an anticipated NS-NS range of 40-60 Mpc. Only the aLIGO detectors will be operational for a three month science run, with the Advanced Virgo (AdV) detector joining them a year later (with a modest range of 20-60 Mpc [58]). At the end of the decade the average NS-NS

range for aLIGO/AdV is expected to be 200/130 Mpc, their design sensitivity [58]. The number of NS-NS coalescence rates is thought to be between $10^{-3} - 10$ Mpc^{-3}Myr^{-1}, with the most likely rate to be 1 Mpc^{-3}Myr^{-1} [34]. This translates to ~ 40 detections from NS-NS systems by the Advanced detectors every year [34]. By considering GW signals from NS-BH $(1.4 - 10 M_\odot)$ systems these numbers change slightly. At design sensitivity aLIGO/AdV will have an average NS-BH range of $\sim 410/260$ Mpc. The expected number of NS-BH mergers is between 6×10^{-4}-1 Mpc^{-3}Myr^{-1} where the most likely coalescence rate is 0.03 Mpc^{-3}Myr^{-1} which equates to $\sim$10 detections per year [58].

The merger of NS-NS and NS-BH systems is expected to produce EM transients as well as GWs. These events are the favoured progenitor model for SGRBs and have been extensively modelled in terms of GRB/EM emitters [76, 79, 92, 93, 94]. Should a SGRB be missed, for example if the SGRB was not beamed towards the Earth, an orphan afterglow may still be detected. Independent of either of these two EM counterparts, an isotropic thermal emission, known as a kilonova, is expected to accompany the merger of these systems [95, 96, 97]. These sources have been comprehensively studied and lightcurves exist for their expected evolution over time. A more detailed discussion of these sources follows in Section 2.2.1.

Another proposed joint GW-EM mechanism from NS-NS systems concerns the case where the merger results in a short-lived massive neutron star, rather than a black hole [98]. Provided the original neutron stars are sufficiently small, such that the post-merger object has a mass below the maximum mass of a rapidly spinning neutron star, the merger could produce a GW burst devoid of a SGRB followed by an early x-ray and optical afterglow. This x-ray afterglow could be as bright as 10^{-8}erg s^{-1} cm^{-2} and the optical around magnitude 17 in the R-band, lasting between $10^3 - 10^4$ s for a source at 300 Mpc [98].

There are also joint sources of GW and EM signals originating from systems other than compact binary objects. For example the central engine for LGRBs is thought to be either a millisecond magnetar (an extremely magnetised and rapidly spinning neutron star, for example [99]) or a collapsar (black hole with an accretion disk, for example [25]). In the collapsar model GWs, with a frequency of 100-3000 Hz, are produced during the formation of a newborn black hole. The GW strain is expected to be $h \sim 10^{-20}$ at 10 kpc, meaning they could only be detected within our Galaxy [26] every 30-100 years [27, 28]. Numerical studies indicate these sources have a weak emission of GWs, but

there are a number of analytical models that propose strong emission (for example [24]). The collapsar model is an extreme case of a supernova and the GW emission mechanisms for supernovae are quite uncertain [21, 26, 85]. Various mechanisms have been proposed that would produce GW emissions detectable to tens of Mpc [100]. For example, Corsi et al. [101] propose the progenitor may lead to the formation of a highly magnetised millisecond pulsar; Piro et al. [102] suggest gravitational instability in the outer parts of a collapsar disk lead to fragmentation; Shibata et al. [103] present bar-mode instability of rotating neutron stars.

Within the Advanced detector era the odds favour detections from the merger of binary objects compared with burst like events. For this reason we focus efforts on well modelled sources which produce both GW and EM signals from the merger of NS-NS and/or NS-BH systems. In the following section we discuss EM emission expected from these systems in the context of SGRBs.

2.2.1 Gamma-Ray Bursts, Afterglows, and Kilonovae

GRBs are some of the most energetic and brightest EM sources in our Universe with isotropic luminosities usually in excess of 10^{50} erg s^{-1} [104]. They were discovered by the US Vela satellite, quite by accident, at the end of the 1960s, occur approximately once per day and are isotropically distributed over the sky (e.g. [105] and references therein). It was not until 1997 that the extragalactic nature of GRBs was confirmed by the observation of a GRB afterglow [106]. Since then GRB afterglows have been extensively studied and redshift measurements have shown that they originate outside of the Galaxy. Depending upon their duration and spectral hardness, GRBs can be separated in to two classes [76, 107, 108, 109]. Those events with a duration less than two seconds and have a hard spectra are known as short GRBs (SGRBs), which typically have energies $\lesssim 10^{51}$ erg [78, 92] and are thought to be due to the merger of compact binaries. Long GRBs (LGRBs), on the other hand, last longer than two seconds, have a soft spectra and are 100 times more luminous than SGRBs [110] and are associated with core collapse of massive stars. Since binary mergers are expected to be strong GW emitters, we focus primarily on SGRBs.

Short-Hard Gamma-Ray Bursts

The most accepted model for SGRBs is mergers of NS-NS/NS-BH systems, where the GRB is powered by accretion on to the central object [111, 112, 113]. However there is no conclusive observational evidence to verify this. Rapid follow up observations of SGRBs however, have found that they originate from more evolved stellar populations than LGRBs, such as elliptical galaxies which have no recent star formation, which is consistent with the theory of NS-NS/NS-BH mergers [75, 78, 79]. These mergers are believed to lead to the formation of a black hole, either directly or by first forming a highly magnetised neutron star, with a lifetime of up to ~ 100 ms, which will then collapse to a black hole [114, 115, 116, 117]. The formation of a highly magnetised, massive torus around the final black hole governs the gamma-ray emission. The acceleration of matter in the torus, to relativistic velocities, forms a collimated jet of EM radiation [118]. Evidence for collimation first came from GRB051221A (e.g. [77, 119]). However not all SGRBs are thought to originate uniquely from binary mergers. Up to a few percent of SGRBs may be due to giant flares of SGRs in nearby galaxies [80, 120, 121]. These other progenitors are not interesting as GW sources at extra-galactic distances.

The local rate density of SGRBs is thought to be $\rho_{SGRB} \sim 10^{-7} - 10^{-6}$ Mpc^{-3}yr^{-1} after correcting for beaming effects [104, 120, 122], which are a key issue as highly collimated gamma ray emission means that most GRBs would be beamed away from us. This local rate density is similar to the density of NS-NS mergers which is estimated to be $\rho_{NS-NS} \sim 10^{-8} - 10^{-5}$Gpc^{-3}yr^{-1} [34].

Since Swift was launched in 2004, it has detected on average 10 SGRBs per year, of which a third have measured redshifts [123]. None of these events, with a known redshift, occurred within the aLIGO/AdV range for NS-NS mergers, ~ 200 Mpc, and only two events occurred within the advanced NS-BH range of ~ 400 Mpc [34, 123]. However the Swift satellite's field of view (FoV) only covers approximately a sixth of the sky [124] while the GBM instrument on Fermi the GRB satellite [125] covers approximately two thirds but with poor localisation ($\sim$5 degree accuracy). Therefore the majority of SGRBs which are beamed towards the Earth are either not detected or found with poor localisation between these two satellites. Of the observed SGRBs, Metzger et al. [123] estimate that $\leq$0.03 (0.3) SGRBs per year are being localised by Swift within the advanced NS-NS (NS-BH) range. These numbers can be explained by assuming at low redshift $\dot{N}_{obs\ GRB} \propto z^3$. If we were however to consider all detectable SGRBs, not only from Swift but also from Fermi, with or without

redshift data, the same authors estimate these detected rates to increase by a factor of 10. Chen et al. [126] on the other hand estimate an event rate of 1.7 yr^{-1}, assuming a two detector network consisting of the aLIGO interferometers at an early stage of operation (2015-2017), whereas Kelley et al. [127] propose a detection rate of $\sim$30 yr^{-1}. All these rates are lower (most by an order of magnitude) than the expected $\sim$40 yr^{-1} detection rate of NS-NS systems assuming the "most likely" NS-NS rate density of 10^{-6} $Mpc^{-3}yr^{-1}$ [34]. This discrepancy may be due to a number of factors, such as the true merger rate being lower than expected, not all mergers are accompanied by a SGRB or that the gamma-ray emission is beamed. Even taking in to account these lower rates, if an all sky GRB satellite such as Fermi is operational in the advanced detector era, within a few years of running GW detectors at design sensitivity, a joint GW-GRB detection should be made and the nature of SGRBs could be determined conclusively.

Afterglows

An afterglow is the emission which follows a GRB in lower energy parts of the EM spectrum, such as the optical and radio. It is thought to be produced by relativistic ejecta interacting with the surrounding medium and can last anywhere from a few days in the optical to several years in the radio. The early afterglow is expected to be highly beamed, however at later times the energy is expected to be emitted over wider angles as ejecta decelerates [123]. Even if a SGRB has been missed, perhaps due to incomplete sky coverage by the gamma-ray satellites or the SGRB pointing away from the Earth, the afterglow emission may still be detected [123]. Although none have been observed to date, such "orphan afterglows" appear naturally through current theories of how GRBs form (e.g. [128]).

There have been many observations of afterglows in the optical band from rapid follow-up observations, particularly of GRBs detected by Swift. These have shown that early afterglows are fainter than thought in the pre-Swift era. In addition, the lightcurves for afterglows are observed to have fainter magnitudes, due in part to fainter afterglows being discovered, and are also found at greater redshifts than previously thought [129, 130, 131, 132]. The afterglow emission peaks in the optical band on the timescale of days after the merger and at later times (weeks-months) in the radio band.

Kann et al. [133, 134] present optical lightcurve data for over seventy GRBs exhibiting both SGRB and LGRB characteristics, starting minutes after the

burst to many weeks later. Typically one day after a GRB burst is detected, the magnitude of a LGRB will be in the range 18-24 mag and SGRB 24-30 mag (based upon observations where the afterglows are scaled to be at $z = 1$). Most lightcurves seem to follow a similar power law decay $L \propto t^{-1.1}$ (L is luminosity and t is time) however the LGRB lightcurves start at a much brighter magnitude. For those GRBs with a secure redshift, and it is not thought that the distribution of luminosities will differ significantly if the redshifts are not known, LGRBs are found on average to be 5.8 ± 0.5 mag brighter than SGRBs, making them $\approx 210^{+130}_{-80}$ times more luminous [110].

It is estimated that optical telescopes capable of attaining magnitudes of at least ∼23 or even ∼26.5 for typical events are needed to make a confident afterglow detection for NS-NS mergers at a typical aLIGO sensitive range of 200 Mpc [123]. Pan-STARRS [135] can be capable of achieving the former and LSST [136] the latter magnitudes, however these numbers assume ideal observing scenarios. In addition the potential of making a detection depends heavily on the parameters of the SGRB, particularly whether the afterglow is on or off-axis. Figure 2.1 illustrates the on-axis case. This figure shows a number of detected SGRB afterglows (red squares) and upper limits (blue triangles) as well as curves illustrating an afterglow model assuming a range of plausible parameters. For the brightest events, PTF [137] and Pan-STARRS should be capable of detecting afterglows for events at 200 Mpc for several days. However LSST should detect approximately half of the SGRBs within the aLIGO/AdV range, even those which are missed because of incomplete sky coverage, for at least several days after the initial burst [123]. However the scenario changes drastically for an off-axis afterglow, as shown in Figure 2.2. The same parameter curves are shown, however PTF and Pan-STARRS are only capable of detecting afterglows for the largest jet energies ($E_{jet} \sim 10^{50}$ erg) and circumburst medium densities (n∼ 1cm^{-3}). It is even more essential in this off-axis case that deep optical surveys like LSST are operational in the Advanced detector era. With its faint limiting magnitude, LSST should be able to image optical afterglows from most afterglow models.

In addition to the optical afterglow, there is thought to be a radio afterglow several minutes after the gamma-ray emission (for example [76, 142]). This radio emission is thought to be the result of synchrotron emission of electrons in the plasma resulting from the merger of neutron stars. The flux from such an event is expected to be on the order of mJy, within the sensitivity of current radio telescopes [143]. There are other models which could produce a prompt
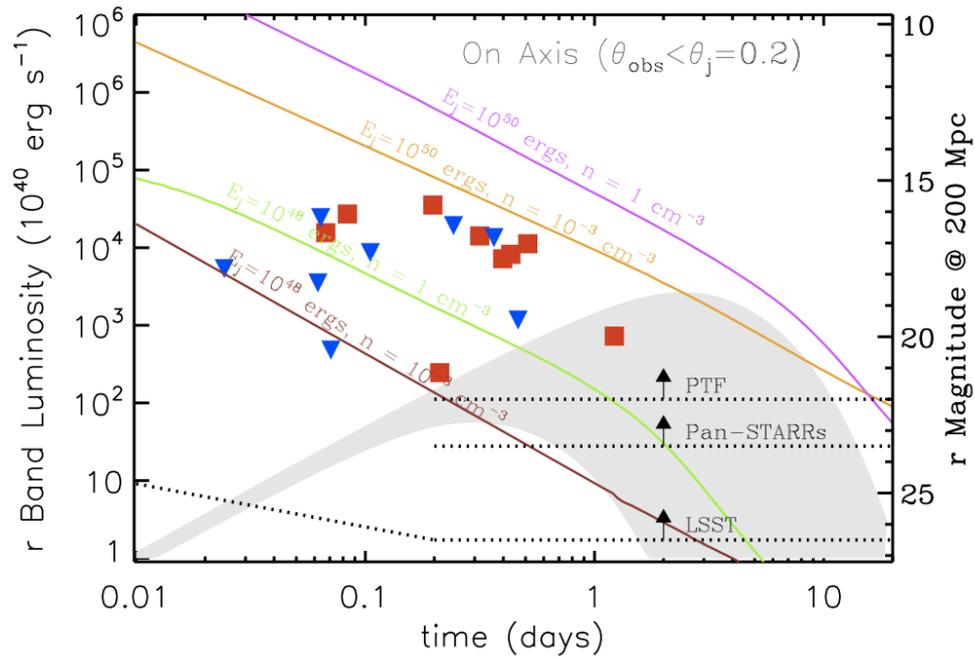
Figure 2.1: Measured luminosities and upper limits on luminosities for SGRB optical afterglows. Red squares indicate detections and blue triangles upper limits [138, 139]. Solid lines are afterglow models [140, 141] with parameters including jet energy (E_j) and circumburst density (n) for an on-axis observer ($\theta_{obs} < \theta_j = 0.2$). The grey shaded region indicates the range of plausible kilonova luminosities. Also shown by horizontal dashed lines are the 5σ limiting magnitudes of three telescopes: PTF, Pan-STARRS and LSST. Taken from [123].
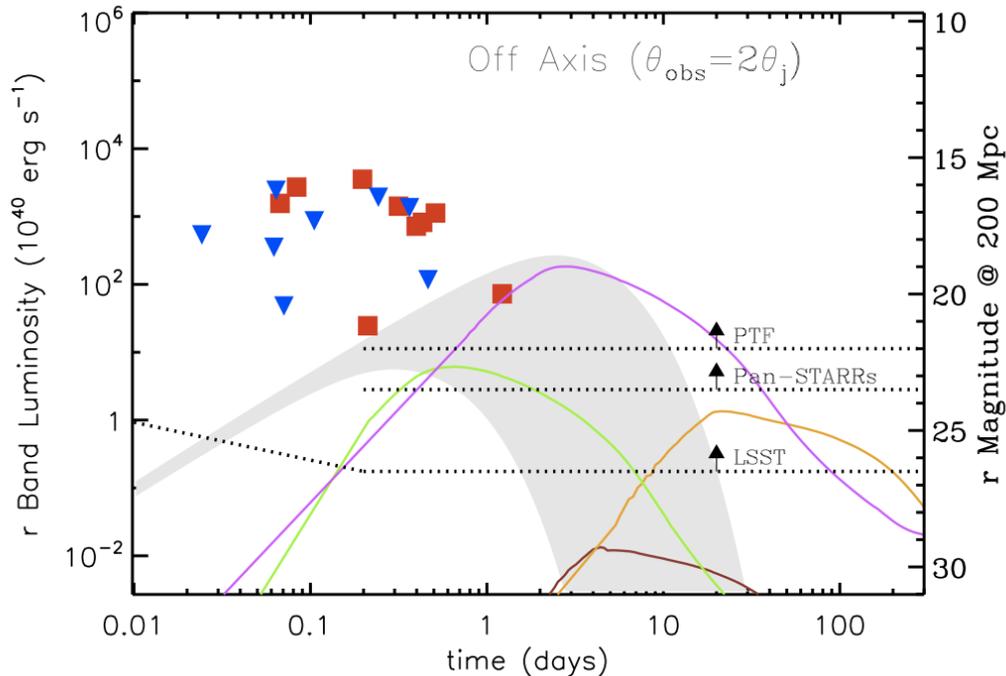
Figure 2.2: Same as Figure 2.1 but for an off-axis observer, i.e. $\theta_{obs} \approx 2\theta_j \approx 0.4$. Taken from [123].

radio emission from the merger of a binary neutron star system, such as that proposed by Lipunov et al. [144]. This model requires one of the neutron stars within the binary to have a large magnetic field ($10^{12} - 10^{15}$G). Time dependent magnetic fields, and therefore induced electric and magnetic fields, are produced from the orbital motion of the binary. The motion of these induced fields could then result in a radio emission at an observable flux equal to the flux from the Crab pulsar at a distance of 2 Mpc [144].

X-ray afterglows have also been observed, typically starting a few hours after the intial GRB and lasting up to a few days. This x-ray emission is thought to occur in a similar manner to the radio and optical emissions - through synchrotron emission of merger ejecta which is accelerated to relativistic velocities. These afterglows have been greatly studied since the launch of Swift and its on board X-Ray Telescope (XRT) [124]. Through rapid follow-up this telescope has captured many early x-ray observations which has allowed investigations in to the various possible physical processes which contribute to the x-ray afterglow. For example the tail emission of the prompt gamma-ray emission, the forward and reverse shock emission components [145]. In addition observations has allowed synthetic lightcurves to be constructed [145].

Kilonovae

A kilonova is a hypothesised supernova-like transient of near isotropic optical/near infra-red emission which is expected from the merger of either a NS-NS or NS-BH system. Unlike conventional type Ia supernovae which are powered by the decay of ^{56}Ni (e.g. [146]), a kilonova is powered by the radioactive decay of ejecta from the merger [95, 96, 97]. Most of this ejecta is rich in neutrons, producing little Ni. Via rapid neutron capture nucleosynthesis (r-process) much heavier radioactive elements are formed and undergo nuclear fission. When the ejecta expands enough that photons can escape, a detectable thermal emission is produced. Simulations by Metzger et al. [97] predict that neutron star merger transients typically have a luminosity 1000 times larger than the Eddington luminosity for an object of solar mass. Since typical novae are approximately the Eddington luminosity, Metzger et al. have called these supernova-like transients 'kilo-novae'.

One of the defining characteristics of a kilonova transient is its lightcurve, which peaks at ∼1 day as illustrated by the grey shaded regions in Figures 2.1 and 2.2. This is quite different to a conventional supernova which peaks weeks after the event. It is thought that within one second of merger the heating of the ejecta is due to the r-process, and after this time due to the synthesised isotopes decaying to stability. The short time between the merger and peak in brightness is due to the short half-life of the isotopes [97]. After this peak in brightness the luminosity decreases as $L \propto t^{-\alpha}$ where $\alpha \approx$1-1.4 and the spectrum is expected to redden [97]. The peak in the kilonova lightcurve is expected to occur at ∼19-22.5 mag (this range spans the expected range of ejecta mass and velocity) for a source at ∼200 Mpc [97]. This is dimmer than a typical supernova which peaks between ∼16.5-21.5 at 200 Mpc depending on supernova type [147]. There are a number of optical telescopes which will be operating at this time, such as PTF, Pan-STARRS and LSST, which will be capable of detecting a range of these sources. It is however only LSST which will have the required optical depth to gather images from several nights to confirm a detection, assuming the mass of the ejecta is within the region 10^{-1} - $10^{-3}M_\odot$ [123].

To date there has not been a confirmed detection of a kilonova transient. The most promising candidate came following GRB080503 which showed a peak in its optical afterglow at ∼1 day which quickly faded over the following days [148]. No obvious host galaxy was found coincident with the GRB however.

2.3 Gravitational Wave Searches Associated with an Electromagnetic Counterpart

GWs have not been directly detected, however searches have been performed in collaboration with conventional astronomers in one of two manners; GW follow-up and EM follow-up. The former search involves the EM community advertising a detection of an EM source and the GW community performing a search for GWs in coincidence. EM follow-up is a newer form of search which uses GW triggers to prompt astronomers to point conventional telescopes to search for an EM counterpart.

2.3.1 Externally Triggered Searches

There are a number of searches for GWs coincident with external triggers, including high-energy neutrinos [149]; SGRs [30, 150, 151]; magnetars [152]; pulsar glitches [153, 154] and GRBs [29, 33, 36, 155, 156, 157, 158]. Most recently satellite-based gamma-ray experiments between 2009 and 2010 found over 150 GRBs during LIGO's sixth and the second and third Virgo science run. A search was thereby performed to find a GW signal coincident with a GRB [100]. This search was split in to two distinct searches; an unmodelled GW burst search and a modelled search for NS-NS/NS-BH coalescences. The burst search involves scanning the data from the GW detectors for energy which is significantly higher than what is expected from the background. In principle this form of search is sensitive to any GW signal, though with a lower sensitivity than a search dedicated to a specific waveform model. The modelled search correlates the GW data against theoretical predicted waveforms using match filtering [33]. Neither of these searches found a GW associated to any of the GRBs.

Despite the null detection of GWs thus far, there have been some astrophysically interesting results. Specifically, GRB070201 and GRB051103 were unique in they were directionally consistent with nearby galaxies within the LIGO/Virgo NS-NS sensitive range. GRB051103 was a SGRB whose sky position coincided with M81, a spiral galaxy 3.6 Mpc away. GRB070201 was directionally consistent with the outer spiral arms of Andromeda (M31) at 0.77 Mpc. Searches for the GW data in each case excluded the hypothesis of a binary progenitor at $\gtrsim 99\%$ confidence [157, 158]. This lends support to the hypothesis that these SGRBs were due to SGR flares. Indeed if the SGRB for GRB051103 originated in M81, then the SGRB flare would be the most
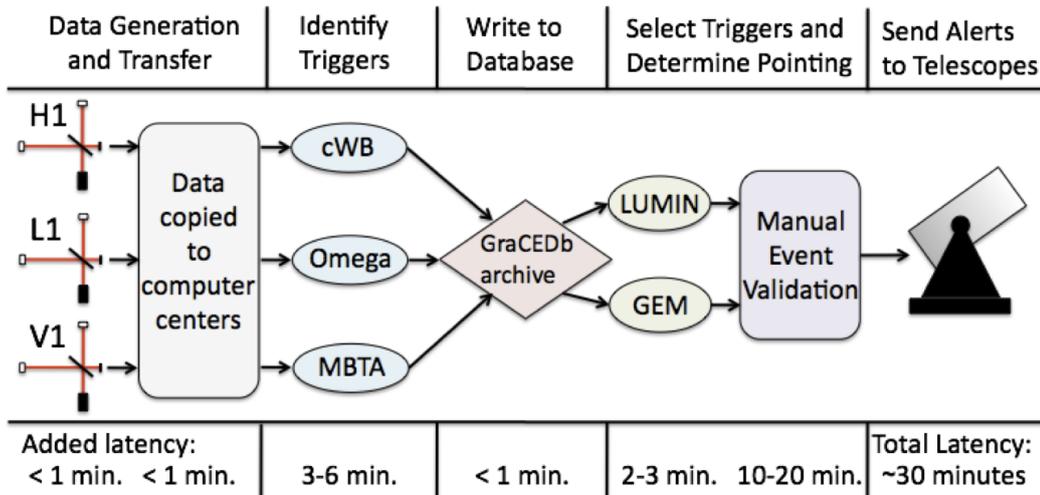
Figure 2.3: A flowchart of the analysis performed to search for an EM counterpart from a GW event with approximate times required for each stage. H1, L1 and V1 are the LIGO-Hanford, LIGO-Livingston and Virgo detectors respectively. Omega and cWB are search packages for detecting generic GW bursts while MBTA is a matched-filter binary search package. LUMIN and GEM are software packages which determine the location on the sky to point telescopes. Image taken from [31].

distant extragalactic magnetar ever observed [157].

2.3.2 Electromagnetic Follow-Up of Gravitational Wave Events

Unlike externally triggered searches that use information from an EM source such as time and sky location to search for a GW signal, EM follow-up is the reverse: conducting a search for an EM counterpart triggered by the observation of a candidate GW event. Between December 17 2009 to January 8 2010 and September 2 to October 20 2010 the first search of this kind was performed, whereby data from the GW detectors was analysed in real-time and a sky location for each candidate GW event was found and sent to conventional astronomers for follow up. One of the main goals of this search was to send alerts to conventional telescopes as quickly as possible after a GW event was identified, to maximise the probability of detecting fading EM counterparts from some of the most likely sources already detailed. In this section we give a brief description of the observation program, known as the LOOC UP project (Locating and Observing Optical Counterparts to Unmodelled Pulses in Gravitational Waves). For details see [159, 160].

Figure 2.3 depicts the format of the search. The online analysis begins at the GW detectors, namely LIGO-Hanford, LIGO-Livingston and Virgo, which were taking science data at the time of this search. Data from these detectors was collected and transferred to several computing centres within minutes. Three independent GW detection algorithms, or "trigger generators" were run as data became available. The coherent WaveBurst (cWB) algorithm performs a time-frequency analysis of the data in the wavelet domain by coherently combining data from all the detectors [31, 161]. The Omega pipeline identifies triggers by performing a matched filter search with a bank of waveforms which are approximately (co)sine-Gaussians [31]. Both of these algorithms are used to search for transients without a specific waveform morphology, i.e. bursts. The third algorithm, Multi-Band Template Analysis (MBTA) uses templates from second order post-Newtonian approximations to specifically target waveforms expected from NS-NS, NS-BH and BH-BH inspirals [162]. Any triggers these three algorithms identified were then ranked according to their 'detection statistic'. For cWB and MBTA this is related to the amplitude of the signal-to-noise ratio (SNR) of the signal across all the GW detectors whereas for Omega it comes from the Bayesian likelihood of a GW signal being present [160]. Triggers from any of the three algorithms having a detection statistic above some threshold and occurred at a time when all three interferometers were taking science quality data, are recorded in the Gravitational-wave Candidate Event Database (GraCEDb). Triggers were also automatically checked against lists of times when the detectors were not operating nominally, such as periods of high seismic activity or non-standard interferometer configurations. From the GW data taking to this point, typically 10 minutes have elapsed.

The next step of the search is to identify statistically significant triggers from GraCEDb. This is done by finding the average rate at which fluctuations due to noise will create a spurious event with a detection statistic value equal to or greater than that of the GW candidate. This is known as the false alarm rate (FAR). For the first observing period (December 2009-January 2010), a trigger was deemed significant if it was found to have a probability of occurring less than once per day of detector livetime. This is the time all three GW detectors were collecting science data simultaneously. For the second period (September-October 2010) this probability was dropped to 0.25 events per day [160]. Certain partner telescopes partaking in the search however required different thresholds for selecting events for follow-up.

Once a trigger has been identified as significant the most likely source lo-

cation is determined. In addition to identifying triggers, the three detection algorithms produce maps over the sky (skymap) to indicate the most likely location of an event. A typical skymap is tens to hundreds of square degrees [72] which could be made up of many disjointed regions. It is impractical to image this entire area, therefore two algorithms were used to prioritise regions (typically the size of the FoV of the telescopes taking part) within this skymap as the most likely location of the GW source. The LUMIN software package uses the skymaps from the three trigger generators and the location of known galaxies to select regions to observe. LUMIN also includes software to communicate with robotic telescopes and tools which are used in trigger validation. The Gravitational to Electro-Magnetic Processor (GEM) used slightly different criteria as it was selecting the location for the Swift satellite to observe [160].

The Gravitational Wave Galaxy Catalogue (GWGC) contains information such as sky position, distance, blue magnitude etc of 53,225 galaxies, out to 100 Mpc, and 150 Milky Way globular clusters [163]. The authors claim this catalogue is nearly complete to ∼40 Mpc. Using the skymaps previously generated, the search volume is limited by only considering galaxies out to 50 Mpc as this was the limit of detecting a binary system containing a neutron star at the time of the search. These skymaps are tiled into $0.4° \times 0.4°$ pixels and on average approximately 8% of the pixels within a typical skymap contain a local galaxy or globular cluster [160]. Each of the pixels is then assigned a relative likelihood following:

$$P \propto \sum_i \frac{M_i L}{D_i} \tag{2.1}$$

where L is the likelihood skymap value from the GW data, M_i is the blue light luminosity and D_i is the distance of a galaxy or globular cluster associated to that tile, and the sum is over all galaxies or globular clusters in the tile. This weighting is given to promote galaxies which have a greater blue luminosity as this is a rough proxy for mass. The more luminous a galaxy, the greater number of sources which the galaxy contains. More distant galaxies are disfavoured as it is expected a closer galaxy will contain more detectable sources than a more distant galaxy of similar mass. We discuss equation (2.1) in more detail in Section 3.2. In the case where no galaxies are found within a skymap the likelihood from the GW skymap is used ($P = L$). The actual coordinates which are sent to the telescopes are selected to maximise this P which is
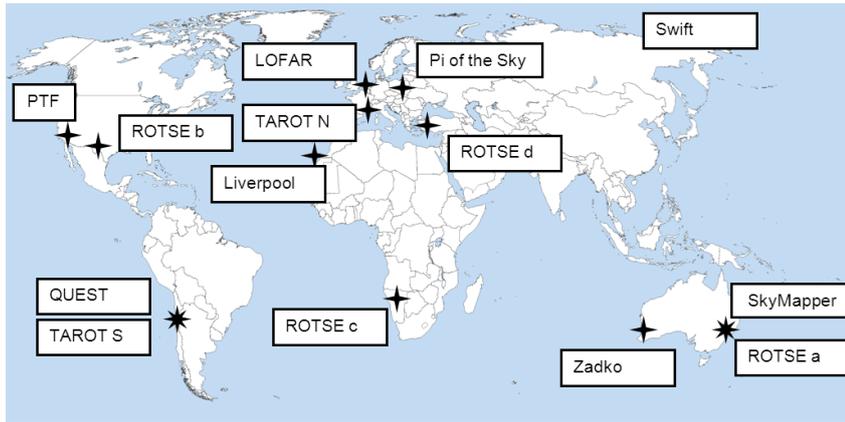
Figure 2.4: The approximate location of all the EM telescopes which participated in the search. The Swift satellite has an arbitrary location. Taken from [160].

summed over pixels within the FoV of a particular telescope [160]. This entire procedure thus far, starting with collecting the GW data, takes approximately 12 minutes.

The next stage in the search is manual event validation, which takes the greatest length of time. Although quality of the GW data was assessed at the time the triggers were identified, additional checks were performed manually. When a significant trigger was identified, an alert was broadcast to collaboration members via email, text message and a website. These scientists provided 24/7 coverage during 8 hour shifts and would confer with personnel at each of the three GW detectors to validate an event when one was identified. The intention of these checks was to discard events caused by man-made occurrences that were not caught by the automated low-latency data quality checks. At this stage, the aim is that no more than 30 minutes have elapsed since the event occurred. The observational coordinates are then sent to partner telescopes for follow-up.

The telescope network used in this search primarily consisted of wide FoV optical telescopes to try to accommodate the large skymaps produced from GW position estimates. There were however narrow FoV optical telescopes as well as radio and x-ray instruments which were used in the search. Optical partners included PTF [137], Pi of the Sky [164], QUEST [165], ROTSE-III [166], SkyMapper [167], TAROT [168], Zadko Telescope [169] and the Liverpool Telescope [170] while Swift [124] was the only x-ray instrument and both LOFAR [171] and the Expanded Very Large Array (EVLA) [172] radio instruments. Figure 2.4 shows the location of each observatory.

During the two observing (December 17 2009 to January 8 2010 and September 2 to October 20 2010) periods 9 candidate GW events were sent to partner telescopes for follow-up. Each observatory responded to at least one event. A separate analysis of the images taken by each EM observatory was undertaken due to the different nature of each telescope. Chapter 4 details the methods used to process the images taken with the ROTSE-III telescope system and Chapter 5 details the results of the analysis. No significant optical, x-ray or radio transients were identified to be associated with any of these GW events [173, 174, 175].

Chapter 3

Identifying the Host Galaxy of Gravitational Wave Sources

3.1 Introduction

One of the main obstacles in conducting an electromagnetic (EM) follow-up search of a gravitational wave (GW) signal (as detailed in Section 2.3.2) is identifying the host galaxy of the GW source based on the GW emission. GW interferometers are capable of detecting a signal from most parts of the sky and localise the position of a source based upon triangulation techniques. This produces large source localisation regions, typically hundreds of times larger than the typical field of view (FoV) (few square degrees) of conventional telescopes. Externally triggered searches (discussed in Section 2.3.1) use the EM signal, independently observed by a satellite, to estimate the location, on the sky, of the source. This type of search is not considered in this chapter.

We focus on binary merger signals; potential EM counterparts (optical afterglows, kilonovae) are discussed in Chapter 2. Mergers of binary neutron stars (NS-NS) or binaries consisting of a neutron star and a stellar mass black hole (NS-BH) are the best understood in terms of GW range and expected rate [34], and are the most likely sources for producing both detectable GW signals and optical transients. They are also the favoured progenitor model for SGRBs [76][1]. These events will emit a significant proportion of their binding energy in GWs at frequencies to which the current and next generation of GW detectors are sensitive.

The distance to which a GW signal can be detected depends on the masses

---

[1]The gamma-ray emission might itself be used to identify the host galaxy for those cases where the emission is beamed towards us.

of the binary components. There are two conventions for the sensitivity of a GW detector to binary inspiral signals. The horizon distance R_H is the maximum distance to which an optimally positioned and orientated system would produce a signal-to-noise ratio (SNR) of at least 8 in a given detetcor. The "sensemon range" R_S is the volume- and orientation-averaged distance at which a system would produce SNR ≥ 8. The expected rate of signals with SNR ≥ 8 in a single detector is therefore

$$\frac{4}{3}\pi R_S^3 D \tag{3.1}$$

where D is the source rate density [34, 176]. The horizon distance is a factor 2.26 larger than the sensemon distance.

Assuming fiducial masses of 1.4 $M_\odot$ for neutron stars and 10 $M_\odot$ for black holes, the Initial LIGO observatories could detect NS-NS binary systems with SNR ≥ 8 out to a maximum distance of approximately $R_H \approx 30$ Mpc, and NS-BH systems out to $R_H \approx 65$ Mpc. With this sensitivity, Abadie et al. [34] estimate the most likely rate of detectable signals at ~ 0.02 yr^{-1} for NS-NS and ~ 0.004 yr^{-1} for NS-BH systems. For Advanced LIGO (c. 2015+) the GW horizon range increases to approximately $R_H \approx 450$ Mpc for NS-NS systems and $R_H \approx 930$ Mpc for NS-BH systems, with most likely rate estimates of ~ 40 yr^{-1} and ~ 10 yr^{-1} respectively.

GW interferometers are non-imaging detectors with a large FoV which produce large error regions, on the sky, of the source location. Their antenna response is greater than half-maximum over 65% of the sky. Source localisation for short-lived signals therefore requires multiple detectors, in order to use the measured time delay between detectors as well as the amplitude of the measured signal in each detector to triangulate a sky location. Several methods of localisation have been investigated [72, 177, 178, 179, 180, 181, 182, 183, 184, 185, 186]. Fairhurst [72] gives the following approximation for the timing accuracy of a GW signal:

$$\sigma_t \sim \frac{1}{2\pi\sigma_f\rho}, \tag{3.2}$$

where σ_f is the effective bandwidth of the signal and ρ is the SNR. For nominal values $\sigma_f = 100$ Hz and $\rho = 8$, timing accuracies are on the order of 0.1 ms. This can be compared to the light travel time between detectors, $10 - 30$ ms for the LIGO-Virgo network. For example, for a binary coalescence signal at the threshold of detectability, Fairhurst [72] estimates a best-case localisation of 20 deg^2 (90% containment), and a typical localisation of twice this. During

the last science run of LIGO and Virgo (2009-2010) the LOOC UP project (as detailed in Section 2.3.2) sought to localise GW signals using similar techniques and found typical localisations areas of ~ 100 deg^2.

3.2   A Galaxy Ranking Statistic

It is impractical to image typical localisation areas predicted by Fairhurst ($\sim$40 deg^2) and actual GW signal candidates during the last LIGO/Virgo science run ($\sim$100 deg^2). During this period a network of telescopes (for more details see Section 2.3.2) were available for follow-up which typically had a FoV of a few square degrees. To confidently identify an EM counterpart, the localisation region needs to be imaged on several consecutive nights to high magnitudes. However we can reduce the area that needs to be imaged by assuming the GW source to be associated with a galaxy [159]. Since a galaxy at a typical LIGO distance has an angular size of a few arcminutes or less, restricting to galaxies also makes it feasible for narrow FoV instruments (such as Zadko [169]) to participate.

Restricting to galaxies within a typical LIGO-Virgo GW error box can contain over one hundred galaxies out to 100 Mpc. Imaging all to search for an EM counterpart will likely be impractical. This motivates considering ways to rank the galaxies by their likelihood of hosting the source of the observed GW event. We expect a nearby galaxy to be more likely *a priori* to be the host of a detectable GW signal source than a more distant galaxy. Furthermore, larger galaxies contain more potential sources. We therefore propose to rank each galaxy as the possible host for a GW signal by the following statistic:

$$R = e^{-\frac{\chi^2}{2}} \frac{L}{d^\alpha} \,. \tag{3.3}$$

Here L is the luminosity of the putative host galaxy, d is the distance to the galaxy, α is a constant, and χ^2 is the chi-squared match between the measured and predicted time of arrival of the signal in each detector [179], given by

$$\chi^2 = \sum_i \frac{(t_i - p_i)^2}{\sigma_i^2} \,. \tag{3.4}$$

Here σ_i is the timing uncertainty in each detector, t_i is the measured arrival time, p_i is the predicted arrival time based on the sky direction of the putative host galaxy, and the sum is taken over all detectors. We include $\exp\left(-\chi^2/2\right)$

in our ranking statistic as this is the likelihood associated with a Gaussian timing error in each detector. It determines which galaxies have sky positions consistent with the observed time delays between detectors; i.e., it represents the GW triangulation error box. For the LIGO-Virgo network that we will simulate, the χ^2 sky map is mirror-symmetric through the plane of the detectors, thus usually yielding two error boxes. In principle, the measured signal SNRs can be used to break this degeneracy and determine which box contains the correct sky location. For our tests, we use both boxes. Therefore, a more sophisticated GW analysis than that assumed here may reduce the number of galaxies that need to be imaged by up to a factor of 2.

R is scaled with luminosity because we assume the luminosity of each galaxy to be approximately proportional to the number of sources within it. The $d^{-\alpha}$ factor favours intrinsically weak signals from nearby galaxies as being more likely than strong signals from distant galaxies. More generally, assume the rate of GW events of intrinsic amplitude h_0 within each galaxy takes the form

$$\frac{dN}{dh_0} \sim h_0^{-\beta}. \tag{3.5}$$

For any given distance R, the smallest intrinsic amplitude that we are able to detect, $\bar{h}_0$, is related to the minimum amplitude we can detect on Earth, h_{thresh}, as

$$\frac{\bar{h}_0}{R} = h_{thresh}. \tag{3.6}$$

The number of observable signals in a galaxy can be defined as

$$N_{obs}(R) = \int_{\bar{h}_0}^{\infty} \frac{dN}{dh_0} dh_0 \tag{3.7}$$

and it can be shown

$$N_{obs} \propto \bar{h}_0^{-\beta+1}. \tag{3.8}$$

From equation (3.6) the following relationship can be found

$$N_{obs} \propto R^{-\alpha} \tag{3.9}$$

where $\alpha = \beta - 1$.

In our simulations we test $\alpha = 1, 2, 3$. We find $\alpha = 2$ gives marginally better performance for the initial LIGO detectors, and $\alpha = 1$ the best for Advanced LIGO. However, the variation in the probability of identifying the host galaxy is only a few percent; we conclude that our ranking is not sensitive

to the precise distance weighting used.

For comparison, we also test ranking based purely on the error box, with no luminosity or distance weighting:

$$R = e^{-\frac{\chi^2}{2}}. \tag{3.10}$$

This statistic is poor at identifying the host galaxy; the probability of correct identification is a factor of 2-4 lower (depending on binary mass) than when including the L/d weighting.

3.3 Host Galaxies Within 100 Mpc

GW signals are simulated from known external galaxies, using the Gravitational Wave Galaxy Catalogue (GWGC) [163]. This catalogue contains approximately 53,000 galaxies out to a distance of 100 Mpc. There are $22,000$ galaxies within 65 Mpc, the maximum distance to which a 1.4-10.0 $M_\odot$ NS-BH system can be detected with SNR ≥ 8 by Initial LIGO, and 7300 galaxies within 30 Mpc, the maximum distance for a NS-NS binary. White et al. estimate the catalogue to have a completeness of 60% to 100 Mpc, 75% to 50 Mpc, and a completeness consistent with 100% out to 40 Mpc. Approximately 50% of the galaxies have a defined type in the de Vaucouleurs classification [187]; these account for 80% of the total luminosity in the catalogue. The catalogue only extends to 100 Mpc, we therefore perform tests of the ranking statistic in two phases. Firstly we use the GWGC and only consider sources within 100 Mpc. This is appropriate for the first generation detectors and also for a small fraction ($\sim 10\%$) of detections in the advanced era. Second, to test the performance with the full range of Advanced detectors, we simulate a galaxy catalogue that is complete to 750 Mpc.

To evaluate how well the ranking statistic identifies the true host galaxy of a GW signal, we simulate how GWs will appear in a realistic search. We consider inspiralling NS-NS and NS-BH binaries. The strength of their GWs has a well-defined dependence on the system's mass, distance, and inclination of the binary orbital axis to the line of sight. Three different mass pairs are studied: 1.4-1.4 $M_\odot$ NS-NS, 1.4-5.0 $M_\odot$ NS-BH, and 1.4-10.0 $M_\odot$ NS-BH systems. The orientations are random and isotropic. The true host galaxy is selected randomly with weight proportional to the galaxy luminosity and with an additional weighting based on galaxy type as discussed below.

We simulate the LIGO-Hanford, LIGO-Livingston and Virgo network, as-

suming all three detectors to have sensitivity given by the Initial LIGO design [51], or the Advanced LIGO design [188]. For each GW, we compute the received SNR in each detector based on the binary mass and distance, and the detector sensitivity to that sky direction and binary orientation. In a single GW detector the SNR, ρ, of a GW signal, $h(f)$, is defined as [14]

$$\rho^2 = 4 \int_0^\infty df \frac{|\tilde{h}(f)|^2}{S(f)} \tag{3.11}$$

where $S(f)$ is the noise power spectral density and $\tilde{h}(f)$ is the Fourier transform of the received signal

$$h(t) = F_+(\theta, \phi, \psi)h_+(t) + F_\times(\theta, \phi, \psi)h_\times(t). \tag{3.12}$$

This equation represents a linear combination of the detector responses (F_+ and $F_\times$) to the two GW polarisations (h_+ and $h_\times$) where (θ, ϕ) is the sky position and ψ the polarisation angle of the source. Finn et al. [176] define the Fourier transform of the received signal as

$$|\tilde{h}(f)|^2 = \mathcal{A}^2 \mathcal{M}^4 \left(\frac{5\pi}{384} \right) (\pi f \mathcal{M})^{-\frac{7}{3}} \tag{3.13}$$

where $\mathcal{M}$ is the chirp mass of the binary system and $\mathcal{A}$ is the GW amplitude which is defined as [176]

$$\mathcal{A}^2 = \frac{4}{d_L^2} \left[F_+^2(1 + \cos^2 \iota)^2 + 4F_\times^2 \cos^2 \iota \right]. \tag{3.14}$$

The source distance is denoted by d_L and ι is the angle between the plane of the source and the line of sight. The SNR of a GW signal in one detector is therefore

$$\rho = \left(\frac{5}{24\pi^{\frac{4}{3}}} \right)^{\frac{1}{2}} \frac{\mathcal{M}^{\frac{5}{6}}}{d_L} \left[F_+^2(1 + \cos^2 \iota)^2 + 4F_\times^2 \cos^2 \iota \right]^{\frac{1}{2}} \left[\int_0^\infty df \frac{1}{f^{\frac{7}{3}} S(f)} \right]^{\frac{1}{2}}. \tag{3.15}$$

The simulations generate random d_L, θ, ϕ, ψ and ι where the first three quantities are taken from the GWGC. The SNR and timing uncertainty σ_t (equation (3.2)) is computed for each signal, and for every detected signal the error region is generated. The ranking statistic (equation (3.3)) then ranks every galaxy within this error region and notes the rank of the true host.

The measured amplitudes and times are "jittered" by additive Gaussian

errors to simulate the detector noise background. To be considered detected, a GW needs to have an SNR of $\rho \geq 8$ in at least two detectors, and a quadrature-sum SNR ≥ 12 over all three detectors. For each Monte Carlo run we generate enough binaries to give approximately 800 detected signals.

While the ranking statistic (equation (3.3)) treats all galaxy types equally, the rate of binary coalescences is likely to be different in different galaxy types. O'Shaughnessy et al. [189] estimate the rate of NS-NS and NS-BH mergers in elliptical and spiral galaxies for a large range of plausible binary evolution scenarios. They produce a total of 488 samples of merger rates, and find the relative rate in spirals and ellipticals to vary widely in their models. We account for this uncertainty in our simulations by performing 50 separate Monte Carlo runs for each waveform type; in each run, the relative rate of mergers in spirals and ellipticals is determined by a random draw from the models by O'Shaughnessy et al. Lenticular galaxies are treated as equivalent to ellipticals and irregular galaxies as spirals for these simulations. For those galaxies without a specified type, one is assigned randomly in proportion to the number of galaxies of each type in the catalogue. In all, 70% of the galaxies are treated as spiral, and 30% as elliptical galaxies.

Finally, to simulate the effect of measurement errors in the galaxy catalogue the luminosity and distance of each galaxy is jittered by a random amount consistent with the stated uncertainties. This is done by creating a second copy of the galaxy catalogue and using this jittered catalogue for signal generation (keeping the original catalogue for ranking).

After the GW signals are generated, we compute the χ^2 match (equation (3.4)) between the predicted and the measured GW arrival time at each detector. All the galaxies are then ranked as potential hosts for each GW using equation (3.3). The distribution of ranks assigned to the true host galaxy for each GW then tells us the probability of observing the true host as a function of the number of galaxies imaged. This probability is shown in Figure 3.1. We find that for a narrow FoV telescope ($O(10)$ arcmin, sufficient to image one galaxy at 10 Mpc) the probability of the true host being the top-ranked galaxy is $50 \pm 3\%$ for a 1.4-1.4 $M_\odot$ NS-NS system, $32 \pm 2\%$ for a 1.4-5.0 $M_\odot$ NS-BH, and $21 \pm 3\%$ for a 1.4-10.0 $M_\odot$ NS-BH system. When imaging the 5 highest-ranked galaxies, the chances of including the true host increase to $78 \pm 3\%$, $63 \pm 3\%$, and $48 \pm 3\%$ respectively. For the Advanced LIGO detectors, and considering only binaries within 100 Mpc, the probabilities are approximately independent of binary type: $39 \pm 3\%$ / $43 \pm 4\%$ / $40 \pm 3\%$ for 1 image and
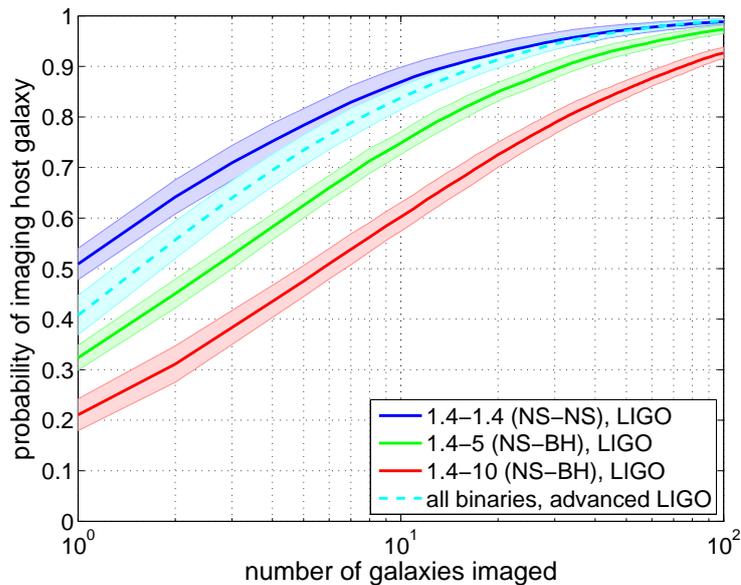
Figure 3.1: Narrow field of view case. The probability of imaging the true host galaxy for each type of binary system versus the number of images taken. The shaded regions denote the 1-sigma uncertainty in the probability estimate.

$72 \pm 3\%$ / $75 \pm 3\%$ / $73 \pm 3\%$ for 5 images. In each case the uncertainties are dominated by the range of possible relative rates for mergers in spiral versus elliptical galaxies. These probabilities assume the galaxy catalogue to be complete. For a completeness $c < 1$ these probabilities should by multiplied by c.

We note that the success rate for initial LIGO is highest for NS-NS systems, and decreases with increasing binary mass. This is due to two factors. The effective bandwidth σ_f is larger for low-mass systems, giving smaller timing uncertainties (see equation (3.2)). Furthermore, less massive binaries are detectable to smaller distances, hence there are fewer potential hosts for these systems, so the probability of imaging the true host increases. Indeed, in the NS-NS simulations for current detectors, we find that 10% of all detected signals are due to only 10 galaxies: PGC047885, NGC0224 (Andromeda galaxy), NGC4594 (Sombrero galaxy), ESO468-020, NGC0253, NGC5457 (Pinwheel galaxy), NGC6964, PGC2802329, PGC009892 and NGC4472.

For the Advanced LIGO detectors, we find that the probability of imaging the true host galaxy is approximately the same for all binary types. This is due to the restriction to signals originating within a fixed distance of 100 Mpc. Higher-mass systems give larger SNR at a fixed distance; this offsets the effect of their lower effective bandwidth in the timing uncertainty (equation (3.2)).

The LOOC UP program [159] used wide FoV telescopes to image potential
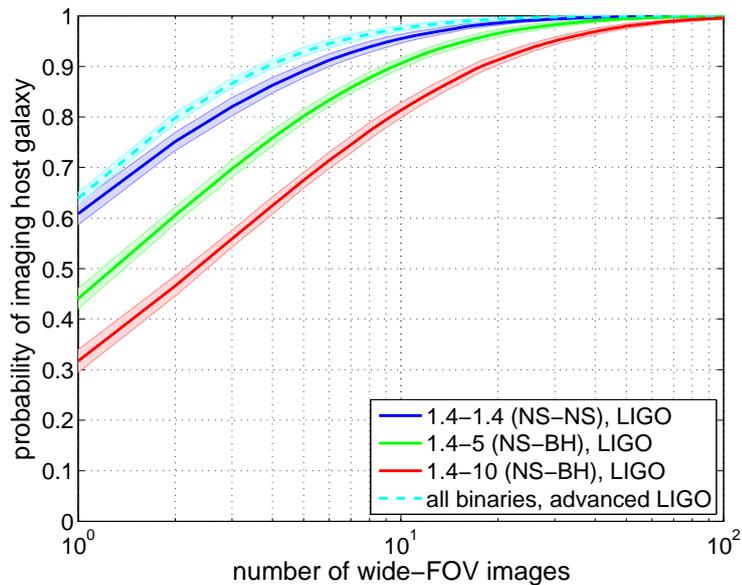
Figure 3.2: Wide field of view case. The probability of imaging the true host galaxy for each type of binary system versus the number of images taken. The shaded regions denote the 1-sigma uncertainty in the probability estimate.

host galaxies, including TAROT [168], QUEST [165], SkyMapper [167], and ROTSE [166], as well as narrow-field telescopes such as Zadko [169]. Depending on the length of exposure (between 60 s and 180 s) and the filter used, these telescopes have limiting magnitudes ranging from 17 to 22, sufficient to detect the EM emission from binary mergers predicted by Metzger et al. [97] to 15 − 150 Mpc. The wide-field telescopes can image several square degrees at once, allowing multiple galaxies to be observed simultaneously and therefore increasing the probability of observing the true host in a given number of exposures. We simulate imaging with a 3-4 deg^2 FoV telescope by grouping galaxies which lie within 1 degree of one another when computing the probability of imaging the host. That is, we consider the true host as having been imaged if it lies within 1 degree of any of the N top-ranked galaxies, where N is the number of wide-field images taken. The results are shown in Figure 3.2. We find that for Initial LIGO, for 1.4-1.4 $M_\odot$ / 1.4-5.0 $M_\odot$ / 1.4-10.0 $M_\odot$ systems the chances of observing the true host are $61 \pm 2\%$ / $44 \pm 2\%$ / $32 \pm 2\%$ for 1 image and $89 \pm 1\%$ / $80 \pm 1\%$ / $67 \pm 2\%$ for 5 images. These are a factor of about 1.2 better than the narrow FoV results. For the Advanced LIGO detectors the probabilities are $64 \pm 1\%$ / $68 \pm 1\%$ / $64 \pm 1\%$ for 1 image and $93 \pm 1\%$ / $94 \pm 1\%$ / $92 \pm 1\%$ for 5 wide-field images, a factor of 1.3-1.5 better than in the narrow FoV.

3.4 Host Galaxies Within 750 Mpc: A Simulated Galaxy Catalogue

Thus far all Monte Carlo simulations have used the GWGC from which to draw host galaxies within 100 Mpc. Although this is valid for the Initial LIGO design the restriction to 100 Mpc is not appropriate for Advanced LIGO where the detectors reach far exceeds that of the galaxy catalogue. Unfortunately no catalogue exists which is nearly complete out to the limit of the advanced detectors. Therefore to test the basic idea we create a simulated complete catalogue.

A simulated galaxy catalogue was created out to 750 Mpc, the reach for a NS-BH system (of mass 1.4-5.0 $M_\odot$) for Advanced LIGO at design sensitivity. Galaxies were drawn at random from the GWGC and a fake catalogue was created by selecting positions distributed randomly and uniformly in volume out to 750 Mpc. We used a density of galaxies of ~ 0.02 Mpc^{-3}, consequently this catalogue contains $\sim 3.5 \times 10^7$ galaxies. With the number of galaxies under consideration increasing by a factor of 700 (compared to the previous simulations), it was no longer computationally feasible to consider galaxies individually. Instead, by tiling the sky in to equal areas with a number of specified points, using a HEALPix algorithm [190], galaxies can be grouped together. It was decided to investigate tiles the size of ~ 0.84 deg^2 and 3.36 deg^2 as this approximates the FoV of both narrow and wide FoV optical telescopes which were used in the LOOC UP project.

The Advanced LIGO detectors are expected to come online in 2015, with Advanced Virgo following one year later. However the initial sensitivity of these detectors is expected to be much less than design sensitivity; it will take several years and commissioning phases until this goal is reached. Table 3.1 outlines the expected observing schedule and sensitivities of the Advanced detectors from 2015-2022+ (shown in Figure 3.3). The ranges quoted are the "sensemon ranges" R_S (described in Section 3.1), a factor of 2.26 smaller than the maximum reach of the detectors for an optimally oriented source which produces a GW signal detected with an SNR of 8. The percentage (90% containment) of localised NS-NS systems in Table 3.1 only considers information from the detectors; no galaxy weighting is used.

Simulations were conducted in the same manner as described in Section 3.3, with the GWGC being replaced by the simulated galaxy catalogue and galaxies being grouped together in to tiles as discussed. Only NS-NS (1.4-1.4

Label	Epoch	NS-NS Range (Mpc)		NS-BH Range (Mpc)		% NS-NS localised within	
		LIGO	Virgo	LIGO	Virgo	5 deg^2	20 deg^2
early	2015	40-80	-	65-135		-	-
mid	2016-17	80-120	20-60	135-200	35-105	2	5-12
late	2017-2018	120-170	60-85	200-285	105-140	1-2	10-12
final	2019+	200	65-130	325	105-190	3-8	8-28
india	2022+	200	130	325	190	17	48

Table 3.1: Observing schedule, expected sensitivities, and source localisation for the Advanced LIGO and Advanced Virgo detectors, taken from [58]. The NS-NS (1.4-1.4 $M_\odot$), NS-BH (1.4-5.0 $M_\odot$) range and localisations (complete to 90%) reflect the uncertainty in the detector noise spectra. In addition the localisations take in to account the uncertainty in the source rate density of NS-NS systems [34].
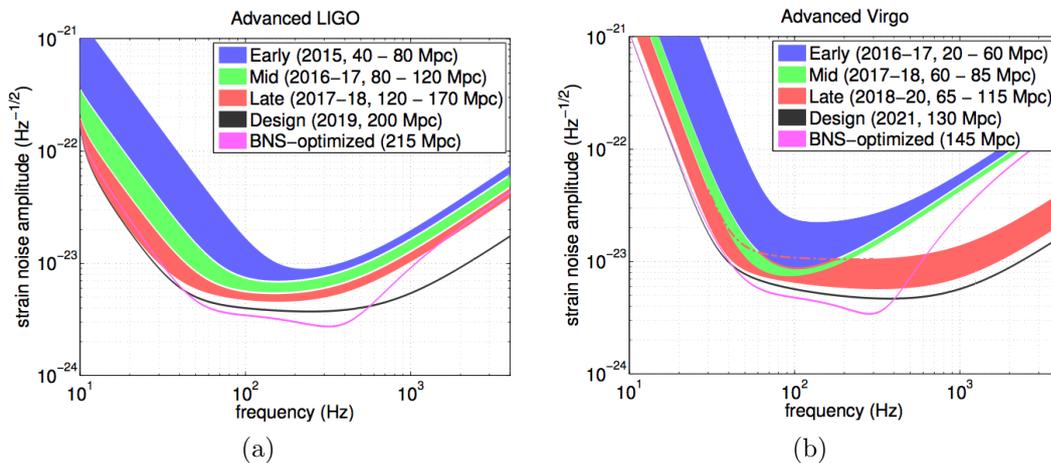
Figure 3.3: One possible evolution of the (a) aLIGO and (b) AdV expected strain sensitivities with frequency. The curves are shown for early, middle, and late commissioning periods, in addition to the final design sensitivity and the BNS-optimised sensitivity. The target date to achieve these sensitivities is shown as well as the average distance a BNS signal could be seen. Taken from [58].

$M_\odot$) and NS-BH (1.4-5.0 $M_\odot$) systems were investigated due to the reach of the simulated catalogue. In addition α is set to 1 in the ranking statistic (equation (3.3)) as previously discussed. All observing scenarios for the Advanced detector era were investigated, to determine how often the true host galaxy of a GW signal can be found at any point over the evolution of the Advanced detectors. Due to the spread in the expected ranges of each epoch, they are investigated separately. For example the "mid" epoch has a NS-NS range 80-120 Mpc for the LIGO detectors and 20-60 Mpc for the Virgo detector. Therefore the "mid-low" simulations assume a LIGO (Virgo) range of 80 (20) Mpc and "mid-high" assumes a LIGO (Virgo) range of 120 (60) Mpc. The "india" epoch assumes a four detector network with the LIGO-India detector having the same sensitivity as the other aLIGO detectors.

The probability of imaging the tile containing the host galaxy of a GW signal using a narrow FoV telescope is shown in Figure 3.4. Plots (a) and (b) illustrate the ability to identify the host tile for a signal from a NS-NS system and plots (c) and (d) for a NS-BH system. The plots show the evolution of the probability throughout the Advanced detector era. It is evident that the ranking statistic performs better at identifying the host tile of a signal from a NS-NS system compared to a NS-BH system because the range is smaller, and thus encompasses less galaxies. In the early epoch, where only the two LIGO detectors are in operation, the localisation is very poor. By imaging the ten most likely tiles less than 20% (10%) of signals from a NS-NS (NS-BH) are correctly linked to the host galaxy tile. When Virgo comes online in the mid epoch the ability to identify the host galaxy tile greatly improves to ∼28-36% (20%) for a NS-NS (NS-BH) signal. The increase in LIGO sensitivity in the late epoch is more pronounced than that of the Virgo detector, leading to a slight decrease in localisation probability. However in the final epoch when all detectors are at or near design sensitivity, the probability of imaging, with ten images, the true galaxy tile is at its highest for a three detector network, ∼30-40% (20-30%) for a NS-NS (NS-BH) GW signal. Only by adding a fourth detector (LIGO-India) to the network does the sky localisation dramatically improve. For a GW signal from a NS-NS (NS-BH) system, by imaging the ten most likely tiles ∼80% (65%) of GW signals are identified to the correct galaxy tile. Similar features are seen for the plots illustrating the wide FoV case in Figure 3.5. In general the probability of imaging the tile containing the true host galaxy improves 10-20 percentage points when going from a narrow to wide FoV telescope. However this is not true for the early epoch;

the probabilities between the narrow and wide FoV telescopes are comparable. This can be attributed to the poor localisation ability of a two detector network and probably also the relatively small density of galaxies within 40-80 Mpc.

For comparison simulations were conducted without the galaxy weighting; the GW source was determined using triangulation techniques alone (equation (3.10)). The results of these simulations in addition to the results obtained using the galaxy weighting technique (equation (3.3)) are compared in Table 3.2. This table shows the percentage of correctly identified host galaxies for both narrow (0.84 deg^2 tiles) and wide (3.36 deg^2 tiles) FoV telescopes using both 5 and 20 pointings. In both the NS-NS and NS-BH situation the galaxy weighting technique performs better at identifying the host galaxy in the early, mid and late epochs. It provides a significant advantage in the early epoch when only the two LIGO detectors are operational. In the NS-NS case this can provide a ten fold improvement and the NS-BH case a factor of 5. Once Virgo comes online in the mid epoch galaxy weighting still proves useful, particularly for a narrow FoV telescope which can see almost double improvement in imaging the host galaxy. However for a wide FoV telescope the galaxy weighting in this epoch only provides an improvement of a few percent. This is also the case in the late epoch. However once the detectors reach their design sensitivity in the final and india epochs, the galaxy weighting technique provides little advantage in identifying the host galaxy tile. This is because the localisation region determined from timing information alone is sufficiently small that a typical telescope can cover this entire region.

3.5 Concluding Remarks

A galaxy ranking statistic has been presented to better localise a GW source than using timing information from a network of GW detectors alone. Triangulation techniques can localise a GW signal to 10-100 deg^2 in a three detector Initial LIGO-Virgo network. This error region is too large to cover with typical optical telescopes used in the LOOC UP program. Using the GWGC, which provides a reasonably complete list of galaxies within 100 Mpc, galaxies within the reach of the Initial LIGO/Virgo detectors can be ranked. This ranking scheme proves much more successful in determining the host galaxy of a signal than triangulation alone, by a factor 2-4 with one or five pointings. The coverage of narrow FoV and wide FoV optical telescopes is considered as well as a GW signal originating from a binary system consisting of NS-NS

NS-NS 1.4-1.4 $M_\odot$

Epoch	No Galaxy Weighting				Galaxy Weighting			
	Narrow FoV		Wide FoV		Narrow FoV		Wide FoV	
	% Hosts Imaged With		% Hosts Imaged With		% Hosts Imaged With		% Hosts Imaged With	
	5 pointings	20 pointings	5 pointings	20 pointings	5 pointings	20 pointings	5 pointings	20 pointings
early	0-1	2-3	1-2	7-8	3-10	8-23	3-10	11-25
mid	14-15	39-41	32-35	72-73	18-26	43-50	35-40	75-76
late	12-14	35-39	31-34	69-73	13-19	37-45	32-37	69-75
final	19-26	49-62	43-53	81-88	20-27	50-63	44-54	82-90
india	59	93	87	99	60	93	87	99

NS-BH 1.4-5.0 $M_\odot$

Epoch	No Galaxy Weighting				Galaxy Weighting			
	Narrow FoV		Wide FoV		Narrow FoV		Wide FoV	
	% Hosts Imaged With		% Hosts Imaged With		% Hosts Imaged With		% Hosts Imaged With	
	5 pointings	20 pointings	5 pointings	20 pointings	5 pointings	20 pointings	5 pointings	20 pointings
early	0-1	1-2	1-2	6-9	1-5	4-11	2-5	7-13
mid	10-11	31-33	29-30	64-66	12-13	32-34	28-30	66-68
late	8-10	28-32	26-29	62-66	10-13	30-34	27-30	63-68
final	11-17	35-45	31-40	69-78	12-17	35-47	32-41	70-80
india	44	82	77	98	45	83	77	98

Table 3.2: Localisation ability of the network of Advanced detectors, throughout its observing schedule, to a GW signal from a NS-NS (1.4-1.4 $M_\odot$) and NS-BH (NS-BH 1.4-5.0 $M_\odot$) system. The percentage of correctly localised signals is shown i) using triangulation alone and ii) when a galaxy weighting scheme is employed. The percentage of identified events is shown with the area imaged. For a narrow (wide) FoV telescope 5 pointings is roughly equivalent to 4.2 (16.8) deg^2 and 20 pointings to 16.8 (67.2) deg^2.
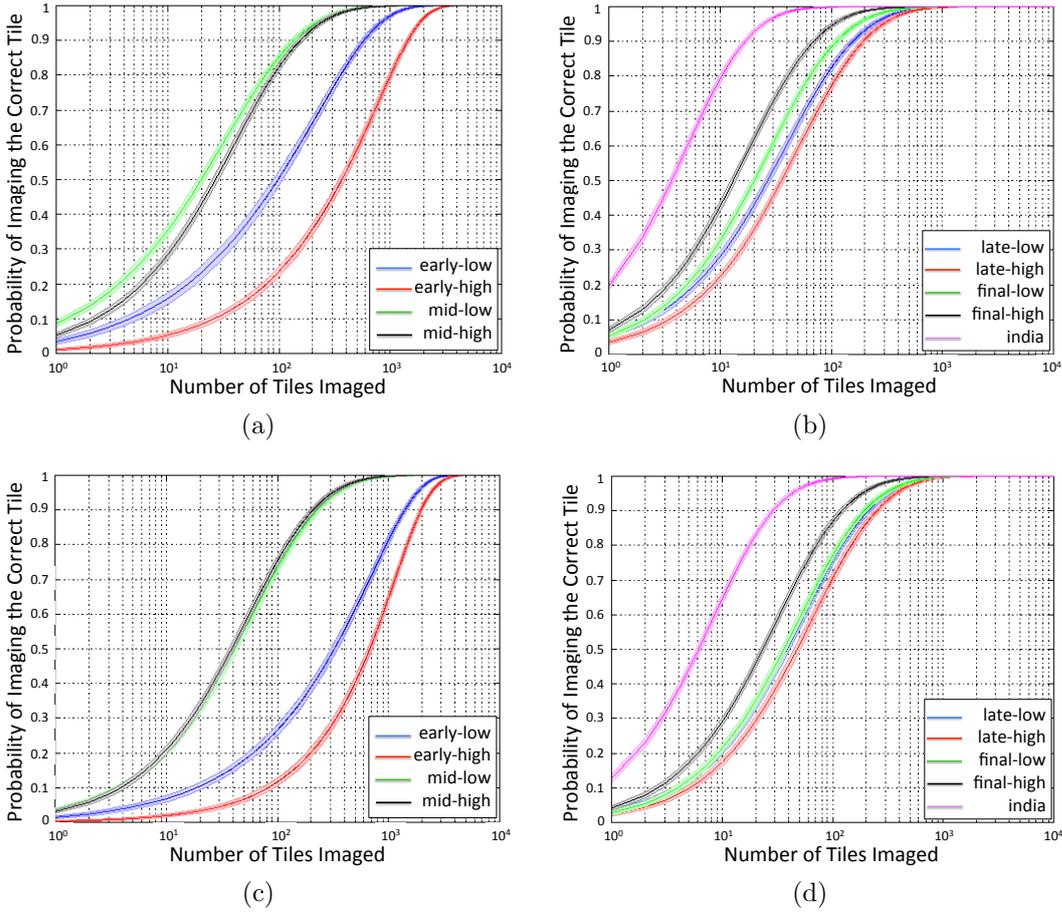
Figure 3.4: Narrow FoV case (0.84 deg^2 tiling). The probability of imaging the tile which contains the true host galaxy versus the number of tiles imaged. Plots (a) and (b) represent a NS-NS (1.4-1.4 $M_\odot$) and plots (c) and (d) a NS-BH (1.4-5.0 $M_\odot$). The shaded regions denote the 1-sigma uncertainty in the probability estimate. These results assume a galaxy catalogue that is complete to 750 Mpc.
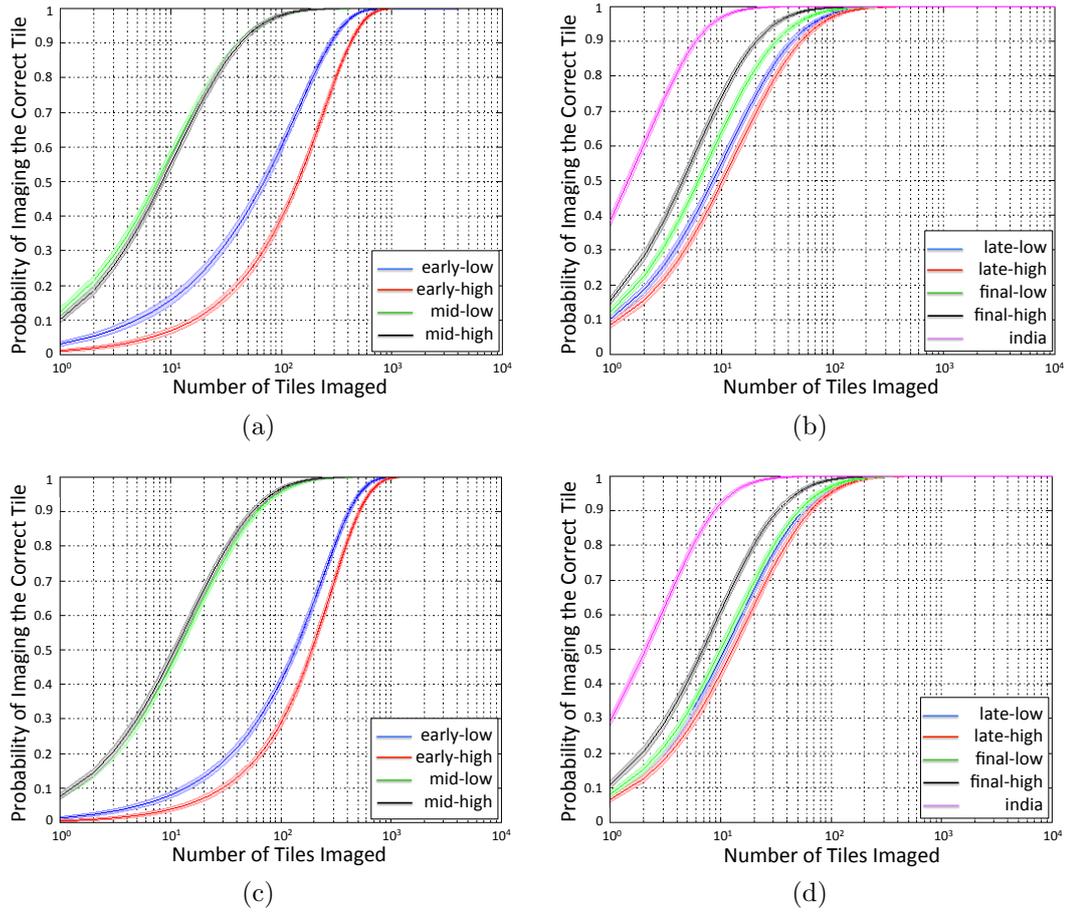
Figure 3.5: Wide FoV case (3.36 deg^2 tiling). The probability of imaging the tile which contains the true host galaxy versus the number of tiles imaged. Plots (a) and (b) represent a NS-NS (1.4-1.4 $M_\odot$) and plots (c) and (d) a NS-BH (1.4-5.0 $M_\odot$). The shaded regions denote the 1-sigma uncertainty in the probability estimate. These results assume a galaxy catalogue that is complete to 750 Mpc.

(1.4-1.4$M_\odot$) and NS-BH (1.4-5$M_\odot$ and 1.4-10$M_\odot$), the most likely sources of the first GW detections. For an Initial LIGO configuration, should a narrow FoV telescope (which images only one galaxy at a time) image the top five most likely galaxies, the probability of imaging the correct host is $78 \pm 3\%$ / $63 \pm 3\%$ / $48 \pm 3\%$ for a 1.4-1.4$M_\odot$ NS-NS / 1.4-5$M_\odot$ NS-BH / 1.4-10$M_\odot$ NS-BH. Considering a wide FoV telescope, and grouping galaxies which lie with 1 deg^2 of one another so that groups of galaxies are imaged at once, the probabilities increase by a factor of 1.2.

For the Advanced detectors two scenarios were considered. The first was using the GWGC and only considering those sources within 100 Mpc (as this is the reach of the catalogue). Therefore considering a three detector network at design sensitivity, the top five most likely hosts, for a narrow FoV telescope there is $\sim$69-78% chance of imaging the correct host galaxy and 91-95% for a wide FoV telescope.

In reality the reach of the GW detectors to binary merger sources is much larger, however complete catalogues do not exist to these distances. Therefore the second scenario was to create a simulated galaxy catalogue using information from the GWGC out to 750 Mpc. This encompasses the reach for a 1.4-1.4 $M_\odot$ NS-NS and 1.4-5$M_\odot$ NS-BH systems. Due to the 700 fold increase in galaxies being considered, we tiled the sky in to areas of a typical narrow ($\sim$1 deg^2) and wide ($\sim$3.4 deg^2) FoV telescope. The observing schedule for the Advanced detector era shows a changing network sensitivity over several years. Therefore to understand the networks ability to identify the host galaxy of a GW signal throughout this period a range of network sensitivities was investigated. Again it can be shown that galaxy ranking improves the probability of localising a GW signal to the correct host galaxy. This will be a valuable asset particularly in the early years of Advanced LIGO and Virgo where regular GW detections are expected to be made, but the localisation region (from timing information alone) too large for conventional telescopes to cover. This motivates construction of galaxy catalogues that are complete out to distances of $\sim$ 1 Gpc.

Chapter 4

Large Scale Image Processing with the ROTSE Pipeline

The first attempts to detect electromagnetic (EM) counterparts to candidate gravitational wave (GW) events were made during the 2009-2010 science run of the LIGO and Virgo detectors [51, 191]. This search was outlined in Chapter 2, and documented in detail in [160]. Given the GW detector sensitivities at the time of the search, it is unlikely that any of the GW triggers represent true astrophysical events. However these joint observations are a useful exercise in preparing for the era of advanced GW detectors [188, 192] (c. 2015+), when EM follow- ups will be performed on GW triggers of astrophysical origin.

A number of optical telescopes participated in the 2009-2010 campaign, one system being ROTSE-III. The ROTSE collaboration has a well established image processing pipeline. This pipeline makes use of astronomical image subtraction by cross-convolution, removing the need for high quality reference images, with similar computational efficiency to other image processing procedures [193]. Transient identification is based on human scanning of potential candidates identified by the pipeline, and separate generation of lightcurves of the most interesting candidates. The pipeline has proven to be successful in finding supernovae as well as GRB afterglows etc. [194, 195, 196]. However, the detection of optical transients associated to GW triggers presents new challenges, in particular the need to process large numbers of images to cover a typical GW error region, and the ability to assign a quantitative false alarm probability on any detected optical transient. It is therefore essential that we have an automated image processing pipeline, where large numbers of images can be processed.

In this chapter we present modifications made to the ROTSE pipeline to

allow the processing of large numbers of images with automated detection and tentative classification of transients for the 2009-2010 observation campaign. We evaluate the performance using archival ROTSE images, and use custom-built software to add simulated transients to images. The results of the 2009-2010 images associated with candidate GW events are presented in Chapter 5.

4.1 The Challenges in Detecting an Electromagnetic Counterpart of a Gravitational Wave Event

Many systems which produce detectable GWs should also be observable in EM wavebands [160]. As discussed in Chapter 2, the most promising GW sources which are also expected to have EM counterparts are mergers of binary neutron stars (NS-NS) or binaries consisting of a neutron star and stellar mass black hole (NS-BH). These systems are also the favoured progenitor model for short gamma-ray bursts (SGRBs) [76]. Abadie et al. [34] summarise predictions of the rate of detection of such systems by the advanced LIGO detectors. Metzger et al. [123] review various possible EM counterparts. In addition to SGRBs, these include orphan optical/radio afterglows, supernova-like optical transients ("kilonovae") are thought to be generated by the decay of heavy nuclei produced in the merger ejecta [95, 97]. Another system which may produce detectable GWs are long gamma-ray bursts (LGRBs); see [100] for a summary of possible GW emission scenarios. There is a wealth of observational data detailing the afterglow of both SGRBs and LGRBs. Observations detailed in Kann et al. [133, 134] estimate one day after a GRB burst is detected, the magnitude of a LGRB will be in the range 18-24 mag and SGRB 24-30 mag (based upon observations where the afterglows are at scaled to be at $z = 1$) and follow a power-law decay $L \propto t^{-1.1}$ (L is luminosity and t is time). The optical kilonova transient is expected to produce an optical emission peak at magnitude 18 at one day for a source at 50 Mpc and fade over the course of a few days [97].

GW events which produce high-energy EM counterparts such as gamma-ray bursts (GRBs) may be promptly identified and localised by satellites such as Swift [124] and Fermi [197]. However, for GW events where high-energy emission is absent, or beamed away from Earth, or where the source is outside

the field of view of these satellites, the detection of an EM counterpart to a GW event will be challenging. First, sky localisation using GW data alone will produce a large error box, typically 10-100 deg^2 [72, 198]. The field of view of one of the ROTSE-III telescopes is ~ 3 deg^2, making it impractical to image the entire error region. Instead, we make use of the fact that first-generation GW detectors had a maximum distance sensitivity of between 30-65 Mpc for NS-NS and NS-BH binary mergers [34] and focus observations upon galaxies in the error region within the reach of GW detectors using the Gravitational Wave Galaxy Catalogue (GWGC) described in [163]. Despite there being hundreds of galaxies in a typical GW error box, the galaxies can be ranked according to their distance and luminosity as the most likely host from which the signal originated (see Chapter 3). Considering a typical pointing with a ROTSE-III telescope, the probability of successfully imaging the correct host galaxy is estimated at between 30%-60%, not including galaxy catalogue incompleteness [199]. For the Advanced GW detectors, which will have an order of magnitude larger distance reach at design sensitivity [188, 192], estimates indicate that ~ 10 pointings will be required to have reasonable probability of imaging the host galaxy. More details of this can be found in Chapter 3.

Another complication of detecting EM counterparts to GW events is that the magnitude and decay timescale of possible EM counterparts are uncertain [160]. This uncertainty necessitates observations at both early and late times, ideally from seconds to weeks after the trigger. Combined with the large error regions associated with GW triggers, this implies the need to process many images. Given the uncertain nature of the counterpart lightcurve, the image analysis should be capable of detecting any transient that is inconsistent with typical background events (which may be real astrophysical transients unrelated to the GW trigger or image artefacts).

Finally, there has not been a confirmed detection of a GW to date, making it desirable to be able to assign a high statistical confidence in any putative EM counterpart. Analysing both "background" images (images from pointings not associated with a GW trigger) and "injection" images (images containing simulated transients with known lightcurves) will be vital to quantify the rate at which simulated transients are detected as well as the performance of the pipeline. In particular, we need to test any background rejection steps on injected transients to verify they are "safe". All of these factors point to the need to automate the EM image analysis (see for example [200]) to allow large-scale processing and quantitative characterisation of the pipeline.

4.2 The ROTSE-III Telescope System

The Robotic Optical Transient Search Experiment (ROTSE) is dedicated to rapid follow up observations of GRBs and other fast optical transients on the time scale of seconds to days. ROTSE has undergone two phases of development thus far, ROTSE-I and III. ROTSE-I consisted of a 2 x 2 array of telephoto camera lenses co-mounted on a rapid-slewing platform, located in northern New Mexico. The array was fully automated and started taking data in 1998. Observations made by ROTSE-I of GRB 990123 revealed the first detection of an optical burst occurring during the gamma-ray emission, demonstrating the value of autonomous robotic telescope systems [201].

The ROTSE-III telescope system came online in 2003 and consists of four 0.45 m robotic reflecting telescopes located in New South Wales, Australia (ROTSE- IIIa), Texas, USA (ROTSE-IIIb), Namibia (ROTSE-IIIc) and Turkey (ROTSE-IIId). The instruments are fully automated and make use of fast optics to give a 1.85×1.85 degree field of view. ROTSE-III is capable of attaining 17th magnitude with a 5 second exposure and 18.5 magnitude with a 60 second exposure. If multiple images are stacked on top of one another or "coadded" ROTSE-III can reach ∼19th magnitude [202].

Between September 2 and October 20 2010, ROTSE-III took over 700 images in response to 5 candidate GW triggers as part of the latest science run of the LIGO and Virgo detectors [160]. All four ROTSE telescopes were used to gather the images, which span from the first night following the event to one month later and vary in exposure length (either 20 or 60 seconds). When a LIGO/Virgo trigger was sent to the ROTSE telescopes, typically 30 images were taken on the first night and 8 images taken on subsequent follow-up nights, per telescope, for the first ten nights following the trigger, with additional observations around nights 15 and 30. We use archival images selected with this cadence so as to characterise the automated ROTSE pipeline in conditions matching that of GW followup observations.

4.3 The ROTSE Image Processing Pipeline

4.3.1 Basic features

The ROTSE image processing pipeline [193] was developed by the ROTSE collaboration to search for transient objects in images taken with the ROTSE-III telescopes. The pipeline makes use of cross-convolution to perform image sub-

traction. Image subtraction is an essential tool needed to remove contributions from static sources and amplify any subtle changes. For example, without image subtraction it would be almost impossible to find a source buried within a host galaxy. In this section we give a brief summary of the pipeline; more details can be found in [193].

The pipeline starts by processing images through SEXTRACTOR [203], giving a list of objects with precise stellar coordinates. These coordinates are used to compute corrections for image warping, so that the stellar objects within the image overlay as closely as possible with those in the reference image. It is essential to use an image or stacked set of images (see Section 4.3.2) of the same region from an uninteresting time as the reference image so that a new transient may be identified. At this point in the analysis pixels within either image which exceed the saturation level are excluded. To estimate the background as precisely as possible the background difference is found between the two images, instead of the individual background for each image separately. The sky difference map is generated by performing a pixel-by-pixel subtraction between the warped and the reference image and it is this which is subtracted from the original image. The main benefit of this sky difference map is that the final subtracted image will be background-free. This procedure is repeated for all images which are to be processed before the cross-convolution algorithm is invoked.

4.3.2 Coadding

On a typical night, two sets of four images of 60 second exposure[1] with a 30 minute cadence are taken. These images are of the same part of the sky, so that images may be stacked on top of one another or "coadded". Coadding increases, by about one magnitude, the limiting magnitude to which we are sensitive, allowing fainter objects to be seen without saturating the brightest objects within the image. Each four-image set is coadded, as well as the eight images taken for the night, resulting in three co-additions. These three images are then subtracted from the same reference image, and the three difference images processed through SEXTRACTOR to reveal the residual objects.

The ROTSE pipeline can also perform a "non-coadded" analysis, in which just the images taken from the first night are processed without coadding to see if there are any fast transients on the hour time scale. Since the non-

---

[1]A 20 second exposure is used if the target is in the vicinity of a bright galaxy or if the moon is in a bright phase.

coadded analysis does not stack images, the images have a shallower limiting magnitude than those images which have been coadded. We will only present examples using the coadded method, i.e. characterising the ability to detect transients with a characteristic timescale of a few days.

4.3.3 Candidate Selection

In the coadded analysis, we have two images made from two sets of four images (called hereafter the "4-fold images") and one image made from the coadditions of all the images taken over the night (the "8-fold image") as described in Section 4.3.2. Any residual objects identified in these images by the pipeline are required to fulfil certain criteria to be considered candidate transients, as detailed in [204]. First, the object must have a signal-to-noise ratio (SNR) above 2.5 in the 4-fold images and above 5 in the 8-fold image. Next, the position of the object between the 4-fold and 8-fold images must match to within 1.5 pixels for candidates with SNR < 15 and to within 1 pixel for objects with SNR > 15. The full width half maximum (FWHM) of the object must be no bigger than twice the median FWHM of the stars in the convolved reference image, as well as be within the range of one pixel. The change in flux is also checked in a circular region of diameter ~ 6 pixels around the object. Different cuts are applied depending on whether the potential candidate corresponds to a stellar object or lies in a known galaxy. For example, if an object matches a star or an unknown object a flux change of 60% is required, whereas if the object is within 20% of the semi-major axis length from the galaxy centre, but not consistent with a core, only a 3% flux change is required [204].

After the potential candidates have gone through these checks, further criteria are applied should more than twenty candidates remain. Many candidates remaining may indicate that the subtraction did not work correctly, or that the image quality is poor. First source crowding is checked, wherein potential candidates are rejected if they have more than 15 other potential candidates within 250 pixels. If there are still more than 20 potential candidates remaining, objects near the edge of the image are discarded, since the edges are liable to fringing and aberrations [204]. Again, if more than 20 potential candidates remain, the area is reduced and the process repeated until the area of the image is 800 pixels in width or there are less than 20 potential candidates remaining. In these situations it is not very likely that something of astrophysical significance will be found due to the quality of the images.

Objects which have passed all the criteria outlined above form the can-

didate list. In fact, several candidate lists are generated: one for each night in the coadded case, and one for each consecutive pair of images in the non-coadded case. These lists need to be combined to produce a single list of unique candidates. The vast majority ($\sim 95\%$) of these potential candidates will be image subtraction artefacts, with a minority ($\sim 2\%$) due to known variable objects such as variable stars or asteroids. We identify and remove these known transients by comparing to the SIMBAD catalogue [205] and the Minor Planet Checker [206].

4.3.4 Webpages

For each candidate list the pipeline also generates a webpage such as the one shown in Figure 4.1. At the top of the webpage three images are shown. On the left is the coadded image for one night, in the middle is the reference image, and on the right is the subtracted image. The example subtracted image shows four candidates. Below this are a list of links, one for each candidate. Selecting a link (in this case the first) displays a table of sub-images for that candidate. The top left panel of this table shows the first coadded image (from images 1-4 taken on that night), the top middle shows the second coadded image (from images 5-8), and the top right shows the reference image, all zoomed in to the vicinity of the candidate. The bottom left plot shows the first subtracted image (the first coadded image minus the reference), the bottom middle shows the second subtracted image. The bottom right panel displays information about the candidate, including the right ascension, declination, magnitude, signal-to-noise, FWHM (these last three quantities are calculated by comparing the reference image with the coadded image of the entire night), motion (this is the variation in distance between the first and second coadded images in units of pixels), percentage flux change (between the coadded image of the night and the reference image) and whether a candidate has been found at these coordinates before. As well there are links to the SIMBAD catalogue, Minor Planet Checker, SDSS [207], 2MASS [208] and DSS [209] to help decide the importance of the candidate. From this information, the user manually selects candidates of interest and lightcurves for these candidates are generated. It is possible to produce two lightcurves; one which includes both the transient and background and one which subtracts the background (estimated using an annulus of inner radius $\sim$6 pixels and outer radius of $\sim$14 pixels) away producing the lightcurve for just the transient.
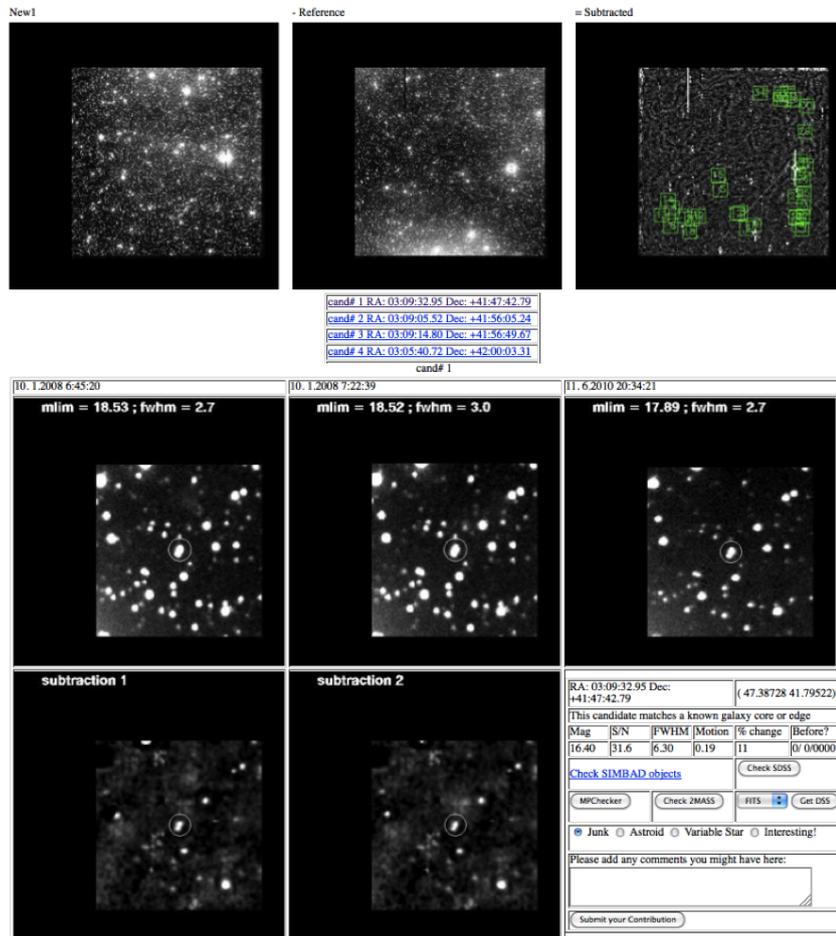
Figure 4.1: A sample ROTSE pipeline webpage, showing links to all the candidates found as well as a table displaying subimages and information for the first candidate. The full webpage displays one table for each candidate. At the top are three images, the coadded image for one night, the reference image, and the subtracted image respectively. Below this are a list of links, one for each candidate. Selecting a link (in this case the first) displays a table of sub-images for that candidate. Starting from the top left panel of this table is the first coadded image, second coadded image and the reference image all zoomed in to the vicinity of the candidate respectively. The bottom left panel shows the first subtracted image and the second subtracted image respectively. The bottom right panel displays information about the candidate, including the right ascension, declination, magnitude, signal-to-noise, FWHM, motion, percentage flux change and whether a candidate has been found at these coordinates before. In addition are a number of links to help decide the significance of a candidate.

4.4 Automating the Pipeline

The ROTSE image processing pipeline has been used to make some significant discoveries of optical transients [194, 201, 210, 211, 212]. However the follow up of GW events requires processing larger numbers of images that is not feasible with a widget-based, user driven setup designed to handle one set of images at a time. For example, a series of commands in the IDL environment [213] are used to produce the various lists of candidates and their corresponding webpages. Human scanning is then required to distinguish candidates of astrophysical interest from those due to poor image subtraction, those due to minor planets, etc. Further widget-based commands are then needed to produce the lightcurve of each interesting candidate. This procedure is user intensive and time consuming. However, many of these steps are algorithmic, such as checking for candidates at the same right ascension and declination across nights, and suitable for automation. We have therefore written a wrapper to the pipeline that automates the processing of large sets of images. A single command now runs the complete end-to-end pipeline: looping over image sets, finding transients, identifying transients detected across multiple nights, and generating light curves for all transients.

Other barriers to processing large numbers of images are the need to have an IDL license for each instance of a running pipeline, and a pipeline architecture that is designed to process only a single set of events at one time. We have altered the pipeline architecture to automatically create separate directory structures for each set of images, allowing multiple instances of the pipeline to run simultaneously without conflict. Furthermore, we have removed the need for separate IDL licenses for each instance of the pipeline by compiling the pipeline in an IDL virtual machine [214]. Only one license is required, and only at the compilation stage. Combined, the change in architecture and freedom from license restrictions enables the processing of multiple sets of images simultaneously on computer clusters. We have written scripts for large scale processing using the CONDOR/DAGMAN job management system [215]. The automated processing is able to perform a complete analysis, identifying candidates and generating lightcurves, within a few hours [216]. We have verified that the automated version of the pipeline produces lists of candidates that are identical to those produced by the original manual analysis[2].

---

[2]The source code repository can be found at https://gravity.astro.cf.ac.uk/cgit/rotse and all documentation at https://wiki.ligo.org/Bursts/LoocUpROTSE.

4.4.1 Candidate Validation and Classification

Once the automated code has produced the lightcurve information for all the potential candidates identified by the pipeline, a series of pass/fail tests are applied to each candidate. Specifically, we test whether the candidate appears on more than one night, whether its coordinates overlap with a known variable source (by querying the SIMBAD catalogue) or with an asteroid (by querying the Minor Planet Checker), and if the lightcurve of the potential candidate varies sufficiently. This last test has two components: a check that the lightcurve decays sufficiently 48 hours after the event took place, and a chi-square test to check that the candidate's lightcurve is not too flat, given by equation (4.1).

$$\sum_i \left(\frac{\mathrm{mag}_i - \mathrm{inter}}{\mathrm{error}_i} \right)^2 \leq 200. \tag{4.1}$$

Equation (4.1) represents the flatness condition, where mag_i is the magnitude of a transient in image i with a magnitude error, error_i. A least squares linear fit is used to calculate the best fit intercept, inter, to the data. This same method is used to calculate the gradient of the candidate lightcurve 48 hours to one month after the event took place. We required that the gradient ≤ -1 to pass this test. This condition along with that in equation (4.1) were decided upon through tests comparing lightcurve data from simulated transients and background artefacts.

The multiple-night and flatness tests are very effective at rejecting non-astrophysical background, particularly image-subtraction artefacts. The decay test is seen to reduce significantly the background of astrophysical transients unrelated to the GW trigger while not rejecting simulated astrophysical transients correlated with the GW trigger (see Section 4.6). The specific requirement of decay after 48 hours is motivated by models of EM counterparts for systems with strong GW emission, specifically kilonovae and SGRB/LGRB afterglows. While there are astrophysical optical transients that do not decay on this timescale, such as supernovae [217], the expected GW emission by these sources make them less likely to produce GW triggers than compact-object mergers.

We refer to these pass/fail tests collectively as the "hard" cuts in the analysis. Any candidate which fails one or more of the hard cuts is discarded. Those which survive the hard cuts are looked at further in two ways. Firstly we see whether the candidate's coordinates overlap (to within three times the size of

the major diameter) with a known galaxy. We use the GWGC [163], considering only galaxies within 50 Mpc, as this is approximately the maximum range of current GW detectors to NS-NS and NS-BH binaries [160]. Secondly, we perform a chi-square test comparing the candidate's lightcurve with several theoretical models: kilonovae, SGRB afterglows, and LGRB afterglows. Candidates that fulfil any of these conditions are highlighted in the final candidate list.

The final candidate list following application of these tests typically contains fewer than 5 candidates. In order to better assess the statistical significance of any surviving candidates, we assign to each an *ad hoc* ranking statistic R defined as

$$R \equiv \sum_i (18 - m_i)\Theta(18 - m_i) \times w_i \,. \tag{4.2}$$

Here $\Theta(x)$ is the step function, m_i is the background-subtracted magnitude of the transient in image i, and w_i is a weight factor defined by

$$w_i = \begin{cases} 1 & t_i - t_{\mathrm{GW}} < 1\,\mathrm{day} \\ \left(1 + \log_{10}\frac{t_i - t_{\mathrm{GW}}}{1\,\mathrm{day}}\right)^{-a} & t_i - t_{\mathrm{GW}} \geq 1\,\mathrm{day} \end{cases} \tag{4.3}$$

where t_{GW} is the time of the GW trigger and t_{i} is the time of image i. The power law index a is chosen to be 3 as this is the approximate gradient of the three target theoretical lightcurves, and magnitude 18 is the approximate limit of the majority of the ROTSE images we are analysing. Candidates with magnitude $m_i > 18$ are likely to be processing artefacts, so the Θ factor ensures a rank of zero for those cases. While equation (4.2) is *ad hoc*, it has the desirable property of favouring brighter candidates which appear in multiple images close in time to the GW trigger.

4.4.2 Simulated Transients & Detection Efficiency

Adding simulated transients ("injecting") into the ROTSE images is key to quantifying both the detection efficiency and the magnitude limit of the pipeline. We therefore use the injection code developed specifically to add transients to ROTSE images by White et al. [218]. Since the processing uses image subtraction to remove the background, it is not so trivial as copying a model star and placing it somewhere else in the image. The variation in background around the transient in question has to be taken into account to realistically inject a simulated transient into the ROTSE images.

To begin, the user selects a number of real stars from the image as model stars. These stars must be sufficiently bright and isolated, so that the injection code does not take into account the flux of any unwanted stars and is able to accurately determine the point spread function (PSF) of the model star. We note that simple models for the PSF (e.g. a Gaussian) are not applicable for wide field of view images such as those from ROTSE, as the PSF varies across the image. An injection is performed by selecting a random position within 100 pixels of the model star, and selecting the distance to the source. The flux of the model star (minus the background) is scaled to follow the desired lightcurve, such as the kilonova or afterglow models discussed in Sections 4.1 and 4.4.1. The magnitude required in each image is calculated by taking into account the time between the GW trigger and the image being taken; for our tests we assume an interval of 0.5 days elapsed between the trigger time and the first image [218].

It is vital to inject a transient not only with the correct parameters, but also with the correct background. Simply copying a model star to a new location in the image would produce a background around the injection that is significantly higher than elsewhere in the image, as the post-injection background would comprise both the pre-injection background at that location and the background around the original model star. This could lead to the image processing pipeline identifying fainter injected transients than is realistic. We therefore scale the background around the injection by a constant amount so that the background before and after the injection is comparable; see Figure 4.2 for an example and [218] for further details.

A slight limitation of this injection procedure is that sometimes, injections are placed at slightly different coordinates in each set of images. To add the injection at exactly the same right ascension and declination, the injection pipeline needs to know how to compensate for image warping. However it does not do this in the same way as the ROTSE pipeline (due to different code packages) so the warping correction does not always match that done by the automated pipeline. As a consequence the effective location of the injection changes from image to image by more than that of a real star. The location of real stars matches from image to image by ∼1 pixel, whereas the location of injections may vary by several pixels. Since the pipeline requires a transient's location to be fixed within 3.5 pixels, some injections are mistakenly rejected by this procedure.
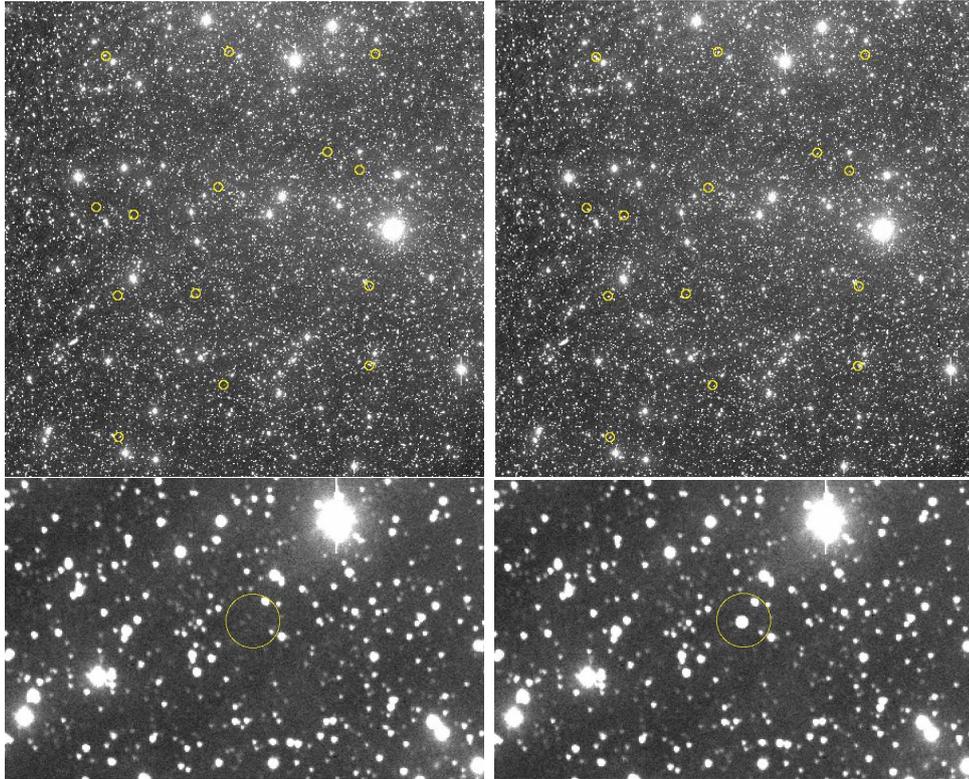
Figure 4.2: An example of injecting a number of transients into an image: (top left) original image (top right) same image with 14 injections. The regions where the injections occurred are highlighted by yellow circles in both images for comparison. (bottom) Same images as top, focussed on the region around a single injection. Note the smoothness of the background around the injection.

4.5   Background Study

Assigning a statistical significance to an event identified by the pipeline as associated with a GW trigger requires quantifying the false alarm probability. This is the probability of obtaining a similar event due to background, where for our purposes "background" includes both image-processing artefacts and real astrophysical transients that are not associated with a GW trigger. To quantify this probability we have performed a background study using archival ROTSE data. We selected at random 102 sets of images taken in response to non-GW pointings over 2 years. To better mimic a GW trigger follow-up, each set was required to have observations spanning at least a month. This yielded a total of 103 sets of images. One of these was selected at random to be our test "GW trigger", and the other 102 were used for background estimation. The background is characterised as follows: each set of background images is processed by the automated pipeline and the highest rank R in equation (4.2) is found. If a background set has no surviving candidates after the hard cuts, a rank of zero is recorded. The distribution of highest-ranked events for our 102 background pointing sets is shown in Figure 4.3. We find a bimodal distribution where approximately 80% of the pointings having a ranking statistic of less than 1 and approximately 10% have a rank greater than 11. The highest-ranked background event has $R \approx 30$. A candidate in the GW trigger image set would therefore require $R \gtrsim 11$ ($R \gtrsim 30$) to have a false alarm probability of 0.1 (0.01) or smaller.

4.6   Injection Study

In order to test the robustness of the pipeline we have performed an injection study whereby transients of a given model (either kilonova, SGRB afterglow, or LGRB afterglow) are injected into the archival ROTSE images selected as our test 'GW trigger'. The exact formulae[3] used to inject transients of a given magnitude, mag_{KILO}, mag_{SGRB}, mag_{LGRB}, following a kilonova, SGRB or LGRB afterglow respectively, are shown below.

$$L_{\text{star}} = \begin{cases} 10^{41.97} \times \text{days}^{0.43} & \text{days} < 0.7 \\ 10^{\frac{-\log_{10}\text{days}}{\log_{10} 6} + \frac{\log_{10} 0.59}{\log_{10} 6} + 42} & \text{days} \geq 0.7 \end{cases} \qquad (4.4)$$

---

[3]The equations are taken from https://trac.ligo.caltech.edu/loocup/browser/trunk/images/catalog_search/pipeline3/mfiles
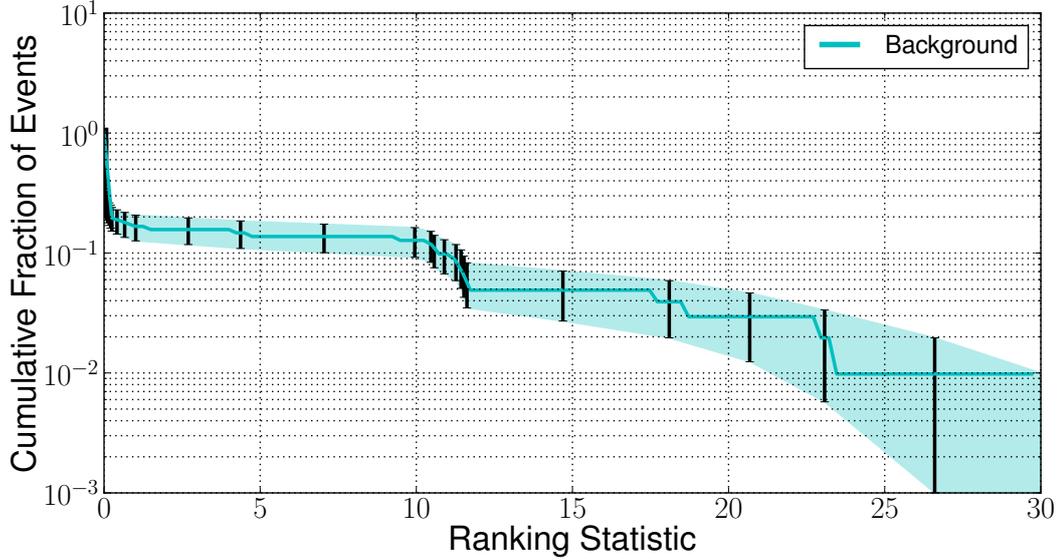
Figure 4.3: The distribution of ranking statistic R (equation (4.2)) for the highest-ranked transient in each of the 102 background image sets from the ROTSE archive. The poisson errors for the background distribution are also plotted. Image sets with no candidates surviving after the hard cuts are assigned a rank of zero. The highest-ranked background transient over the 102 sets has a rank of $R = 29.5$.

$$\begin{aligned} \text{mag}_{\text{KILO}} = \quad & M_{\text{sun}} - \tfrac{5}{2} \log_{10} \tfrac{L_{\text{star}}}{L_{\text{sun}}} \\ & + 5 \log_{10} \left(\text{distance} \times 10^6 \right) - 5.3 \end{aligned} \tag{4.5}$$

$$\begin{aligned} \text{mag}_{\text{SGRB}} = \quad & 23 + \text{offset} + \tfrac{8}{3} \log_{10} \text{daysOF} \\ & + 5 \log_{10} \tfrac{\text{distance}}{\text{refdist}} \end{aligned} \tag{4.6}$$

$$\begin{aligned} \text{mag}_{\text{LGRB}} = \quad & 16 + \text{offset} + \tfrac{8}{3} \log_{10} \text{daysOF} \\ & + 5 \log_{10} \tfrac{\text{distance}}{\text{refdist}} \end{aligned} \tag{4.7}$$

Equation (4.4) and (4.5) give the kilonova model taken from [97] where L_{star} is the luminosity of the source (erg s^{-1}), M_{sun} is the bolometric absolute magnitude of the Sun, L_{sun} is the luminosity of the Sun, and days is the time since the trigger (in days). Equation (4.6) shows the SGRB model taken from [134] and equation (4.7) the LGRB model from [133]. Since the data taken from [133, 134] are of GRBS at $z = 1$, the time since the trigger needs to be corrected to obtain magnitudes in the cosmological frame rather than the observer frame, given as

$$\text{cosmological frame time} = \text{observer frame} \times (1 + z). \tag{4.8}$$

Therefore the time since the trigger is defined as daysOF=2×day; distance is the distance to the source (Mpc) and refdist is the distance to $z = 1$ in Mpc. The offset quantity has been added to equations (4.6) and (4.7) to represent the spread in observational data taken from [133, 134]. The brightest afterglow lightcurves have an offset of 0 and the dimmest lightcurves a value of 8; offset can take a value between 0-8. Therefore at a given distance two GRB afterglows can differ by ~ 8 magnitudes.

We choose 14 reference stars in the first image as our models for the injections. These reference stars are chosen as uniformly as possible so injection performance may be tested across the image. This is then repeated 10 times so that 140 injections of each model are performed at a given distance. For convenience, we choose to inject all the models at similar magnitudes, corresponding to different source distances. For example, a kilonova at 1 Mpc corresponds to a SGRB afterglow at a distance between 0.2 and 8 Mpc and a LGRB afterglow between 5 and 200 Mpc. Injection magnitudes between 8 and 17 were tested, corresponding to distances between 0.4 and 30 Mpc for the kilonova model and larger distances for the afterglow models. The lightcurve of an injected transient following both a kilonova and GRB model are shown in Figure 4.4. The injected magnitudes of a model transient are shown in addition to the measured magnitudes. For comparison, the variation in the weight factor, ω_i (equation (4.3)), is given over the time period.

Figure 4.5 shows the efficiency of the pipeline in finding the injections in terms of distance and magnitude. This figure assumes the GRB afterglows are the brightest possible (offset=0), however the distances quoted could be a factor of up to 40 lower if the dimmest afterglow was considered (offset=8). In this case an injection is considered to be detected if a transient with $R > 0$ is found within 3.5 pixels of the injection location. At very close distances or low magnitudes all efficiencies suffer from saturation: the injections are so bright that their image pixels are saturated. As described in Section 4.3.1, the pipeline removes saturated pixels at a very early stage as they are assumed bad and not astrophysically interesting. Attempts have been made to overcome this issue by fitting each of the injection models to the data. The best-fit model is selected and used to predict the magnitude at the time of each image. For any images for which the candidate is not reported by the pipeline and for which the predicted magnitude is low enough to cause saturation, a new rank is calculated using the predicted magnitude for that time. We find that this procedure successfully retrieves transients ~ 1 magnitude too bright for the
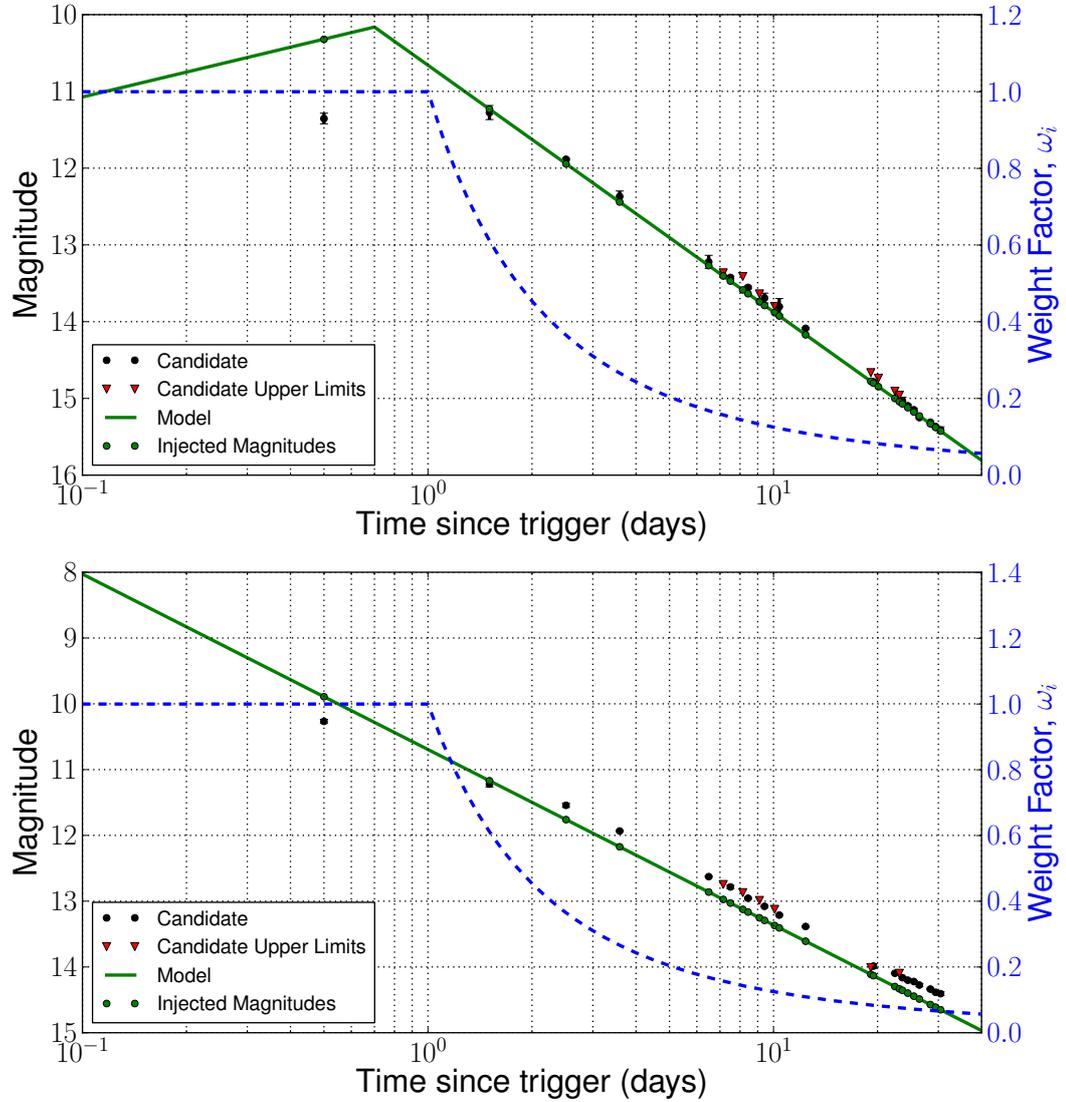
Figure 4.4: Magnitude versus time of an injected transient following a (top) kilonova and (bottom) GRB afterglow. Shown is the transient as identified by the automated ROTSE pipeline (black points) and times when the transient was not found by the pipeline (red upper limits). The magnitude of the injected transients are shown (green points) along with the model (green line). For comparison the weight factor, ω_i (equation (4.3)), is shown by the blue dashed line.

unaltered pipeline, but it is not effective for even brighter (closer) transients.

Figure 4.5 shows that the automated pipeline achieves detection efficiencies above 50% for all models over magnitudes of approximately $9 - 14$. The maximum detection efficiency is greater than 60% for all models tested. Of the $35\% - 40\%$ of injections which are not found, more than half are lost because insufficient lightcurve data could be generated. As described in Section 4.3.4, the pipeline generates two lightcurves for each candidate, one without background subtraction, and one with the background subtracted. To determine the lightcurve data for a candidate, a sub image is made (300×300 pixels) around the candidate (as well as a reference sub image). The data for the former lightcurve can be found at this point. To obtain the data for the latter lightcurve, the background needs to be subtracted from the candidate sub image. The candidate sub image is therefore warped so certain objects/stars overlay with the same objects/stars in the reference sub image. The USNO-B catalogue is used for this step. However if there are not enough "reference objects" in the candidate sub image to overlay it with the reference sub image, the background cannot be subtracted accurately. At least 16 points of reference are needed in the candidate sub image to overlay with the reference sub image.

The ranking statistic R (equation (4.2)) is based on the background-subtracted lightcurve which is highly dependent on image quality and the position of the transient in the image. In reality the edges of an image can have a much lower limiting magnitude than the centre of the image. It is therefore more likely that the background could not be subtracted accurately in these regions and a transient not be identified. If we were to only require a transient to pass the hard cuts described in Section 4.4.1, the peak efficiency for each model would be closer to 90%. Therefore a future study would potentially incorporate the lightcurve generated before background subtraction. As well, to combat the poor image quality around the edge of an image, ROTSE could take images which would overlap to build a mosaic of a region of the sky.

The efficiency of detecting injections with a false alarm probability of less than 10% (i.e., with $R \gtrsim 11$) is shown in Figure 4.6. The efficiencies are not as high as those found in Figure 4.5, with maximum efficiencies between $\sim$45% and $\sim$60% depending on the model. This would therefore suggest that all candidates which pass the hard cuts should be looked at further to see whether they are astrophysically interesting. Figure 4.7 shows the distribution of injections, in terms of rank, at various distances. At close distances the rank

of injections is higher than the loudest candidate found in the background. At a kilonova distance of 1 Mpc the loudest injections are comparable to the loudest background event. As the distance/magnitude is increased the ranks slowly fall to much lower numbers, making them unexceptional when compared to the loudest events in the background. This again supports the suggestion that any candidate to make the final candidate list be further investigated for significance even if it had a low rank.

4.7 Concluding Remarks

An autonomous pipeline for large scale processing of images taken with the ROTSE-III telescope system has been presented, in addition to a ranking scheme for classify potential candidates. The ranking scheme favours a transient which is seen on multiple nights, has a bright magnitude and a decaying lightcurve. A background study of more than 100 random pointings taken from the ROTSE archives has been performed as well as an injection study of more than 4500 simulated transients added to additional archival images. Results show that the pipeline and ranking scheme are good at identifying transients which are injected with magnitudes brighter than 13.5 on the second night. Injections which are in the range 7.5-9 magnitude have a $\sim$50% chance of suffering from saturation. Those injected transients which are found however, tend to have very low FAR. From Figure 4.6 only 10-50% of injections (depending on magnitude) fall into this category of "recovered best" (i.e. FAR < 10%). At greater magnitudes the injections fall within the background, and have a false alarm probability comparable to $\sim$20% of the background.

An important limiting factor in recovering injections is the availability of background-subtracted lightcurves, $\sim 40\%$ of injections are lost due to this. The ability of the pipeline to produce this data for a transient depends on both its position in the image and on good image quality. If the pipeline is not able to identify 16 reference objects within a 300×300 pixel area of the transient then the background cannot be subtracted accurately and the injection is not recovered. A potential solution to this is if the lightcurve before background subtraction is considered or if images are taken by ROTSE overlap with one another to build a mosaic of the region.

The maximum injection efficiency, for all three models, is $\sim$60% for magnitudes $10 - 13$ in the second night's image. Requiring only that the pipeline identify an injection, regardless of lightcurve data, the maximum detection
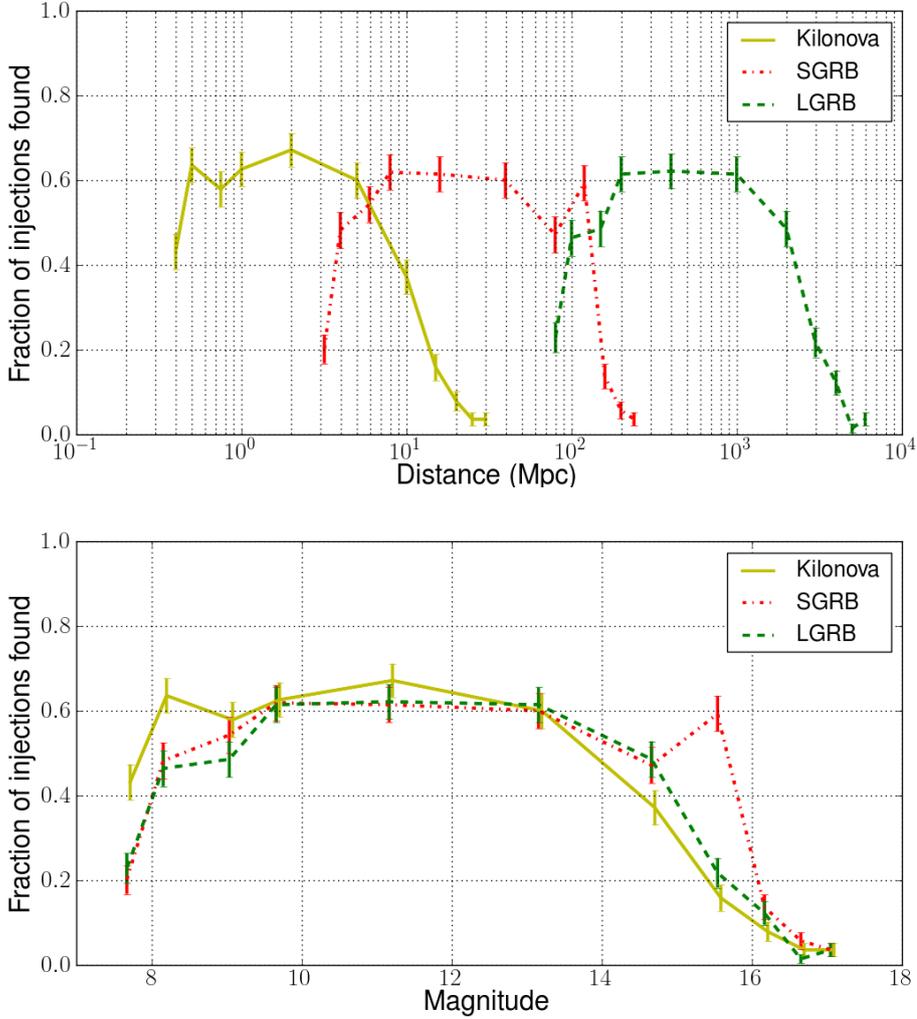
Figure 4.5: (top) Efficiency of injections found by the automated ROTSE pipeline, with $R > 0$, versus distance for an archival ROTSE event. The distances quoted for the gamma-ray burst models assume the brightest afterglows from Kann et al. [133, 134] (i.e. offset $= 0$ in equations (4.6) and (4.7)) but could be smaller by up to a factor of 40 (if the dimmest afterglows with an offset $= 8$ were considered). (bottom) Efficiency versus injection magnitude (1.5 days after the trigger time). All the models suffer from poor efficiency at very close distances / low magnitudes due to saturation.
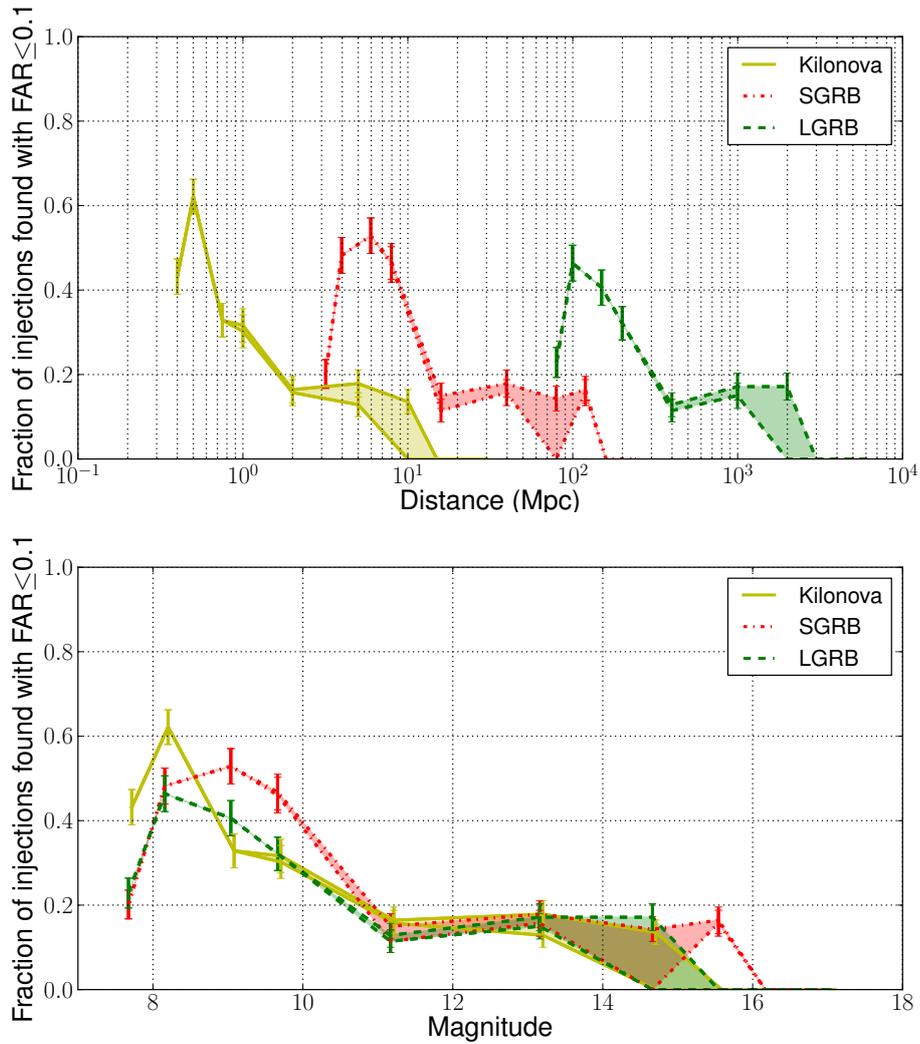
Figure 4.6: Fraction of injections found with a rank $R \geq 11$, for which the background false alarm probability is $< 10\%$ in terms of distance (top) and magnitude (1.5 days after the trigger time) (bottom) for an archival ROTSE event. The distances quoted for the gamma-ray burst models assume the brightest afterglows from Kann et al. [133, 134] (i.e. offset $= 0$ in equations (4.6) and (4.7)) but could be a factor of 40 lower.
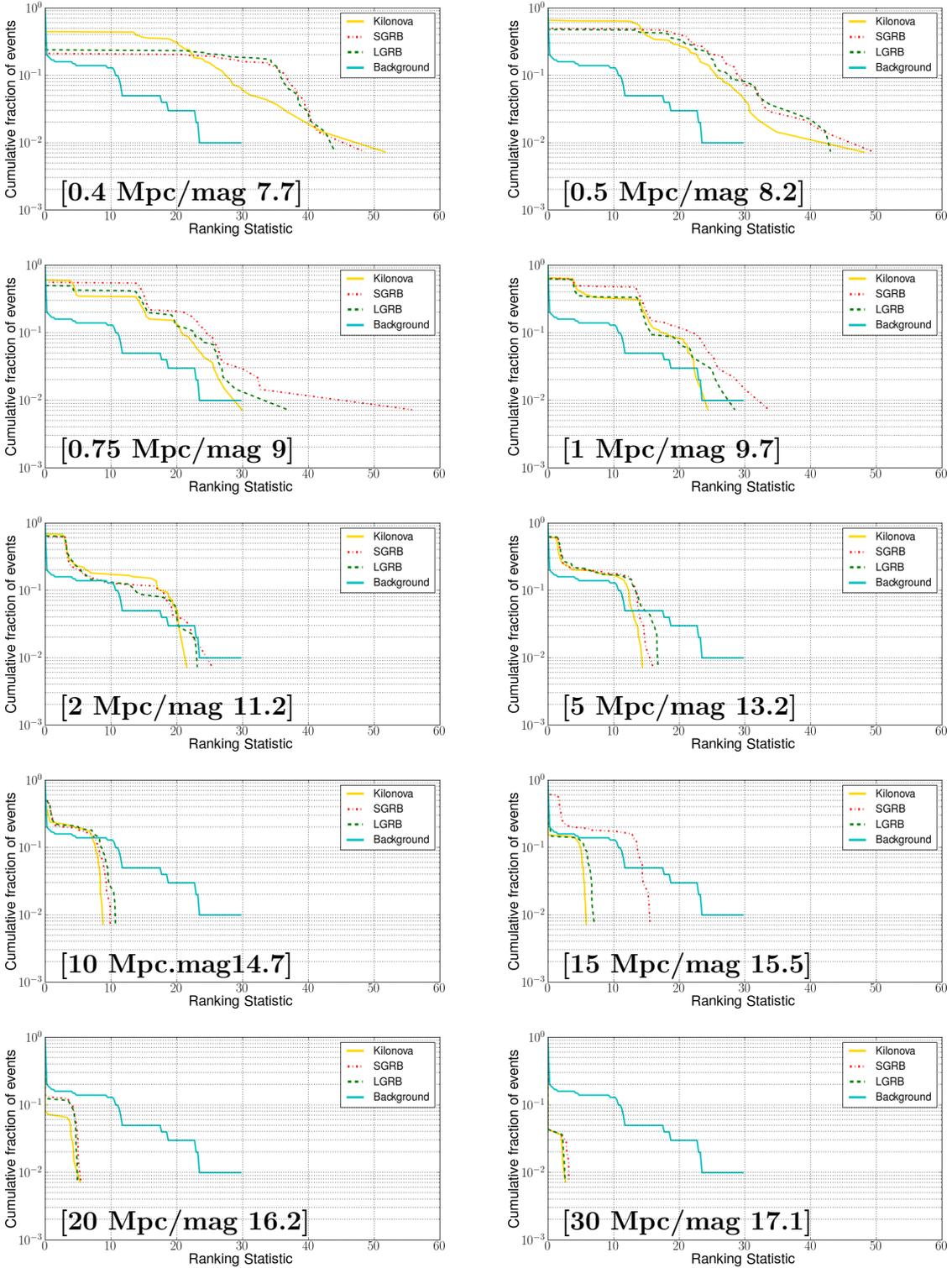
Figure 4.7: Distribution of injections compared to the background. The distance and magnitudes (1.5 days after the trigger) quoted are the values at which the injections were made. At a kilonova distance of 1 Mpc the SGRB could be at a distance between 0.2 and 7.9 Mpc and the LGRB between 5 and 200 Mpc. However in these figures we assumed the gamma-ray burst models to have the brightest afterglows from Kann et al. [133, 134] (i.e. offset = 0 in equations (4.6) and (4.7)).

efficiency is closer to 90%. Efficiencies fall to a few percent at the largest magnitudes. All these results motivate the need for further human scanning of the handful of interesting candidates identified by the pipeline, as well as further study of ranking statistics and possible background-rejection tests.

The background distribution (Figure 4.3) has a large tail from the $\sim 20\%$ of background pointings with candidates surviving the 'hard' cuts. The majority of these candidates come about due to poor image subtraction with a sufficiently varying lightcurve. Consequently a new cut would need to be employed to reject these poor subtractions, for example the shape of the transient could be taken in to account. Poor subtractions tend to have a ring or arc which masks as varying magnitude. Therefore a boosted decision tree could be used to classify and reject candidates based upon their geometrical properties, such as that used in [219] and [220].

The ability to process large sets of images in a matter of hours will be essential in the Advanced GW detector era, where GW detections will be a regular occurrence. Within this chapter we have demonstrated the ability to process images taken of one ~ 4 deg^2 region. In the Advanced detector era it is likely we will need to process ten times this. Therefore it is vital that a method is found which eliminates the tail of the background (shown in Figure 4.3). In addition a much lower FAR per image set would be imposed. For example to obtain a FAR of 10% on the whole image set (i.e. 40 deg^2) a 1% FAR would be required on each 4 deg^2 image. To further this work, a possible method to explore would be using a multi-variate analysis approach, such as that adopted by the Ice Cube collaboration [220] or Bloom et al. [200]. During the next few years it is vital we build tools to cope with the demand to process EM data triggered from GW events.

Chapter 5

Analysis of the Images Taken by ROTSE in Response to Gravitational Wave Events

5.1 ROTSE and the LOOC UP Project

The most recent science run (July 2009 - October 2010) of LIGO and Virgo saw the first efforts to detect electromagnetic (EM) counterparts in response to candidate gravitational wave (GW) events. At the time of collecting this data, the GW detectors could detect binary neutron star (NS) and stellar mass black hole (BH) systems (NS-NS/NS-BH) to 30-65 Mpc. The LOOC UP project [159] ran two observing periods, December 17 2009 to January 8 2010 and September 2 to October 20 2010 [160]. During the latter "autumn" observing period the ROTSE-III telescope system (Section 4.2) followed up on five GW events, alongside other EM telescopes which are detailed in Section 2.3.2. All four ROTSE telescopes were used in this effort to capture over 780 images, however over 100 images had to be discarded due to poor image quality.

Each GW event is named by an identification tag as shown in Table 5.1. This table also shows the date and time of the GW trigger, as well as the algorithm which identified the event, either coherent WaveBurst (cWB) [31, 161], Multi-Band Template Analysis (MBTA) [162] or the Omega pipeline (Ω) [31]. A discussion of these three algorithms can be found in Section 2.3.2. The false alarm rate (FAR) for each trigger is also reported, which is the average rate at which noise fluctuations will create an event with the same or lower probability. The lower this value the more significant an event is. For example,

ID	Date	UTC	Algorithm	FAR (day^{-1})	Analysable Images	ROTSE Telescope
G18666	Sep 7, 2010	21:37:48	cWB	0.13	125	c
G19377	Sep 16, 2010	06:42:23	cWB	<0.01	117	a,c
G20190	Sep 19, 2010	12:02:25	MBTA	0.16	257	a,b,c,d
G21852	Sep 26, 2010	20:24:32	cWB	0.02	130	b
G23004	Oct 3, 2010	16:48:23	Ω	0.21	153	b,c,d

Table 5.1: Triggers in the autumn run which the ROTSE telescopes responded to. Details include the trigger ID tag, date and time (UTC) of the trigger, the false alarm rate (FAR), the number of analysable images and which telescopes responded to the trigger and took images. Event G19377 was later revealed to be a "blind injection" secretly added to the GW data as a test of the search and follow-up procedures.

it is expected there would be 0.13 events per day similar to the G18666 trigger (i.e. you would expect 1 event every 7.7 days), whereas the G19377 event was much rarer. Also reported are the number of analysable images taken and which ROTSE telescopes were used, where ROTSE-IIIa is located in Australia, -IIIb in Texas, USA, -IIIc in Namibia and -IIId in Turkey.

The analysis of the images taken in response to each event is detailed below, separated into subsections named after the identification tag given to each GW trigger. The automated ROTSE pipeline, as described in Chapter 4, was used to analyse these images. A background study for each event was conducted in the same manner as that detailed in Section 4.5 but incorporating the ROTSE archival event which was used to test the pipeline. This means that 103 random archival ROTSE events, taken over a 1 month period, were used in the background study. The background for each GW event can be approximated separately using the same 103 pointings by considering the latency of the images taken for each GW event. For example, if a GW event had images taken on nights 1, 2, 3, 15 and 30, the background for this GW event is found by only considering those images in the 103 archival events on nights 1, 2, 3, 15 and 30. The location on the sky of all these archival events as well as the GW events are shown in Figure 5.1. The archival events were chosen blindly, therefore there are areas of the sky where more of them occur. However there does seem to be background events in the vicinity of all the GW events.

In addition to the background study we perform an injection study for each of the GW events, identical to that documented in Section 4.6. In this study simulated transients following kilonova [97], short gamma-ray burst (SGRB)
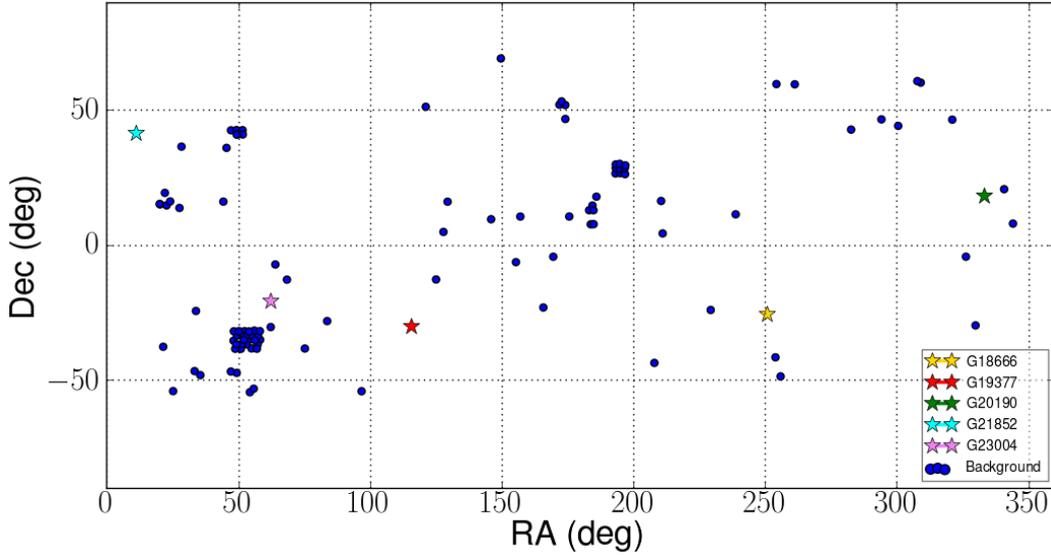
Figure 5.1: Location on the sky of all the background and GW events. The background events were chosen blindly from the ROTSE archives by selecting image sets with a similar latency to the GW images (i.e. over a month timescale). The clustering of background events in certain regions of the sky is due to surveys of those regions by ROTSE.

[134] and long gamma-ray burst (LGRB) [133] lightcurves are placed at random locations in the GW image at various distances to test the pipeline's ability to identify theoretical lightcurves of some of the most promising GW-EM sources (more discussion of these sources is found in Chapter 2).

5.2 G18666

Event G18666 occurred on September 7 2010 at 21:39:48 UTC. ROTSE-IIIc observed a single field centred on RA: 250.69500° Dec: −25.54000° beginning 20 hours 38 minutes after the event, returning on 13 subsequent nights up to day 29. In total 125 images were taken, with 77% (23%) of them having a 60s (20s) exposure time. No galaxies within 50 Mpc are within the field of view (FoV) for this event. The probability skymap as generated by cWB is shown in Figure 5.2, along with a box illustrating the area imaged by ROTSE. The top plot in this figure shows the full sky and the bottom plot is zoomed in on the region of interest, with galaxies within 50 Mpc according to the Gravitational Wave Galaxy Catalogue (GWGC) [163] marked. The coloured regions show the estimated likelihood that each pixel contains the true source direction independent of any galaxy weighting (more information on this weighting can

be found in Section 2.3.2). The cumulative probability summed over the entire coloured regions is ∼25%; i.e., the cWB skymap has containment of ∼ 25%. This Figure shows that ROTSE did not search over any of this likelihood region. Upon further investigation it was found ROTSE was meant to localise on RA: 178.90° Dec: 52.80° which would have been within one of the most likely regions, however a computing error occurred which pointed the telescope to an incorrect location. The ROTSE images are therefore not useful for detecting an EM counterpart. However, they do provide another opportunity to test the automated pipeline under the conditions of the autumn run, so the results of the G18666 analysis are included in the Appendix.

5.3 G19377

Event G19377 occurred on September 16 2010 at 06:42:23 UTC. The ROTSE-IIIc telescope responded ∼12 hours after the event when 30 (20-second exposure) images were taken within ∼15 minutes. On subsequent follow up nights (6-29) both ROTSE-IIIa and c telescopes gathered 80 (20-second exposure) images, all centred on the region RA: 115.56000° Dec:−30.00000°. Due to image quality only 72 of these images could be used in the analysis. There are three galaxies (PGC078133, PGC078144, PGC086068) visible within the FoV all at ∼24 Mpc. The probability skymap as generated by cWB is shown in Figure 5.3, along with a box illustrating the area imaged by ROTSE. The top plot in this figure shows the full sky and the bottom plot is zoomed in on the region of interest, with galaxies within 50 Mpc marked. The coloured regions show the estimated likelihood that each pixel contains the true source direction independent of any galaxy weighting (more information on this weighting can be found in Section 2.3.2). The cumulative probability summed over the entire coloured regions is ∼19.2% (i.e. the cWB skymap has containment of ∼19.2%) and the cumulative probability contained within the region imaged by ROTSE (without accounting for galaxy weighting) is ∼0.4%.

It was later revealed that this event was a "blind injection" which was secretly added to the GW data. To test our ability of making a confident GW detection, search procedures are trained and tested on simulated signals which are injected into the GW data stream or the detectors themselves. A "blind" test is when select members of the GW community secretly insert a simulated signal in to the data and the details of this blind injection placed in an "envelope" to be opened once the searches are complete [22, 221]. We used
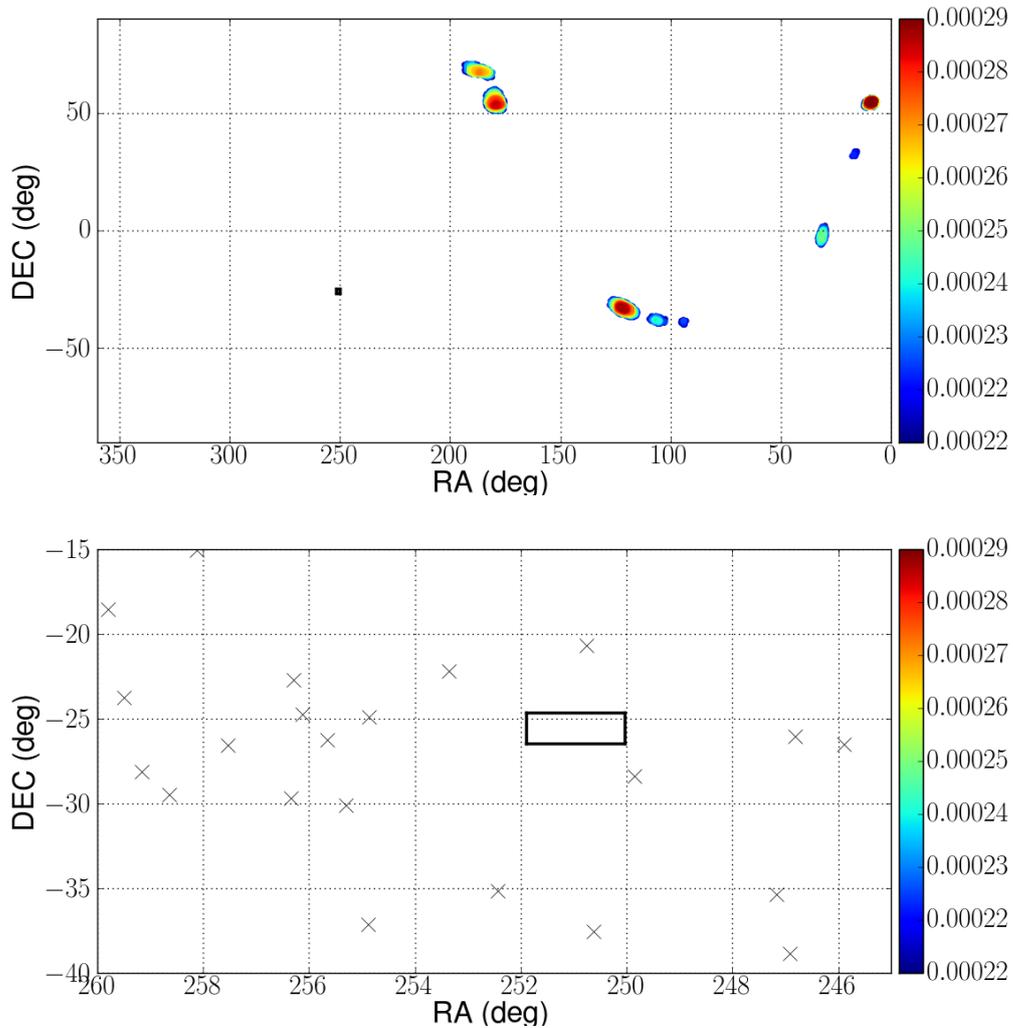
Figure 5.2: G18666: Skymap showing the estimated likelihood that each coloured location is the correct source location. This is the likelihood before the galaxy weighting is applied. The top plot shows the full sky and the bottom plot zoomed in on the location which ROTSE observed, which is shown by the black box in both plots. The ×'s in the bottom plot indicate galaxies within 50 Mpc according to the GWGC. The total likelihood over the whole coloured map is ∼25%.
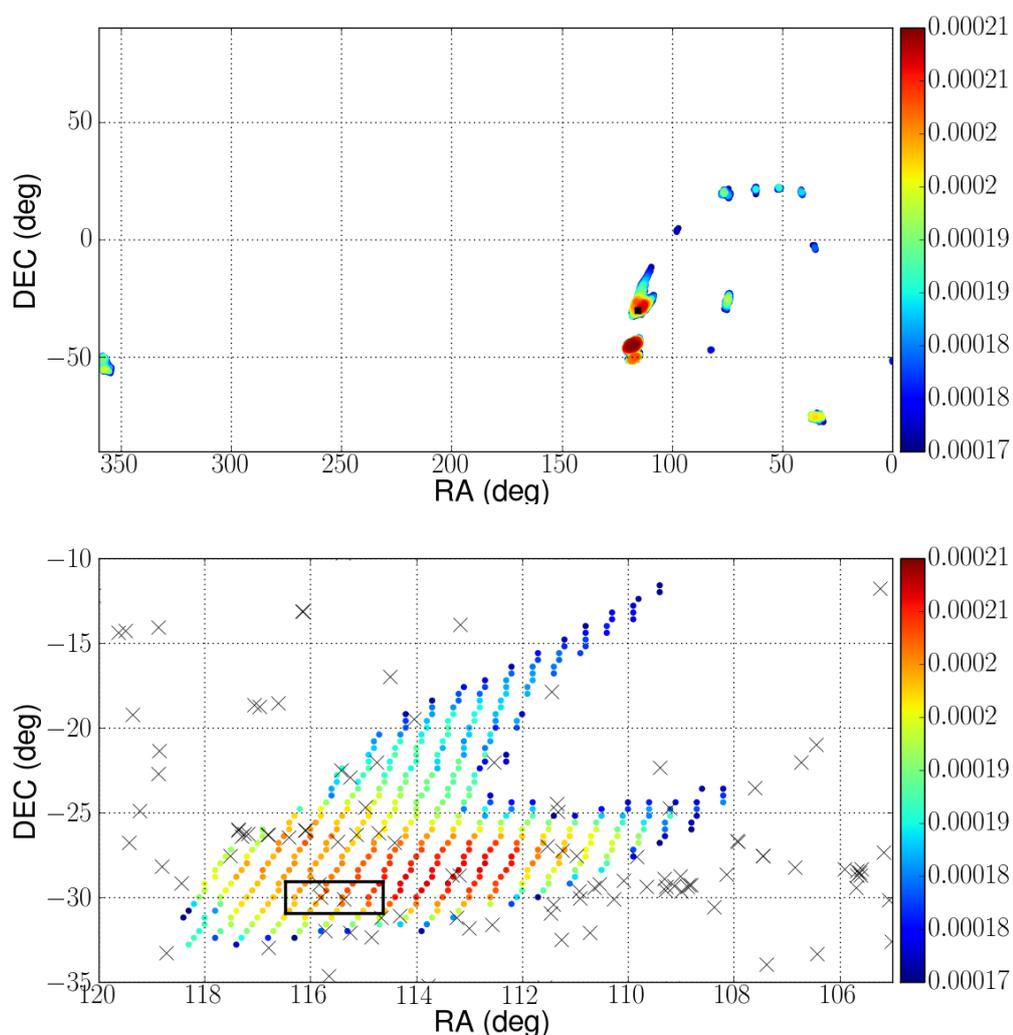
Figure 5.3: G19377: Skymap showing the estimated likelihood that each coloured location is the correct source location. This is the likelihood before the galaxy weighting is applied. The top plot shows the full sky and the bottom plot zoomed in on the location which ROTSE observed, which is shown by the black box in both plots. The ×'s in the bottom plot indicate galaxies within 50 Mpc according to the GWGC. The total likelihood over the whole coloured map is ∼19.2%.

this event as a test case for prototyping the automated analysis procedure. Here we present the full analysis results, like for all the other GW events.

A timeline of the limiting magnitudes of the analysable images is shown in Figure 5.4 along with the evolution of models which are expected to produce joint GW-EM transients, all scaled for a source at 50 Mpc (approximate farthest distance a GW source could have been detected at the time of data taking). These models include kilonovae, on- and off-axis gamma-ray bursts (GRBs) and supernova data (taken from SN1998bw [222]). There are four kilonova curves. The light blue curves illustrate a kilonova produced from NS-NS (1.4-1.4 $M_\odot$) (solid line) and NS-BH (1.4-10 $M_\odot$) (dashed line) systems according to models presented by Piran et al. [93]. The dark blue curves are taken from Figure 5 in [97]. These include kilonovae models, powered by the radioactive decay of elements produced in the merger of NS-NS and NS-BH systems as put forward by Metzger et al. [97]. The solid line assumes a total ejecta mass of $10^{-2} M_\odot$, electron fraction of $Y_e = 0.1$, mean outflow speed of $\simeq 0.1c$ and thermalisation energy $\epsilon_{therm} = 1$ whereas the dashed line represents the same parameters based upon the LP98 model (first suggested in [95] and as implemented in [96, 223]). On-axis long and short GRBs are shown by the light green curves and taken from Figures 4 and 5 in [133] and [134] respectively. The dark green curves represent off-axis GRBs taken from [224], assuming jet energies $\sim 10^{50}$ erg, a uniform interstellar medium (ISM) density of 1 atom cm^{-3}, jet angle of 0.2 rad and an observer angle of 0.4 rad.

From Figure 5.4 it is evident that if a bright LGRB (on- or off-axis) occurred at 50 Mpc the limiting magnitude of these images are sufficient for a detection. The images could also have captured the optical signature of a supernova similar to SN1998bw in ∼60% of images. However the images are not sensitive enough to detect a kilonova, SGRB or off-axis low luminosity GRB at 50 Mpc.

209 potential candidates were identified by the automated pipeline, of which 176 potential candidates were not seen on more than one night (within 3.5 pixels of the original location), 11 potential candidates lightcurves were considered too flat and 21 potential candidates lightcurves did not decay by a sufficient amount from 48 hrs to 1 month after the event (as outlined in Section 4.4.1). No candidates were coincident with any asteroids in the Minor Planet Checker or variable stars in the SIMBAD catalogue. This resulted in 1 candidate which survived the event validation tests. This candidate was not highlighted as near a galaxy (within three times the semi-major diameter) or following a model theoretical lightcurve.

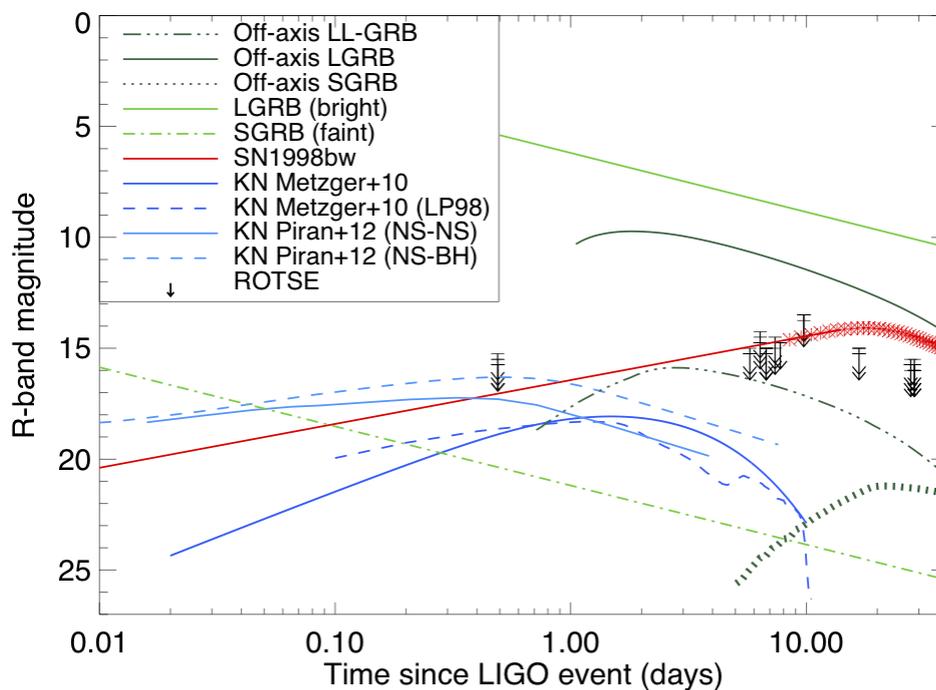Figure 5.4: Timeline illustrating the limiting magnitudes of the images taken in response to G19377 (black) and expected models/EM observations, all scaled for sources at 50 Mpc. These include kilonovae [93, 97] (blue), supernova 1998bw [222] (red) and both short (SGRB) and long (LGRB), on-axis (light green) [133, 134] and off-axis (dark green) GRB afterglows [224]. LL-GRB represents a low luminosity GRB [224].
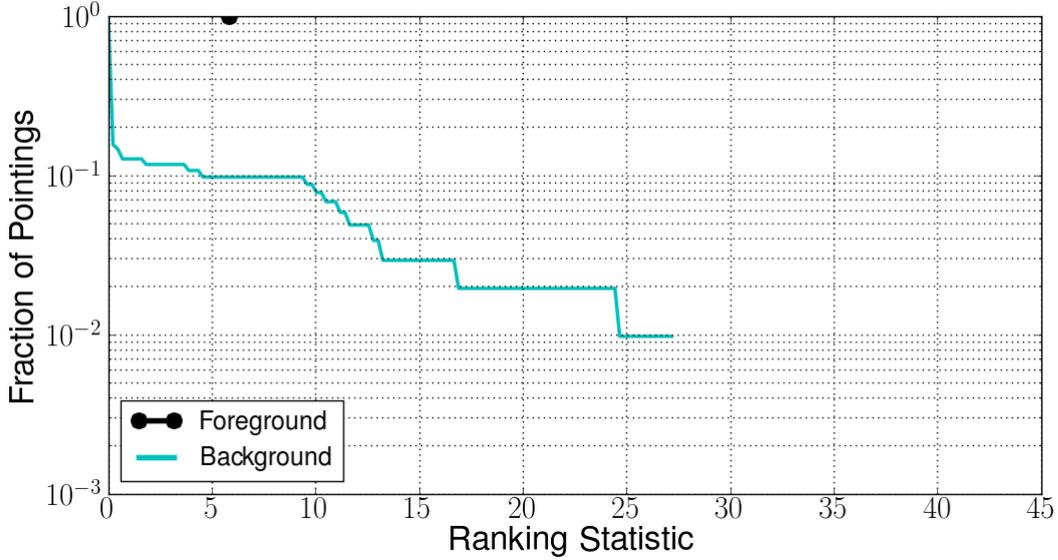
Figure 5.5: G19377: Distribution of the background events (cyan) and the candidate (black) in terms of rank against the cumulative fraction of pointings. To be considered significant (false alarm probability less than 1%) the candidate would need to have a ranking of greater than 27.

Figure 5.5 shows the background distribution (cyan curve) in addition to the rank ($R \simeq 6$) of the candidate (black point). A significant candidate would need to have a rank of 27 or greater as this is the rank of the most significant background event. However the potential candidate has a rank comparable to 10% of the background with a value of ~6 and is therefore not interesting. Nonetheless, we investigated this candidate further by examining its lightcurves.

The ROTSE pipeline is capable of producing two lightcurves; one which incorporates the transient and the background, and one with the background subtracted revealing the lightcurve of just the transient. The first lightcurve is generated by taking the data within a circle of radius ~6 pixels with the transient at the centre. The second lightcurve however is generated the same but with the background removed. This is done by overlaying the reference image with the original image and subtracting it to reveal the data from the transient alone. However it is not always possible to construct this second lightcurve. Should the transient in question lie in a region of the image where there are less than 16 reference stars (i.e. stars which are catalogued in USNO-B) within a 300 by 300 pixel box around the transient, the pipeline is not accurately able to overlay the reference image with the original image to subtract the background.

Figure 5.6 shows the two lightcurves for this single candidate, where lightcurve 1 shows the lightcurve generated from both the transient and the background whereas lightcurve 2 shows the background-subtracted transient only. Greater confidence is given to the second lightcurve as it should more accurately represent the true behaviour of the transient. The black curve in lightcurve 1 shows the magnitude of the transient to vary by less than one magnitude over the observations. No upper limits are reported as the transient was found in every image. The best chi-square fit lightcurves following a kilonova, SGRB and LGRB are also plotted in this figure and the distances at which these sources would have to be to produce these lightcurves reported. (The SGRB and LGRB models produce the same curve, only the distance to the source is different.) When the transient is found in an image, a point is placed on the theoretical lightcurves which corresponds to the same time the transient was seen in an image, with the aim to highlight the difference between the measured magnitude and the magnitude the transient would need to have to follow one of the models. If an upper limit is quoted for an image however there is no point on the theoretical lightcurve. From Figure 5.6 it is clear that the theoretical curves are not a good match to the data, implying the candidate does not look like a kilonova or GRB afterglow.

When the background is subtracted, lightcurve 2 reveals the data from the transient only. With the background is subtracted, the candidate's lightcurve is seen to be much more variable. It does not appear to follow a decaying trend in the manner illustrated by the model lightcurves, but rises until day 10 and then declines, in a similar fashion a supernova might be expected. It is worth noting however that the candidate only appears on 3 nights and is not found between day 1-10, where images with a sufficient sensitivity are available to definitively show this trend if it were real. Therefore it is not thought that this candidate is of astrophysical origin.

5.3.1 G19377 Injection Study

Simulated transients following lightcurves for a kilonova, SGRB and LGRB between 0.4-30 Mpc away were injected in to the images taken in response to event G19377, following the procedure as described in Section 4.6. Over 4000 injections were made at random locations within the images after which the automated pipeline was invoked. Figure 5.7 shows the efficiency of identifying these simulated transients versus distance (top plot) or magnitude (bottom plot). The magnitudes used to characterise the simulation are those which

G19377: Candidate 1

Lightcurve 1 - Transient and Background
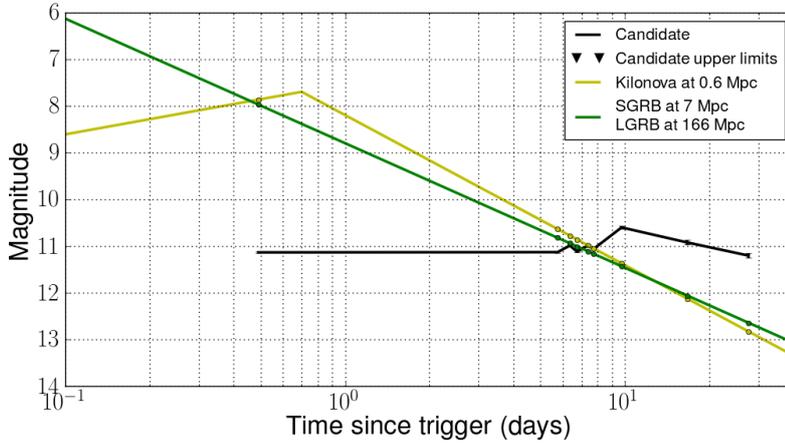
Lightcurve 2 - Transient with Background Subtracted
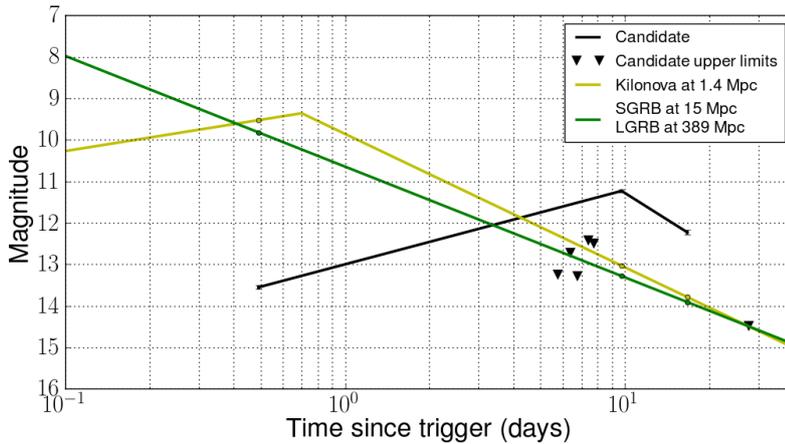
Figure 5.6: The top figure shows the lightcurve of the G19377 candidate which includes the background and the bottom figure shows the lightcurve with the background subtracted. In each plot the candidate's data points and error bars are plotted in black. Open circles on the model lightcurves indicate times at which the transient was detected. If a candidate was not identified in a given image, an upper limit is shown. This reports the limiting magnitude of the image at the location of the candidate. For comparison we also show the model lightcurves for both kilonovae (equations (4.4) and (4.5)) and afterglows (equations (4.6) and (4.7) with an offset=0) scaled to source distances which produce the best match to the measured magnitudes of the candidate. The SGRB and LGRB models give identical lightcurves the source distance is different as shown.

the transient would have in the second set of images (usually the second night of observations). This is motivated by the first test in the event validation procedure described in Section 4.4.1, which is that the transient be seen on at least two nights. Since all of the model lightcurves are decaying by the second night, we expected the magnitude on the second to be one of the most important factors in determining whether an injection will be detected. The fact that the efficiencies versus magnitude for the kilonova and afterglows are essentially identical (Figure 5.7, bottom) supports this assumption.

The distances quoted for the GRB models are the largest possible. Equations (4.6) and (4.7) define the GRB models. In each of these equations is the offset quantity, which can take any value between 0 and 8, and represents the range in observational data taken from [133, 134]. An offset of 0 represents those brightest afterglows and 8 the dimmest. Therefore the GRB distances quoted in the lightcurve figures could be anywhere up to a factor of 40 smaller. All the models suffer from poor efficiency at the closest distances/brightest magnitudes due to saturation issues. This is because during the image processing saturated pixels are discarded as they are thought to be telescope, rather than astrophysical, artefacts. Consequently $\sim$50% of the injected transients between magnitude 7.5 and 9 are not recovered. Between the magnitudes of 9-12 the pipeline correctly identifies between 70-80% of injected transients, meaning we are most sensitive to finding transients resembling a kilonova / SGRB / LGRB at distances $\sim$ 1 Mpc / 10 Mpc / 300 Mpc. As the distance/magnitude increases the efficiency falls and it is not possible to identify transients with magnitudes above 15 or distances $\gtrsim$ 10 Mpc / 80 Mpc / 2 Gpc for a kilonova / SGRB / LGRB.

An efficiency of 100% is not attained due to the background-subtracted lightcurve not being generated or the injections sometimes being placed at slightly different coordinates in each set of images. To be coincident the automated pipeline requires a candidate to be within 3.5 pixels in each set of images. This is the radius used to set the area over which data is taken to determine a candidate's lightcurve. This movement of the injections is an artefact of the injection pipeline. To add the injection at exactly the same right ascension and declination, the injection pipeline needs to know how to compensate for image warping. However it does not do this in the same way as the ROTSE pipeline (due to different code packages) so the warping correction does not always match that done by the automated pipeline. As a consequence the effective location of the injection changes from image to image by more

than that of a real star. The location of real stars matches from image to image by $\sim$1 pixel, whereas the location of injections may vary by several pixels. Since the pipeline requires a transient's location to be fixed within 3.5 pixels, some injections are mistakenly rejected by this procedure. Approximately 10% of injections are lost in this event.

Figure 5.8 illustrates the efficiency of identifying those simulated transients with a rank ($R \geq 4.4$) comparable to 10% of the background. Again the efficiency at close distances/bright magnitudes is low due to the saturation problem already discussed and peaks at the same efficiency as Figure 5.7. However the fraction of injections with a FAR ≤ 0.1 suddenly drops at magnitude $\sim$11 to between 10-30% and rises again to between 30-40% at magnitude 13. This behaviour is unexpected as the efficiency should monotonically decrease with increasing magnitude/distance. The distribution of the injections, and background in terms of rank is illustrated in Figure 5.9. These ten plots show the evolution of the injection distributions with increasing distance. Of those injections which are correctly identified at a distance $\lesssim$ 1 Mpc / 8 Mpc / 200 Mpc for a kilonova / SGRB / LGRB, the loudest injections have a rank comparable to or larger than the background. However the sudden drop in the efficiency already discussed can be seen from plots (d) to (f). It is unknown why the rank of those injections at magnitude $\sim$11 is lower than those at magnitude $\sim$13 as image quality should not be a factor.

5.3.2   G19377 Conclusions

G19377 occurred on September 16 2010 at 06:42:23 UTC when ROTSE-IIIa and c were triggered to follow-up on this event for one month. The error box containment in the region imaged by ROTSE was $\sim$0.4%. The automated pipeline would have been able to detect an associated kilonova counterpart with $R > 0$ with $\geq$50% probability to a distance of $\sim$5 Mpc, assuming the true source direction was within the area imaged by ROTSE. For a SGRB (LGRB) afterglow the corresponding distance is $\sim$3-45 Mpc ($\sim$90-1000 Mpc), depending on offset factor. A bright SGRB (LGRB) within 3 Mpc (100 Mpc) might have been missed by the automated pipeline due to saturation. Only one potential candidate was identified by the pipeline which was not coincident with a galaxy. The rank of this candidate was comparable to 10% of the background and the lightcurves for this candidate did not suggest it to be of astrophysical origin. Therefore the ROTSE telescope system did not identify any EM candidates associated to event G19377. It should be noted however
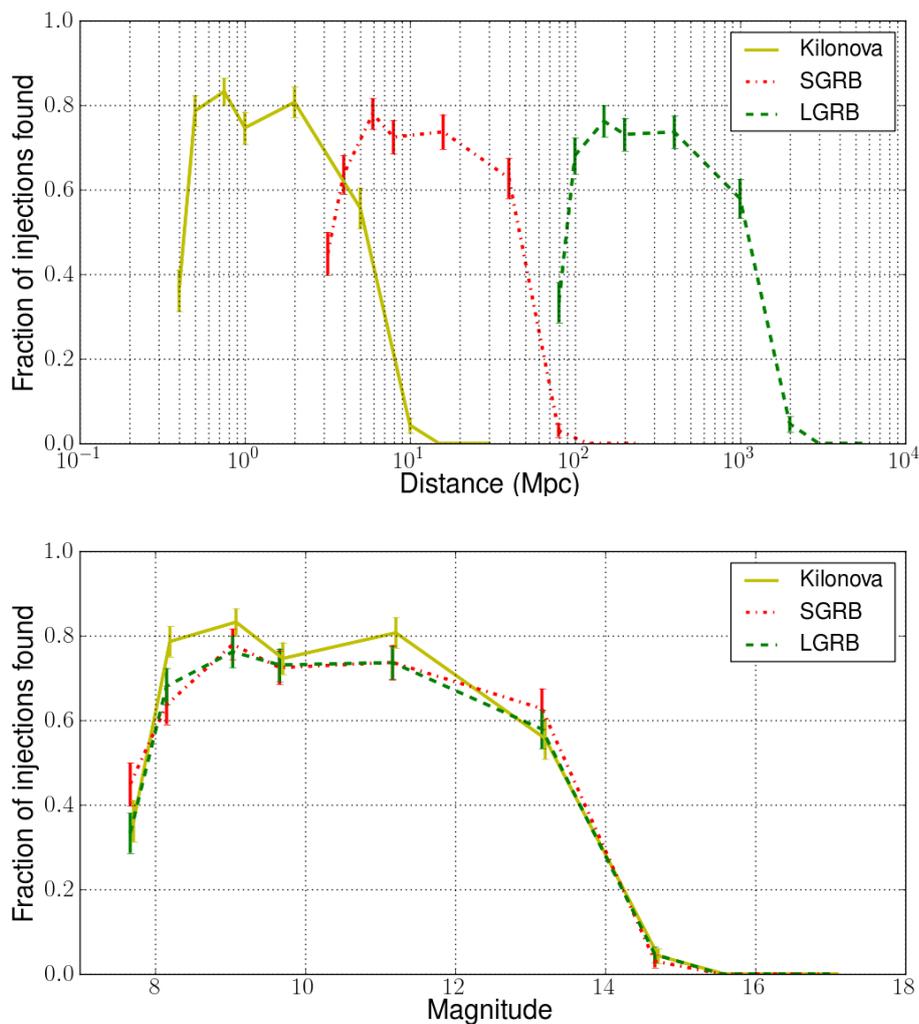
Figure 5.7: G19377: Efficiency of finding simulated transients with $R > 0$ versus distance (top) and magnitude (1.5 days after the trigger time) (bottom). The distances quoted for the gamma-ray burst models assume the brightest afterglows from Kann et al. [133, 134] (i.e. offset = 0 in equations (4.6) and (4.7)) but could be smaller by a factor of up to 40. All the models suffer from poor efficiency at very close distances / low magnitudes due to saturation.
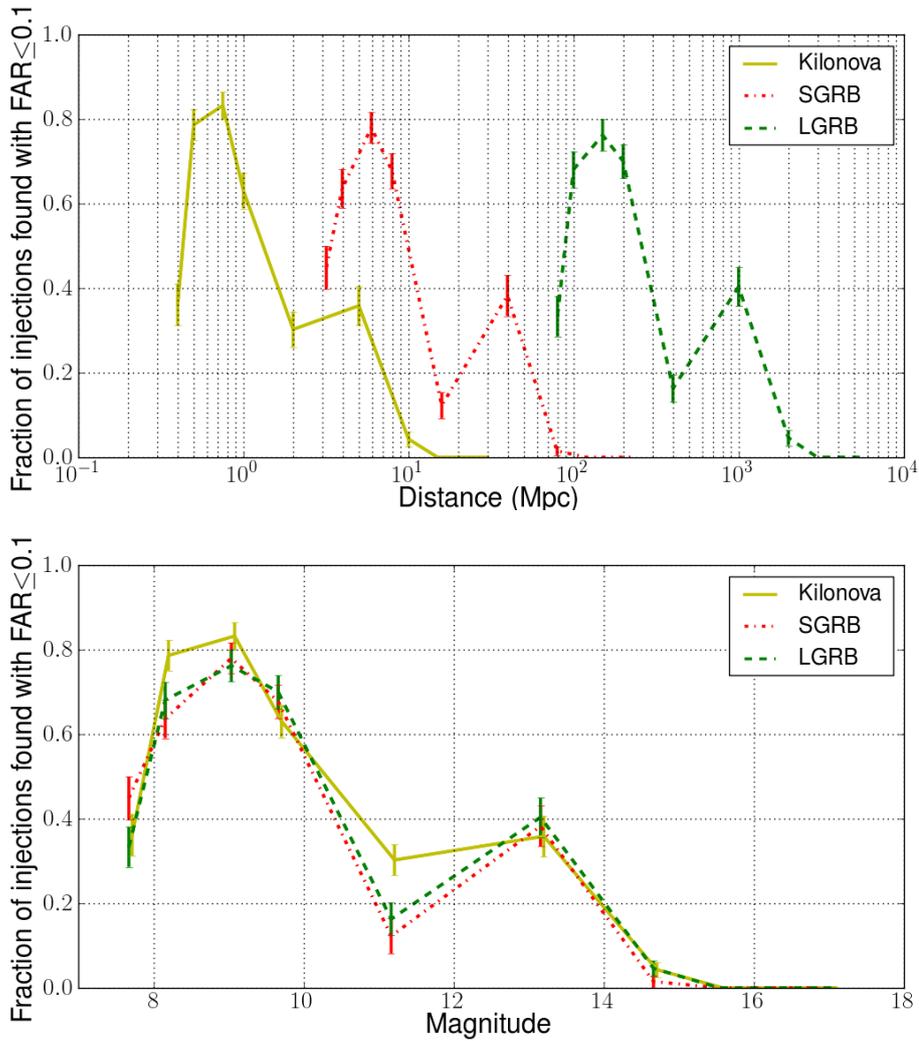
Figure 5.8: G19377: Efficiency of injections found with a false alarm probability of ≤ 0.1 ($R \geq 4.4$). The injections performed for the SGRB and LGRB models show the largest distance possible; the numbers could be a factor 40 smaller. The distances for the GRB models assume the brightest afterglows from Kann et al. [133, 134] (i.e. offset $= 0$ in equations (4.6) and (4.7)).

(a) 0.4 Mpc/mag 7.7

(b) 0.5 Mpc/mag 8.2

(c) 0.75 Mpc/mag 9

(d) 1 Mpc/mag 9.7

(e) 2 Mpc/mag 11.2

(f) 5 Mpc/mag 13.2

(g) 10 Mpc/mag 14.7

(h) 15 Mpc/mag 15.5

(i) 20 Mpc/mag 16.2

(j) 30 Mpc/mag 17.1

Figure 5.9: G19377: The distribution of injections (kilonova-yellow, SGRB-red and LGRB-green) and background (cyan) at various distances and magnitudes (1.5 days after the trigger). Plot (a) kilonova $\simeq$ 0.4 Mpc / SGRB $\simeq$ 3.3 Mpc / LGRB $\simeq$ 80 Mpc, (b) kilonova $\simeq$ 0.5 Mpc / SGRB $\simeq$ 4 Mpc / LGRB $\simeq$ 100 Mpc etc. In these figures we assumed the GRB models to have the brightest afterglows from Kann et al. [133, 134] (i.e. offset = 0 in equations (4.6) and (4.7)). Therefore the GRB distances could be a factor 40 smaller.

that after the analysis took place it was revealed this GW event was a simulated signal secretly added to the data known as a "blind injection" [221]. The purpose of the blind injection was to test search procedures.

5.4 G20190

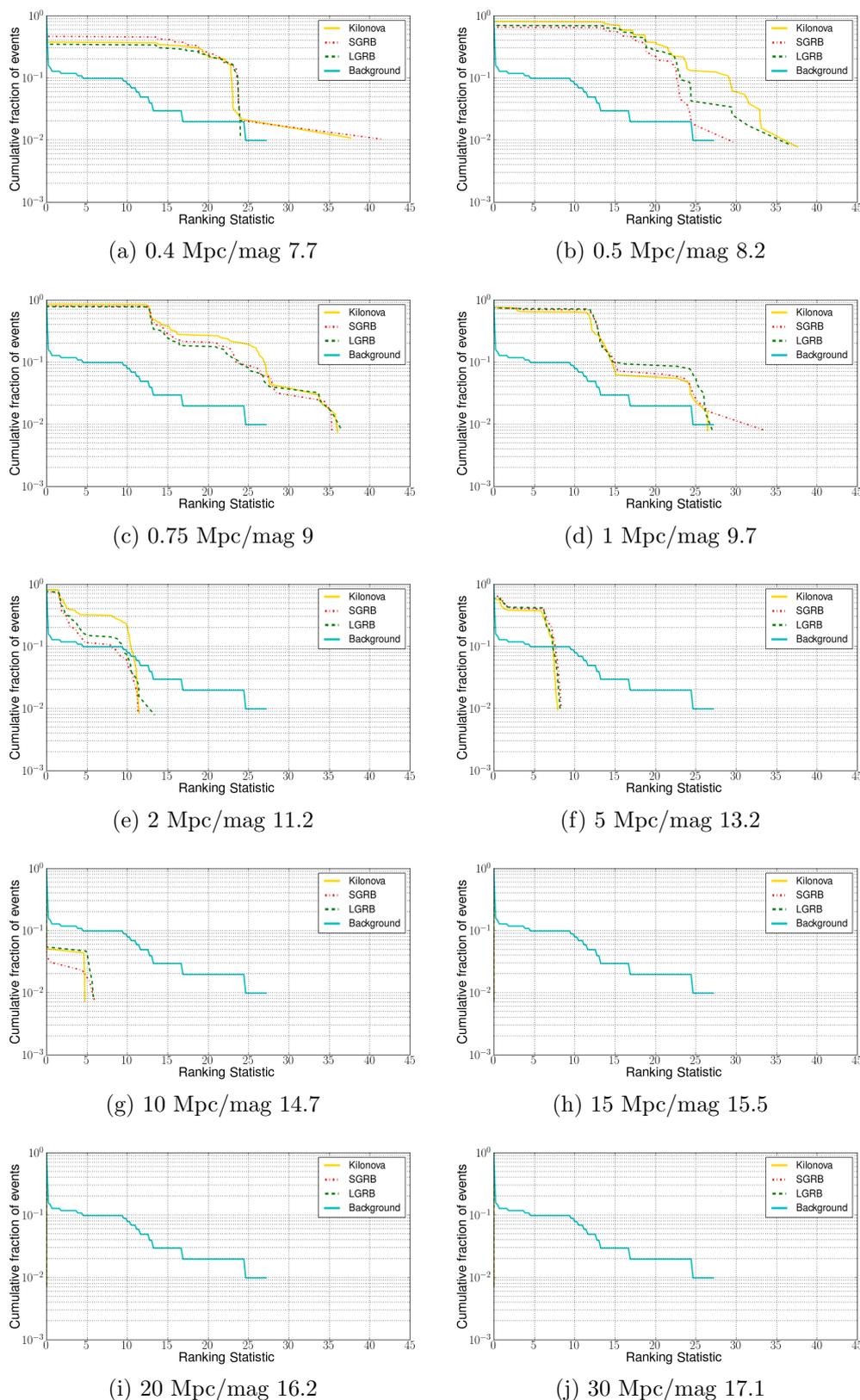Event G20190 occurred on September 19 2010 at 12:02:25 UTC. All four ROTSE-III telescopes responded to this GW trigger, taking images spanning from 34 hours 38 minutes after the event to 29 days later, centred on the region RA: 333.25000° Dec: 18.03400°. Due to image quality, all images taken with the ROTSE-IIIa, b and d telescopes had to be discarded, resulting in only 56 images being used for the analysis. There is one galaxy within the FoV for this event, namely UGC11944 at ∼24 Mpc. The probability skymap as generated by cWB is shown in Figure 5.10, along with a box illustrating the area which ROTSE searched over. The top plot in this figure shows the full sky and the bottom plot is zoomed in on the region of interest, with galaxies within 50 Mpc marked. The coloured regions show the estimated likelihood that each pixel contains the true source direction independent of any galaxy weighting. The cumulative probability summed over the entire coloured regions is ∼100% (i.e. the cWB skymap has containment of ∼100%) and the cumulative probability contained within the region imaged by ROTSE (without accounting for galaxy weighting) is ∼10%.

A timeline of the limiting magnitudes of the analysable images is shown in Figure 5.11 along with the evolution of models which are expected to produce joint GW-EM transients. These include kilonova models [93, 97], on- and off-axis GRB afterglows (data taken from [133, 134, 224]) and data from SN1998bw [222]. All these models are scaled for a source at 50 Mpc as this was the approximate farthest distance a GW source could have been detected at the time of data taking. A full description of how these curves were generated is discussed in Section 5.3. From this figure it is evident that if there was a bright or off-axis LGRB the limiting magnitude of these images are sufficient for a detection. It is also possible to detect a supernova similar to SN1998bw in most of the images. Some of the images could also have captured the optical signature of an off-axis low luminosity LGRB. However the images are too faint to detect SGRB and kilonovae.

The automated pipeline identified 77 potential candidates associated to this event. 68 candidates were discarded because they were only seen on one
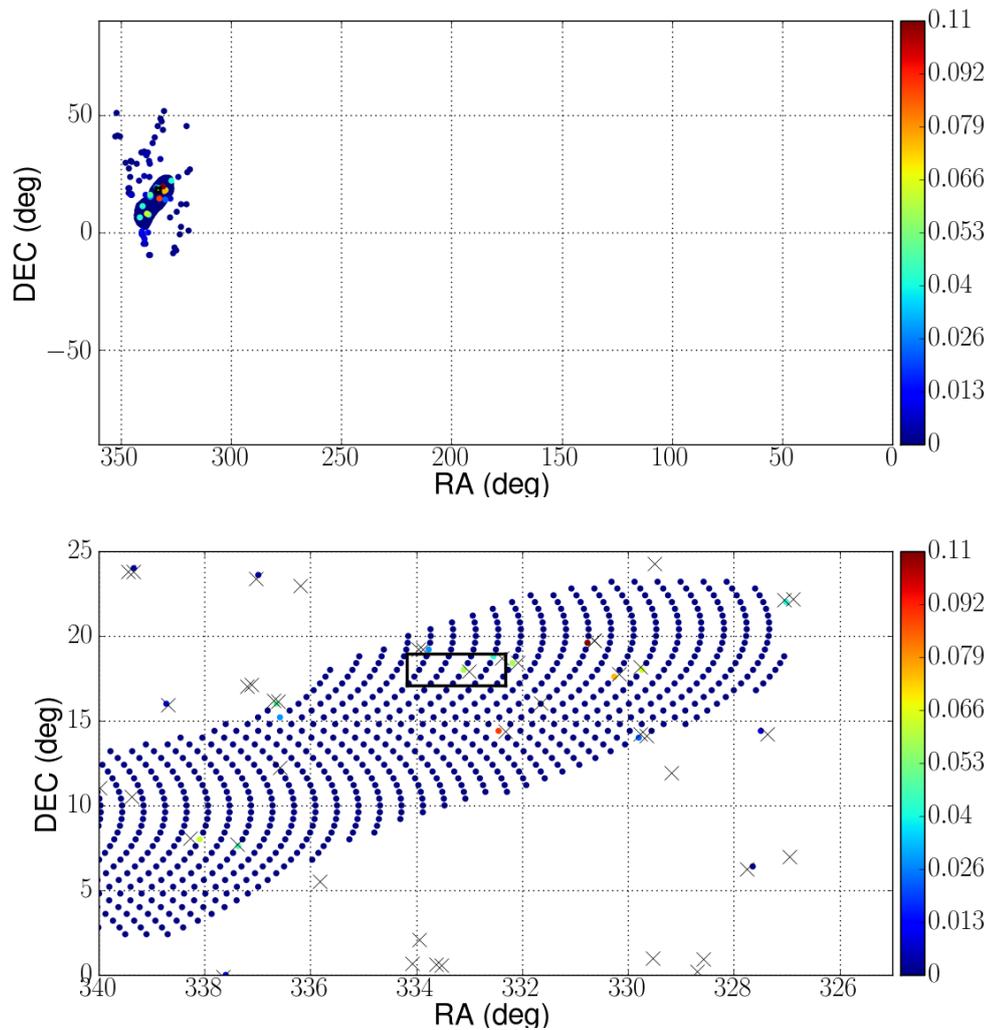
Figure 5.10: G20190: Skymap showing the estimated likelihood that each coloured location is the correct source location. This is the likelihood before the galaxy weighting is applied. The top plot shows the full sky and the bottom plot zoomed in on the location which ROTSE observed, which is shown by the black box in both plots. The ×'s in the bottom plot indicate galaxies within 50 Mpc according to the GWGC. The total likelihood over the whole coloured map is ∼100%.
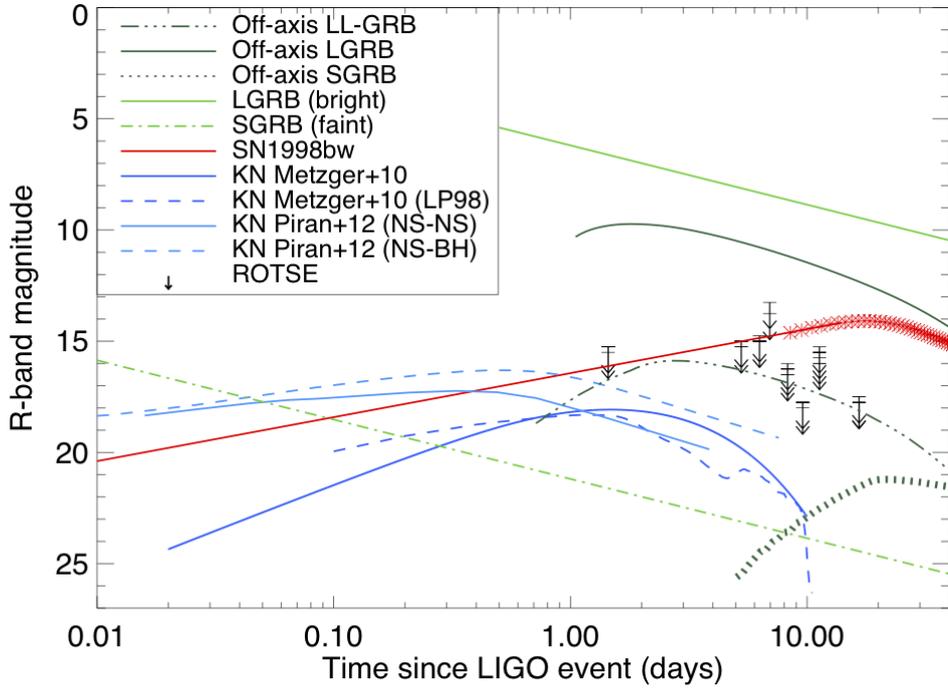
Figure 5.11: Timeline illustrating the limiting magnitudes of the images taken in response to G20190 (black) and expected models/EM observations, all scaled for sources at 50 Mpc. These include kilonovae [93, 97] (blue), supernova 1998bw [222] (red) and both short (SGRB) and long (LGRB), on-axis (light green) [133, 134] and off-axis (dark green) GRB afterglows [224]. LL-GRB represents a low luminosity GRB [224].

Figure 5.12: G20190: Distribution of the background events (cyan) and the candidate (black) in terms of rank against the cumulative fraction of pointings. To be considered significant (false alarm probability less than 1%) the candidate would need to have a ranking of greater than 17.

night, 5 candidates had a lightcurve which was considered too flat, 3 candidates lightcurves did not decay sufficiently 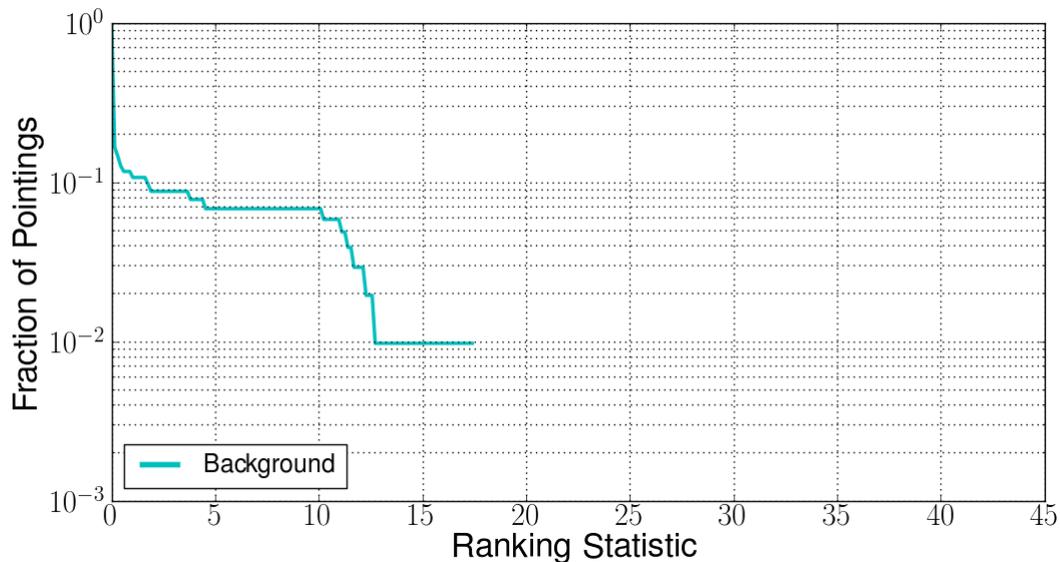between 48 hours to 1 month after the event and 1 candidate's coordinates were in the vicinity of a variable star in the SIMBAD catalogue. No candidates were discarded by the Minor Planet Checker. For this GW event no candidates survived the event validation tests.

Since no candidates were identified by the pipeline, only the background distribution for this event is shown in Figure 5.12. If a candidate were to be identified it would need to have a rank greater than the loudest background event, i.e. rank of 17, to be considered significant.

5.4.1 G20190 Injection Study

As described in Section 4.6 over 4000 simulated transients following kilonova, SGRB and LGRB lightcurves at a range of distances were placed at various locations in the images. Figure 5.13 shows the fraction of injections identified versus either distance or magnitude. The distances quoted for the GRB models are the largest possible (offset=0); they could be anywhere up to a factor of 40 smaller (since offset is between 0 and 8). Equations (4.6) and (4.7) define the GRB models. In each of these equations the offset quantity represents the range in observational data taken from [133, 134] and can take any value between 0 and 8. An offset of 0 (which was used here) represents those

brightest afterglows and 8 the dimmest. The magnitudes reported are from the second set of images as the first requirement in the event validation checks (as described in Section 4.4.1) is that a candidate is found in more than one set of images. All the models suffer from poor efficiency at close distances/bright magnitudes with over 50% of those candidates with a magnitude between 7.5 and 9 being missed. This is due to the injections saturating and the pipeline discarding them since they are assumed to be telescope artefacts rather than of astrophysical origin. As the magnitude/distances increase so does the efficiency which peaks at $\sim$80% between magnitudes 9-11. For this event we are most sensitive to sources similar to a kilonova / SGRB / LGRB at distances of $\sim$ 2 Mpc / 20 Mpc / 200 Mpc. The reason we do not reach an efficiency of 100% is due to the injections not always being placed at the same coordinates in each set of images (as discussed in Section 5.3.1) or the background-subtracted lightcurve not being generated. The efficiency however begins to decrease as the injections are placed at greater distances/dimmer magnitudes until $\sim$15th magnitude where the efficiency is only a few percent. In terms of distance this implies a transient could not be detected if it followed a kilonova / SGRB / LGRB at distances $\gtrsim$ 10 Mpc / 100 Mpc / 2 Gpc.

To differentiate between all found injections and those which are the most interesting, i.e. those with a high rank, the fraction of those injections with a FAR $\leq$ 0.1 ($R \geq 1.7$) with distance and magnitude is shown in Figure 5.14. This figure is very similar to Figure 5.13 which means that the majority of injections were favourably ranked against the background. This is because the background distribution falls below FAR$\simeq$ 10% at very low rank ($R \sim 1.7$); see Figure 5.12.

The distribution of injections and background with increasing distance are depicted in Figure 5.15. Plots (a) shows injections made at the closest distances, i.e. kilonova $\simeq$ 0.4 Mpc / SGRB $\simeq$ 3.3 Mpc / LGRB $\simeq$ 84 Mpc and (j) at the farthest distances, i.e. kilonova $\simeq$ 30 Mpc / SGRB $\simeq$ 250 Mpc / LGRB $\simeq$ 6.3 Mpc. Unfortunately even the injections made at the closest distances do not have a rank greater than the loudest event within the background, which suggests if a potential candidate was found for this event the rank alone could not be used to demonstrate a very high significance. More information, such as the lightcurve shape, would need to be considered.
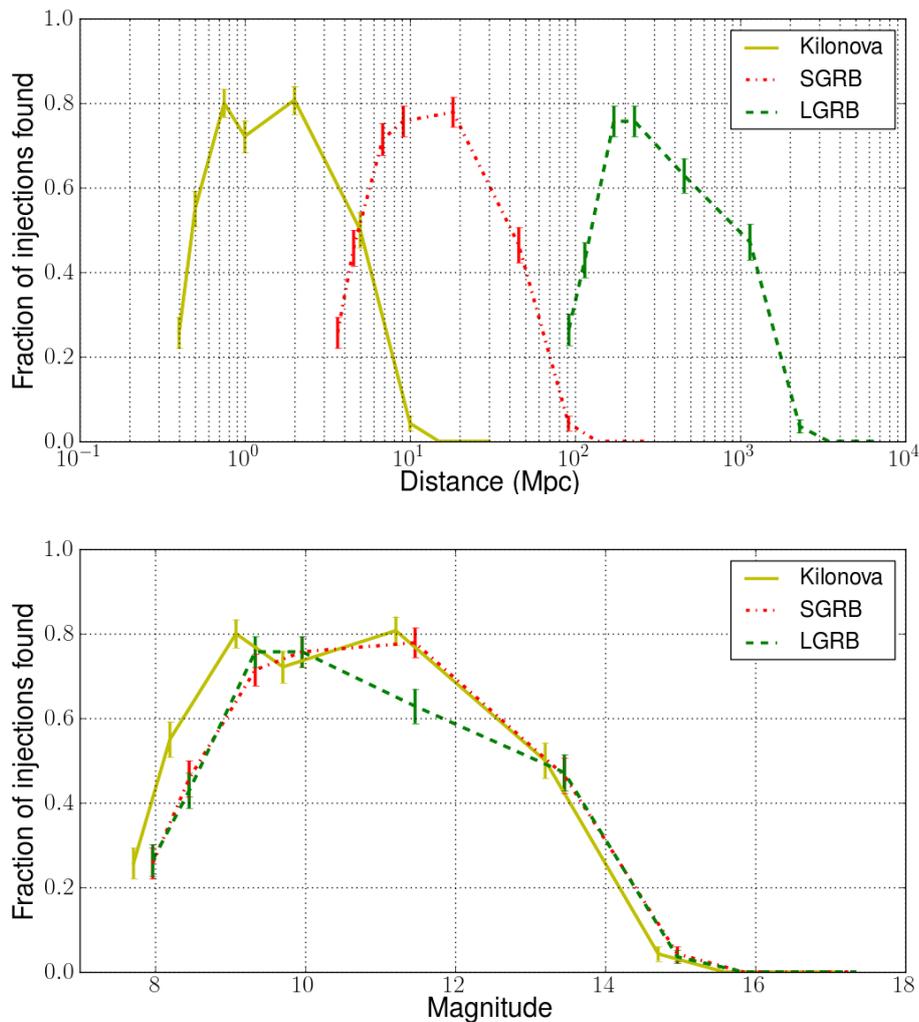
Figure 5.13: G20190: Efficiency of finding simulated transients with $R > 0$ versus distance (top) and magnitude (1.5 days after the trigger time) (bottom). The distances quoted for the gamma-ray burst models assume the brightest afterglows from Kann et al. [133, 134] (i.e. offset = 0 in equations (4.6) and (4.7)) but could be smaller by a factor of up to 40. All the models suffer from poor efficiency at very close distances / low magnitudes due to saturation.
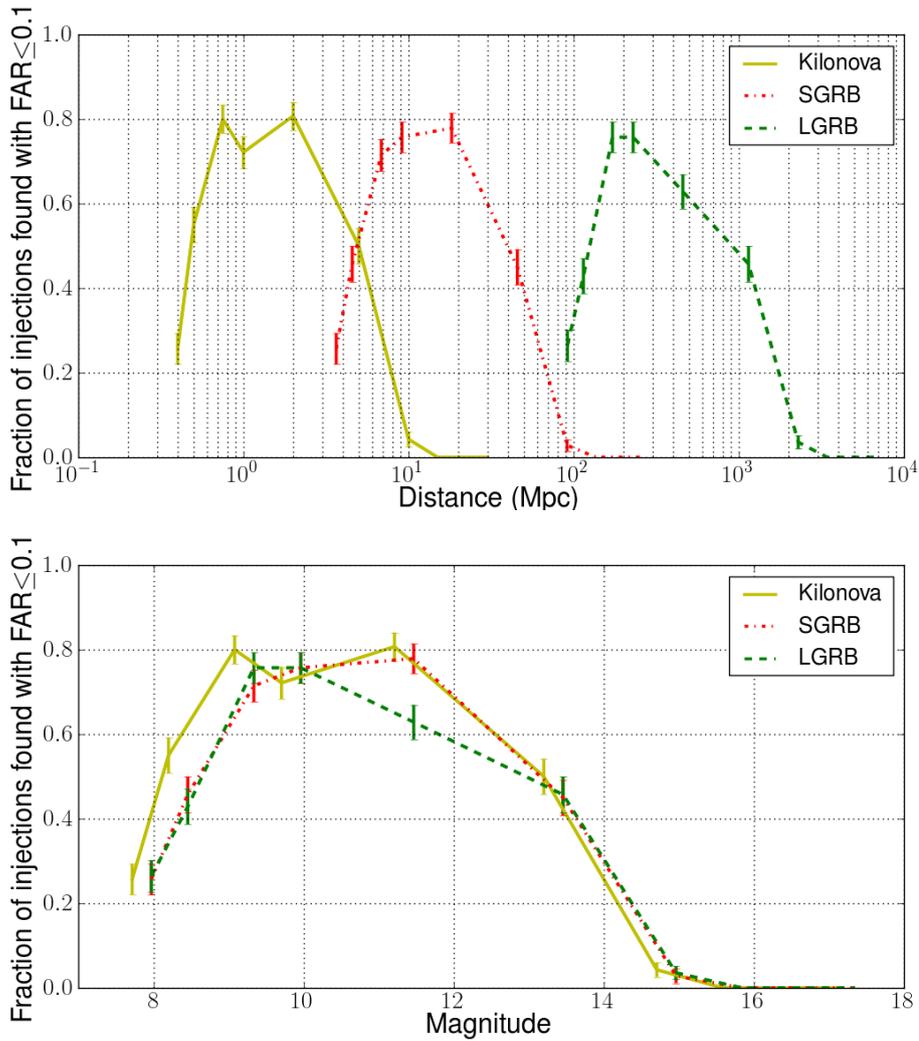
Figure 5.14: G20190: Efficiency of injections found with a false alarm probability of ≤ 0.1 ($R \geq 1.7$). The injections performed for the SGRB and LGRB models show the largest distance possible; the numbers could be a factor 40 smaller. The distances for the GRB models assume the brightest afterglows from Kann et al. [133, 134] (i.e. offset = 0 in equations (4.6) and (4.7)).
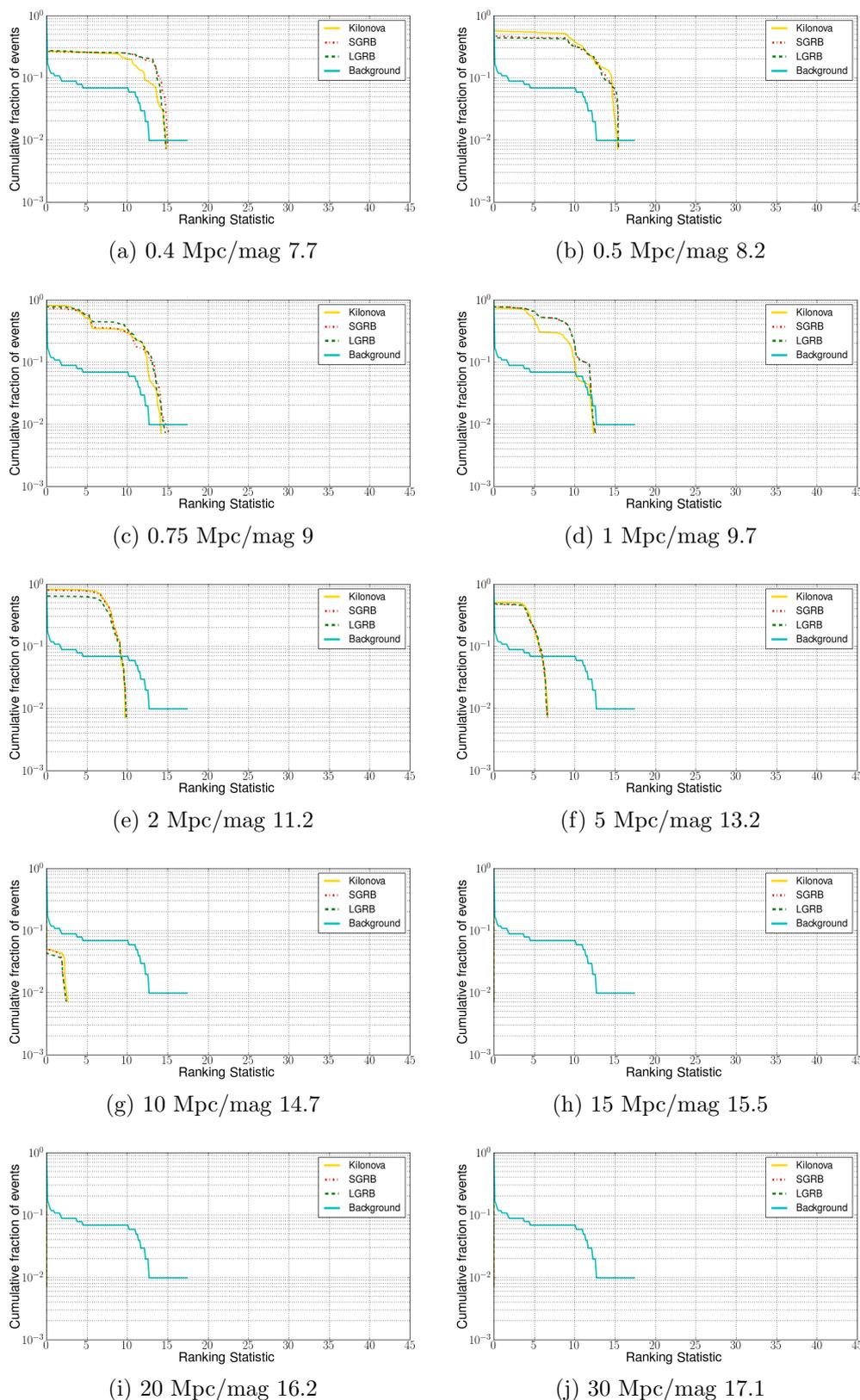
Figure 5.15: G20190: The distribution of injections (kilonova-yellow, SGRB-red and LGRB-green) and background (cyan) at various distances and magnitudes (1.5 days after the trigger). Plot (a) kilonova $\simeq$ 0.4 Mpc / SGRB $\simeq$ 3.3 Mpc / LGRB $\simeq$ 80 Mpc, (b) kilonova $\simeq$ 0.5 Mpc / SGRB $\simeq$ 4 Mpc / LGRB $\simeq$ 100 Mpc etc. In these figures we assumed the GRB models to have the brightest afterglows from Kann et al. [133, 134] (i.e. offset $= 0$ in equations (4.6) and (4.7)). Therefore the GRB distances could be a factor 40 smaller.

5.4.2 G20190 Conclusions

All the ROTSE telescopes were used to follow up on this event which took place on September 19 2010 at 12:02:25 UTC, however only images taken with ROTSE-IIIc were of sufficient image quality to analyse. The error box containment in the region imaged by ROTSE was ∼10%. The automated pipeline would have been able to detect an associated kilonova counterpart with $R > 0$ with ≥50% probability to a distance of ∼5 Mpc, assuming the true source direction was within the area imaged by ROTSE. For a SGRB (LGRB) afterglow the corresponding distance is ∼5-45 Mpc (∼100-1000 Mpc), depending on offset factor. A bright SGRB (LGRB) within 5 Mpc (120 Mpc) might have been missed by our automated pipeline due to saturation. No candidates were identified by the automated pipeline for this event and therefore no EM counterpart was identified for event G20190.

5.5 G21852

This event occurred on September 26 2010 at 20:24:31 UTC. ROTSE-IIIb took images spanning from 11 hours 53 minutes to 29 days later centred on the region RA: 11.04000° Dec: 41.61000° which, within its FoV, contained three galaxies (NGC0205, NGC0221 and NGC0224) all within 1 Mpc. Due to image quality one follow-up night had to be ignored. 81% (19%) of the images had an exposure time of 60s (20s). The probability skymap as generated by cWB is shown in Figure 5.16, along with a box illustrating the area imaged by ROTSE. The top plot in this figure shows the full sky and the bottom plot is zoomed in on the region of interest, with galaxies within 50 Mpc marked. The coloured regions show the estimated likelihood that each pixel contains the true source direction independent of any galaxy weighting. The cumulative probability summed over the entire coloured regions is ∼87% (i.e. the cWB skymap containment is ∼87%) and the cumulative probability contained within the region imaged by ROTSE (without accounting for galaxy weighting) is ∼0.3%.

A timeline of the limiting magnitudes of the analysable images is shown in Figure 5.17 along with the evolution of models which are expected to produce both GW-EM data. These include kilonova models [93, 97], on- and off-axis GRB afterglows (data taken from [133, 134, 224]) and data from SN1998bw [222]. All these models are scaled for a source at 50 Mpc as this was the approximate farthest distance a GW source could have been detected at the time of data taking. A full description of how these curves were generated
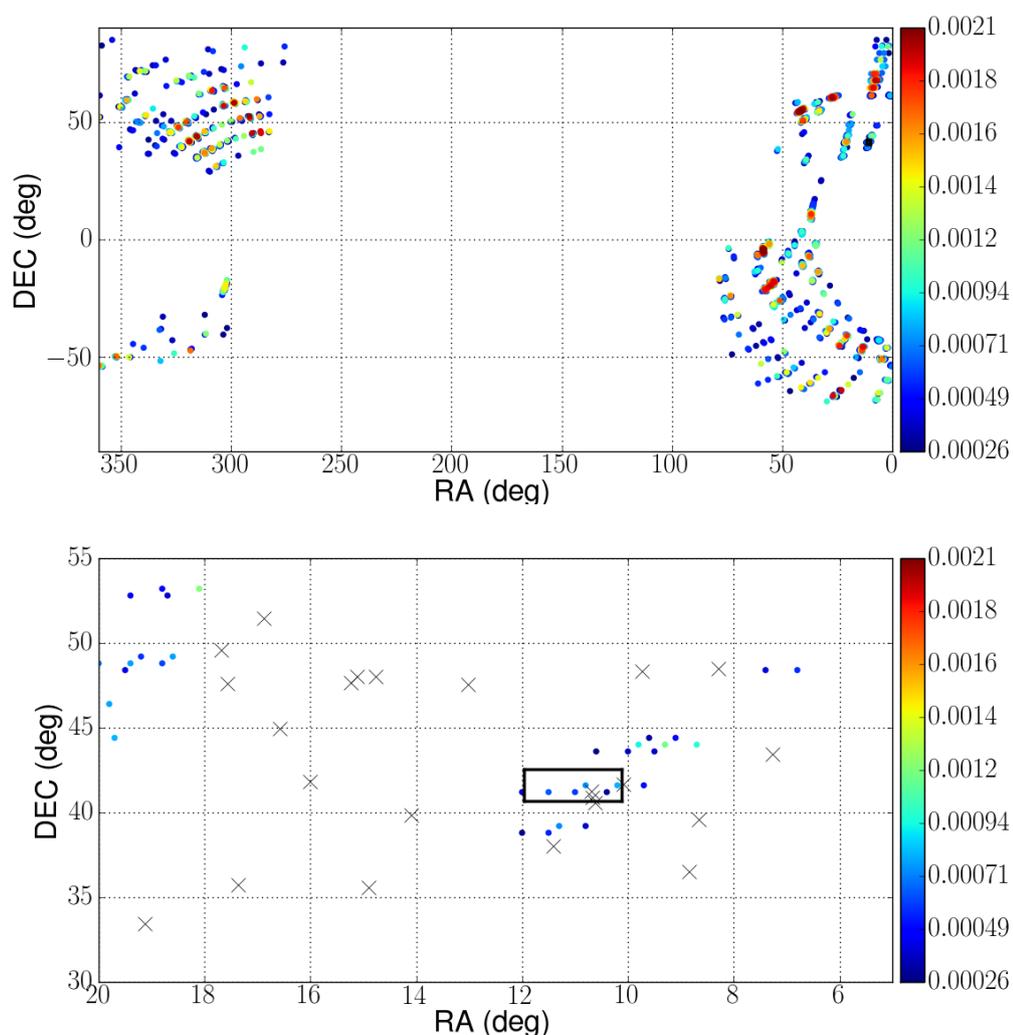
Figure 5.16: G21852: Skymap showing the estimated likelihood that each coloured location is the correct source location. This is the likelihood before the galaxy weighting is applied. The top plot shows the full sky and the bottom plot zoomed in on the location which ROTSE observed, which is shown by the black box in both plots. The ×'s in the bottom plot indicate galaxies within 50 Mpc according to the GWGC. The total likelihood over the whole coloured map is ∼87%.
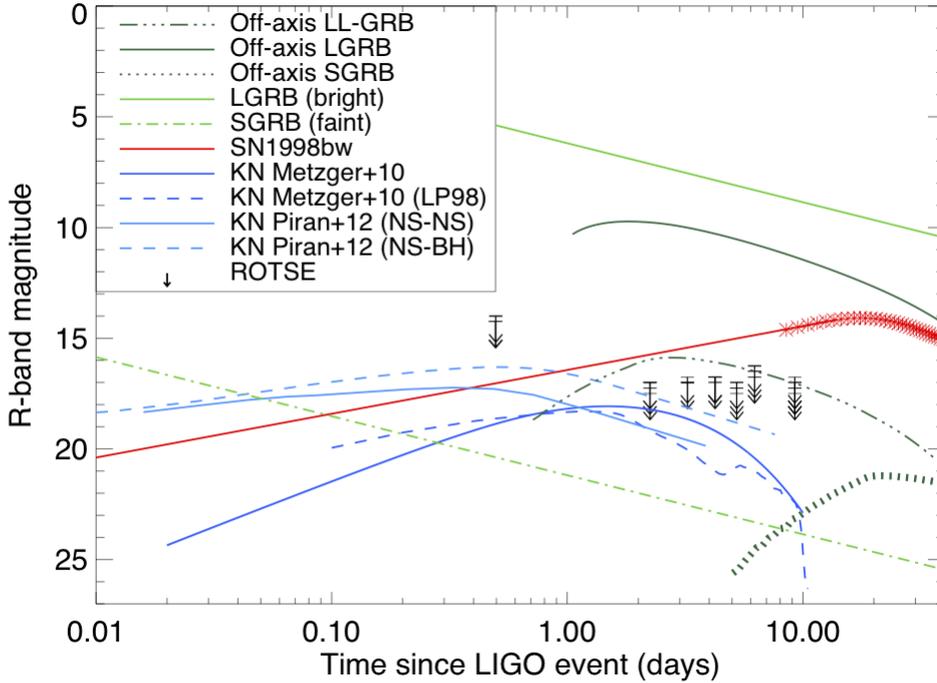
Figure 5.17: Timeline illustrating the limiting magnitudes of the images taken in response to G21852 (black) and expected models/EM observations, all scaled for sources at 50 Mpc. These include kilonovae [93, 97] (blue), supernova 1998bw [222] (red) and both short (SGRB) and long (LGRB), on-axis (light green) [133, 134] and off-axis (dark green) GRB afterglows [224]. LL-GRB represents a low luminosity GRB [224].

is discussed in Section 5.3. From this figure it is evident that if a supernova occurred similar to SN1998bw or there was a bright or off-axis LGRB (including low luminosity) the limiting magnitude of most of the images is sufficient for a detection. The images have a limiting magnitude too faint to detect SGRBs and kilonovae at 50 Mpc.

187 potential candidates were identified by the automated pipeline, of which 4 survived the event validation tests (as outlined in Section 4.4.1). 134 potential candidates did not appear in more than one set of images and were discarded, as were 23 potential candidates because their lightcurves were considered too flat, 24 potential candidates since their lightcurves did not decay sufficiently 48 hours to 1 month after the event took place and 2 candidates which were too close to stars in the SIMBAD catalogue. No candidates were discarded by the Minor Planet Checker. All four potential candidates are highlighted as near (within three times the semi-major diameter) a galaxy (either NGC0224 (Andromeda) or NGC0205 (dwarf galaxy that is a satellite of Andromeda). They have ranks of $R \simeq 3.7, 3.6, 3.3$ and 0.1.
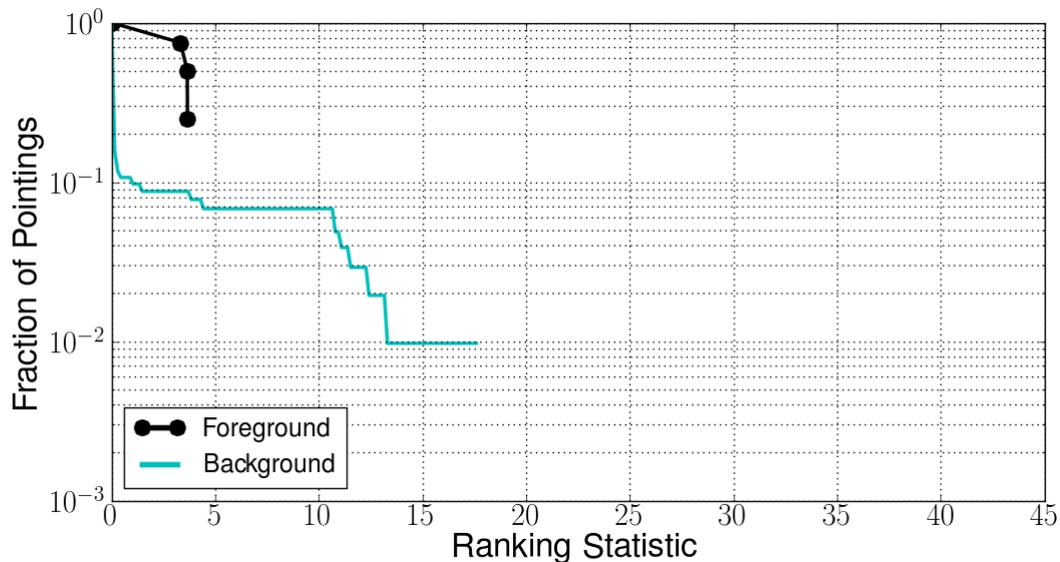
Figure 5.18: G21852: Distribution of the background events (cyan) and the candidate (black) in terms of rank against the cumulative fraction of pointings. To be considered significant (false alarm probability less than 1%) the candidate would need to have a ranking of greater than 17.5.

The rank of each of the 4 potential candidates (illustrated by black points) as well as the background distribution (cyan curve) are shown in Figure 5.18. In order to be significant a candidate would need to have a rank larger than the greatest background event, i.e. rank ≥ 17.5. None of the potential candidates however have a rank close to this; the most significant candidate has a rank of ~ 4. This is equivalent to $\sim 9\%$ of the background.

The four potential candidates were investigated further by plotting their lightcurves. The lightcurves are generated in the same way as described in Section 5.3 and are shown in Figures 5.19, 5.20, 5.21 and 5.22. Candidate 1 is the highest ranked candidate from Figure 5.18 and candidate 4 the lowest. Greater confidence is given to the second lightcurve of each candidate as this shows the lightcurve of just the transient with the background subtracted, and therefore reports dimmer magnitudes. For all the potential candidates, lightcurve 1 shows the potential transient and background to vary by less than one magnitude over the range of images. The best chi-square fit lightcurves which follow a kilonova, SGRB and LGRB are also plotted, along with the distance these sources would be to produce the model lightcurve. Note that the SGRB and LGRB models give the same curve but the sources are located at different distances.

The second lightcurve for candidate 1 shows the potential transient to

be quite variable. The lightcurve increases and decreases in magnitude over the range of images. It does not suggest however that the candidate follows one of the theoretical models or that the source produces both GW and EM waves. It appears to be consistent with a telescope artefact. Candidate 2 was only found in two sets of images when the background was subtracted. The limiting magnitudes of the images on most occasions were sufficient to detect the candidate if it were to follow one of the models. These conclusions can also be applied to candidate 3. Candidate 4 does seem to follow the model lightcurves quite well but was only found in three sets of images. The limiting magnitude of the images which did not detect the potential candidate were insufficient to have detected the transient if it were to follow one of the theoretical models. The distance the source would have to be to produce one of the GRB lightcurves is likely to be outside the range at which the GW detectors were able to detect a source. As well the distance the kilonova source is expected to be too distant to be found by the pipeline for these images. This will now be discussed further.

5.5.1 G21852 Injection Study

As previously described, over 4000 simulated transients, at various distances, were randomly placed in to the images for this event and processed through the automated pipeline. Figure 5.23 illustrates the efficiency of finding these injections with distance and magnitude. The distances quoted for the GRB models are the largest possible; they could be anywhere up to a factor of 40 smaller. Equations (4.6) and (4.7) define the GRB models. In each of these equations the offset quantity represents the range in observational data taken from [133, 134] and can take any value between 0 and 8. An offset of 0 (which was used here) represents those brightest afterglows and 8 the dimmest. The distances quoted for the GRB models are the largest that can be expected. They could however be a factor of 40 smaller due to the range in observational data for GRBs [133, 134]. The magnitudes reported are those which the injection would have in the second set of images as the first requirement in the event validation procedure (as detailed in Section 4.4.1) is to test whether a candidate appears on more than one night. As shown in the previous GW event injection studies, it is expected that the efficiency of the injections at close distances/bright magnitudes to be ∼50% as a number of the simulated transients are discarded due to saturation. However the efficiency for this event is ∼0% at magnitudes below 8 and only rises to a maximum of ∼50% between

G21852: Candidate 1

Lightcurve 1 - Transient and Background
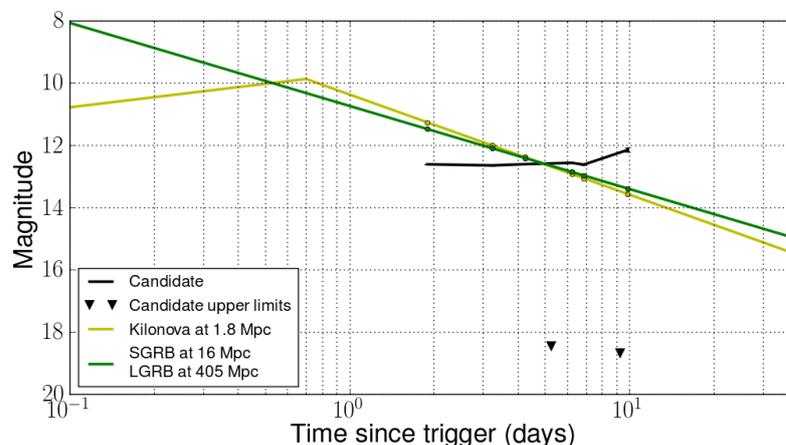
Lightcurve 2 - Transient with Background Subtracted

Figure 5.19: The top figure shows the lightcurve of the G21852 candidate which includes the background and the bottom figure shows the lightcurve with the background subtracted. In each plot the candidate's data points and error bars are plotted in black. Open circles on the model lightcurves indicate times at which the transient was detected. If a candidate was not identified in a given image, an upper limit is shown. This reports the limiting magnitude of the image at the location of the candidate. For comparison we also show the model lightcurves for both kilonovae (equations (4.4) and (4.5)) and afterglows (equations (4.6) and (4.7) with an offset=0) scaled to source distances which produce the best match to the measured magnitudes of the candidate. The SGRB and LGRB models give identical lightcurves the source distance is different as shown. This candidate has a rank $R \simeq 3.7$.

G21852: Candidate 2

Lightcurve 1 - Transient and Background

Lightcurve 2 - Transient with Background Subtracted

Figure 5.20: The top figure shows the lightcurve of the G21852 candidate which includes the background and the bottom figure shows the lightcurve with the background subtracted. In each plot the candidate's data points and error bars are plotted in black. Open circles on the model lightcurves indicate times at which the transient was detected. If a candidate was not identified in a given image, an upper limit is shown. This reports the limiting magnitude of the image at the location of the candidate. For comparison we also show the model lightcurves for both kilonovae (equations (4.4) and (4.5)) and afterglows (equations (4.6) and (4.7) with an offset=0) scaled to source distances which produce the best match to the measured magnitudes of the candidate. The SGRB and LGRB models give identical lightcurves the source distance is different as shown. This candidate has a rank $R \simeq 3.6$.

G21852: Candidate 3

Lightcurve 1 - Transient and Background

Lightcurve 2 - Transient with Background Subtracted
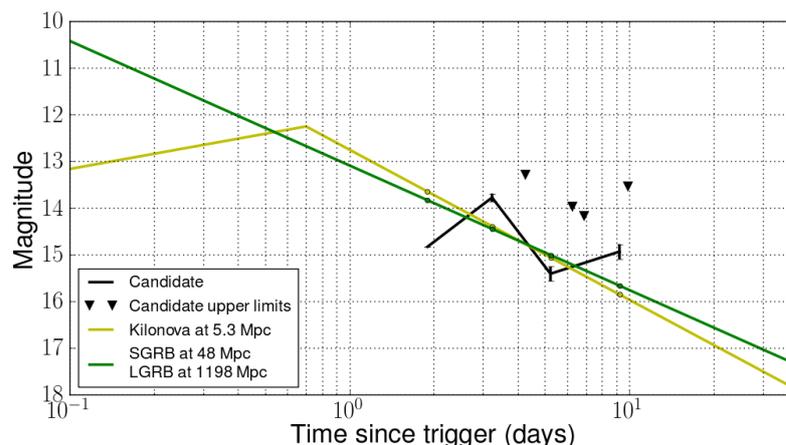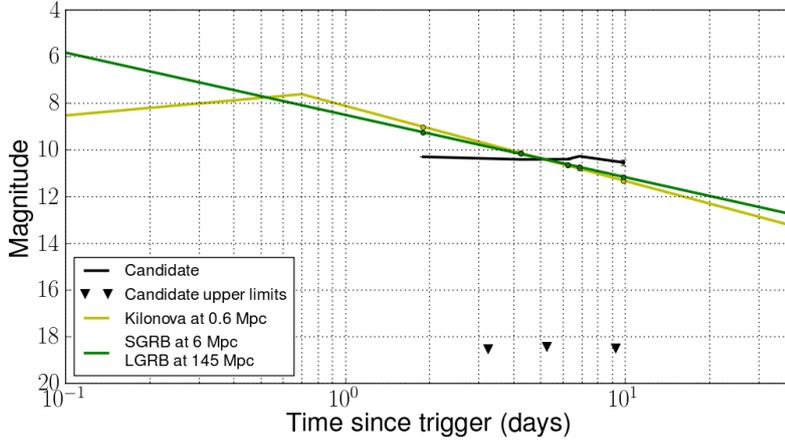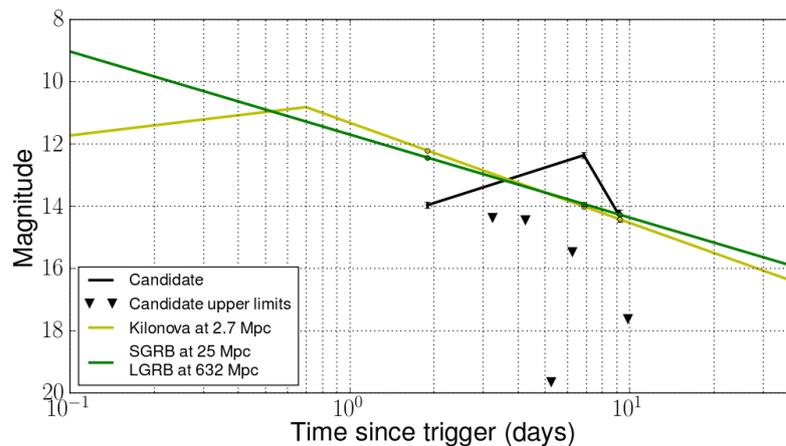

Figure 5.21: The top figure shows the lightcurve of the G21852 candidate which includes the background and the bottom figure shows the lightcurve with the background subtracted. In each plot the candidate's data points and error bars are plotted in black. Open circles on the model lightcurves indicate times at which the transient was detected. If a candidate was not identified in a given image, an upper limit is shown. This reports the limiting magnitude of the image at the location of the candidate. For comparison we also show the model lightcurves for both kilonovae (equations (4.4) and (4.5)) and afterglows (equations (4.6) and (4.7) with an offset=0) scaled to source distances which produce the best match to the measured magnitudes of the candidate. The SGRB and LGRB models give identical lightcurves the source distance is different as shown. This candidate has a rank $R \simeq 3.3$.

G21852: Candidate 4

Lightcurve 1 - Transient and Background

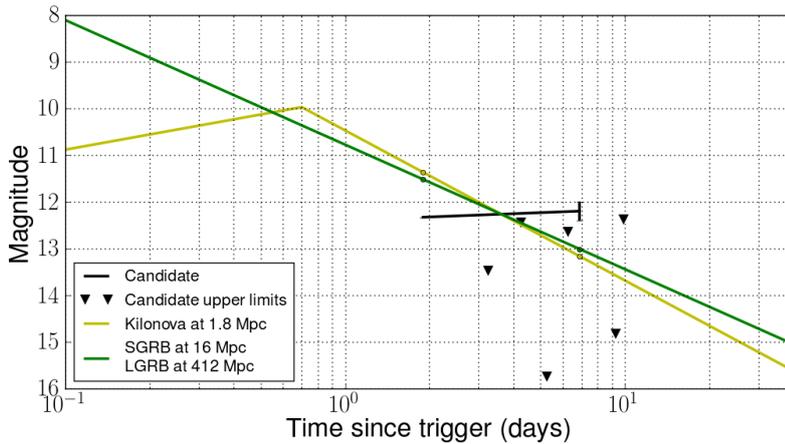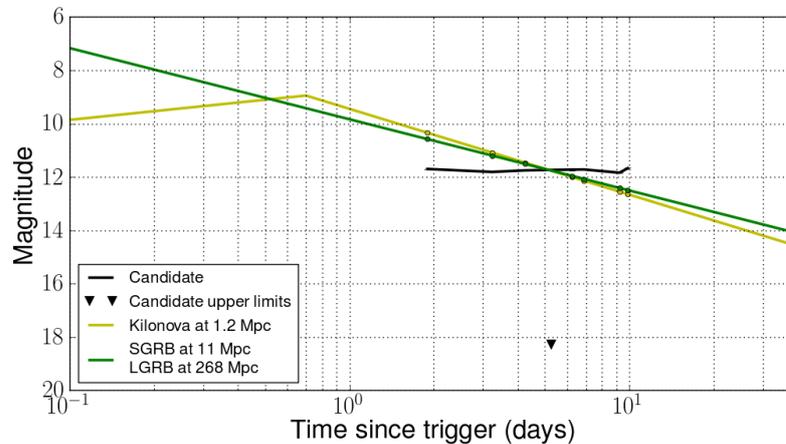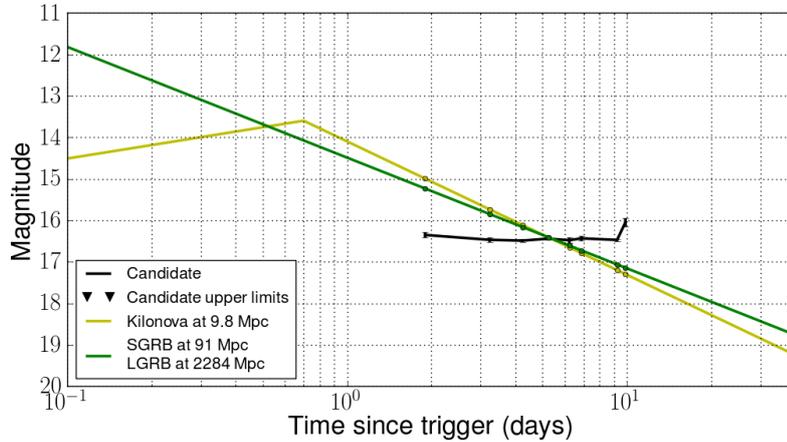### Lightcurve 2 - Transient with Background Subtracted
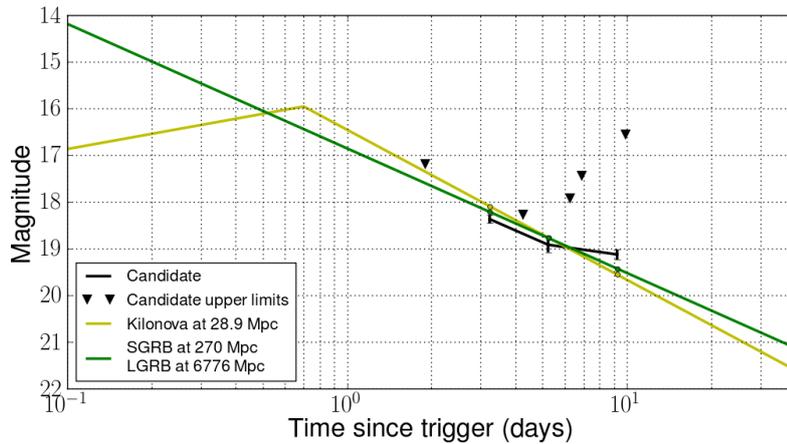
Figure 5.22: The top figure shows the lightcurve of the G21952 candidate which includes the background and the bottom figure shows the lightcurve with the background subtracted. In each plot the candidate's data points and error bars are plotted in black. Open circles on the model lightcurves indicate times at which the transient was detected. If a candidate was not identified in a given image, an upper limit is shown. This reports the limiting magnitude of the image at the location of the candidate. For comparison we also show the model lightcurves for both kilonovae (equations (4.4) and (4.5)) and afterglows (equations (4.6) and (4.7) with an offset=0) scaled to source distances which produce the best match to the measured magnitudes of the candidate. The SGRB and LGRB models give identical lightcurves the source distance is different as shown. This candidate has a rank $R \simeq 0.1$.

magnitudes 11-13 or distances of 2 Mpc / 40 Mpc / 1 Gpc for a kilonova / SGRB / LGRB before the efficiency drops again to 0% at magnitude ~17. This would suggest that in ~50% of the regions where simulated transients were placed, it would not be possible to detect them. This is due to poor image quality in certain regions of the image; the image quality is not uniform across the image. In general the edges of the image are at a lower limiting magnitude compared to the centre of the image. However in the images for this event, there seems to be more variation in the limiting magnitude in different regions of the images. In particular, the fact that the efficiency of the injections extends as far as magnitude 17 suggests that in certain regions of the image, the image quality is better than for the other GW events. Indeed, Figure 5.24 shows that injections recovered by the pipeline tend to have FAR < 10% ($R \geq 0.9$).

The distribution of the injections, as well as the background in terms of rank, is illustrated in Figure 5.25. These ten plots show the evolution of the injection distributions with increasing distance. Plot (a) shows the injections made at the closest distances, i.e. kilonova $\simeq 0.4$ Mpc / SGRB $\simeq 3.3$ Mpc / LGRB $\simeq 84$ Mpc whereas plot (j) at the furthest distances i.e. kilonova $\simeq 30$ Mpc / SGRB $\simeq 250$ Mpc / LGRB $\simeq 6.3$ Gpc. Unfortunately none of the injections, even at the closest distances/brightest magnitudes have a rank greater than the loudest background event. This would suggest the rank of a candidate alone cannot establish a very high significant candidate; other information such as the lightcurve must also be taken in to account.

5.5.2   G21852 Conclusions

ROTSE-IIIb followed up on event G21852 which occurred on September 26 2010 at 20:24:31 UTC. The error box containment in the region imaged by ROTSE was ~0.3%. Investigations showed the image quality played a large role in processing these images, as injections which were placed in certain regions of the images were not found. It can be estimated ~50% of injections were missed for this reason. To 50% confidence, it would be possible to identify a kilonova (SGRB) at ~2 Mpc (40 Mpc). A LGRB however would be missed because the efficiency of detecting a LGRB within the range of the GW detectors (within 50 Mpc) is zero. Four potential candidates were identified by the automated pipeline, however the rank of the candidates suggest they are not dissimilar to the background. The loudest candidate had a rank comparable to 9% of the background. The lightcurves for these potential candidates were
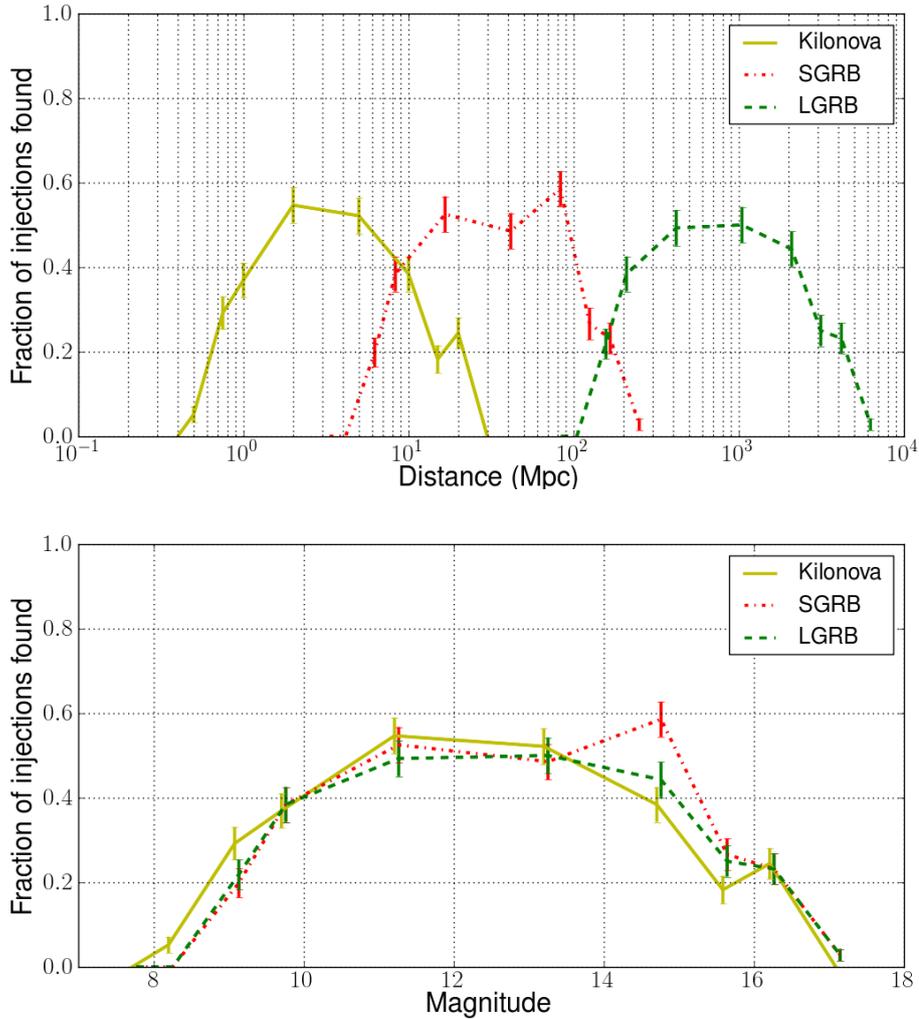
Figure 5.23: G21852: Efficiency of finding simulated transients with $R > 0$ versus distance (top) and magnitude (1.5 days after the trigger time) (bottom). The distances quoted for the gamma-ray burst models assume the brightest afterglows from Kann et al. [133, 134] (i.e. offset = 0 in equations (4.6) and (4.7)) but could be smaller by a factor of up to 40. All the models suffer from poor efficiency at very close distances / low magnitudes due to saturation.
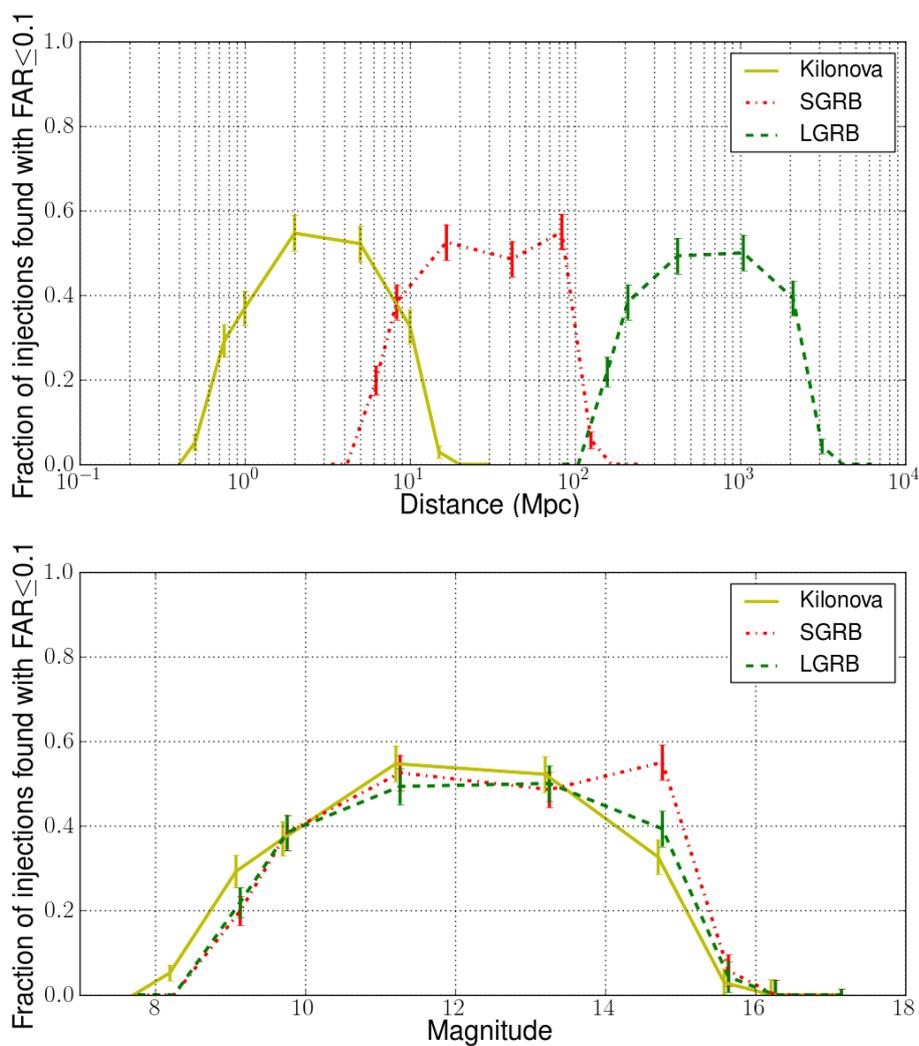
Figure 5.24: G21852: Efficiency of injections found with a false alarm probability of ≤ 0.1 ($R \geq 1$). The injections performed for the SGRB and LGRB models show the largest distance possible; the numbers could be a factor 40 smaller. The distances for the GRB models assume the brightest afterglows from Kann et al. [133, 134] (i.e. offset = 0 in equations (4.6) and (4.7)).

(a) 0.4 Mpc/mag 7.7

(b) 0.5 Mpc/mag 8.2

(c) 0.75 Mpc/mag 9

(d) 1 Mpc/mag 9.7

(e) 2 Mpc/mag 11.2

(f) 5 Mpc/mag 13.2

(g) 10 Mpc/mag 14.7

(h) 15 Mpc/mag 15.5

(i) 20 Mpc/mag 16.2

(j) 30 Mpc/mag 17.1

Figure 5.25: G21852: The distribution of injections (kilonova-yellow, SGRB-red and LGRB-green) and background (cyan) at various distances and magnitudes (1.5 days after the trigger). Plot (a) kilonova $\simeq$ 0.4 Mpc / SGRB $\simeq$ 3.3 Mpc / LGRB $\simeq$ 80 Mpc, (b) kilonova $\simeq$ 0.5 Mpc / SGRB $\simeq$ 4 Mpc / LGRB $\simeq$ 100 Mpc etc. In these figures we assumed the GRB models to have the brightest afterglows from Kann et al. [133, 134] (i.e. offset = 0 in equations (4.6) and (4.7)). Therefore the GRB distances could be a factor 40 smaller.

also generated for further validation, however they showed little evidence to be considered astropysically interesting. We conclude that no significant EM counterparts to event G21852 were identified by the ROTSE telescope system.

5.6 G23004

Event G23004 occurred on October 3 2010 at 16:48.23 UTC. The ROTSE-IIIb, c and d telescopes responded to this trigger beginning at 6 hours 25 minutes and took images up to days 29. These images were centred on RA: 61.97000° Dec: -20.91000 and contained four galaxies (within 17 Mpc) in the FoV. Due to the quality of the images, $\sim75\%$ had to be discarded, resulting in the analysis of 30 images. The probability skymap as generated by cWB is shown in Figure 5.26, along with a box illustrating the area which ROTSE searched over. The top plot in this figure shows the full sky and the bottom plot is zoomed in on the region of interest, with galaxies within 50 Mpc marked. The coloured regions show the estimated likelihood that each region is the true source direction independent of any galaxy weighting. The cumulative probability summed over the entire coloured regions is $\sim17.1\%$ (i.e. the cWB skymap has containment of $\sim17.1\%$) and the cumulative probability contained within the region imaged by ROTSE (without accounting for galaxy weighting) is $\sim0.11\%$.

A timeline of the limiting magnitudes of the analysable images is shown in Figure 5.27 along with the evolution of models whic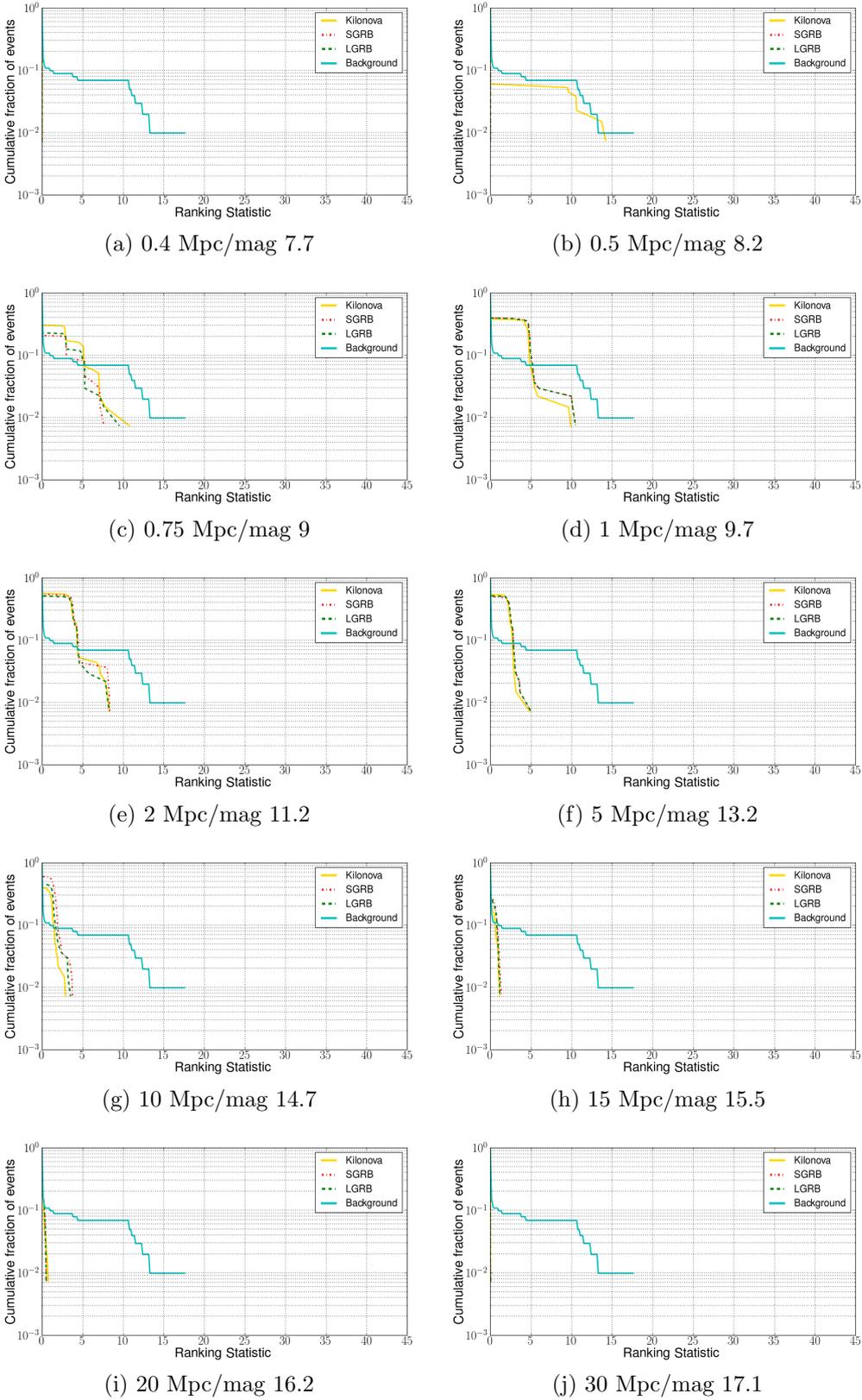h are expected to produce both GW-EM transients. These include kilonova models [93, 97], on- and off-axis GRB afterglows (data taken from [133, 134, 224]) and data from SN1998bw [222]. All these models are scaled for a source at 50 Mpc as this was the approximate farthest distance a GW source could have been detected at the time of data taking. A full description of how these curves were generated is discussed in Section 5.3. From this figure it is evident that if a supernova occurred similar to SN1998bw or there was a bright or off-axis LGRB the limiting magnitude of most of the images is sufficient for a detection. In approximately half the images an off-axis low-luminosity GRB at 50 Mpc would also be detected. However a kilonova signature or a SGRB at 50 Mpc would be missed.

The automated pipeline identified 124 potential candidates of which 122 did not appear in more than one set of images and were discarded. In addition 1 candidate's lightcurve was considered to flat and one other candidate's
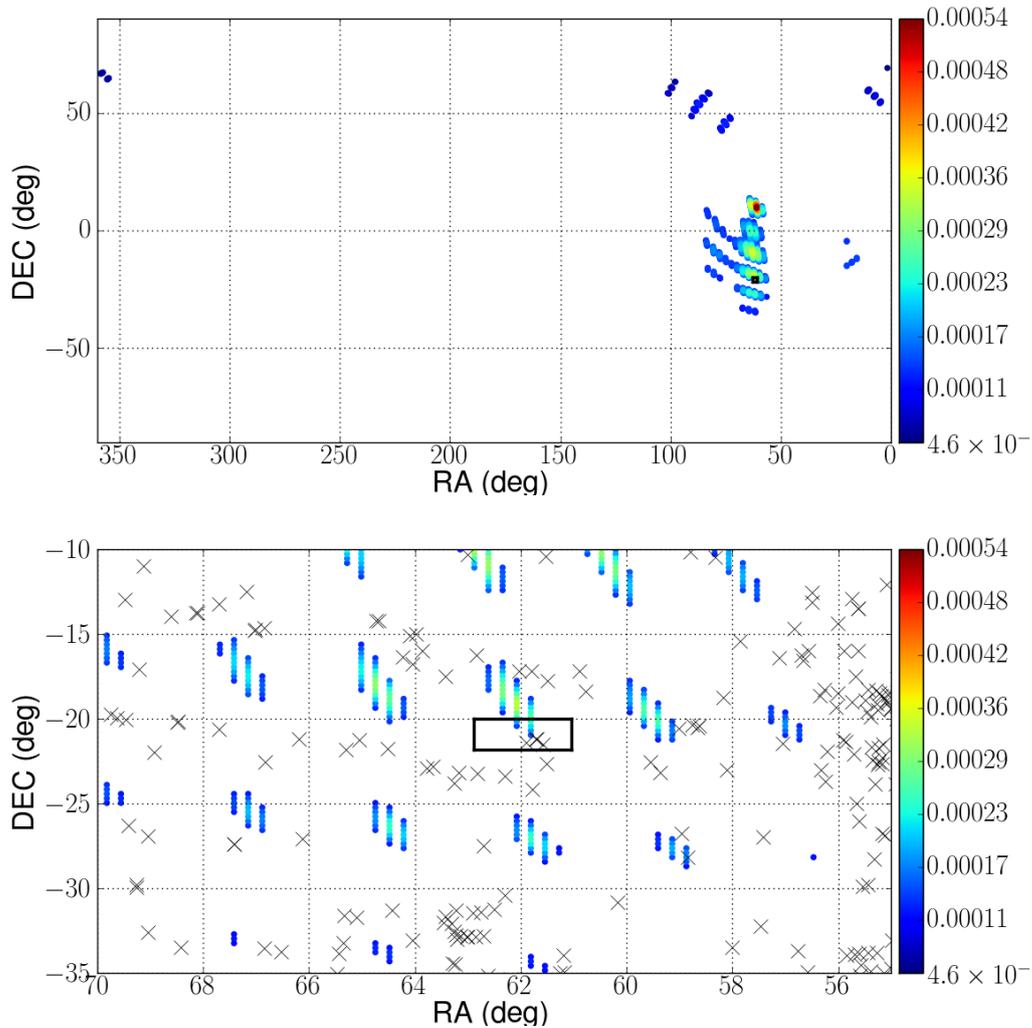
Figure 5.26: G23004: Skymap showing the estimated likelihood that each coloured location is the correct source location. This is the likelihood before the galaxy weighting is applied. The top plot shows the full sky and the bottom plot zoomed in on the location which ROTSE observed, which is shown by the black box in both plots. The ×'s in the bottom plot indicate galaxies within 50 Mpc according to the GWGC. The total likelihood over the whole coloured map is ∼17.1%.
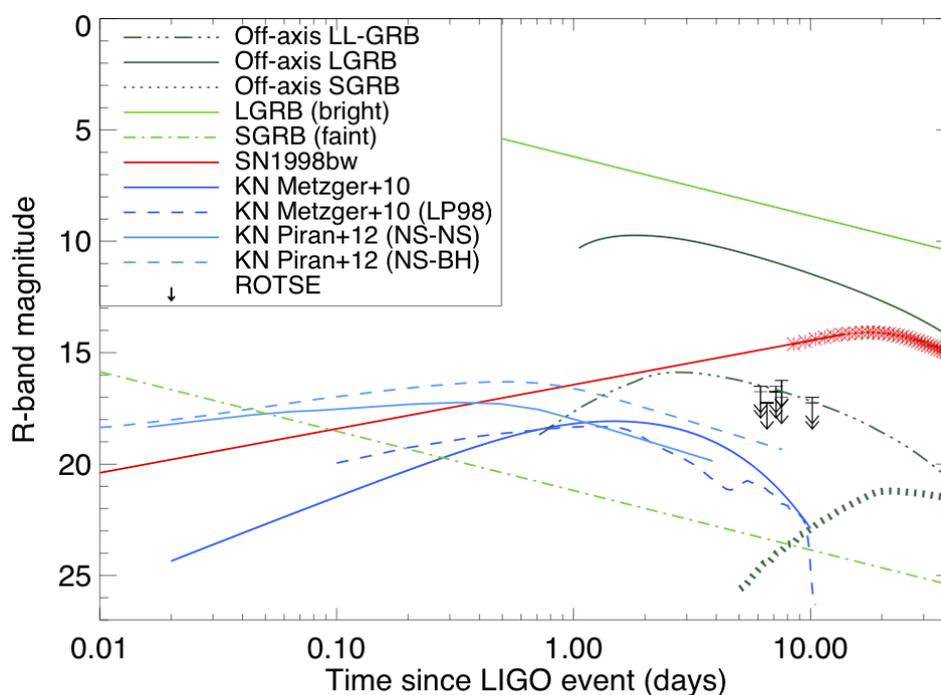
Figure 5.27: Timeline illustrating the limiting magnitudes of the images taken in response to G23004 (black) and expected models/EM observations, all scaled for sources at 50 Mpc. These include kilonovae [93, 97] (blue), supernova 1998bw [222] (red) and both short (SGRB) and long (LGRB), on-axis (light green) [133, 134] and off-axis (dark green) GRB afterglows [224]. LL-GRB represents a low luminosity GRB [224].
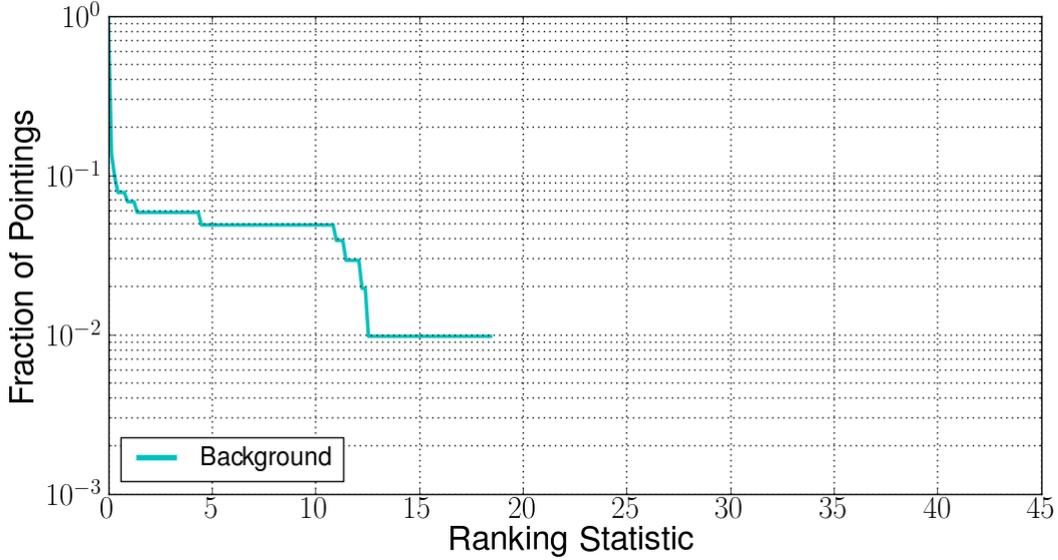
Figure 5.28: G23004: Distribution of the background events (cyan) and the candidate (black) in terms of rank against the cumulative fraction of pointings. To be considered significant (false alarm probability less than 1%) the candidate would need to have a ranking of greater than 18.

lightcurve did not decay sufficiently 48 hours to 1 month after the event took place. No candidates were rejected because of the Minor Planet Checker or the SIMBAD catalogue. This left zero potential candidates associated to event G23004.

Since no candidates were identified by the pipeline, only the distribution of the background for this event is shown in Figure 5.28. If a candidate were to be identified it would need to have a rank greater than the loudest background event, i.e. rank of 18, to be considered significant (FAR $\lesssim$ 1%).

5.6.1 G23004 Injection Study

Over 4000 simulated transients following kilonova, SGRB and LGRB lightcurves at a range of distances, were placed at various locations in the images, as described in Section 4.6. Figure 5.29 shows the fraction of injections identified with either distance or magnitude. The distances quoted for the GRB models are the largest possible; they could be anywhere up to a factor of 40 smaller. Equations (4.6) and (4.7) define the GRB models. In each of these equations the offset quantity represents the range in observational data taken from [133, 134] and can take any value between 0 and 8. An offset of 0 (which was used here) represents those brightest afterglows and 8 the dimmest. The magnitudes reported are from the second set of images as the first requirement in

the event validation checks (as detailed in Section 4.4.1) is that a candidate is found in more than one set of images. Unfortunately for this set of images the maximum efficiency of correctly identifying injections is only ∼20%, between magnitudes 9-13. At the closest distances/brightest magnitudes the efficiency is zero, then rises to this maximum efficiency before falling to zero again at magnitude ∼15. This low efficiency is due to poor image quality. As already mentioned the majority of images taken in response to this GW trigger had to be rejected due to poor image quality which only left a few nights of images to analyse. Injections are randomly placed throughout the images, and in this situation it is evident that there are only a few regions where we would be able to identify a transient. Figure 5.30 shows the same information, which implies that of the identified injections, they are favourably ranked compared to the background because the background distribution falls sharply in Figure 5.28; the rank for a FAR < 10% is $R \sim 0.3$. However due to the low efficiency over the range of magnitudes/distances, if this GW event did produce an EM counterpart it is unlikely to have been detected.

The distribution of injections and background with increasing distance are depicted in Figure 5.31. Plots (a) shows injections made at the closest distances, i.e. kilonova $\simeq$ 0.4 Mpc / SGRB $\simeq$ 3.3 Mpc / LGRB $\simeq$ 84 Mpc and (j) at the farthest distances, i.e. kilonova $\simeq$ 30 Mpc / SGRB $\simeq$ 250 Mpc / LGRB $\simeq$ 6.3 Mpc. The loudest background event has a rank of 18, and the most significant injections have a rank less than half this value. This suggests that if a potential candidate were to be found for this event the rank alone could not be used to establish a very high significance; lightcurve or other data would also need to be considered.

5.6.2 G23004 Conclusions

ROTSE-IIIb, c and d followed up on event G23004 which took place on October 3 2010 at 16:48.23 UTC. The error box containment in the region imaged by ROTSE was ∼0.11%. The majority of the images taken in response to this GW event however had to be discarded due to poor image quality. The remaining images were investigated by injecting simulated transients following kilonova, SGRB and LGRB models. The maximum efficiency of identifying these injections was found to be ∼20% between a kilonova / SGRB / LGRB distance of ∼ 1-5 Mpc / 6-50 Mpc / 150-1000 Mpc. These GRB distances assume the brightest afterglows, i.e. an offset of 0, and could therefore be a factor of 40 smaller. The cause of this low efficiency can be attributed to poor
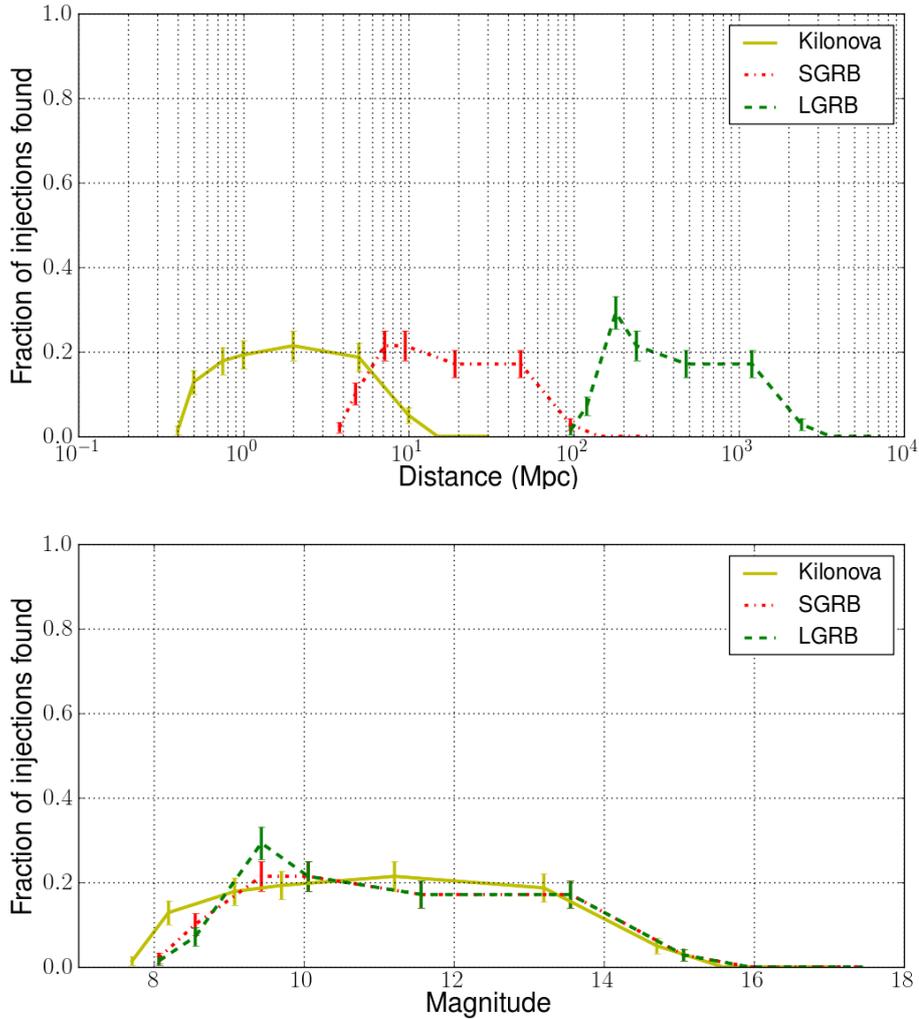
Figure 5.29: G23004: Efficiency of finding simulated transients with $R > 0$ versus distance (top) and magnitude (1.5 days after the trigger time) (bottom). The distances quoted for the gamma-ray burst models assume the brightest afterglows from Kann et al. [133, 134] (i.e. offset = 0 in equations (4.6) and (4.7)) but could be smaller by a factor of up to 40. All the models suffer from poor efficiency at very close distances / low magnitudes due to saturation.
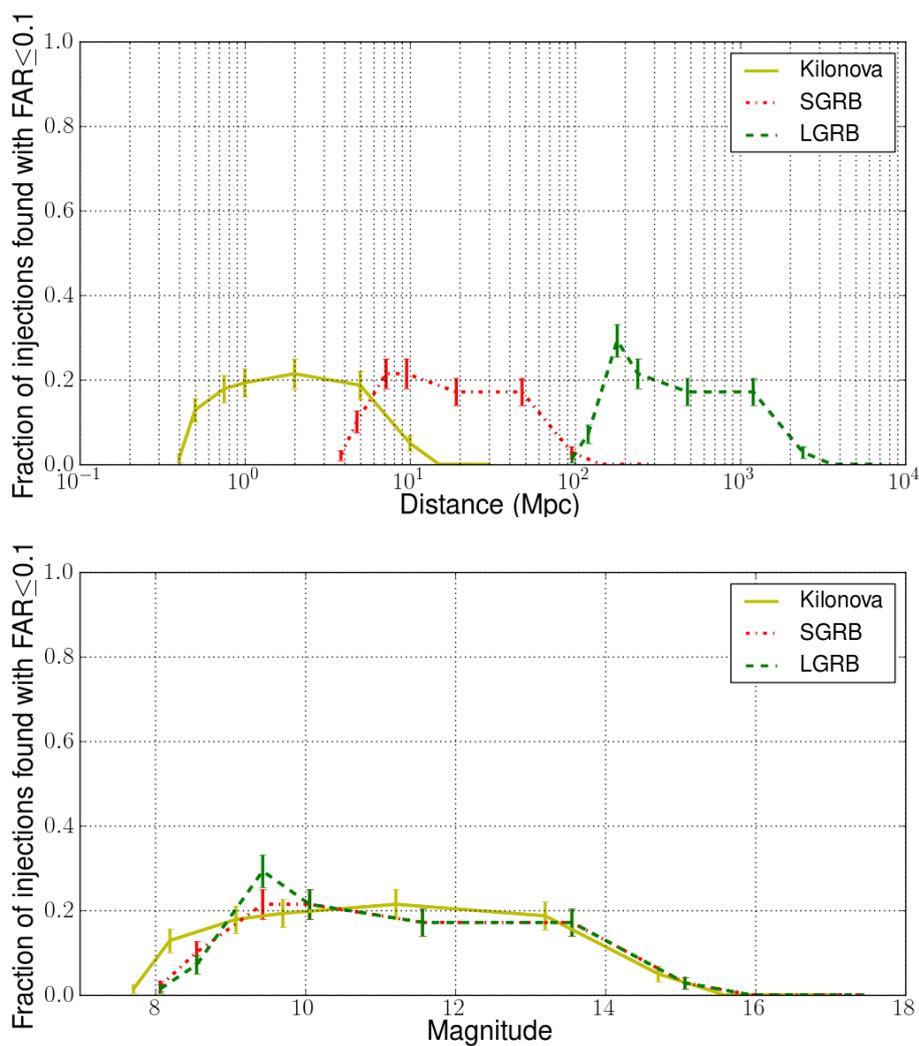
Figure 5.30: G23004: Efficiency of injections found with a false alarm probability of ≤ 0.1 ($R \geq 0.3$). The injections performed for the SGRB and LGRB models show the largest distance possible; the numbers could be a factor 40 smaller. The distances for the GRB models assume the brightest afterglows from Kann et al. [133, 134] (i.e. offset = 0 in equations (4.6) and (4.7)).

(a) 0.4 Mpc/mag 7.7

(b) 0.5 Mpc/mag 8.2

(c) 0.75 Mpc/mag 9

(d) 1 Mpc/mag 9.7

(e) 2 Mpc/mag 11.2

(f) 5 Mpc/mag 13.2

(g) 10 Mpc/mag 14.7

(h) 15 Mpc/mag 15.5

(i) 20 Mpc/mag 16.2

(j) 30 Mpc/mag 17.1

Figure 5.31: G23004: The distribution of injections (kilonova-yellow, SGRB-red and LGRB-green) and background (cyan) at various distances and magnitudes (1.5 days after the trigger). Plot (a) kilonova $\simeq$ 0.4 Mpc / SGRB $\simeq$ 3.3 Mpc / LGRB $\simeq$ 80 Mpc, (b) kilonova $\simeq$ 0.5 Mpc / SGRB $\simeq$ 4 Mpc / LGRB $\simeq$ 100 Mpc etc. In these figures we assumed the GRB models to have the brightest afterglows from Kann et al. [133, 134] (i.e. offset = 0 in equations (4.6) and (4.7)). Therefore the GRB distances could be a factor 40 smaller.

image quality, where only in select regions of the images could a transient be identified. Consequently it would be highly unlikely that a transient associated to this GW event would be found. In fact, the automated pipeline did not find any potential candidates attributed to this event. Therefore no EM candidates were found for event G23004 by the ROTSE telescope system.

5.7 Concluding remarks

The analysis of images taken in response to five GW events by the ROTSE telescope system has been performed using the automated ROTSE pipeline, developed specifically for this analysis (details of this pipeline can be found in Chapter 4). Background studies have revealed the expected distribution of background transients for each of the five GW events. In addition studies have been performed where simulated transients, following a kilonova, SGRB and LGRB model, have been placed at random locations within the GW images to access the efficiency of identifying a transient. The background distribution and efficiencies vary greatly between GW events, due in part to the quality of the images. Over 100 images for various candidates had to be discarded before the analysis could begin due to poor image quality, and in some instances (such as G21852 and G23004) the image quality hampered the search.

No significant optical counterpart to any of the five GW events has been identified. However for the first GW trigger (G18666) this was expected as a computer error caused the ROTSE-IIIc telescope to point at an arbitrary sky location. The result for the other four GW triggers is cons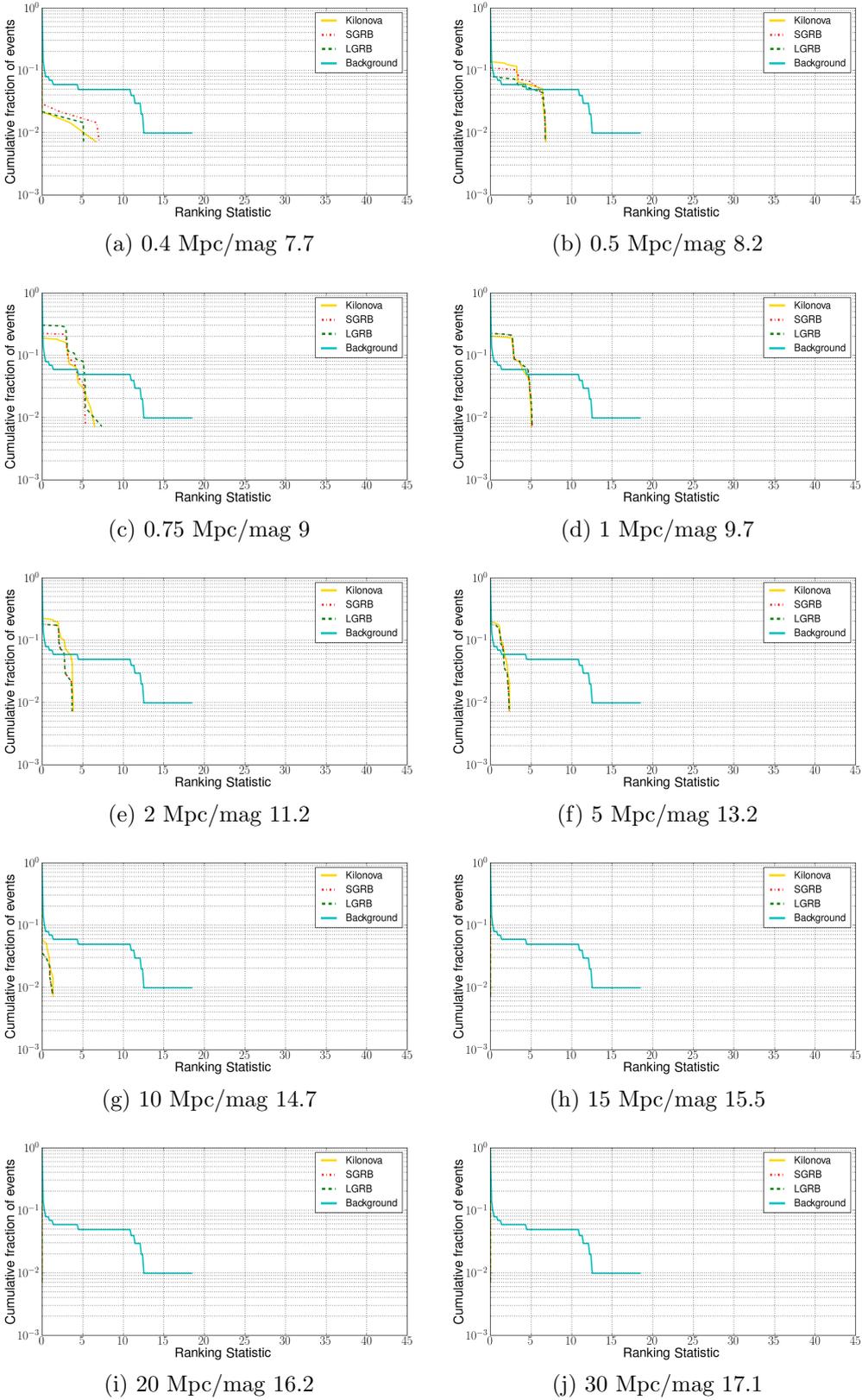istent with the findings that none of these events were triggered by actual GWs [22], but more likely from serendipitous environmental factors. However, of the five potential candidates the automated pipeline identified to events G19377 and G21852, four of them had a FAR∼ 10%. This is probably due to systematic differences between images taken in the LOOC UP program and those used for background study. With GW detectors at the sensitivities they were at the time of this search, none of the triggers were likely to represent true astrophysical events.

This analysis completes the LOOC UP search which began in 2009 [159, 160]. This search was the first of its kind in which GW information was used to point EM telescopes in an attempt to capture the signal from both channels. Although a detection was not expected, this search and subsequent development of pipelines, such as this one, have lead to improved practises which will be an advantage in the Advanced detector era where regular GW detections

are expected. This analysis demonstrates the ability to characterise the background of optical images and place a statistical significance on any potential candidates the pipeline may identify. This procedure will be necessary when the first GW-EM detections are being made.

Chapter 6

Conclusions

The second generation of gravitational wave (GW) detectors, Advanced LIGO [188] and Virgo [57], are due to come online in 2015 and they promise to bring the first direct detection of GWs. The first signal is likely to be from the merger of compact objects, consisting of neutron stars (NS) and/or stellar mass black holes (BH). GW interferometers, past and future, are optimised to detect signals from these sources. They are the best understood sources in terms of rate; Advanced detectors are expected to detect $\sim$40 GW events per year [34]. The merger of NS-NS and NS-BH systems are the favoured progenitor model for short gamma-ray bursts (SGRBs). In addition kilonovae are another expected EM signature of mergers.

Multi-messenger astronomy promises much scientific reward as electromagnetic (EM) and GW information will be completely complementary. Benefits of EM follow-up of GW events include precise source localisation, determination of the host galaxy and also an independent measurement of H_0. SGRBs have been extensively modelled and studied and have real potential to provide detectable signals in both the EM and GW bands, in addition to their afterglows. As well, the hypothesised supernova-like transient known as a kilonova is believed to hold real potential. The lightcurves (either from data or simulations) of these models are expected to be detectable by current and future EM observatories, such as Pan-STARRS [135] and LSST [136], which have both suitable cadence and sensitivity. However this all relies on prompt notification of a source, as the lightcurves decline rapidly within hours or days in the optical band.

During the last science run of LIGO and Virgo a new form of search was performed in which GW data was analysed in real-time and the sky location of the candidate GW sources was estimated and sent to conventional EM

telescopes for follow up. One of the main challenges this form of search presents is locating where on the sky the signal originated. GW interferometers are sensitive to signals from a large portion of the sky; a single detector is not capable of locating a source. Therefore triangulation between a network of interferometers is used to determine the source direction. With the three GW detectors (LIGO-Hanford, LIGO-Livingston and Virgo) at the sensitivities they had during the last science run, they were likely to localise a source to tens or hundreds of square degrees. The majority of telescopes used in this follow up search were wide field of view optical telescopes, with 3-4 deg^2 typical coverage. Such telescopes require tens or hundreds of pointings to cover a typical source region which is not feasible. We therefore propose a ranking statistic (equation (3.3)) which considers all galaxies within the reach of the detectors (using the Gravitational Wave Galaxy Catalogue (GWGC) [163]) and ranks them based upon their luminosity and distance as being the most likely host of a GW source. Simulations suggest this statistic performs 2-4 times better at identifying the location of the source compared to triangulation alone. A form of this statistic was consequently used to aid sky localisation in this EM follow up search.

The Advanced detector era, which begins in 2015, is expected to pass through many phases where the detectors become increasingly sensitive until they reach design c. 2020-22 [58]. Sky localisation is expected to be poor in the early phases until the network of detectors is able to localise just a few square degrees at design sensitivity. Simulations suggest that once three detectors are in operation (2016+) the galaxy ranking scheme performs much better at localising a GW signal to a host galaxy, between a 10-20% improvement, provided a complete galaxy catalogue exists. Current catalogues with the desired information (such as luminosity, distance, type etc) only go to 100 Mpc. This work strongly recommends that efforts be placed on constructing a deeper catalogue, to $\sim$ few hundred Mpc or even $\sim$ Gpc.

Even with an effective galaxy ranking statistic, many pointings are required to have a high probability of imaging the true host. This requires automated analysis. We demonstrate such an analysis using ROTSE-III, which was one of the wide field of view optical telescopes used in the EM follow up search. The ROTSE-III telescope system consists of four robotic optical telescopes across the world which are capable of slewing on to a source within seconds. ROTSE followed up on five GW events and took over 700 images using all four telescopes. Although the ROTSE collaboration have an image processing pipeline,

the analysis of images taken in response to GW events presents new challenges. As already discussed the localisation of GW signals is poor. In addition the decay timescale and magnitude of a possible EM counterpart are uncertain. These two factors point to the need to analyse a large number of images. As well, since a GW detection has not been made yet, it is desirable to place a statistical significance on any EM counterpart. These factors necessitated the automation of the image processing pipeline in addition to the construction of automated validation tests and classification techniques. The automated pipeline typically identified a few hundred potential candidates during the analysis of a set of images. Therefore a series of cuts were constructed with the aim of identifying the most astrophysically interesting transients. These cuts included discarding a potential candidate which was not seen on more than one night, if the candidate's lightcurve was not varying sufficiently and if the potential candidate's coordinates coincided with an asteroid or variable star. These cuts proved effective in removing most background transients, typically leaving less than five potential candidates. The automated pipeline is presented in Chapter 4.

The automation of the image processing pipeline allowed both background and efficiency studies to be performed. A background study of over 100 archival ROTSE pointings allowed the optical background to be ascertained. This therefore allows a significance to be placed on any EM candidate which is identified by the automated pipeline. To test the pipeline's ability to identify a source, simulated transients resembling some of the most likely GW-EM sources (i.e. kilonovae and GRBs) were placed in to a set of images. To highlight the most interesting candidates which the pipeline may identify, a statistic (equation (4.2)) was proposed which favours brighter transients that appear in multiple images close in time to the GW event. This *ad hoc* statistic proves quite useful in highlighting the most interesting candidates. The background distribution typically has a bimodal distribution with ∼90% having low ranks and ∼10% having high ranks. The "tail" of the 10% highly ranked background indicates more work needed to identify actual EM counterparts with a high significance, for example more use of lightcurve information. The analysis of a set of images taken from the ROTSE archives (not associated to a GW event) as a "test run" is presented in Chapter 4.

The analysis, using the automated pipeline, of the images taken in response to the five GW events, during the LOOC UP program, are presented in Chapter 5. No significant optical counterparts to the GW events were found,

however with the detectors at the sensitivity they were in the previous science run, a joint detection was unlikely to be made. The analysis of event G18666 was unlikely to be interesting because of a pointing error which caused images to be taken of an incorrect region of the sky. In addition event G19377 was revealed to be a simulated GW or "blind injection". For the remaining three events the automated pipeline identified no potential candidates for events G20190 and G23004. However the images taken for event G21852 overlapped with Andromeda, and four potential candidates were identified, of which three had false alarm probabilities of ≤ 0.1. Upon further investigation of these candidates they appeared to be consistent with background subtraction artifacts.

The analysis of the LOOC UP images using the automated pipeline revealed that most of the surviving candidates had unusually low false alarm rates ($<10\%$), indicating the background images were statistically dissimilar from the LOOC UP images. This suggests that we need to collect images specifically for background studies for advanced detector follow-up. In addition the $\sim10\%$ tail in the background distribution needs to be reduced as this limits the significance of any candidate identified by the automated pipeline. This indicates the need for further research, perhaps using the lightcurve shape or considering different analysis techniques such as multi-variate analysis.

A major limitation in the injections studies performed for each GW event is that in some instances $\sim50\%$ of injections were lost due to a background-subtracted lightcurve not being generated or due to poor image quality. This motivates investigations in to perhaps using the lightcurve which is generated before background subtraction or pointing the ROTSE telescopes in such a way that images overlap with one another to build a mosaic of a sky region. In addition transients in galaxies were not sufficiently investigated due to the limitation of the injection software. This again needs to be addressed for the Advanced detector era.

Despite the likelihood of a joint EM-GW detection being low in the last science run, the methods and analysis techniques learnt from performing an EM follow-up search will prove invaluable in the Advanced detector era. Within the next few years GW detectors will come online, ushering in the epoch of regular GW detections and start of GW astronomy.

Appendix A

Image Analysis of Event G18666

Event G18666 occurred on September 7 2010 at 21:39:48 UTC. ROTSE-IIIc observed a single field centred on RA: 250.69500° Dec: $-25.54000°$ beginning at 20 hours 38 minutes and returning on 13 subsequent nights up to days 29. In total 125 images were taken, with 77% (23%) of them having a 60s (20s) exposure time. No galaxies within 50 Mpc are within the field of view (FoV) for this event.

A timeline of the limiting magnitudes of the analysable images is shown in Figure A.1 along with the evolution of models which are expected to produce both GW and EM transeints. These include kilonova models [93, 97], on- and off-axis GRB afterglows (data taken from [133, 134, 224]) and data from SN1998bw [222]. All these models are scaled for sources at 50 Mpc as this was the approximate farthest distance a GW source could have been detected at the time of data taking. A full description of how these curves were generated is discussed in Section 5.3. From this figure it is evident that if a supernova occurred similar to SN1998bw or there was a bright LGRB (on- or off-axis) the limiting magnitude of these images are sufficient for a detection. However the models for a kilonova, SGRB and some low luminosity off-axis LGRBs are too faint for these images. However since ROTSE-IIIc did not observe the correct sky region, it is extremely unlikely an optical counterpart to this GW trigger would be found. However these images provide a useful "dry run" of the analysis under conditions of the 2009-2010 observing run.

The automated image processing pipeline identified 309 potential candidates, of which 3 survived the event validation tests (these tests are documented in Section 4.4.1). 242 potential candidates were discarded because they were only seen on one night, 31 candidates had too flat a lightcurve, 29 candidates did not decay by a sufficient amount 48 hours to 1 month after

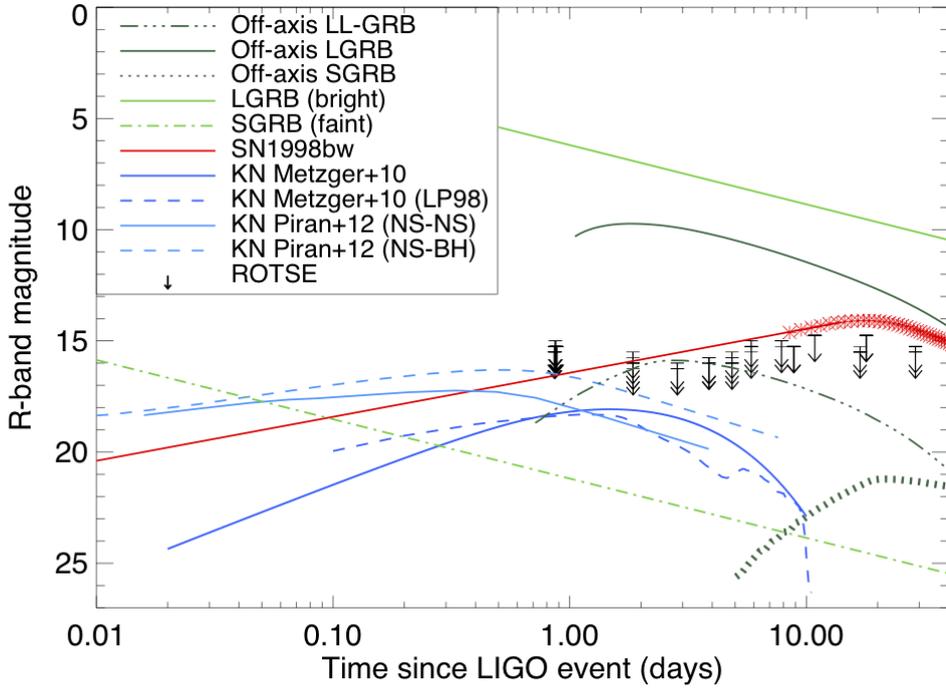Figure A.1: Timeline illustrating the limiting magnitudes of the images taken in response to G18666 (black) and expected models/EM observations, all scaled for sources at 50 Mpc. These include kilonovae [93, 97] (blue), supernova 1998bw [222] (red) and both short (SGRB) and long (LGRB), on-axis (light green) [133, 134] and off-axis (dark green) GRB afterglows [224]. LL-GRB represents a low luminosity GRB [224].
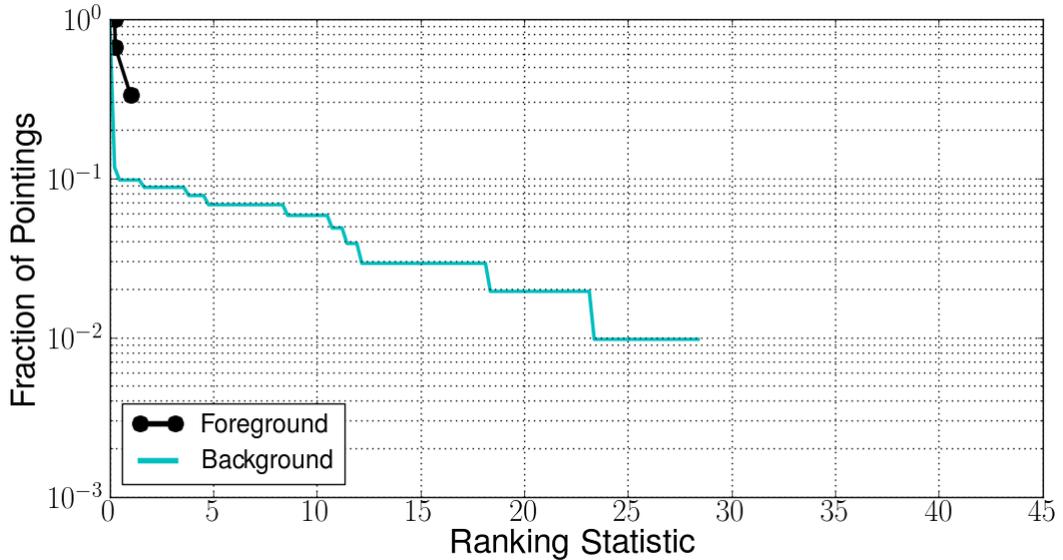
Figure A.2: G18666: Distribution of the background events (cyan) and the candidate (black) in terms of rank against the cumulative fraction of pointings. To be considered significant (false alarm probability less than 1%) the candidates would need to have a ranking of greater than 29.

the event took place and 4 candidates coordinates were too close to a star as identified by the SIMBAD catalogue. No candidates were rejected due to the Minor Planet Checker. None of the three candidates were identified as being in the vicinity (within three times the semi-major diameter) of a galaxy. They have ranks of $R \simeq 1.0$, 0.3 and 0.2.

The background distribution as well as the rank (defined by equation (4.2)) of each of the candidates for this event were found and plotted in Figure A.2. The cyan curve shows the distribution of the background, with the three candidates shown by black points. To be considered significant a candidate would need to have a rank greater than the loudest background event, i.e. a rank of 29 or more. However none of the candidates have a rank above ~ 1, and are therefore not significant. The strongest candidate has a false alarm probability of ~ 0.1. The three surviving candidates were investigated further by plotting their lightcurves (a description of how lightcurve are generated is found in Section 5.3). Candidate 1 is the highest ranked candidate from Figure A.2, with candidate 3 the lowest.

Figure A.3 shows the lightcurves for candidate 1, where lightcurve 1 shows the lightcurve generated from both the transient and the background data whereas lightcurve 2 shows the transient with the background subtracted. The black curve in lightcurve 1 shows the transient to be approximately constant

in magnitude. No upper limits are reported as the transient was found in every image. Lightcurve 2 reveals the data from the transient only; the potential candidate is observed on these separate nights and follows the theoretical lightcurves well. However for the remainder of the images the transient was not found as shown by the numerous upper limits which report the limiting magnitude of the image where the transient should be located. At the time of taking this data the GW interferometers could detect NS-NS and NS-BH systems to ~ 50 Mpc. In addition the candidate is not thought to be a kilonova or SGRB as it was not found in the other eight images where the sensitivity was sufficient to detect the transients according to the models. Figures A.4 and A.5 show the lightcurves for the other two, lower ranked candidates. For the same reasons as candidate 1, both candidate 2 and 3 are not thought to be astrophysically interesting.

G18666 Injection Study

In the same manner as described in Section 4.6 simulated transients following a kilonova, SGRB and LGRB, at various distances, were placed at random locations in the G18666 images. Over 4000 transients were injected and the automated pipeline run to show the performance of the pipeline in identifying these sources. Figure A.6 shows the fraction of simulated transients which were identified with distance or magnitude. The magnitudes reported are from the second night of observation as one of the requirements for the pipeline to identify a candidate is that it appears more than once (i.e. on at least two nights). The distances quoted for the GRB models are the largest possible; they could be anywhere up to a factor of 40 smaller. Equations (4.6) and (4.7) define the GRB models. In each of these equations the offset quantity represents the range in observational data taken from [133, 134] and can take any value between 0 and 8. An offset of 0 (which was used here) represents those brightest afterglows and 8 the dimmest. The distances quoted for the GRB models are the largest that can be expected. They could however be a factor of 40 smaller due to the range in observational data for GRBs [133, 134]. All the models have a low efficiency at bright magnitudes/close distances due to saturation. Early in the image processing the pipeline discards transients which are too bright as the assumption is that they are telescope artefacts and not of astrophysical origin as they saturate the image. Therefore $\sim 50\%$ of the injections between magnitudes 7.5 and 9 are discarded. However as the injected magnitude drops the efficiency rises to its maximum between 80-90%

G18666: Candidate 1

Lightcurve 1 - Transient and Background
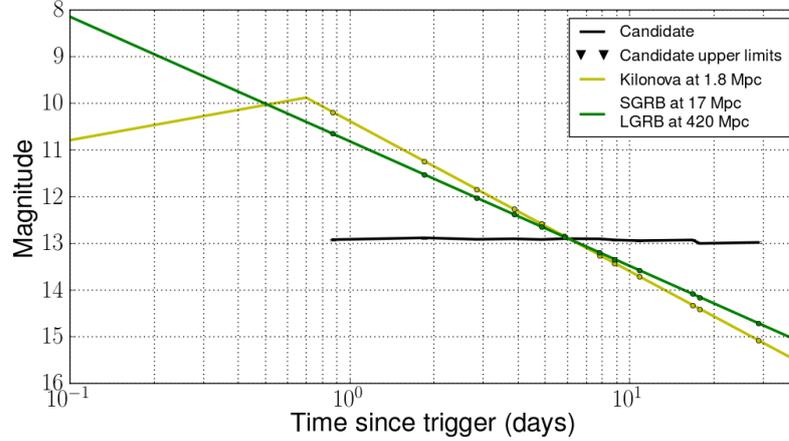
Lightcurve 2 - Transient with Background Subtracted

Figure A.3: The top figure shows the lightcurve of the G18666 candidate which includes the background and the bottom figure shows the lightcurve with the background subtracted. In each plot the candidate's data points and error bars are plotted in black. Open circles on the model lightcurves indicate times at which the transient was detected. If a candidate was not identified in a given image, an upper limit is shown. This reports the limiting magnitude of the image at the location of the candidate. For comparison we also show the model lightcurves for both kilonovae (equations (4.4) and (4.5)) and afterglows (equations (4.6) and (4.7) with an offset=0) scaled to source distances which produce the best match to the measured magnitudes of the candidate. The SGRB and LGRB models give identical lightcurves the source distance is different as shown. This candidate has a rank $R \simeq 1.0$.

G18666: Candidate 2

Lightcurve 1 - Transient and Background

Lightcurve 2 - Transient with Background Subtracted
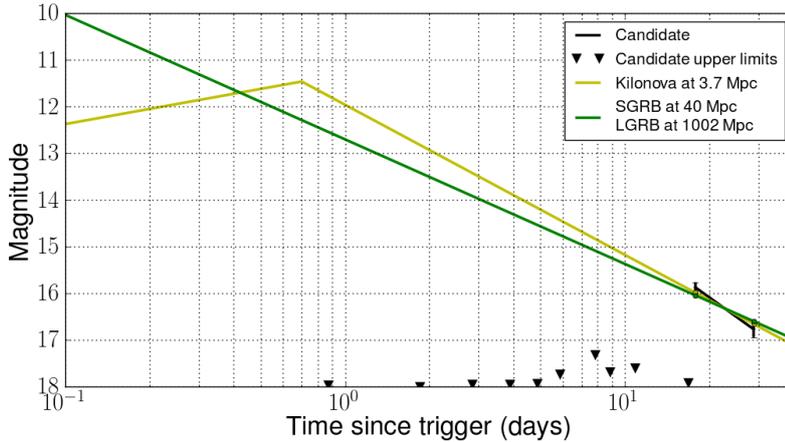
Figure A.4: The top figure shows the lightcurve of the G18666 candidate which includes the background and the bottom figure shows the lightcurve with the background subtracted. In each plot the candidate's data points and error bars are plotted in black. Open circles on the model lightcurves indicate times at which the transient was detected. If a candidate was not identified in a given image, an upper limit is shown. This reports the limiting magnitude of the image at the location of the candidate. For comparison we also show the model lightcurves for both kilonovae (equations (4.4) and (4.5)) and afterglows (equations (4.6) and (4.7) with an offset=0) scaled to source distances which produce the best match to the measured magnitudes of the candidate. The SGRB and LGRB models give identical lightcurves the source distance is different as shown. This candidate has a rank $R \simeq 0.3$.

G18666: Candidate 3

Lightcurve 1 - Transient and Background

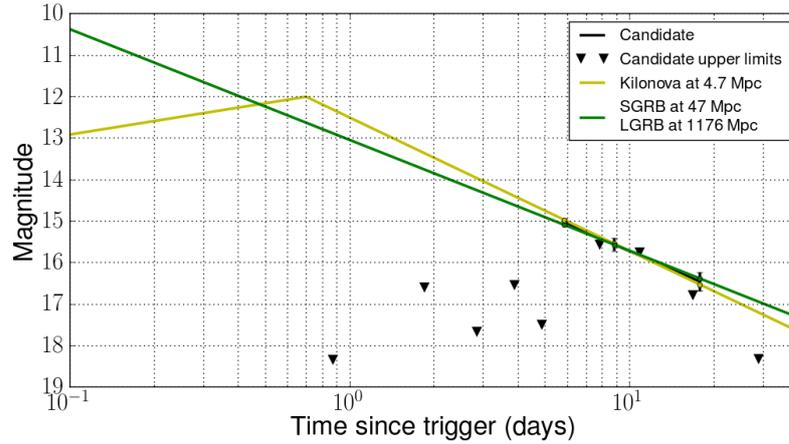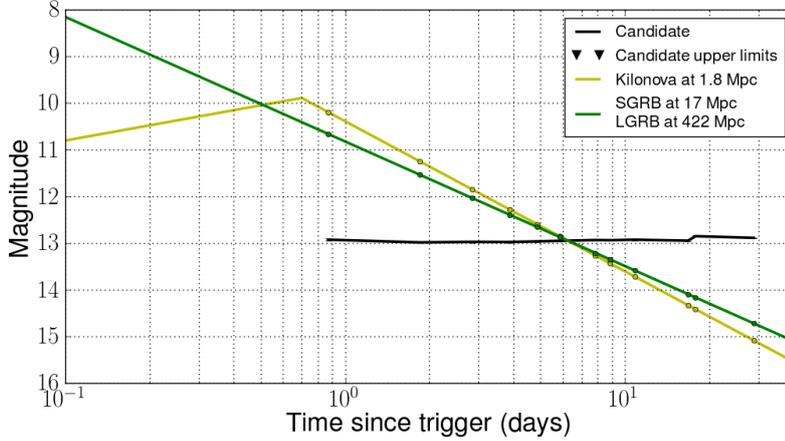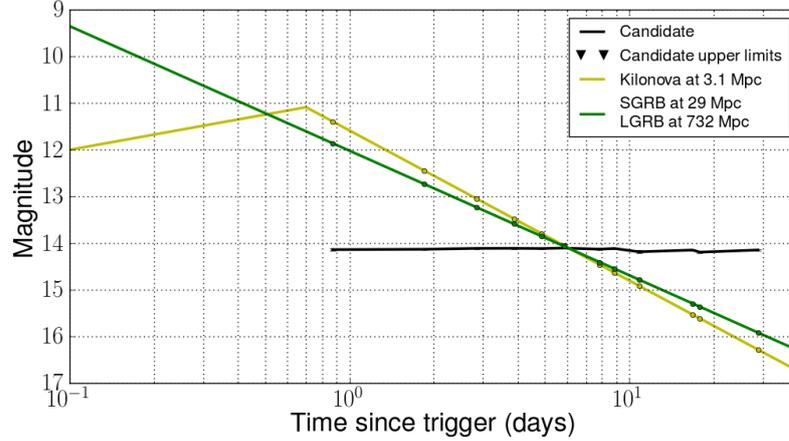
Lightcurve 2 - Transient with Background Subtracted
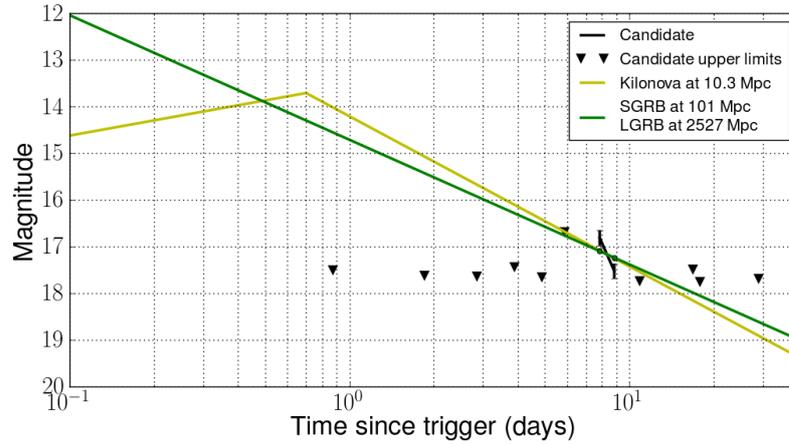
Figure A.5: The top figure shows the lightcurve of the G18666 candidate which includes the background and the bottom figure shows the lightcurve with the background subtracted. In each plot the candidate's data points and error bars are plotted in black. Open circles on the model lightcurves indicate times at which the transient was detected. If a candidate was not identified in a given image, an upper limit is shown. This reports the limiting magnitude of the image at the location of the candidate. For comparison we also show the model lightcurves for both kilonovae (equations (4.4) and (4.5)) and afterglows (equations (4.6) and (4.7) with an offset=0) scaled to source distances which produce the best match to the measured magnitudes of the candidate. The SGRB and LGRB models give identical lightcurves the source distance is different as shown. This candidate has a rank $R \simeq 0.2$.

when the magnitude on the second night is between 9.5-11.5. We are most sensitive to sources resembling a kilonova / SGRB / LGRB at distances of ~ 1 Mpc / 20 Mpc / 300 Mpc. The reason we do not reach an efficiency of 100% is either due to the background-subtracted lightcurve not being generated or due to the injections not always being placed at the same coordinates in each set of images (see Section 4.4.2 for details). With increasing distance/magnitude the efficiency begins to decrease until injected transients with a magnitude of 16, on the second night, are not found. In terms of distance, this means we cannot detect a transient which approximates a kilonova / SGRB / LGRB at $\gtrsim 20$ Mpc / 100 Mpc / 3 Gpc.

In an attempt to differentiate between all the identified injections and those which are the most interesting, i.e. those which have a high rank, Figure A.7 shows the fraction of injections which have a FAR ≤ 0.1 with distance and magnitude ($R \gtrsim 0.4$). These figures are essentially identical to Figure A.6, meaning that approximately all detected injections are favourably ranked compared to the background. This is due to the fact that the background distribution falls below FAR $\sim 10\%$ at very low rank, $R \gtrsim 0.4$.

Figure A.8 depicts the distribution of injections and the background with increasing distance. Plot (a) shows the injections made at the closest distances, i.e. kilonova $\simeq 0.4$ Mpc / SGRB $\simeq 3.3$ Mpc / LGRB $\simeq 84$ Mpc whereas plot (j) at the farthest distances i.e. kilonova $\simeq 30$ Mpc / SGRB $\simeq 250$ Mpc / LGRB $\simeq 6.3$ Gpc. When injections are made at a close distances (kilonova < 1 Mpc / SGRB < 8 Mpc / LGRB < 200 Mpc) their ranks are comparable to or greater than the loudest background events. However as the simulated transients are placed at greater distances and therefore dimmer magnitudes, their distributions fall within the background and the rank is no longer useful in separating the injections from the background.

G18666 Conclusions

ROTSE-IIIc followed up on event G18666 which occurred at 21:37:48 UTC on Sep 7, 2010. However a computer error meant the telescope was pointed to an incorrect point on the sky unassociated to this GW trigger. The images taken in response to this trigger were analysed as normal before this discovery was made. Investigations showed that should a kilonova (SGRB) within the region imaged by ROTSE the automated pipeline would be able to detect the source with 50% probability out to ~ 5 Mpc (45 Mpc). The pipeline would however miss the brightest LGRB within this distance due to the source saturating
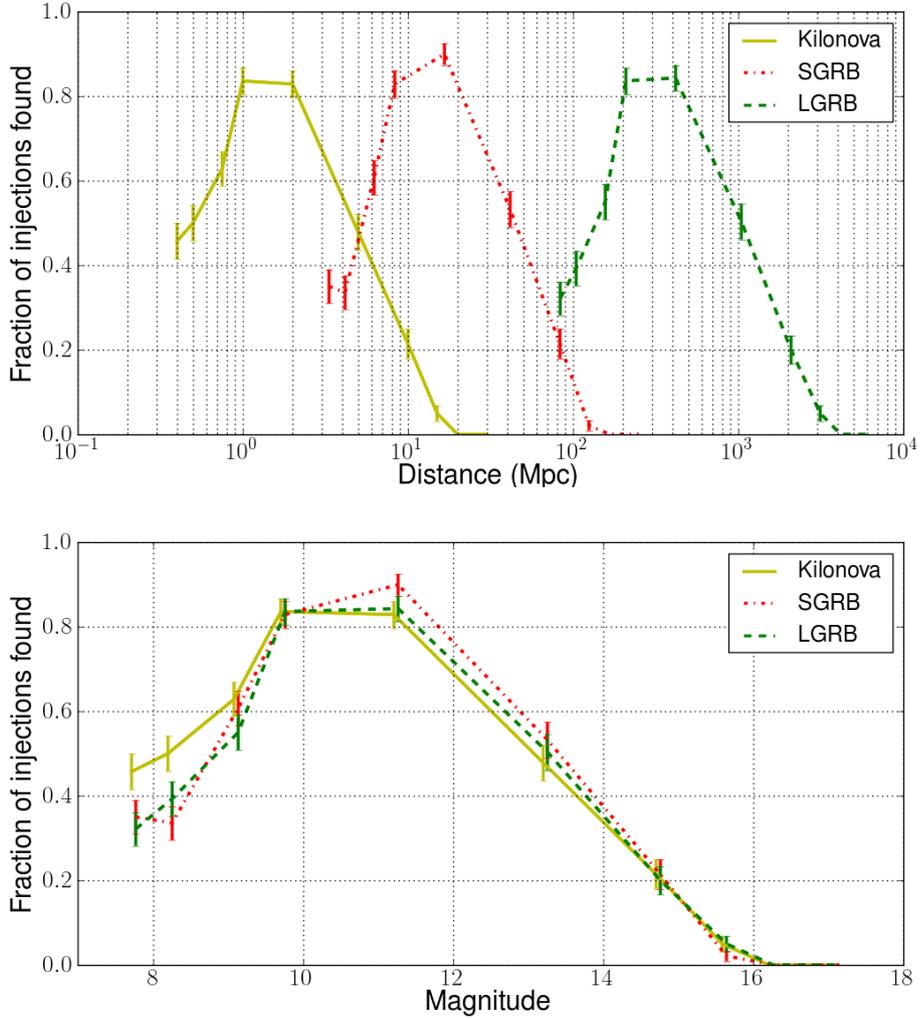
Figure A.6: G18666: Efficiency of finding simulated transients with $R > 0$ versus distance (top) and magnitude (1.5 days after the trigger time) (bottom). The distances quoted for the gamma-ray burst models assume the brightest afterglows from Kann et al. [133, 134] (i.e. offset $= 0$ in equations (4.6) and (4.7)) but could be smaller by a factor of up to 40. All the models suffer from poor efficiency at very close distances / low magnitudes due to saturation.
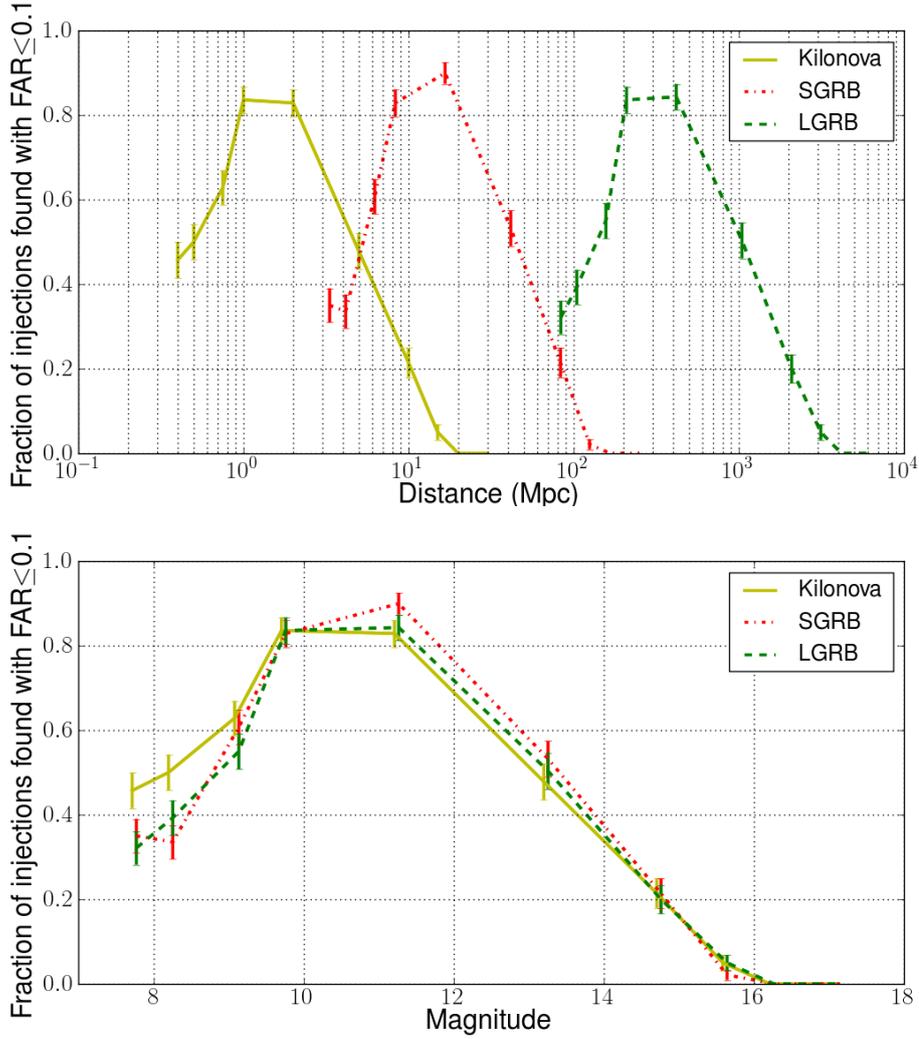
Figure A.7: G18666: Efficiency of injections found with a false alarm probability of ≤ 0.1 ($R \geq 1$). The injections performed for the SGRB and LGRB models show the largest distance possible; the numbers could be a factor 40 smaller. The distances for the GRB models assume the brightest afterglows from Kann et al. [133, 134] (i.e. offset $= 0$ in equations (4.6) and (4.7)).
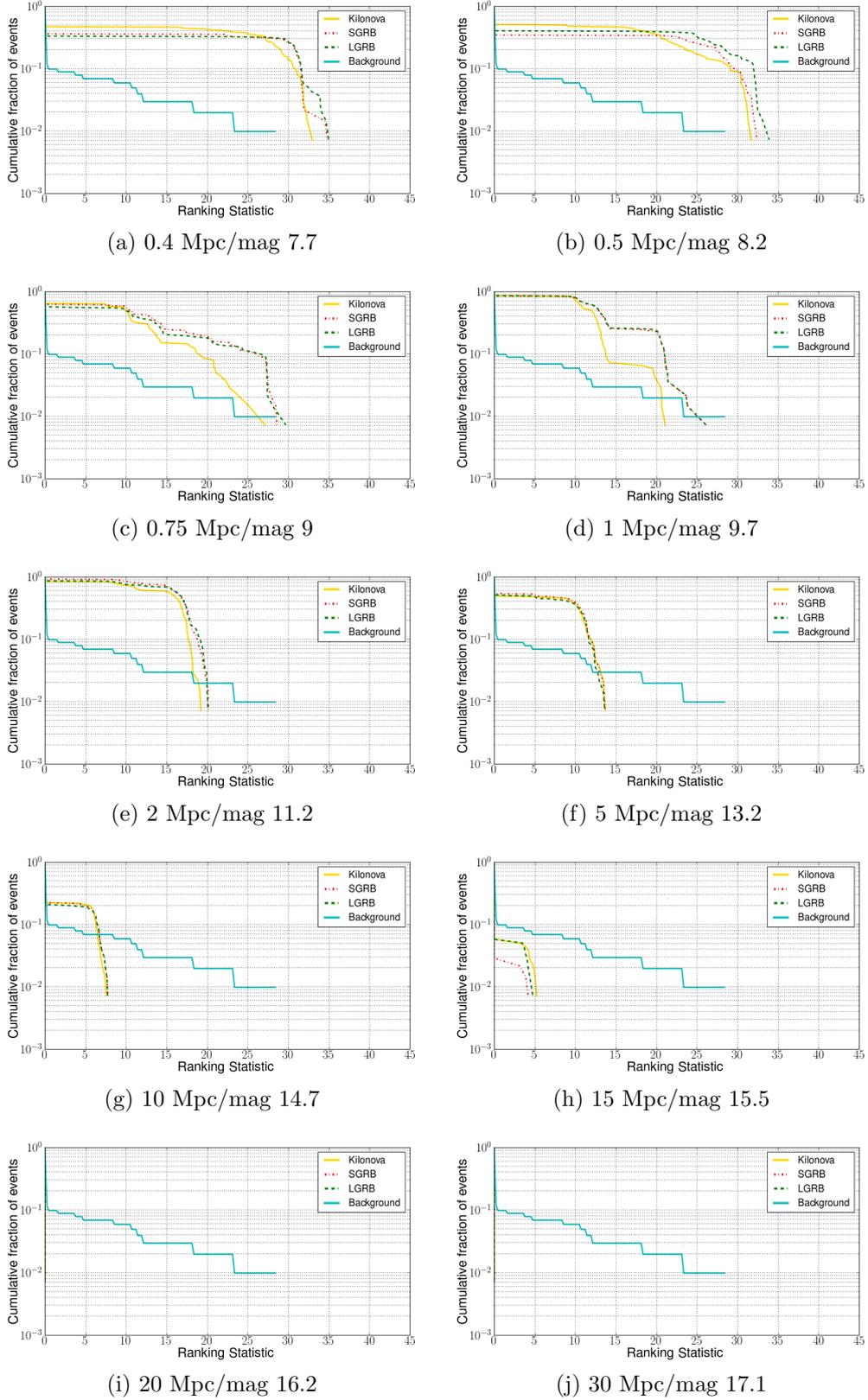
Figure A.8: G18666: The distribution of injections (kilonova-yellow, SGRB-red and LGRB-green) and background (cyan) at various distances and magnitudes (1.5 days after the trigger). Plot (a) kilonova $\simeq$ 0.4 Mpc / SGRB $\simeq$ 3.3 Mpc / LGRB $\simeq$ 80 Mpc, (b) kilonova $\simeq$ 0.5 Mpc / SGRB $\simeq$ 4 Mpc / LGRB $\simeq$ 100 Mpc etc. In these figures we assumed the GRB models to have the brightest afterglows from Kann et al. [133, 134] (i.e. offset = 0 in equations (4.6) and (4.7)). Therefore the GRB distances could be a factor 40 smaller.

the images and the pipeline discarding it. Three potential candidates were identified by the automated pipeline. The rank for each of these potential candidates was found and compared with that expected from background. The most significant potential candidate was found to be comparable to 10% of the background. The lightcurves for these three candidates were also generated and studied. They showed no evidence to be considered astrophysically interesting. Therefore we conclude that no significant EM candidates were found for event G18666 by the ROTSE telescope system.

Bibliography

[1] A. Einstein. The Formal Foundation of the General Theory of Relativity. *Sitzungsber. Preuss. Akad. Wiss. Berlin (Math. Phys.)*, 1914:1030–1085, 1914.

[2] A. Einstein. On the General Theory of Relativity. *Sitzungsber. Preuss. Akad. Wiss. Berlin (Math. Phys.)*, 1915:778–786, 1915.

[3] A. Einstein. The Field Equations of Gravitation. *Sitzungsber. Preuss. Akad. Wiss. Berlin (Math. Phys.)*, 1915:844–847, 1915.

[4] A. Einstein. Approximative Integration of the Field Equations of Gravitation. *Sitzungsber. Preuss. Akad. Wiss. Berlin (Math. Phys.)*, 1916:688–696, 1916.

[5] H. Bondi. Plane Gravitational Waves in General Relativity. *Nature*, 179:1072–1073, 1957.

[6] B.F. Schutz. *Gravity From the Ground Up*. Cambridge University Press, 2003.

[7] (ed.) I. Ciufolini, (ed.) V. Gorini, (ed.) U. Moschella, and (ed.) P. Fre. Gravitational Waves. Bristol, UK: IOP (2001) 412 p.

[8] R. A. Hulse and J. H. Taylor. Discovery of a Pulsar in a Binary System. *Astrophys. J.*, 195:L51–L53, 1975.

[9] J. M. Weisberg and J. H. Taylor. Relativistic Binary Pulsar B1913+16: Thirty Years of Observations and Analysis. *ASP Conf. Ser.*, 328:25, 2005.

[10] C. Kim, V. Kalogera, and D. R. Lorimer. Effect of PSR J0737-3039 on the DNS Merger Rate and Implications for GW Detection. *New Astron.Rev.*, 2006.

[11] M. Kramer, I. H. Stairs, R.N. Manchester, M.A. McLaughlin, A.G. Lyne, et al. Tests of General Relativity from Timing the Double Pulsar. *Science*, 314:97–102, 2006.

[12] J. Weber. Detection and Generation of Gravitational Waves. *Phys. Rev.*, 117:306, 1960.

[13] J. Weber. Evidence for Discovery of Gravitational Radiation. *Phys. Rev. Lett.*, 22:1320, 1969.

[14] Michele Maggiore. *Gravitational Waves*. Oxford University Press, 2008.

[15] C.W. Misner, K.S. Thorne, and J.A. Wheeler. *Gravitation*. Freeman, 1973.

[16] B.F. Schutz. *A First Course in General Relativity*. Cambridge University Press, 1985.

[17] W. Rindler. *Relativity*. Oxford University Press, Second edition, 2006.

[18] Polarisations. *http://www.itp.uzh.ch/ chuwyler/gravwaves/polarisations2.png*, 2013.

[19] B.S. Sathyaprakash and B.F. Schutz. Physics, Astrophysics and Cosmology with Gravitational Waves. *Living Rev.Rel.*, 12:2, 2009.

[20] L. Blanchet, T. Damour, G. Esposito-Farese, and B. R. Iyer. Gravitational Radiation from Inspiralling Compact Binaries Completed at the Third Post-Newtonian Order. *Phys.Rev.Lett.*, 93:091101, 2004.

[21] C. D. Ott. The Gravitational Wave Signature of Core-Collapse Supernovae. *Class. Quant. Grav.*, 26:063001, 2009.

[22] J. Abadie et al. Search for Gravitational Waves from Low Mass Compact Binary Coalescence in LIGO's Sixth Science Run and Virgo's Science Runs 2 and 3. *Phys.Rev.*, D85:082002, 2012.

[23] M. B. Davies, A. King, S. Rosswog, and G. Wynn. Gamma-Ray Bursts, Supernova Kicks, and Gravitational Radiation. *Astrophys.J.*, 579:L63–L66, 2002.

[24] S. Woosley and A. Heger. The Progenitor Stars of Gamma-Ray Bursts. *Astrophys.J.*, 637:914–921, 2006.

[25] S.E. Woosley and J.S. Bloom. The Supernova Gamma-Ray Burst Connection. *Ann.Rev.Astron.Astrophys.*, 44:507–556, 2006.

[26] C.D. Ott, C. Reisswig, E. Schnetter, E. O'Connor, U. Sperhake, et al. Dynamics and Gravitational Wave Signature of Collapsar Formation. *Phys.Rev.Lett.*, 106:161103, 2011.

[27] G.A. Tammann, W. Loeffler, and A. Schroder. The Galactic Supernova Rate. *Astrophys.J.Suppl.*, 92:487–493, 1994.

[28] E. Cappellaro, R. Evans, and M. Turatto. A New Determination of Supernova Rates and a Comparison with Indicators for Galactic Star Formation. *Astron.Astrophys.*, 351:459, 1999.

[29] B.P. Abbott et al. Search for Gravitational-Wave bursts Associated with Gamma-Ray Bursts using Data from LIGO Science Run 5 and Virgo Science Run 1. *Astrophys.J.*, 715:1438–1452, 2010.

[30] B.P. Abbott et al. Stacked Search for Gravitational Waves from the 2006 SGR 1900+14 Storm. *Astrophys.J.*, 701:L68–L74, 2009.

[31] J. Abadie et al. All-sky Search for Gravitational-Wave Bursts in the First Joint LIGO-GEO-Virgo Run. *Phys.Rev.*, D81:102001, 2010.

[32] J. Abadie et al. All-sky Search for Periodic Gravitational Waves in the Full S5 LIGO Data. *Phys.Rev.*, D85:022001, 2012.

[33] M.S. Briggs et al. Search for Gravitational Waves Associated with Gamma-Ray Bursts during LIGO Science Run 6 and Virgo Science Runs 2 and 3. *Astrophys.J.*, 760:12, 2012.

[34] J. Abadie et al. Predictions for the Rates of Compact Binary Coalescences Observable by Ground-based Gravitational-Wave Detectors. *Class. Quant. Grav.*, 27(17):173001, 2010.

[35] J. Abadie et al. Search for Gravitational Waves from Compact Binary Coalescence in LIGO and Virgo Data from S5 and VSR1. *Phys.Rev.*, D82:102001, 2010.

[36] J. Abadie et al. Search for Gravitational-Wave Inspiral Signals Associated with Short Gamma-Ray Bursts During LIGO's Fifth and Virgo's First Science Run. *Astrophys.J.*, 715:1453–1461, 2010.

[37] J. Aasi et al. Search for Gravitational Waves from Binary Black Hole Inspiral, Merger and Ringdown in LIGO-Virgo Data from 2009-2010. *arXiv:1209.6533*, 2012.

[38] B. Abbott et al. Beating the Spin-down Limit on Gravitational Wave Emission from the Crab Pulsar. *Astrophys.J.*, 683:L45–L50, 2008.

[39] P. Jaranowski, A. Krolak, and B. F. Schutz. Data Analysis of Gravitational - Wave Signals from Spinning Neutron Stars. 1. The Signal and its Detection. *Phys.Rev.*, D58:063001, 1998.

[40] B.P. Abbott et al. Searches for Gravitational Waves from Known Pulsars with S5 LIGO Data. *Astrophys.J.*, 713:671–685, 2010.

[41] J. Abadie et al. First Search for Gravitational Waves from the Youngest Known Neutron Star. *Astrophys.J.*, 722:1504–1513, 2010.

[42] J. Aasi et al. Einstein@Home All-sky Search for Periodic Gravitational Waves in LIGO S5 Data. *Phys. Rev. D 87,*, 042001, 2013.

[43] Michele Maggiore. Gravitational Wave Experiments and Early Universe Cosmology. *Phys.Rept.*, 331:283–367, 2000.

[44] J. Abadie et al. Upper Limits on a Stochastic Gravitational-Wave Background using LIGO and Virgo Interferometers at 600-1000 Hz. *Phys.Rev.*, D85:122001, 2012.

[45] B. Allen. The Stochastic Gravity Wave Background: Sources and Detection. *arXiv:9604033*, 1996.

[46] B. Abbott et al. Searching for a Stochastic Background of Gravitational Waves with LIGO. *Astrophys.J.*, 659:918–930, 2007.

[47] B.P. Abbott et al. An Upper Limit on the Stochastic Gravitational-Wave Background of Cosmological Origin. *Nature*, 460:990, 2009.

[48] J. Abadie, B.P. Abbott, R. Abbott, M. Abernathy, T. Accadia, et al. Directional Limits on Persistent Gravitational Waves using LIGO S5 Science Data. *Phys.Rev.Lett.*, 107:271102, 2011.

[49] P. Astone, R. Ballantini, D. Babusci, M. Bassan, P. Bonifazi, et al. EXPLORER and NAUTILUS Gravitational Wave Detectors: A Status Report. *Class.Quant.Grav.*, 25:114048, 2008.

[50] B. F. Schutz. Gravitational Wave Astronomy. *Class. Quant. Grav.*, 16:A131–A156, 1999.

[51] B. Abbott et al. LIGO: The Laser Interferometer Gravitational-Wave Observatory. *Rept. Prog. Phys.*, 72:076901, 2009.

[52] F. Acernese et al. Status of Virgo. *Class. Quant. Grav.*, 25:114045, 2008.

[53] B. Willke et al. GEO600: Status and Plans. *Class.Quant.Grav.*, 24:S389–S397, 2007.

[54] M. Ando et al. Current Status of TAMA. *Class.Quant.Grav.*, 19:1409–1419, 2002.

[55] The LIGO Scientific Collaboration. Best Strain Sensitivities for the LIGO Interferometers . *http://www.ligo.caltech.edu/docs/G/G060009-03/G060009-03.pdf*, 2007.

[56] G. M. Harry. Advanced LIGO: The Next Generation of Gravitational Wave Detectors. *Class. Quant. Grav.*, 27:084006, 2010.

[57] F. Acernese et al. Advanced Virgo Baseline Design. 2009. https://pub3.ego-gw.it/codier/includes/showTmpFile.php?doc=2219&calledFile=VIR-027A-09.pdf.

[58] J. Aasi et al. Prospects for Localization of Gravitational Wave Transients by the Advanced LIGO and Advanced Virgo Observatories. *arXiv:1304.0670*, 2013.

[59] R. Adhikari, P. Fritschel, and S. Waldman. Enhanced LIGO. *LIGO Technical Document LIGO-T060156*, http://www.ligo.caltech.edu/docs/T/T060156-01.pdf.

[60] J. R Smith. The Path to the Enhanced and Advanced LIGO Gravitational- Wave Detectors. *Class. Quant. Grav.*, 26:114013, 2009.

[61] T. T. Fricke, N. D. Smith-Lefebvre, R. Abbott, R. Adhikari, K. L. Dooley, et al. DC Readout Experiment in Enhanced LIGO. *Class.Quant.Grav.*, 29:065005, 2012.

[62] P. Fritschel, R. Bork, G. Gonzalez, N. Mavalvala, D. Ouimette, H. Rong, D. Sigg, and M. Zucker. Readout and Control of a Power-Recycled

Interferometric Gravitational-Wave Antenna. *Appl. Opt.*, 40:4988–98, 2001.

[63] K. McKenzie, M.B. Gray, P.K. Lam, and D.E. McClelland. Technical Limitations to Homodyne Detection at Audio Frequencies. *Appl. Opt.*, 17:3389–3395, 2007.

[64] P.R. Saulson. *Fundamentals of Interferometric Gravitational Wave Detectors*. World Scientific, 1994.

[65] S. A. Hughes. Listening to the Universe with Gravitational-Wave Astronomy. *Annals Phys.*, 303:142–178, 2003.

[66] K. Kuroda et al. Status of LCGT. *Class. Quant. Grav.*, 27(8):084004, 2010.

[67] Gravitational Wave Astronomy in Space: eLISA/NGO. 2013. http://www.elisa-ngo.org/.

[68] J. R. Smith, T. Abbott, E. Hirose, N. Leroy, D. Macleod, et al. A Hierarchical Method for Vetoing Noise Transients in Gravitational-Wave Detectors. *Class.Quant.Grav.*, 28:235005, 2011.

[69] D.M. MacLeod, S. Fairhurst, B. Hughey, A.P. Lundgren, L. Pekowsky, et al. Reducing the Effect of Seismic Noise in LIGO Searches by Targeted Veto Generation. *Class.Quant.Grav.*, 29:055006, 2012.

[70] J. Aasi et al. The Characterization of Virgo Data and its Impact on Gravitational-Wave Searches. *Class.Quant.Grav.*, 29:155002, 2012.

[71] J. Aasi et al. Characterization of the LIGO Detectors During their Sixth Science Run. 2013. In Preparation.

[72] S. Fairhurst. Triangulation of Gravitational Wave Sources with a Network of Detectors. *New J. Phys.*, 11:123006, 2009.

[73] A. K. Leroy, F. Bigiel, W.J.G. de Blok, S. Boissier, A. Bolatto, et al. Estimating the Star Formation Rate at 1 kpc Scales in Nearby Galaxies. *Astron.J.*, 144:3, 2012.

[74] R. C. Kennicutt Jr. and II Evans, N. J. Star Formation in the Milky Way and Nearby Galaxies. *Annu. rev. astron. astrophys.*, 50:531–608, 2012.

[75] J.S. Bloom, J.X. Prochaska, D. Pooley, C.W. Blake, R.J. Foley, et al. Closing in on a Short-hard Burst Progenitor: Constraints from Early-time Optical Imaging and Spectroscopy of a Possible Host Galaxy of GRB 050509b. *Astrophys.J.*, 638:354–368, 2006.

[76] E. Nakar. Short-Hard Gamma-Ray Bursts. *Physics Reports*, 442:166, 2007.

[77] A. M. Soderberg, E. Berger, M. Kasliwal, D.A. Frail, P.A. Price, et al. The Afterglow and Host Galaxy of the Energetic Short-hard Gamma-Ray Burst 051221. *Astrophys.J.*, 650:261–271, 2006.

[78] E. Berger, P.A. Price, S.B. Cenko, A. Gal-Yam, A.M. Soderberg, et al. The Afterglow and Elliptical Host Galaxy of the Short Gamma-Ray Burst GRB 050724. *Nature*, 438:988–990, 2005.

[79] E. Berger. The Environments of Short-Duration Gamma-Ray Bursts and Implications for their Progenitors. *New Astron.Rev.*, 55:1–22, 2011.

[80] R. C. Duncan and C. Thompson. Formation of Very Strongly Magnetized Neutron Stars - Implications for Gamma-Ray Bursts. *Astrophys.J.*, 392:L9, 1992.

[81] A. Krolak and B.F. Schutz. Coalescing binaries - probe to the universe. *General Relativity and Gravitation*, 19:1163, 1987.

[82] D. E. Holz and S. A. Hughes. Using Gravitational-Wave Standard Sirens. *Astrophys. J.*, 629:15–22, 2005.

[83] S. Nissanke, D. E. Holz, S. A. Hughes, N. Dalal, and J. L. Sievers. Exploring Short Gamma-Ray Bursts as Gravitational-Wave Standard Sirens. *Astrophys.J.*, 725:496–514, 2010.

[84] J. S. Bloom et al. Astro2010 Decadal Survey Whitepaper: Co-ordinated Science in the Gravitational and Electromagnetic Skies. *arXiv:0902.1527*, 2009.

[85] K. Kotake, T. Takiwaki, Y. Suwa, W. I. Nakano, S. Kawagoe, et al. Multimessengers from Core-collapse Supernovae: Multidimensionality as a Key to Bridge Theory and Observation. *Adv.Astron.*, 2012:428757, 2012.

[86] B. F Schutz. Determining the Hubble Constant from Gravitational Wave Observations. *Nature*, 323:310–311, 1986.

[87] B. F. Schutz. Networks of Gravitational Wave Detectors and Three Figures of Merit. *Class.Quant.Grav.*, 28:125023, 2011.

[88] J. Sylvestre. Prospects for the Detection of Electromagnetic Counterparts to Gravitational Wave Events. *Astrophys.J.*, 591:1152–1156, 2003.

[89] E.S. Phinney. Finding and Using Electromagnetic Counterparts of Gravitational Wave Sources. *arXiv:0903.0098*, 2009.

[90] M. Stamatikos, N. Gehrels, F. Halzen, P. Meszaros, and P.W.A. Roming. Multi-Messenger Astronomy with GRBs: A White Paper for the Astro2010 Decadal Survey. *arXiv:0902.3022*, 2009.

[91] L. Blanchet. Gravitational Radiation from Post-Newtonian Sources and Inspiralling Compact Binaries. *Living Reviews in Relativity*, 5(3), 2002.

[92] E. Berger. The Prompt Gamma-Ray and Afterglow Energies of Short-Duration Gamma-Ray Bursts. *Astrophys. J.*, 670:1254, 2007.

[93] T. Piran, E. Nakar, and S. Rosswog. The Electromagnetic Signals of Compact Binary Mergers. *arXiv:1204.6242*, 2012.

[94] S. Rosswog, T. Piran, and E. Nakar. The Multi-messenger Picture of Compact Object Encounters: Binary Mergers Versus Dynamical Collisions. *arXiv:1204.6240*, 2012.

[95] L.X. Li and B. Paczynski. Transient Events from Neutron Star Mergers. *Astrophys.J.*, 507:L59, 1998.

[96] S.R. Kulkarni. Modeling Supernova-like Explosions Associated with Gamma-Ray Bursts with Short Durations. *arXiv:0510256*, 2005.

[97] B. D. Metzger et al. Electromagnetic Counterparts of Compact Object Mergers Powered by the Radioactive Decay of R-process Nuclei. *arXiv:1001.5029*, 2010.

[98] B. Zhang. Early X-ray and Optical Afterglow of Gravitational Wave Bursts from Mergers of Binary Neutron Stars. *arXiv:1212.0773*, 2012.

[99] B.D. Metzger, D. Giannios, T.A. Thompson, N. Bucciantini, and E. Quataert. The Proto-Magnetar Model for Gamma-Ray Bursts. *arXiv:1012.0001*, 2010.

[100] J. Abadie, B. P. Abbott, R. Abbott, T. D. Abbott, M. Abernathy, T. Accadia, F. Acernese, C. Adams, R. X. Adhikari, C. Affeldt, and et al. Search for Gravitational Waves Associated with Gamma-Ray Bursts during LIGO Science Run 6 and Virgo Science Runs 2 and 3. *Astrophys.J.*, 760:12, 2012.

[101] A. Corsi and P. Meszaros. GRB Afterglow Plateaus and Gravitational Waves: Multi-messenger Signature of a Millisecond Magnetar? *Astrophys.J.*, 702:1171–1178, 2009.

[102] A. L. Piro and E. Pfahl. Fragmentation of Collapsar Disks and the Production of Gravitational Waves. *Astrophys.J.Lett.*, 2006.

[103] M. Shibata, S. Karino, and Y. Eriguchi. Dynamical Bar-mode Instability of Differentially Rotating Stars: Effects of Equations of State and Velocity Profiles. *Mon.Not.Roy.Astron.Soc.*, 343:619, 2003.

[104] D. Guetta and T. Piran. The BATSE-Swift Luminosity and Redshift Distributions of Short-duration GRBs. *Astron.Astrophys.*, 2005.

[105] P. Meszaros. Gamma-Ray Bursts. *Rept.Prog.Phys.*, 69:2259–2322, 2006.

[106] E. Costa, F. Frontera, J. Heise, M. Feroci, J.J.M. Zand, et al. Discovery of the X-ray Afterglow of the Gamma-Ray Burst of February 28 1997. *Nature*, 1997.

[107] C. Kouveliotou, C. A. Meegan, G. J. Fishman, N. P. Bhyat, M. S. Briggs, et al. Identification of Two Classes of Gamma Ray Bursts. *Astrophys.J.*, 413:L101–104, 1993.

[108] J. Hjorth, D. Watson, J. P.U. Fynbo, P. A. Price, B. L. Jensen, et al. The Optical Afterglow of the Short Gamma-Ray Burst GRB 050709. *Nature*, 437:859–861, 2005.

[109] N. Gehrels, J.P. Norris, V. Mangano, S.D. Barthelmy, D. N. Burrows, et al. Swift Detects a Remarkable Gamma-Ray Burst, GRB 060614, that Introduces a New Classification Scheme. *Nature*, 444:1044, 2006.

[110] D. A. Kann. Multi-Wavelength Observations of Short-Duration Gamma-Ray Bursts: Recent Results. *arXiv:1212.0040*, 2012.

[111] B. Paczynski. Gamma-Ray Bursters at Cosmological Distances. *Astrophys.J.*, 308:L43–L46, 1986.

[112] D. Eichler, M. Livio, T. Piran, and D. N. Schramm. Nucleosynthesis, Neutrino Bursts and Gamma-Rays from Coalescing Neutron Stars. *Nature*, 340:126–128, 1989.

[113] L. Rezzolla, B. Giacomazzo, L. Baiotti, J. Granot, C. Kouveliotou, et al. The Missing Link: Merging Neutron Stars Naturally Produce Jet-like Structures and Can Power Short Gamma-Ray Bursts. *Astrophys.J.*, 732:L6, 2011.

[114] M. Shibata, M. D. Duez, Y. T. Liu, S. L. Shapiro, and B. C. Stephens. Magnetized Hypermassive Neutron Star Collapse: A Central Engine for Short Gamma-Ray Bursts. *Phys.Rev.Lett.*, 96:031102, 2006.

[115] M. D. Duez, Y. T. Liu, S. L. Shapiro, M. Shibata, and B. C. Stephens. Collapse of Magnetized Hypermassive Neutron Stars in General Relativity. *Phys.Rev.Lett.*, 96:031101, 2006.

[116] M. Shibata and K. Taniguchi. Merger of Black Hole and Neutron Star in General Relativity: Tidal Disruption, Torus Mass, and Gravitational Waves. *Phys.Rev.*, D77:084015, 2008.

[117] M. Shibata and K. Taniguchi. Merger of Binary Neutron Stars to a Black Hole: Disk Mass, Short Gamma-Ray Bursts, and Quasinormal Mode Ringing. *Phys.Rev.*, D73:064027, 2006.

[118] B. Zhang and P. Meszaros. Gamma-Ray Bursts: Progress, Problems & Prospects. *Int.J.Mod.Phys.*, A19:2385–2472, 2004.

[119] D. N. Burrows, D. Grupe, M. Capalbi, A. Panaitescu, S. K. Patel, et al. Jet Breaks in Short Gamma-Ray Bursts. II: The Collimated Afterglow of GRB 051221A. *Astrophys.J.*, 653:468–473, 2006.

[120] E. Nakar, A. Gal-Yam, and D. B. Fox. The Local Rate and the Progenitor Lifetimes of Short-Hard Gamma-Ray Bursts: Synthesis and Predictions for LIGO. *Astrophys. J.*, 650:281–290, 2006.

[121] K. Hurley, E. Bellm, D. Perley, I.G. Mitrofanov, D.V. Golovin, et al. A New Analysis of the Short-duration, Hard-spectrum GRB 051103, a Possible Extragalactic SGR Giant Flare. *MNRAS*, 403:342, 2010.

[122] D. Guetta and L. Stella. Short Gamma-Ray Bursts and Gravitational Waves from Dynamically Formed Merging Binaries. *A&A*, 498:329, 2009.

[123] B. D. Metzger and E. Berger. What is the Most Promising Electromagnetic Counterpart of a Neutron Star Binary Merger? *Astrophys.J.*, 746:48, 2012.

[124] N. Gehrels et al. The Swift Gamma-Ray Burst Mission. *Astrophys.J.*, 611:1005–1020, 2004.

[125] C. Meegan, G. Lichti, P.N. Bhat, E. Bissaldi, M. S. Briggs, et al. The Fermi Gamma-Ray Burst Monitor. *Astrophys.J.*, 702:791–804, 2009.

[126] H. Chen and D.E. Holz. GRB Beaming and Gravitational-Wave Observations. *arXiv:1206.0703*, 2012.

[127] L.Z. Kelley, I. Mandel, and Enrico Ramirez-Ruiz, E. Electromagnetic Transients as Triggers in Searches for Gravitational Waves from Compact Binary Mergers. *arXiv:1209.3027*, 2012.

[128] H.J. van Eerten, A.J. van der Horst, and A.I. MacFadyen. Gamma-ray Burst Afterglow Broadband Fitting Based Directly on Hydrodynamics Simulations. *Astrophys.J.*, 749:44, 2012.

[129] E. Berger, D. B. Fox, S.R. Kulkarni, W. Krzeminski, A.M. Soderberg, et al. The Discovery of the Optical and Near-IR Afterglows of the First SWIFT Gamma-Ray Bursts. *Astrophys.J.*, 629:328–333, 2005.

[130] P. Jakobsson, A. Levan, J.P.U. Fynbo, R. Priddey, J. Hjorth, et al. A Mean Redshift of 2.8 for Swift Gamma-Ray Bursts. *Astron.Astrophys.*, 447:897–903, 2006.

[131] Z. Bagoly, A. Meszaros, L.G. Balazs, I. Horvath, S. Klose, et al. The Swift Satellite and Redshifts of Long Gamma-Ray Bursts. *Astron.Astrophys.*, 453:797–800, 2006.

[132] F. Fiore, D. Guetta, S. Piranomonte, V. D'Elia, and L.A. Antonelli. Selection Effects Shaping the Gamma Ray Burst Redshift Distributions. *A&A*, 470:515–522, 2007.

[133] D.A. Kann, S. Klose, B. Zhang, D. Malesani, E. Nakar, et al. The Afterglows of Swift-era Gamma-Ray Bursts. I. Comparing pre-Swift and Swift era Long/Soft (Type II) GRB Optical Afterglows. *Astrophys.J.*, 720:1513–1558, 2010.

[134] D.A. Kann, S. Klose, B. Zhang, A.C. Wilson, N.R. Butler, et al. The Afterglows of Swift-era Gamma-Ray Bursts II.: Type I GRB versus Type II GRB Optical Afterglows. *Astrophys.J.*, 734:96, 2011.

[135] Pan-STARRS. *http://pan-starrs.ifa.hawaii.edu/public/home.html*, 2012.

[136] Z. Ivezic, J.A. Tyson, R. Allsman, J. Andrew, and R. Angel. LSST: from Science Drivers to Reference Design and Anticipated Data Products. *arXiv:0805.2366*, 2008.

[137] N.M. Law, S.R. Kulkarni, R.G. Dekany, E.O. Ofek, R.M. Quimby, et al. The Palomar Transient Factory: System Overview, Performance and First Results. *PASP*, 121:1395, 2009.

[138] E. Berger. A Short GRB "No-Host" Problem? Investigating Large Progenitor Offsets for Short GRBs with Optical Afterglows. *Astrophys.J.*, 722:1946–1961, 2010.

[139] W. Fong, E. Berger, R. Chornock, N. R. Tanvir, A. J. Levan, et al. The Optical Afterglow and z=0.92 Early-type Host Galaxy of the Short GRB 100117A. *Astrophys.J.*, 730:26, 2011.

[140] H. van Eerten, W. Zhang, and A. MacFadyen. Off-Axis Gamma-Ray Burst Afterglow Modeling Based On A Two-Dimensional Axisymmetric Hydrodynamics Simulation. *Astrophys.J.*, 722:235–247, 2010.

[141] H.J. van Eerten and A.I. MacFadyen. Synthetic Off-axis Light Curves for Low Energy Gamma-Ray Bursts. *ApJ*, 722:L37, 2011.

[142] J. Moortgat and J. Kuijpers. Gravitational and Magnetosonic Waves in Gamma-Ray Bursts. *Astron.Astrophys.*, 402:905–911, 2003.

[143] V. Predoi, J. Clark, T. Creighton, E. Daw, S. Fairhurst, et al. Prospects for Joint Radio Telescope and Gravitational Wave Searches for Astrophysical Transients. *Class.Quant.Grav.*, 27:084018, 2010.

[144] V. M. Lipunov and I. E. Panchenko. Pulsars Revived by Gravitational Waves. *Astron.Astrophys.*, 312:937, 1996.

[145] B. Zhang, Y.Z. Fan, J. Dyks, S. Kobayashi, P. Meszaros, et al. Physical Processes Shaping GRB X-ray Afterglow Lightcurves: Theoretical Implications from the SWIFT XRT Observations. *Astrophys.J.*, 642:354–370, 2006.

[146] D. Kasen and S.E. Woosley. Type II Supernovae: Model Light Curves and Standard Candle Relationships. *Astrophys.J.*, 703:2205–2216, 2009.

[147] D. Richardson, D. Branch, D. Casebeer, J. Millard, R.C. Thomas, et al. A Comparative Study of the Absolute-magnitude Distributions of Supernovae. *Astron.J.*, 123:745–752, 2002.

[148] D.A. Perley, B.D. Metzger, J. Granot, N.R. Butler, T. Sakamoto, et al. GRB 080503: Implications of a Naked Short Gamma-Ray Burst Dominated by Extended Emission. *Astrophys.J.*, 696:1871–1885, 2009.

[149] S. Adrian-Martinez et al. A First Search for coincident Gravitational Waves and High Energy Neutrinos using LIGO, Virgo and ANTARES data from 2007. *arXiv:1205.3018*, 2012.

[150] B. Abbott et al. Search for Gravitational Wave Radiation Associated with the Pulsating Tail of the SGR 1806-20 Hyperflare of 27 December 2004 using LIGO. *Phys.Rev.*, D76:062003, 2007.

[151] B. Abbott et al. Search for Gravitational Wave Bursts from Soft Gamma Repeaters. *Phys.Rev.Lett.*, 101:211102, 2008.

[152] J. Abadie et al. Search for Gravitational Wave Bursts from Six Magnetars. *Astrophys.J.*, 734:L35, 2011.

[153] J. Abadie et al. A Search for Gravitational Waves Associated with the August 2006 Timing Glitch of the Vela Pulsar. *Phys.Rev.*, D83:042001, 2011.

[154] J. Abadie et al. Beating the Spin-down Limit on Gravitational Wave Emission from the Vela Pulsar. *Astrophys.J.*, 737:93, 2011.

[155] B. Abbott et al. Search for Gravitational Waves Associated with 39 Gamma-Ray Bursts using Data from the Second, Third, and Fourth LIGO runs. *Phys.Rev.*, D77:062004, 2008.

[156] B. Abbott et al. A Search for Gravitational Waves Associated with the Gamma Ray Burst GRB030329 using the LIGO Detectors. *Phys.Rev.*, D72:042002, 2005.

[157] J. Abadie et al. Implications For The Origin Of GRB 051103 From LIGO Observations. *Astrophys.J.*, 755:2, 2012.

[158] B. Abbott et al. Implications for the Origin of GRB 070201 from LIGO Observations. *Astrophys.J.*, 681:1419–1428, 2008.

[159] J. Kanner et al. LOOC UP: Locating and Observing Optical Counterparts to Gravitational Wave Bursts. *Class. Quant. Grav.*, 25:184034, 2008.

[160] J. Abadie et al. Implementation and Testing of the First Prompt Search for Electromagnetic Counterparts to Gravitational Wave Transients. *A&A*, 539:A124, 2011.

[161] S. Klimenko, G. Vedovato, M. Drago, G. Mazzolo, G. Mitselmakher, et al. Localization of Gravitational Wave Sources with Networks of Advanced Detectors. *Phys.Rev.*, D83:102001, 2011.

[162] F. Marion et al. *Proceedings of Rencontres de Moriond 2003, Gravitational Waves and Experimental Gravity*, 2004.

[163] D.J. White, E.J. Daw, and V.S. Dhillon. A List of Galaxies for Gravitational Wave Searches. *Class.Quant.Grav.*, 28:085016, 2011.

[164] M. Katarzyna et al. General Overview of the "Pi of the Sky" System. *Proceedings of SPIE*, 7502:75020D, 2009.

[165] C. Baltay, D. Rabinowitz, P. Andrews, A. Bauer, N. Ellman, W. Emmet, R. Hudson, T. Hurteau, J. Jerke, R. Lauer, J. Silge, A. Szymkowiak, B. Adams, M. Gebhard, J. Musser, M. Doyle, H. Petrie, R. Smith, R. Thicksten, and J. Geary. The QUEST Large Area CCD Camera. *PASP*, 119(861):1278–1294, 2007.

[166] C.W. Akerlof, M.C.B. Ashley, D.E. Casperson, H.W. Epps, R.L. Kehoe, et al. The ROTSE-III Robotic Telescope System. *Publ.Astron.Soc.Pac.*, 115:132–140, 2003.

[167] S.C. Keller et al. The SkyMapper Telescope and The Southern Sky Survey. *PASA*, 24:1–12, 2007.

[168] A. Klotz, M. Boer, J. L. Atteia, and B. Gendre. Early Optical Observations of Gamma-Ray Bursts by the TAROT Telescopes: Period 2001-2008. *The Astronomical Journal*, 137(5):4100, 2009.

[169] D. M. Coward et al. The Zadko Telescope: A Southern Hemisphere Telescope for Optical Transient Searches, Multi-Messenger Astronomy and Education. *arXiv:1006.3933*, 2010.

[170] I. A. Steele et al. The Liverpool Telescope: Performance and First Results. *Proceedings of SPIE*, 5489:679–692, 2004.

[171] R. Fender, R. Wijers, B. Stappers, et al. The LOFAR Transients Key Project. *Proceedings of Science*, MQW6:104, 2006.

[172] R. A. Perley, C. J. Chandler, B. J. Butler, and J. M. Wrobel. The Expanded Very Large Array – a New Telescope for New Science. *arXiv:1106.0532*, 2011.

[173] Aasi et al. First Searches for Optical Counterparts to Gravitational-Wave Candidate Events, 2013. In Preparation.

[174] P.A. Evans et al. Swift Follow-up Observations of Candidate Gravitational-Wave Transient Events. *Astrophys.J.Suppl.*, 203:28, 2012.

[175] J. Lazio, K. Keating, F.A. Jenet, and N.E. Kassim. Search for Electromagnetic Counterparts to LIGO-Virgo Candidates: Expanded Very Large Array. *arXiv:1203.0093*, 2012.

[176] L.S. Finn and D.F. Chernoff. Observing Binary Inspiral in Gravitational Radiation: One Interferometer. *Phys. Rev. D*, 47(6):2198–2219, Mar 1993.

[177] Y. Guersel and M. Tinto. Near Optimal Solution to the Inverse Problem for Gravitational Wave Bursts. *Phys. Rev.*, D40:3884–3938, 1989.

[178] L. Wen and B. F. Schutz. Coherent Network Detection of Gravitational Waves: The Redundancy Veto. *Class. Quant. Grav.*, 22:S1321–S1336, 2005.

[179] F. Cavalier et al. Reconstruction of Source Location in a Network of Gravitational Wave Interferometric Detectors. *Phys. Rev.*, D74:082004, 2006.

[180] M. Rakhmanov. Rank Deficiency and Tikhonov Regularization in the Inverse Problem for Gravitational-Wave Bursts. *Class. Quant. Grav.*, 23:S673–S686, 2006.

[181] F. Acernese et al. Improving the Timing Precision for Inspiral Signals Found by Interferometric Gravitational Wave Detectors. *Class. Quant. Grav.*, 24:S617–S625, 2007.

[182] A. C. Searle, P. J. Sutton, M. Tinto, and G. Woan. Robust Bayesian Detection of Unmodelled Bursts. *Class. Quant. Grav.*, 25:114038, 2008.

[183] L. Wen, X. Fan, and Y. Chen. Geometrical expression of the angular resolution of a network of gravitational-Wave detectors and improved localization methods. *J. Phys. Conf. Ser.*, 122:012038, 2008.

[184] J. Markowitz, M. Zanolin, L. Cadonati, and E. Katsavounidis. Gravitational Wave Burst Source Direction Estimation using Time and Amplitude Information. *Phys. Rev.*, D78:122003, 2008.

[185] A. C. Searle, P.J. Sutton, and M. Tinto. Bayesian Detection of Unmodeled Bursts of Gravitational Waves. *Class. Quant. Grav.*, 26:155017, 2009.

[186] L. Wen and Y. Chen. Geometrical Expression for the Angular Resolution of a Network of Gravitational-Wave Detectors. *Phys. Rev.*, D81:082001, 2010.

[187] G. de Vaucouleurs. Classification and Morphology of External Galaxies. *Handbuch der Physik*, 53:275–310, 1959.

[188] B. Abbott et al. Advanced LIGO Reference Design (LIGO Tech. Rep. M060056). 2007. https://dcc.ligo.org/cgi-bin/DocDB/ShowDocument?docid=m060056.

[189] R. O'Shaughnessy, V. Kalogera, and K. Belczynski. Binary Compact Object Coalescence Rates: The Role of Elliptical Galaxies. *Astrophys. J.*, 716:615–633, 2010.

[190] HEALPix. *http://healpix.jpl.nasa.gov/*, 2013.

[191] T. Accadia et al. Virgo: A Laser Interferometer to Detect Gravitational Waves. *JINST*, 7:P03012, 2012.

[192] Virgo Collaboration. Advanced Virgo Baseline Design, 2009. https://tds.ego-gw.it/itf/tds/file.php?callFile=VIR-0027A-09.pdf.

[193] F. Yuan and C.W. Akerlof. Astronomical Image Subtraction by Cross-Convolution. *arXiv:0801.0336*, 2008.

[194] E. S. Rykoff, S.A. Yost, H.A. Krimm, F. Aharonian, C.W. Akerlof, et al. Prompt Optical Detection of GRB 050401 with ROTSE-IIIa. *Astrophys.J.*, 631:L121–L124, 2005.

[195] R. M. Quimby, J. C. Wheeler, P. Hoflich, C. W. Akerlof, P. J. Brown, et al. SN 2006bp: Probing the Shock Breakout of a Type II-P Supernova. *Astrophys.J.*, 666:1093–1107, 2007.

[196] E.S. Rykoff, F. Aharonian, C.W. Akerlof, M.C.B. Ashley, S.D. Barthelmy, et al. Looking Into the Fireball: ROTSE-III and Swift Observations of Early GRB Afterglows. *Astrophys.J.*, 702:489–505, 2009.

[197] W. B. Atwood, A. A. Abdo, M. Ackermann, W. Althouse, B. Anderson, M. Axelsson, L. Baldini, J. Ballet, D. L. Band, G. Barbiellini, and et al. The Large Area Telescope on the Fermi Gamma-Ray Space Telescope Mission. *Astrophys.J.*, pages 1071–1102, 2009.

[198] S. Fairhurst. Source Localization with an Advanced Gravitational Wave Detector Network. *Class.Quant.Grav.*, 28:105021, 2011.

[199] L.K. Nuttall and P.J. Sutton. Identifying the Host Galaxy of Gravitational Wave Signals. *Phys. Rev.*, D82:102002, 2010.

[200] J.S. Bloom, J.W. Richards, P.E. Nugent, R.M. Quimby, M.M. Kasliwal, et al. Automating Discovery and Classification of Transients and Variable Stars in the Synoptic Survey Era. *arXiv:1106.5491*, 2011.

[201] R. Kehoe, C. Akerlof, R. Balsano, S. Barthelmy, J. Bloch, et al. Prompt Optical Emission from Gamma-Ray Bursts. *arXiv:9909219*, 1999.

[202] D.A. Smith, C. Akerlof, M.C.B. Ashley, D. Casperson, G. Gisler, et al. The ROTSE-IIIa Telescope System. *AIP Conf.Proc.*, 662:514–516, 2003.

[203] E. Bertin and S. Arnouts. SExtractor: Software for Source Extraction. *Astron. Astrophys. Suppl. Ser.*, 117:393–404, 1996.

[204] F. Yuan. PhD Thesis: Chasing the Brightest Cosmic Explosions with ROTSE-III. *http://hdl.handle.net/2027.42/75873*, 2010.

[205] SIMBAD. *http://simbad.u-strasbg.fr/simbad/*, 2012.

[206] Minor Planet Checker. *http://scully.cfa.harvard.edu/cgi-bin/checkmp.cgi*, 2012.

[207] SDSS. *http://www.sdss.org/*, 2012.

[208] 2MASS. *http://www.ipac.caltech.edu/2mass/*, 2012.

[209] DSS. *http://archive.stsci.edu/cgi-bin/dssform*, 2012.

[210] A. Baykal, U. Kiziloglu, N. Kiziloglu, S. Balman, and S. C. Inam. X-ray Outburst of 4U 0115+634 and ROTSE Observations of its Optical Counterpart V635 Cas. *Astron.Astrophys.*, 2005.

[211] S. Gezari, J.P. Halpern, D. Grupe, F. Yuan, R. Quimby, et al. Discovery of the Ultra-Bright Type II-L Supernova 2008es. *Astrophys.J.*, 690:1313–1321, 2009.

[212] E. Chatzopoulos, J. Craig Wheeler, J. Vinko, R. Quimby, E.L. Robinson, et al. SN2008am: A Super-Luminous Type IIn Supernova. *Astrophys.J.*, 729:143, 2011.

[213] IDL. *http://www.exelisvis.com/language/en-us/productsservices/idl.aspx*, 2012.

[214] IDL Virtual Machine. *http://www.exelisvis.com/language/en-us/productsservices/idl/idlmodules/idlvirtualmachine.aspx*, 2012.

[215] Condor. *http://research.cs.wisc.edu/condor/*, 2012.

[216] L.K. Nuttall et al. The Analysis of ROTSE Images of Potential Counterparts to Gravitational Wave Events. *J.Phys.:Conf.Ser*, 363:012033, 2012.

[217] Bruno Leibundgut. Optical light curves of supernovae. In Juan-Mara Marcaide and Kurt W. Weiler, editors, *Cosmic Explosions*, volume 99 of *Springer Proceedings in Physics*, pages 173–182. Springer Berlin Heidelberg, 2005. 10.1007/3-540-26633-X23.

[218] D.J. White et al. Estimating Transient Detection Efficiency in Electromagnetic Follow Up Searches. *J.Phys.:Conf.Ser*, 363:012036, 2012.

[219] A. Franckowiak et al. Optical Follow-Up of High-Energy Neutrinos Detected by IceCube. *arXiv:0909.0631*, 2009.

[220] R. Abbasi et al. Searching for soft relativistic jets in Core-collapse Supernovae with the IceCube Optical Follow-up Program. *Astron.Astrophys.*, 539:A60, 2012.

[221] Blind Injection Stress-Tests LIGO and VIRGO's Search for Gravitational Waves. *http://www.ligo.org/news/blind-injection.php*, 2013.

[222] A. Clocchiatti, N. B. Suntzeff, R. Covarrubias, and P. Candia. The Ultimate Light Curve of SN 1998bw/GRB 980425. *Astron.J.*, 141:163, 2011.

[223] B.D. Metzger, A.L. Piro, and E. Quataert. Time-Dependent Models of Accretion Disks Formed from Compact Object Mergers. *MNRAS*, 390:781, 2008.

[224] Afterglow Library. *http://cosmo.nyu.edu/afterglowlibrary/index.html*, 2012.

[225] L.K. Nuttall et al. Large-Scale Image Processing with the ROTSE Pipeline for Follow-Up of Gravitational Wave Events. *arXiv:1211.6713*, 2012.